



nanomaterials

Nanomaterials for Chemical Engineering

Edited by
Meiwen Cao

Printed Edition of the Special Issue Published in *Nanomaterials*

Nanomaterials for Chemical Engineering

Nanomaterials for Chemical Engineering

Editor

Meiwen Cao

MDPI • Basel • Beijing • Wuhan • Barcelona • Belgrade • Manchester • Tokyo • Cluj • Tianjin



Editor

Meiwen Cao
College of Chemistry and
Chemical Engineering
China University of
Petroleum (Hua Dong)
Qingdao
China

Editorial Office

MDPI
St. Alban-Anlage 66
4052 Basel, Switzerland

This is a reprint of articles from the Special Issue published online in the open access journal *Nanomaterials* (ISSN 2079-4991) (available at: www.mdpi.com/journal/nanomaterials/special_issues/nano_chemical_engineering).

For citation purposes, cite each article independently as indicated on the article page online and as indicated below:

LastName, A.A.; LastName, B.B.; LastName, C.C. Article Title. <i>Journal Name</i> Year , <i>Volume Number</i> , Page Range.
--

ISBN 978-3-0365-7537-7 (Hbk)

ISBN 978-3-0365-7536-0 (PDF)

© 2023 by the authors. Articles in this book are Open Access and distributed under the Creative Commons Attribution (CC BY) license, which allows users to download, copy and build upon published articles, as long as the author and publisher are properly credited, which ensures maximum dissemination and a wider impact of our publications.

The book as a whole is distributed by MDPI under the terms and conditions of the Creative Commons license CC BY-NC-ND.

Contents

About the Editor	vii
Meiwen Cao	
Development of Functional Nanomaterials for Applications in Chemical Engineering Reprinted from: <i>Nanomaterials</i> 2023 , <i>13</i> , 609, doi:10.3390/nano13030609	1
Tatyana Sergeevna Sazanova, Leonid Alexandrovich Mochalov, Alexander Alexandrovich Logunov, Mikhail Alexandrovich Kudryashov, Diana Georgievna Fukina and Maksim Anatolevich Vshivtsev et al.	
Influence of Temperature Parameters on Morphological Characteristics of Plasma Deposited Zinc Oxide Nanoparticles Reprinted from: <i>Nanomaterials</i> 2022 , <i>12</i> , 1838, doi:10.3390/nano12111838	5
Rama Gaur, Syed Shahabuddin, Irfan Ahmad and Nanthini Sridewi	
Role of Alkylamines in Tuning the Morphology and Optical Properties of SnS ₂ Nanoparticles Synthesized by via Facile Thermal Decomposition Approach Reprinted from: <i>Nanomaterials</i> 2022 , <i>12</i> , 3950, doi:10.3390/nano12223950	17
Yabin Shao, Qing He, Lingling Xiang, Zibin Xu, Xiaou Cai and Chen Chen	
Strengthened Optical Nonlinearity of V ₂ C Hybrids Inlaid with Silver Nanoparticles Reprinted from: <i>Nanomaterials</i> 2022 , <i>12</i> , 1647, doi:10.3390/nano12101647	29
Hongyuan Liu, Xunjun He, Jie Ren, Jiuxing Jiang, Yongtao Yao and Guangjun Lu	
Terahertz Modulation and Ultrafast Characteristic of Two-Dimensional Lead Halide Perovskites Reprinted from: <i>Nanomaterials</i> 2022 , <i>12</i> , 3559, doi:10.3390/nano12203559	39
Lintao Wang and Jing Yang	
Zirconia-Doped Methylated Silica Membranes via Sol-Gel Process: Microstructure and Hydrogen Permselectivity Reprinted from: <i>Nanomaterials</i> 2022 , <i>12</i> , 2159, doi:10.3390/nano12132159	51
Liaqat Ali, Abdul Manan and Bagh Ali	
Maxwell Nanofluids: FEM Simulation of the Effects of Suction/Injection on the Dynamics of Rotatory Fluid Subjected to Bioconvection, Lorentz, and Coriolis Forces Reprinted from: <i>Nanomaterials</i> 2022 , <i>12</i> , 3453, doi:10.3390/nano12193453	69
Andrey V. Shkolin, Evgeny M. Strizhenov, Sergey S. Chugaev, Ilya E. Men'shchikov, Viktoriia V. Gaidamavichute and Alexander E. Grinchenko et al.	
Natural Gas Storage Filled with Peat-Derived Carbon Adsorbent: Influence of Nonisothermal Effects and Ethane Impurities on the Storage Cycle Reprinted from: <i>Nanomaterials</i> 2022 , <i>12</i> , 4066, doi:10.3390/nano12224066	89
Chenxiaoyu Zhang, Shaobin Yang, Xu Zhang, Yingkai Xia and Jiarui Li	
Extended Line Defect Graphene Modified by the Adsorption of Mn Atoms and Its Properties of Adsorbing CH ₄ Reprinted from: <i>Nanomaterials</i> 2022 , <i>12</i> , 697, doi:10.3390/nano12040697	113
Veena Sodha, Syed Shahabuddin, Rama Gaur, Irfan Ahmad, Rajib Bandyopadhyay and Nanthini Sridewi	
Comprehensive Review on Zeolite-Based Nanocomposites for Treatment of Effluents from Wastewater Reprinted from: <i>Nanomaterials</i> 2022 , <i>12</i> , 3199, doi:10.3390/nano12183199	131

Qiuming Zhang, Xin Liao, Shaobo Liu, Hao Wang, Yin Zhang and Yongxiang Zhao Tuning Particle Sizes and Active Sites of Ni/CeO ₂ Catalysts and Their Influence on Maleic Anhydride Hydrogenation Reprinted from: <i>Nanomaterials</i> 2022 , <i>12</i> , 2156, doi:10.3390/nano12132156	161
Shaobo Liu, Xin Liao, Qiuming Zhang, Yin Zhang, Hao Wang and Yongxiang Zhao Crystal-Plane and Shape Influences of Nanoscale CeO ₂ on the Activity of Ni/CeO ₂ Catalysts for Maleic Anhydride Hydrogenation Reprinted from: <i>Nanomaterials</i> 2022 , <i>12</i> , 762, doi:10.3390/nano12050762	179
Yihao Li, Hepan Zhao, Wei Xue, Fang Li and Zhimiao Wang Transesterification of Glycerol to Glycerol Carbonate over Mg-Zr Composite Oxide Prepared by Hydrothermal Process Reprinted from: <i>Nanomaterials</i> 2022 , <i>12</i> , 1972, doi:10.3390/nano12121972	195
Ana Luisa Farias Rocha, Ronald Zico de Aguiar Nunes, Robert Saraiva Matos, Henrique Duarte da Fonseca Filho, Jaqueline de Araújo Bezerra and Alessandra Ramos Lima et al. Alternative Controlling Agent of <i>Theobroma grandiflorum</i> Pests: Nanoscale Surface and Fractal Analysis of Gelatin/PCL Loaded Particles Containing <i>Lippia origanoides</i> Essential Oil Reprinted from: <i>Nanomaterials</i> 2022 , <i>12</i> , 2712, doi:10.3390/nano12152712	211
Yujie Yang, Zhen Liu, Hongchao Ma and Meiwen Cao Application of Peptides in Construction of Nonviral Vectors for Gene Delivery Reprinted from: <i>Nanomaterials</i> 2022 , <i>12</i> , 4076, doi:10.3390/nano12224076	233
Syed Sadiq Ali, Agus Arsad, Kenneth L. Roberts and Mohammad Asif Effect of Inlet Flow Strategies on the Dynamics of Pulsed Fluidized Bed of Nanopowder Reprinted from: <i>Nanomaterials</i> 2023 , <i>13</i> , 304, doi:10.3390/nano13020304	255
Silvia Sfameni, Tim Lawnick, Giulia Rando, Annamaria Visco, Torsten Textor and Maria Rosaria Plutino Functional Silane-Based Nanohybrid Materials for the Development of Hydrophobic and Water-Based Stain Resistant Cotton Fabrics Coatings Reprinted from: <i>Nanomaterials</i> 2022 , <i>12</i> , 3404, doi:10.3390/nano12193404	271

About the Editor

Meiwen Cao

Meiwen Cao received his Ph.D. degree in physical chemistry from the Institute of Chemistry, Chinese Academy of Sciences, in 2008 under the supervision of Prof. Yilin Wang. Then he joined the faculty of China University of Petroleum (East China) and works as an associate professor. Between 2017 and 2018, he worked as a senior visiting scholar in the University of Manchester with Prof. Jianren Lu. His research focuses on peptide-based supramolecular assembly for functional materials fabrication and application in drug delivery and gene therapy.



Editorial

Development of Functional Nanomaterials for Applications in Chemical Engineering

Meiwen Cao

State Key Laboratory of Heavy Oil Processing, Department of Biological and Energy Chemical Engineering, College of Chemistry and Chemical Engineering, China University of Petroleum (East China), Qingdao 266580, China; mwcao@upc.edu.cn

Nanomaterials are materials with particle sizes of less than 100 nm in at least one of their dimensions. The special structure of nanomaterials endows them unique characteristics different from those of bulk materials and individual atoms, which are known as surface effect, quantum size effect, and macroscopic quantum tunneling effect, etc. Therefore, nanomaterials usually exhibit novel optical, acoustic, electrical, magnetic, thermal, and catalytic properties, and have been widely applied in various fields. Nowadays, the production and application of nanomaterials in the chemical industry are very common, especially in the fields of new catalysts, selective adsorbents, corrosion prevention coatings, environmental protection, and other biopharmaceuticals and medical instruments, playing important roles in promoting the development of society and human beings.

This Special Issue, Nanomaterials for Chemical Engineering, focuses on the development of functional nanomaterials in the chemical engineering field. It collects 14 original research papers and 2 comprehensive review papers by the excellent scientists from relevant fields, covering the topics of development of novel nanomaterials and synthesis methods, experimental characterization, and computational modeling studies, as well as exploitation in devices and practical applications.

The synthesis, characterization, and property investigation of new nanomaterials are eternal prerequisites to meet the needs of nanotechnology development for chemical engineering applications. Sazanova et al. [1] reported the synthesis and characterization of zinc oxide (ZnO) nanoparticles by plasma-enhanced chemical vapor deposition, establishing that the synthesizing parameters of zinc source temperature and reactor temperature can effectively control the size and morphology of ZnO nanostructures. Gaur and coworkers [2] synthesized SnS₂ nanoparticles using a thermal decomposition approach and produced novel morphologies (e.g., nanoparticles, nanoplates, and flower-like morphologies assembled from flakes) by using different alkylamines as capping agents. Shao and coworkers [3] synthesized the Ag@MXene hybrids and studied their nonlinear optical characteristics, making great contributions to the development of ultrathin optoelectronic nanodevices and optical limiters. Liu et al. [4] fabricated 2D R-P type (PEA)₂(MA)₂Pb₃I₁₀ perovskite films on quartz substrates and studied their terahertz and ultrafast photoelectric response characteristics, demonstrating their potential applications in solar cells and photoelectric devices. Wang and coworkers [5] prepared methyl-modified ZrO₂-SiO₂ (ZrO₂-MSiO₂) membranes via the sol-gel method and characterized their physical-chemical properties. With excellent hydrothermal stability and regeneration capability, the ZrO₂-MSiO₂ membranes have significant potential in steam-stable hydrogen permselective applications. By incorporating Gyrotactic microbes to prevent the bioconvection of small particles and to improve consistency, Ali et al. [6] discussed the relevance of Lorentz and Coriolis forces on the kinetics of gyrotory Maxwell nanofluids flowing against a continually stretched surface, contributing to the areas of elastomers, mineral productivity, paper-making, biosensors, and biofuels.

Citation: Cao, M. Development of Functional Nanomaterials for Applications in Chemical Engineering. *Nanomaterials* **2023**, *13*, 609. <https://doi.org/10.3390/nano13030609>

Received: 22 January 2023

Accepted: 1 February 2023

Published: 3 February 2023



Copyright: © 2023 by the author. Licensee MDPI, Basel, Switzerland. This article is an open access article distributed under the terms and conditions of the Creative Commons Attribution (CC BY) license (<https://creativecommons.org/licenses/by/4.0/>).

Many nanomaterials are highly porous in structure and have high specific surface area, which can be used for gas adsorption in the aims of purification and/or storage. Two research works in this Special Issue studied the adsorption and storage of natural gases on defined nanomaterials. [7,8] First, Shkolin et al. [7] synthesized an active carbon nanomaterial from cheap peat raw materials and investigated its structural–energetic and adsorption properties towards natural gas (ANG). The study provides insights into the solution for improving the safety and storage capacity of low-pressure gas storage systems. Second, Zhang et al. [8] reported the CH₄ adsorption properties on extended line defect (ELD) graphene according to the first principles of density functional theory (DFT). The Mn modification of ELD graphene was found to significantly affect the CH₄ adsorption. The specific molecular configurations and adsorption behaviors were discussed in detail in the paper. In another paper, Sodha et al. [9] presented a comprehensive review on zeolite-based nanocomposites for the treatment of effluents from wastewater. The review provides the basic knowledge about zeolites and highlights the types, synthesis, and removal mechanisms of zeolite-based materials for wastewater treatment along with the research gaps, being helpful for worldwide research on this topic.

Nanomaterials as applied as catalysts play important roles in many chemical engineering fields, being able to control reaction time, improve reaction speed and efficiency, save resources and energy, and improve economic benefits. Therefore, the study on catalytic nanomaterials attracts great research interests. The Special Issue presents two works focusing on fabrication of CeO₂-composited catalysts for maleic anhydride hydrogenation (MAH). Zhang et al. [10] prepared CeO₂-supported Ni catalysts with different Ni loadings and particle sizes by the impregnation method and investigated their hydrogenation performance. The work provides a theoretical and experimental basis for the preparation of high-activity catalysts for MAH. Liu et al. [11] synthesized CeO₂ supports with various shapes (e.g., nanocubes, nanorods, and nanoparticles) by using the hydrothermal technique, which were employed for supporting Ni species as catalysts for MAH. The study demonstrated morphology-dependent performances of the Ni/CeO₂ catalysts, which is helpful for developing novel catalysts for MAH. In another work, Li and coworkers [12] reported the synthesis of a series of Mg–Zr composite oxide catalysts by the hydrothermal method, aiming to catalyze the transesterification of glycerol with dimethyl carbonate to produce glycerol carbonate. The effects of the preparation method and Mg/Zr ratio on the catalytic performance and the deactivation of the catalysts were systematically investigated and discussed.

Nanomaterials have also found extensive applications in the fields of daily chemical products, cosmetics, pesticides, biomedicine etc., where the nanomaterials can be used as nanocarriers to load various active components for targeted delivery and controlled release. Rocha et al. [13] performed a systematic study on polymeric particles based on gelatin and poly- ϵ -caprolactone (PCL) containing essential oil from *Lippia organoides*. The developed biocides have high physical stability and particle surface microtexture as well as pronounced bioactivity, which are efficient alternative controlling agents of *Conotrachelus humeropictus* and *Moniliophthora perniciosa*, the main pests of *Theobroma grandiflorum*. Yang et al. [14] presented a comprehensive review on peptide-based nanocarriers for gene delivery. The review puts forward discussion on the biological barriers for gene delivery, the peptide molecular design and assembly with DNA, the targeted delivery and controlled release of genome, the structure–function relationships of the delivery systems, and the current challenges and future perspectives in related fields, providing guidance towards the rational design and development of nonviral gene delivery systems.

Nanomaterials can also be engineered into the industrial production so as to improve the production process, elevate production efficiency, and optimize product performance. The work by Ali and coworkers [15] studied the effect of inlet flow strategies on the dynamics of pulsed fluidized bed of nanopowder. They changed the conventional single-drainage (SD) flow strategy to the modified double-drainage (MDD) flow strategy, which improved the production process by purging the primary flow during the non-flow period

of the pulse to eliminate pressure buildup in the inlet flow line while providing a second drainage path to the residual gas. Sfameni et al. [16] reported the development of an efficient and eco-friendly procedure to form highly hydrophobic surfaces on cotton fabrics. By using a two-step treatment procedure, that is, first producing a hybrid silane film on cotton fabrics and then modifying with low-surface-energy components, the cotton fabrics were endowed with excellent water repellency. The work provides a new sustainable approach for fabric finishing and treatment.

In short, this Special Issue is expected to be interesting and enriching for readers by virtue of featuring all of the abovementioned high-quality original research works and comprehensive review papers. We give our sincere thanks to the excellent scholars that have made contributions. Currently, we are developing the second volume of the Special Issue, that is, “Nanomaterials for Chemical Engineering II”. We welcome more excellent scholars to submit their excellent works in the area of synthesis and application of functional nanomaterials for chemical engineering.

Acknowledgments: This work was supported by the National Natural Science Foundation of China (22172194, 21872173).

Conflicts of Interest: The authors declare no conflict of interests.

References

1. Sazanova, T.S.; Mochalov, L.A.; Logunov, A.A.; Kudryashov, M.A.; Fukina, D.G.; Vshivtsev, M.A.; Prokhorov, I.O.; Yunin, P.A.; Smorodin, K.A.; Atlaskin, A.A.; et al. Influence of Temperature Parameters on Morphological Characteristics of Plasma Deposited Zinc Oxide Nanoparticles. *Nanomaterials* **2022**, *12*, 1838. [CrossRef] [PubMed]
2. Gaur, R.; Shahabuddin, S.; Ahmad, I.; Sridewi, N. Role of Alkylamines in Tuning the Morphology and Optical Properties of SnS₂ Nanoparticles Synthesized by via Facile Thermal Decomposition Approach. *Nanomaterials* **2022**, *12*, 3950. [CrossRef] [PubMed]
3. Shao, Y.; He, Q.; Xiang, L.; Xu, Z.; Cai, X.; Chen, C. Strengthened Optical Nonlinearity of V₂C Hybrids Inlaid with Silver Nanoparticles. *Nanomaterials* **2022**, *12*, 1647. [CrossRef] [PubMed]
4. Liu, H.; He, X.; Ren, J.; Jiang, J.; Yao, Y.; Lu, G. Terahertz Modulation and Ultrafast Characteristic of Two-Dimensional Lead Halide Perovskites. *Nanomaterials* **2022**, *12*, 3559. [CrossRef] [PubMed]
5. Wang, L.; Yang, J. Zirconia-Doped Methylated Silica Membranes via Sol-Gel Process: Microstructure and Hydrogen Permselectivity. *Nanomaterials* **2022**, *12*, 2159. [CrossRef] [PubMed]
6. Ali, L.; Manan, A.; Ali, B. Maxwell Nanofluids: FEM Simulation of the Effects of Suction/Injection on the Dynamics of Rotatory Fluid Subjected to Bioconvection, Lorentz, and Coriolis Forces. *Nanomaterials* **2022**, *12*, 3453. [CrossRef] [PubMed]
7. Shkolin, A.V.; Strizhenov, E.M.; Chugaev, S.S.; Men'shchikov, I.E.; Gaidamavichute, V.V.; Grinchenko, A.E.; Zherdev, A.A. Natural Gas Storage Filled with Peat-Derived Carbon Adsorbent: Influence of Nonisothermal Effects and Ethane Impurities on the Storage Cycle. *Nanomaterials* **2022**, *12*, 4066. [CrossRef] [PubMed]
8. Zhang, C.; Yang, S.; Zhang, X.; Xia, Y.; Li, J. Extended Line Defect Graphene Modified by the Adsorption of Mn Atoms and Its Properties of Adsorbing CH₄. *Nanomaterials* **2022**, *12*, 697. [CrossRef] [PubMed]
9. Sodha, V.; Shahabuddin, S.; Gaur, R.; Ahmad, I.; Bandyopadhyay, R.; Sridewi, N. Comprehensive Review on Zeolite-Based Nanocomposites for Treatment of Effluents from Wastewater. *Nanomaterials* **2022**, *12*, 3199. [CrossRef]
10. Zhang, Q.; Liao, X.; Liu, S.; Wang, H.; Zhang, Y.; Zhao, Y. Tuning Particle Sizes and Active Sites of Ni/CeO₂ Catalysts and Their Influence on Maleic Anhydride Hydrogenation. *Nanomaterials* **2022**, *12*, 2156. [CrossRef] [PubMed]
11. Liu, S.; Liao, X.; Zhang, Q.; Zhang, Y.; Wang, H.; Zhao, Y. Crystal-Plane and Shape Influences of Nanoscale CeO₂ on the Activity of Ni/CeO₂ Catalysts for Maleic Anhydride Hydrogenation. *Nanomaterials* **2022**, *12*, 762. [CrossRef] [PubMed]
12. Li, Y.; Zhao, H.; Xue, W.; Li, F.; Wang, Z. Transesterification of Glycerol to Glycerol Carbonate over Mg-Zr Composite Oxide Prepared by Hydrothermal Process. *Nanomaterials* **2022**, *12*, 1972. [CrossRef] [PubMed]
13. Rocha, A.L.F.; de Aguiar Nunes, R.Z.; Matos, R.S.; da Fonseca Filho, H.D.; de Araújo Bezerra, J.; Lima, A.R.; Guimarães, F.E.G.; Pamplona, A.M.; Majolo, C.; de Souza, M.G.; et al. Alternative Controlling Agent of Theobroma grandiflorum Pests: Nanoscale Surface and Fractal Analysis of Gelatin/PCL Loaded Particles Containing *Lippia origanoides* Essential Oil. *Nanomaterials* **2022**, *12*, 2712. [CrossRef]
14. Yang, Y.; Liu, Z.; Ma, H.; Cao, M. Application of Peptides in Construction of Nonviral Vectors for Gene Delivery. *Nanomaterials* **2022**, *12*, 4076. [CrossRef] [PubMed]

15. Ali, S.S.; Arsad, A.; Roberts, K.L.; Asif, M. Effect of Inlet Flow Strategies on the Dynamics of Pulsed Fluidized Bed of Nanopowder. *Nanomaterials* **2023**, *13*, 304. [CrossRef]
16. Sfameni, S.; Lawnick, T.; Rando, G.; Visco, A.; Textor, T.; Plutino, M.R. Functional Silane-Based Nanohybrid Materials for the Development of Hydrophobic and Water-Based Stain Resistant Cotton Fabrics Coatings. *Nanomaterials* **2022**, *12*, 3404. [CrossRef] [PubMed]

Disclaimer/Publisher's Note: The statements, opinions and data contained in all publications are solely those of the individual author(s) and contributor(s) and not of MDPI and/or the editor(s). MDPI and/or the editor(s) disclaim responsibility for any injury to people or property resulting from any ideas, methods, instructions or products referred to in the content.

Article

Influence of Temperature Parameters on Morphological Characteristics of Plasma Deposited Zinc Oxide Nanoparticles

Tatyana Sergeevna Sazanova ^{1,*}, Leonid Alexandrovich Mochalov ², Alexander Alexandrovich Logunov ², Mikhail Alexandrovich Kudryashov ², Diana Georgievna Fukina ², Maksim Anatolevich Vshivtsev ², Igor Olegovich Prokhorov ², Pavel Andreevich Yunin ³, Kirill Alexandrovich Smorodin ², Artem Anatolevich Atlaskin ⁴ and Andrey Vladimirovich Vorotyntsev ^{1,2}

¹ Laboratory of Membrane and Catalytic Processes, Nanotechnology and Biotechnology Department, Nizhny Novgorod State Technical University n.a. R.E. Alekseev, Minin Str. 24, 603950 Nizhny Novgorod, Russia; an.vorotyntsev@gmail.com

² Chemical Engineering Laboratory, Research Institute for Chemistry, Lobachevsky State University of Nizhny Novgorod, Gagarin Ave. 23, 603022 Nizhny Novgorod, Russia; mochalovleo@gmail.com (L.A.M.); alchemlog@gmail.com (A.A.L.); mikhail.kudryashov1986@yandex.ru (M.A.K.); dianafuk@yandex.ru (D.G.F.); mvshivtsev@mail.ru (M.A.V.); igorprokhorov1998@yandex.ru (I.O.P.); smorodin.kirill.a@gmail.com (K.A.S.)

³ Department for Technology of Nanostructures and Devices, Institute for Physics of Microstructures of the Russian Academy of Science, Academic Str. 7, Afonino, 603087 Nizhny Novgorod, Russia; yunin@ipmras.ru

⁴ Laboratory of SMART Polymeric Materials and Technologies, Mendeleev University of Chemical Technology, Miusskaya Sq. 9, 125047 Moscow, Russia; atlaskin.a.a@muctr.ru

* Correspondence: yarymova.tatyana@yandex.ru

Citation: Sazanova, T.S.; Mochalov, L.A.; Logunov, A.A.; Kudryashov, M.A.; Fukina, D.G.; Vshivtsev, M.A.; Prokhorov, I.O.; Yunin, P.A.; Smorodin, K.A.; Atlaskin, A.A.; et al. Influence of Temperature Parameters on Morphological Characteristics of Plasma Deposited Zinc Oxide Nanoparticles. *Nanomaterials* **2022**, *12*, 1838. <https://doi.org/10.3390/nano12111838>

Academic Editor: Meiwen Cao

Received: 5 May 2022

Accepted: 25 May 2022

Published: 27 May 2022

Publisher's Note: MDPI stays neutral with regard to jurisdictional claims in published maps and institutional affiliations.



Copyright: © 2022 by the authors. Licensee MDPI, Basel, Switzerland. This article is an open access article distributed under the terms and conditions of the Creative Commons Attribution (CC BY) license (<https://creativecommons.org/licenses/by/4.0/>).

Abstract: Zinc oxide nanoparticles were obtained by plasma-enhanced chemical vapor deposition (PECVD) under optical emission spectrometry control from elemental high-purity zinc in a zinc–oxygen–hydrogen plasma-forming gas mixture with varying deposition parameters: a zinc source temperature, and a reactor temperature in a deposition zone. The size and morphological parameters of the zinc oxide nanopowders, structural properties, and homogeneity were studied. The study was carried out with use of methods such as scanning electron microscopy, X-ray structural analysis, and Raman spectroscopy, as well as statistical methods for processing and analyzing experimental data. It was established that to obtain zinc oxide nanoparticles with a given size and morphological characteristics using PECVD, it is necessary (1) to increase the zinc source temperature to synthesize more elongated structures in one direction (and vice versa), and (2) to decrease the reactor temperature in the deposition zone to reduce the transverse size of the deposited structures (and vice versa), taking into account that at relatively low temperatures instead of powder structures, films can form.

Keywords: zinc oxide; nanoparticles; PECVD; structure; morphology

1. Introduction

Currently, nanosized zinc oxide is one of the important materials in development for various fields of medicine and industry. Zinc oxide is a unique material because of its advantages such as cost efficiency and variable engineering properties, good biocompatibility and antibacterial properties, adjustable band-gap and particle size/shape, and many other features [1], making it applicable in a wide range of fields. In particular, zinc oxide nanoparticles can be used as: excellent antibacterial, antioxidant, antidiabetic and tissue regenerating agents [2]; innovative anticancer agents [3]; material for photocatalytic degradation of organic pollutant [4,5]; material for manufacture of electronic devices over flexible substrates [6]; an electron transport layer for quantum dot light-emitting diodes [7]; nanocomposite electrode material for supercapacitor [8]; and material for the production of gas sensors [9].

Nanosized zinc oxide is obtained in the form of rods (threads), ridges, honeycombs, rings, ribbons, springs (spirals), cells, tetrapods, as well as thin films and coatings. For the

synthesis of all these numerous modifications, numerous preparation methods were proposed, of which two main groups can be distinguished: physical (sputtering, laser ablation, electrospraying, ball milling, electron beam evaporation, etc.) and chemical (microemulsion technique, sol–gel method, co-precipitation method, hydrothermal method, polyol method, chemical vapor deposition, etc.). The main advantage of the chemical methods is the possibility of obtaining particles with a given size, composition, and structure [10]. This is important because the shape and size of nanoparticles directly affects their properties. For example, Hammad T. and co-workers [11] reported changing a red shift from 3.62 to 3.33 eV when the average particle size of ZnO nanoparticles was increased from 11 to 87 nm, respectively. In another work, Mornani E. and co-workers [12] reported a change in the band gap from 4.45 to 4.08 eV with an increase in the average size of ZnO nanoparticles from 46 to 66 nm, respectively. Similarly, controlling nanoparticle sizes to determine their optimal range is significant for mechanical properties of nanoparticle assemblies [13], the rate of gas photofixation using powder catalysts based on nanoparticles [14], and others [15–19].

One of the most promising methods for producing zinc oxide nanoparticles of a given size and shape is plasma-enhanced chemical vapor deposition (PECVD). Plasma initiation makes it possible to significantly reduce the temperature of reactor walls and a deposition zone, as well as to eliminate the pollution possibility of the final product with equipment materials and to control the deposition zone temperature over a wider range, thereby setting the conditions for structure growth. Plasma initiation also makes it possible to achieve 100% conversion of initial substances due to establishing kinetic dependencies during plasma–chemical reactions. Thus, PECVD provides controllability, one stage, cost-effectiveness, high purity of resulting materials, as well as versatility and process scalability [20–22]. However, to widely use PECVD in the preparation of nanosized zinc oxide with given morphology, it is necessary to fundamentally study the influence of process parameters on the resulting product.

This work is devoted to studying zinc oxide nanoparticles obtained by the PECVD method from elemental high-purity zinc in a zinc–oxygen–hydrogen plasma-forming gas mixture with varying deposition parameters, namely a zinc source temperature and a reactor temperature in a deposition zone.

2. Experimental Section

2.1. Materials

Zinc of 5N purity (Changsha Rich Nonferrous Metals Co Ltd., Changsha, Hunan, China), high purity hydrogen (99.9999%) and oxygen 6.0 (99.9999%) (Horst Technologies Ltd., Dzerzhinsk, Nizhny Novgorod region, Russia) were used as components of a plasma-forming mixture. Hydrogen was used as a carrier gas, which also acted as a temperature stabilizer and regulator of the nanostructure growth.

2.2. Plasma–Chemical Synthesis

The scheme of a plasma–chemical installation is shown in Figure 1. The installation consisted of a gas supply system, a pumping system, a cuvette with initial zinc, and a pear-shaped plasma–chemical reactor made of high-purity quartz glass with a total volume of about 1200 cm³. An external inductor, an RF generator (with an operating frequency of 40.68 MHz and a maximum power of 500 W), and a universal matching device were used to ignite an inductively coupled or mixed nonequilibrium plasma discharge.

A loading cuvette in the form of a boat with metal zinc was placed in a furnace with an external resistive heater and an internal thermocouple. A tank for collecting zinc oxide powder was placed into the reactor through a stainless-steel vacuum loading flange and was installed perpendicular to the carrier gas flow on a special movable holder. The loading cuvette, the powder tank, and the movable holder were made of high-purity quartz glass. To cool the reactor in the deposition zone, a circulation thermostat was used.

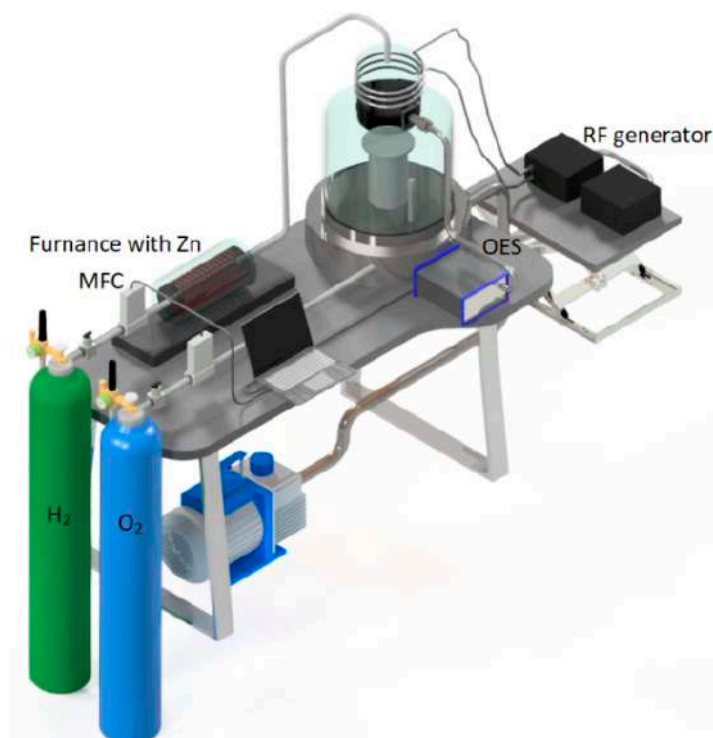


Figure 1. The scheme of a plasma–chemical installation with a pear-shaped reactor.

High-pure granulated Zn was loaded into the quartz furnace. High-pure H₂ was blown through the Zn source with the constant rate of 15 mL/min. The vapors of Zn were delivered by the carrier gas via the quartz lines heated up to 550 °C with the internal diameter of 6 mm directly into the plasma zone, where the formation of ZnO materials took place. The temperature of the lines and external surface of the plasma chamber was measured by a pyrometer. The temperature of the substrate holder was found by the internal thermocouple. High-pure O₂ was fed from below towards the main carrier gas with zinc vapor directly in the plasma zone with the constant rate of 15 mL/min. The total gas flow through the plasma–chemical reactor was set equal to 30 mL/min at a total pressure in the system of 0.1 Pa. The duration of each individual experiment (with the various deposition parameters) was one hour.

Before experiments, the installation was evacuated to a pressure of 1×10^{-3} Pa for several hours to remove traces of nitrogen and water from the walls of the reactor. Then, the powder tank was closed with a magnetic diaphragm of a special design.

The installation was also equipped with a high-resolution optical emission spectrometer HR4000CJ-UV-NIR (Avantes, The Netherlands) operating in the range of 180–1100 nm to control the excited intermediate species in the gas phase during the plasma–chemical process. The upper part of the plasma chamber was equipped with two plane-parallel windows made of special quartz glass of high transparency, maintained just after the inductor where the intensity of the lines was maximal.

According to the optical emission spectroscopy (OES) data (Figure 2), the composition of the plasma-forming mixture in all experiments included Zn (I), O (I), O (II), H (I), OH (I). Zn (II) emission lines were not observed.

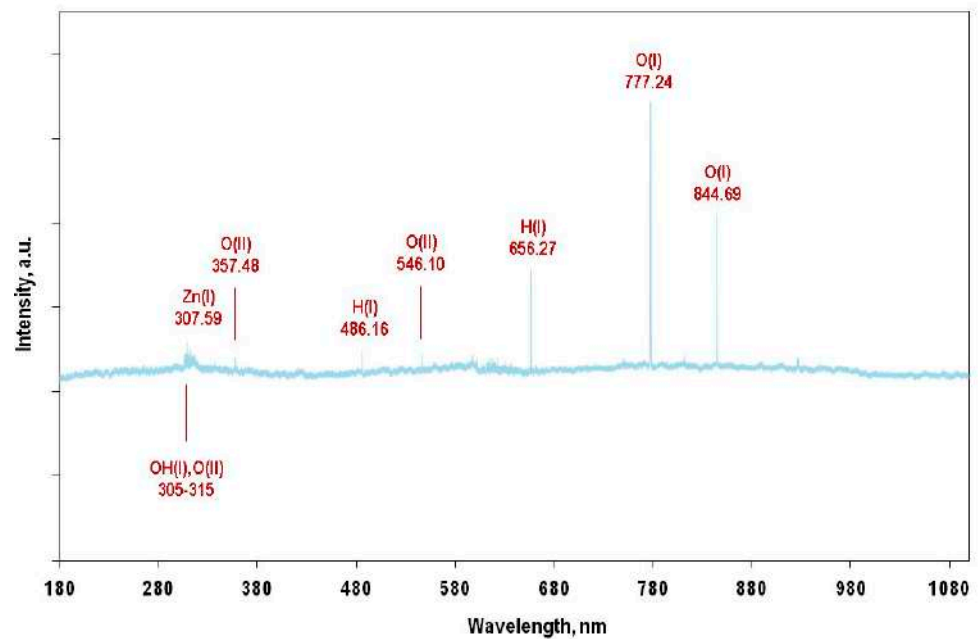


Figure 2. The optical emission spectra of the zinc–hydrogen–oxygen plasma ($\text{Zn}:\text{H}_2:\text{O}_2 = 2:1:1$).

2.3. Scanning Electron Microscopy and Energy-Dispersive X-ray Spectroscopy

The size-morphological characteristics of the zinc oxide samples were studied by scanning electron microscopy (SEM) using an electron microscope JSM-IT300LV (JEOL, Peabody, MA, USA) with an electron probe diameter of about 5 nm and a probe current of less than 0.5 nA (the operating voltage was 20 kV). SEM scanning was performed using low-energy secondary electrons and backscattered electrons under a low vacuum to eliminate the charge. As sample preparation for SEM, zinc oxide powders were applied onto carbon double-sided conductive tapes.

The size of the structures observed on SEM images was measured as the maximal diameter of their cross-section. For additional control of the measurement results, analysis of the images (determination of the average size of equivalent disk (D_{avg}) of structures' cross-section) was carried out using the method of watershed segmentation by a software SPMLab™ v5 (TopoMetrix, Santa Clara, CA, USA).

2.4. X-ray Structural Analysis

The structure of the zinc oxide samples was studied using X-ray diffraction (XRD) analysis on an X-ray diffractometer D8 Discover (Bruker, Germany) equipped with a sealed $\text{CuK}\alpha$ radiation source tube and a position-sensitive detector LynxEye. Diffraction patterns were obtained by $\theta/2\theta$ scanning in the 2θ range of $10\text{--}66^\circ$ with a step of 0.1° .

As sample preparation for the XRD analysis, a small amount of zinc oxide powders was placed in the center of a quartz disk. Then, about 3 drops of distilled water were added to the sample and it was spread to a thin layer with a glass rod. Next, the sample was placed in a desiccator to dry before the XRD analysis.

The results obtained were compared with the database PDF-2 Release 2011, namely PDF 01-071-6424 for ZnO and PDF 00-004-0831 for Zn.

2.5. Raman Spectroscopy

Raman spectra were studied on a spectroscopy complex NTEGRA Spectra Raman (NT-MDT, Moscow, Russia) using a laser with a wavelength of 473 nm. The radiation was focused by a $20\times$ objective lens with an aperture of 0.45. The laser spot diameter was 5 μm . The power of the unfocused laser radiation was controlled by a silicon photodetector 11PD100-Si (Standa Ltd., Vilnius, Lithuania) and varied in the range from 1 mW to 1 μW . The Raman spectra analysis of the samples was carried out according to the scheme for

reflection in the frequency range $80\text{--}800\text{ cm}^{-1}$ with a resolution of 0.7 cm^{-1} . As sample preparation for the Raman spectra analysis, zinc oxide powders were applied onto carbon double-sided conductive tapes. The measurements were carried out at room temperature.

2.6. Varying Temperature Parameters in Plasma–Chemical Deposition

To study the influence of a zinc source temperature on the morphology of ZnO nanoparticles, the temperature was varied from 370 to 470 °C. At the same time, the reactor temperature in the deposition zone was maintained at 250 °C. The plasma discharge power was 50 W.

To study the influence of a reactor temperature on the morphology of ZnO nanoparticles, the temperature was varied from 25 to 350 °C. At the same time, the zinc source temperature was maintained at 420 °C. The plasma discharge power was 50 W.

3. Results and Discussion

3.1. Zinc Source Temperature and Morphology of ZnO Nanoparticles

As a result of the plasma–chemical synthesis, ZnO nanoparticles with different shapes were obtained. According to the SEM images (Figure 3), the observed nanoparticles assumed a sphere-like, columnar, and rod-like shape depending on the zinc source temperature.

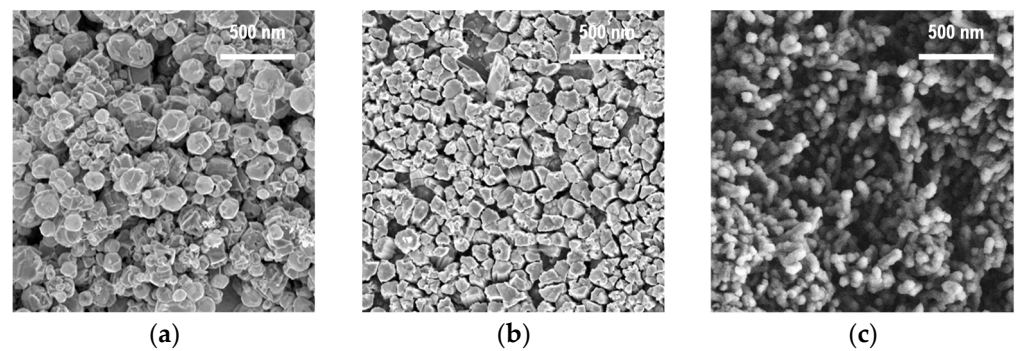


Figure 3. The SEM images of the ZnO nanopowders obtained by the PECVD method at the various zinc source temperatures: (a) 370 °C, (b) 420 °C, (c) 470 °C.

According to statistical processing of the SEM data (the sample size was 100 measurements), it was found that the average size (in the cross-section) of the deposited particles changed with an increase in the zinc source temperature, along with a variation in their shape (Figure 4).

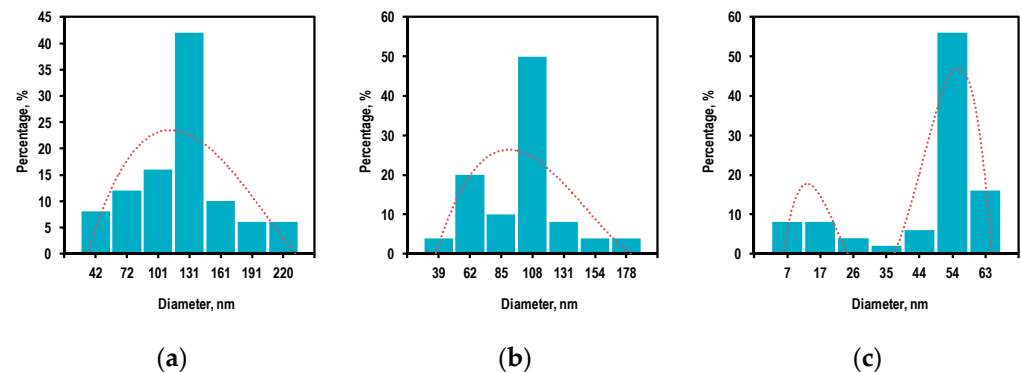


Figure 4. The transverse size distribution of the ZnO structures obtained by the PECVD method at the various zinc source temperatures: (a) 370 °C, (b) 420 °C, (c) 470 °C.

The average size of the ZnO structures decreased from 120 to 100 nm with a simultaneous decrease in the coefficient of variation from 46 to 44% caused by an increase in

temperature from 370 to 420 °C. Next, the average size of the structures approached 45 nm with a coefficient of variation of 32% caused by a further increase in temperature to 470 °C. Such a change in the transverse size of the nanoparticles can be associated with the changeable mechanism of their growth and the corresponding redistribution of the Zn and O atoms in the spherical and elongated crystal structures.

The XRD analysis results for the ZnO structures obtained by the PECVD method at the various zinc source temperatures are shown in Figure 5. The diffraction peaks corresponding to (002), (101), (102), (103), (112), (201), (004), (202) planes are characteristic of a ZnO structure [16,23–29]. Such a diffraction pattern corresponds to a hexagonal structure of the wurtzite type. [23,24,29]. No other peaks associated with impurities were observed, indicating that high-purity ZnO nanoparticles were obtained. However, the diffraction peaks corresponding to (101) and (102) planes, which match with that of pure metallic Zn [30], were observed after increasing the zinc source temperature from 420 to 470 °C (Figure 5c). This means that there was an excess of Zn in this sample.

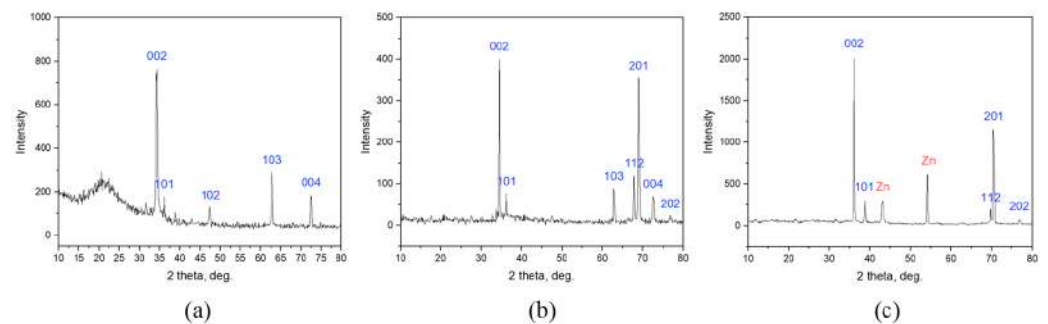


Figure 5. The XRD analysis results for the ZnO structures obtained by the PECVD method at the various zinc source temperatures: (a) 370 °C; (b) 420 °C; (c) 470 °C.

It should be noted that the XRD characterization revealed a strong preferred (002) orientation for all the obtained ZnO structures, indicating that the *c*-axis of the unit cell was aligned perpendicular to the horizontal plane of the deposition zone [28]. However, the (201) orientation became pronounced for the sample obtained at the source temperature of 420 °C (Figure 5b) and was slightly reduced with the increase in temperature from 420 to 470 °C (Figure 5c). Such a reorientation was probably related to the transition of the ZnO structures from spherical to elongated forms.

The Raman spectra for the ZnO structures obtained at the various zinc source temperatures are shown in Figure 6. The peak at about 435 cm^{-1} is typical for ZnO structures, while the peaks at about 275 cm^{-1} and 580 cm^{-1} do not correspond to ZnO normal modes. These peaks are additional vibrational modes and can be associated with defects and bond breaking, respectively [31–33].

Nevertheless, one must take into account the fact that the shape of Raman spectra depends on crystal orientation. In the case under consideration, based on the XRD data (Figure 5), the preferred orientation of the nanoparticles for all samples was (002). Moreover, for the sample obtained at the zinc source temperature of 420 °C (Figure 5b), the (201) orientation became pronounced, and the peak intensities in the Raman spectra (Figure 6) at about 275 cm^{-1} and 580 cm^{-1} had average values relative to other samples. The maximum intensities of these peaks were reached in another sample obtained at the source temperature of 470 °C, when the height of the (201) reflection on the XRD pattern (Figure 5c) was already reduced. Thus, the changes in the form of the Raman spectra can really be associated with defects and bond breaking in the case under consideration.

Analyzing the obtained Raman spectra, it can be concluded that the defectiveness of the ZnO structures (the peak at about 275 cm^{-1}) increases with the rise in the zinc source temperature. The degree of bond breaking (the peak at about 580 cm^{-1}) also has similar temperature dependence. Such a trend can be associated with increasing the Zn excess in

the obtained ZnO structures, which can be led by bond breaking, and thereby causes the formation of defects similar to interstitial Zn.

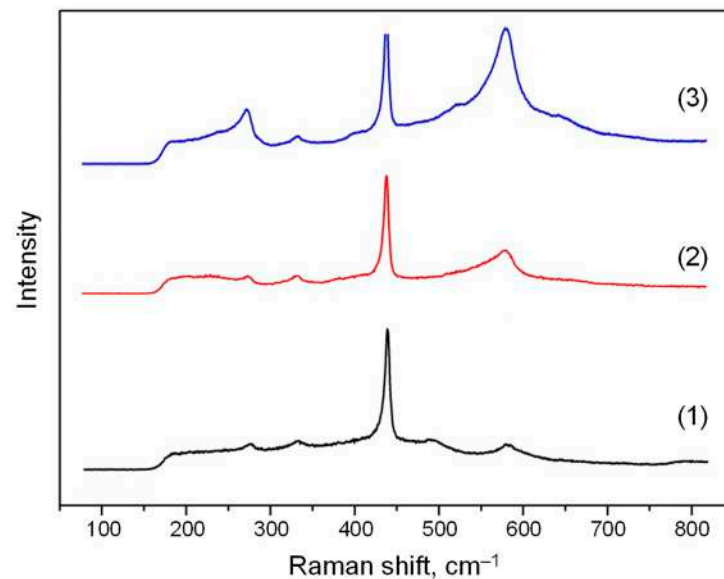


Figure 6. The Raman spectra of the ZnO structures obtained by the PECVD method at the various zinc source temperatures: (1) 370 °C, (2) 420 °C, (3) 470 °C.

3.2. Reactor Temperature and Size Distribution of ZnO Nanoparticles

As a result of the ZnO plasma–chemical synthesis at the reactor temperature in the deposition zone of 25 °C, a planar structure was formed instead of a nanoparticle one (Figure 7). At higher temperatures of the reactor deposition zone (250 and 350 °C), ZnO columnar structures were formed. Moreover, the average diameter (in cross-section) of the observed structures increased with a rise in the temperature.

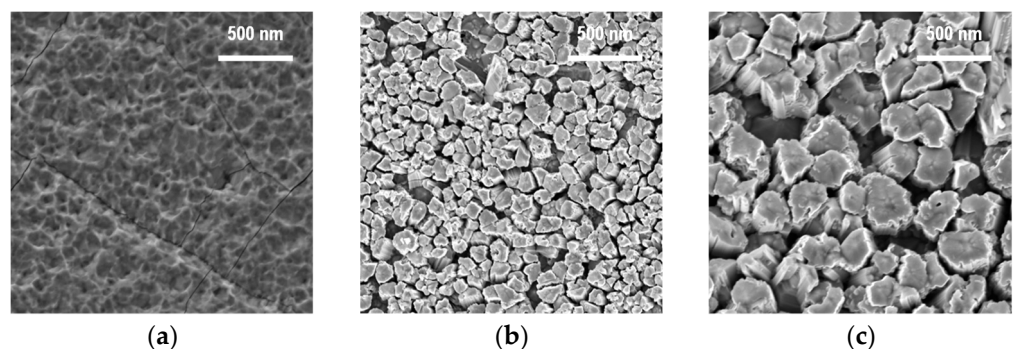


Figure 7. SEM images of ZnO nanopowders obtained by the PECVD method at various temperatures in the reactor deposition zone: (a) 25 °C, (b) 250 °C, (c) 350 °C.

According to statistical processing of the SEM data (the sample size was 100 measurements), it was established that the transverse diameter (at the widest part) of the ZnO columnar structures increased by three times with an increase in the reactor temperature in the deposition zone from 250 to 350 °C (Figure 8), and the coefficient of variation for the size range decreased from 44 to 27%.

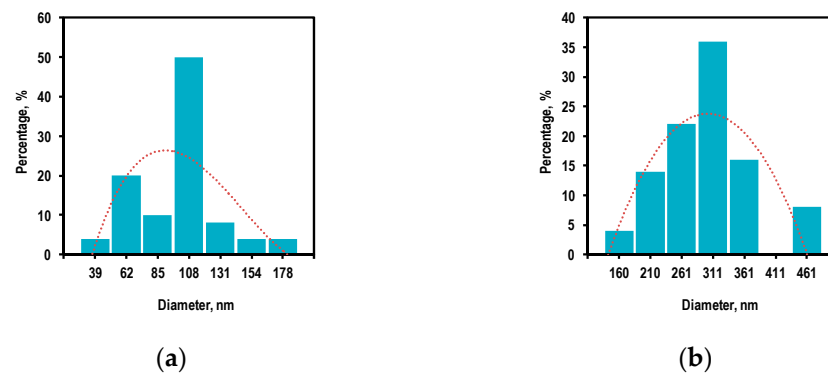


Figure 8. The transverse size distribution of the ZnO structures obtained by the PECVD method at the various temperatures in the reactor deposition zone: (a) 250 °C; (b) 350 °C.

The XRD analysis results for the ZnO structures obtained by the PECVD method at the various temperatures in the reactor deposition zone are shown in Figure 9. The diffraction peaks corresponding to (002), (101), (103), (112), (201), (004), and (202) planes are characteristic of a ZnO structure [16,23–29]. Such a diffraction pattern corresponds to a hexagonal structure of the wurtzite type [23,24,29]. No other peaks associated with impurities were observed, indicating that the high-purity ZnO nanoparticles were obtained.

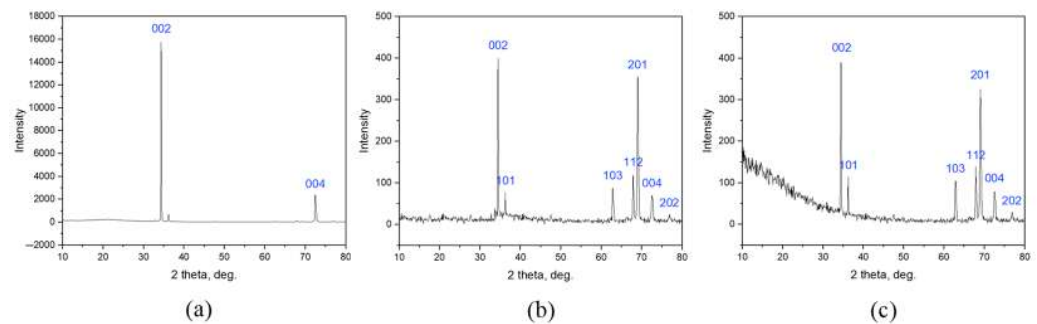


Figure 9. The XRD analysis results for the ZnO structures obtained by the PECVD method at the various temperatures in the reactor deposition zone: (a) 25 °C; (b) 250 °C; (c) 350 °C.

The XRD characterization revealed a strong preferred (002) orientation for all the obtained ZnO structures, indicating that the c-axis of the unit cell was aligned perpendicular to the horizontal plane of the deposition zone [28]. Notably, the diffraction pattern of the sample obtained at the temperature in the reactor deposition zone of 25 °C included only two pronounced peaks, namely (002) and (004). Such a pattern is characteristic of ZnO films [26]. Moreover, the (201) orientation became pronounced for the sample obtained at the temperature in the reactor deposition zone of 250 °C (Figure 9b) and was slightly reduced with the increase in temperature from 250 to 350 °C (Figure 9c). As already shown in Section 3.1, the presence of this peak is characteristic of the elongated ZnO structures.

The Raman spectra for the ZnO structures obtained at the various temperatures in the reactor deposition zone are shown in Figure 10. Similar to the case described in Section 3.1, three main regions can be distinguished: the typical ZnO peak at about 435 cm^{-1} , as well as the peaks at about 275 cm^{-1} and 580 cm^{-1} .

With a decrease in the reactor temperature from 350 to 250 °C, the intensity of all the observed peaks practically did not change; however, at a temperature of 25 °C, the intensity of the peak at about 435 cm^{-1} noticeably increased, and the peaks at about 275 cm^{-1} and 580 cm^{-1} were significantly smoothed out.

Comparing the Raman spectra for two experiments (Figures 6 and 10), it can be concluded that the size of the nanoparticles does not affect their defectiveness and the degree of bond breaking, in contrast with their shape.

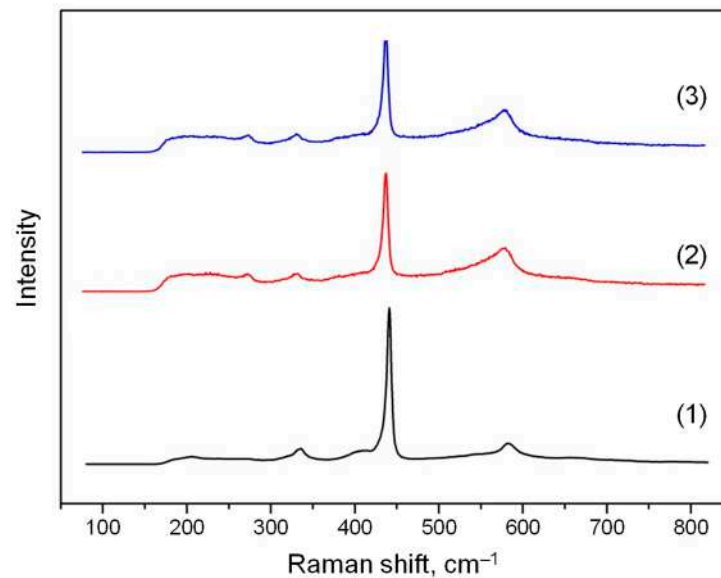


Figure 10. The Raman spectra of the ZnO structures obtained by the PECVD method at the various temperatures in the reactor deposition zone: (1) 25 °C; (2) 250 °C; (3) 350 °C.

3.3. Controlling the Size and Morphological Characteristics of ZnO Nanoparticles

The parameter controlling the morphology (shape) of the obtained nanoparticles is the zinc source temperature. Thus, the ZnO powders were formed with spherical, columnar, and rod-like particle shapes at the temperatures of 370, 420, and 470 °C, respectively; this was probably caused by a change in a mechanism of a plasma–chemical reaction. It was also found that the Zn excess in the deposited powder increased with the rise in the zinc source temperature. Based on the Raman spectra, it was shown that the Zn excess most likely led to intensification for the occurrence of structural defects and bond breaking.

The parameter controlling the dimensional characteristics of the obtained nanoparticles is the reactor temperature in the deposition zone. With a decrease in this parameter from 350 to 250 °C, the transverse size of the deposited ZnO particles was reduced by a factor of three. This effect could be associated with an increase in the specific input energy of the process due to the decrease in the temperature causing a fall in the concentration of the plasma-forming particles. Moreover, it is well known that the lattice parameters are temperature dependent; namely, increasing temperature can lead to lattice expansion with a subsequent increase in the resulting structures [23]. However, active cooling of the reactor in the deposition zone was not applicable in this case, since this parameter affected the relaxation rate of the particles at the surface of the powder tank. The lower the temperature, the more equilibrium the process would be, and therefore, the more perfect the structure to be deposited. When producing nanopowders, “perfect” does not mean “best”, since such an equilibrium process led to the formation of dense monocrystalline layers, which was observed at the reactor temperature in the deposition region equal to 25 °C. It was also found that the size of the nanoparticles did not affect their defectiveness and the degree of bond breaking, in contrast with their shape.

It is also worth noting that an additional process parameter that controls the dimensional characteristics of the obtained nanoparticles can be the plasma discharge power as was shown in the previous work of the authors [34]. In that work, it was shown that the transverse diameter of the ZnO rod-like structures decreased by 30 times (from 900 to 30 nm) with an increase in the plasma discharge power from 30 to 70 W.

4. Conclusions

The direct one-stage synthesis of the ZnO nanoparticles was carried out by the PECVD method from elemental high-purity zinc in the zinc–oxygen–hydrogen plasma-forming mixture with the variable deposition parameters.

The dimensional and morphological parameters of the obtained ZnO powders were studied, as well as their structural properties and homogeneity. The study was carried out using methods such as SEM, XRD, and Raman spectroscopy, as well as statistical methods for processing and analyzing experimental data.

In order to determine the optimal parameters for the PECVD synthesis of the ZnO nanoparticles, a series of experiments were carried out. In each of them, one operating parameter was changed while the rest were constant.

It was found that the zinc source temperature was a parameter controlling the morphology (shape) of the obtained nanoparticles, and the reactor temperature in the deposition zone was a parameter controlling their dimensional characteristics. An additional parameter controlling the dimensional characteristics of the nanoparticles was the plasma discharge power.

Based on the analysis of the obtained experimental data, it can be concluded that, in order to obtain ZnO nanoparticles with given size and morphological characteristics in the PECVD process, it is necessary (1) to increase the zinc source temperature to obtain more elongated structures in one direction (and vice versa), (2) to increase the plasma discharge power for reducing the transverse size of the deposited structures (and vice versa), and (3) to lower the reactor temperature in the deposition zone to reduce the transverse size of the deposited structures (and vice versa). However, take into account that at relatively low temperatures instead of powder ones, film structures can form.

Author Contributions: Conceptualization, T.S.S.; data curation, L.A.M. and A.V.V.; funding acquisition, T.S.S.; investigation, T.S.S., L.A.M., A.A.L., M.A.K., D.G.F., M.A.V., I.O.P., P.A.Y., K.A.S., A.A.A. and A.V.V.; methodology, T.S.S. and L.A.M.; supervision, T.S.S.; visualization, M.A.V.; writing—original draft, T.S.S. All authors have read and agreed to the published version of the manuscript.

Funding: This work was supported by the Russian Science Foundation (grant no. 20-79-00138). Decoding the XRD spectra was supported by the Ministry of Science and Higher Education of the Russian Federation in the Framework of the Basic Part of the State Task [FSWE-2020-0008, project no. 0728-2020-0008].

Institutional Review Board Statement: “Not applicable” for studies not involving humans or animals.

Acknowledgments: The SEM studies were performed by the Collective Usage Center “New Materials and Resource-saving Technologies” (Lobachevsky State University of Nizhny Novgorod).

Conflicts of Interest: The authors declare no conflict of interest.

References

1. Borysiewicz, M.A. ZnO as a functional material, a review. *Crystals* **2019**, *9*, 505. [CrossRef]
2. Singh, T.A.; Sharma, A.; Tejwan, N.; Ghosh, N.; Das, J.; Sil, P.C. A state of the art review on the synthesis, antibacterial, antioxidant, antidiabetic and tissue regeneration activities of zinc oxide nanoparticles. *Adv. Colloid Interface Sci.* **2021**, *295*, 102495. [CrossRef] [PubMed]
3. Wiesmann, N.; Tremel, W.; Brieger, J. Zinc oxide nanoparticles for therapeutic purposes in cancer medicine. *J. Mater. Chem. B* **2020**, *8*, 4973–4989. [CrossRef] [PubMed]
4. Sultana, K.A.; Islam, M.T.; Silva, J.A.; Turley, R.S.; Hernandez-Viezcas, J.A.; Gardea-Torresdey, J.L.; Noveron, J.C. Sustainable synthesis of zinc oxide nanoparticles for photocatalytic degradation of organic pollutant and generation of hydroxyl radical. *J. Mol. Liq.* **2020**, *307*, 112931. [CrossRef]
5. Silva, J.M.P.; Andrade Neto, N.F.; Oliveira, M.C.; Ribeiro, R.A.P.; de Lazaro, S.R.; Gomes, Y.F.; Paskocimas, C.A.; Bomio, M.R.D.; Motta, F.V. Recent progress and approaches on the synthesis of Mn-doped zinc oxide nanoparticles: A theoretical and experimental investigation on the photocatalytic performance. *New J. Chem.* **2020**, *44*, 8805–8812. [CrossRef]
6. Tinoco, J.C.; Hernández, S.A.; Rodríguez-Bernal, O.; Vega-Poot, A.G.; Rodríguez-Gattorno, G.; Olvera, M.d.l.L.; Martínez-Lopez, A.G. Fabrication of Schottky barrier diodes based on ZnO for flexible electronics. *J. Mater. Sci. Mater. Electron.* **2020**, *31*, 7373–7377. [CrossRef]
7. Alexandrov, A.; Zvaigzne, M.; Lypenko, D.; Nabiev, I.; Samokhvalov, P. Al-, Ga-, Mg-, or Li-doped zinc oxide nanoparticles as electron transport layers for quantum dot light-emitting diodes. *Sci. Rep.* **2020**, *10*, 7496. [CrossRef]
8. Kumar, A. Sol gel synthesis of zinc oxide nanoparticles and their application as nano-composite electrode material for supercapacitor. *J. Mol. Struct.* **2020**, *1220*, 128654. [CrossRef]

9. Jaballah, S.; Benamara, M.; Dahman, H.; Lahem, D.; Debliquy, M.; El Mir, L. Formaldehyde sensing characteristics of calcium-doped zinc oxide nanoparticles-based gas sensor. *J. Mater. Sci. Mater. Electron.* **2020**, *31*, 8230–8239. [CrossRef]
10. Parashar, M.; Shukla, V.K.; Singh, R. Metal oxides nanoparticles via sol–gel method: A review on synthesis, characterization and applications. *J. Mater. Sci. Mater. Electron.* **2020**, *31*, 3729–3749. [CrossRef]
11. Hammad, T.M.; Salem, J.K.; Harrison, R.G. The influence of annealing temperature on the structure, morphologies and optical properties of ZnO nanoparticles. *Superlattices Microstruct.* **2010**, *47*, 335–340. [CrossRef]
12. Mornani, E.G.; Mosayebian, P.; Dorrani, D.; Behzad, K. Effect of calcination temperature on the size and optical properties of synthesized ZnO nanoparticles. *J. Ovonic Res.* **2016**, *12*, 75–80.
13. An, L.; Zhang, D.; Zhang, L.; Feng, G. Effect of nanoparticle size on the mechanical properties of nanoparticle assemblies. *Nanoscale* **2019**, *11*, 9563–9573. [CrossRef] [PubMed]
14. Li, J.; Li, Q.; Chen, Y.; Lv, S.; Liao, X.; Yao, Y. Size effects of Ag nanoparticle for N₂ photofixation over Ag/g-C₃N₄: Built-in electric fields determine photocatalytic performance. *Colloids Surfaces A Physicochem. Eng. Asp.* **2021**, *626*, 127053. [CrossRef]
15. Sorichetti, V.; Hugouvieux, V.; Kob, W. Structure and dynamics of a polymer–nanoparticle composite: Effect of nanoparticle size and volume fraction. *Macromolecules* **2018**, *51*, 5375–5391. [CrossRef]
16. Ismail, A.M.; Menazea, A.A.; Kabary, H.A.; El-Sherbiny, A.E.; Samy, A. The influence of calcination temperature on structural and antimicrobial characteristics of zinc oxide nanoparticles synthesized by Sol–Gel method. *J. Mol. Struct.* **2019**, *1196*, 332–337. [CrossRef]
17. Cai, B.; Pei, J.; Dong, J.; Zhuang, H.-L.; Gu, J.; Cao, Q.; Hu, H.; Lin, Z.; Li, J.-F. (Bi,Sb)₂Te₃/SiC nanocomposites with enhanced thermoelectric performance: Effect of SiC nanoparticle size and compositional modulation. *Sci. China Mater.* **2021**, *64*, 2551–2562. [CrossRef]
18. Ramya, M.; Nideep, T.K.; Nampoore, V.P.N.; Kailasnath, M. The impact of ZnO nanoparticle size on the performance of photoanodes in DSSC and QDSSC: A comparative study. *J. Mater. Sci. Mater. Electron.* **2021**, *32*, 3167–3179. [CrossRef]
19. Mahpudiz, A.; Lim, S.L.; Inokawa, H.; Kusakabe, K.; Tomoshige, R. Cobalt nanoparticle supported on layered double hydroxide: Effect of nanoparticle size on catalytic hydrogen production by NaBH₄ hydrolysis. *Environ. Pollut.* **2021**, *290*, 117990. [CrossRef]
20. Mochalov, L.; Logunov, A.; Vorotyntsev, V. Structural and optical properties of As–Se–Te chalcogenide films prepared by plasma-enhanced chemical vapor deposition. *Mater. Res. Express* **2019**, *6*, 56407. [CrossRef]
21. Mochalov, L.; Logunov, A.; Markin, A.; Kitnis, A.; Vorotyntsev, V. Characteristics of the Te-based chalcogenide films dependently on the parameters of the PECVD process. *Opt. Quantum Electron.* **2020**, *52*, 197. [CrossRef]
22. Mochalov, L.; Logunov, A.; Prokhorov, I.; Sazanova, T.; Kudrin, A.; Yunin, P.; Zelentsov, S.; Letnianchik, A.; Starostin, N.; Boreman, G.; et al. Plasma-Chemical Synthesis of Lead Sulphide Thin Films for Near-IR Photodetectors. *Plasma Chem. Plasma Process.* **2021**, *41*, 493–506. [CrossRef]
23. Singh, P.; Kumar, A.; Kaushal, A.; Kaur, D.; Pandey, A.; Goyal, R.N. In situ high temperature XRD studies of ZnO nanopowder prepared via cost effective ultrasonic mist chemical vapour deposition. *Bull. Mater. Sci.* **2008**, *31*, 573–577. [CrossRef]
24. Purica, M. Optical and structural investigation of ZnO thin films prepared by chemical vapor deposition (CVD). *Thin Solid Film.* **2002**, *403–404*, 485–488. [CrossRef]
25. Kocyigit, A.; Orak, I.; Çaldıran, Z.; Turut, A. Current–voltage characteristics of Au/ZnO/n-Si device in a wide range temperature. *J. Mater. Sci. Mater. Electron.* **2017**, *28*, 17177–17184. [CrossRef]
26. Wu, J.-J.; Wen, H.-I.; Tseng, C.-H.; Liu, S.-C. Well-Aligned ZnO Nanorods via Hydrogen Treatment of ZnO Films. *Adv. Funct. Mater.* **2004**, *14*, 806–810. [CrossRef]
27. Savaloni, H.; Savari, R. Nano-structural variations of ZnO:N thin films as a function of deposition angle and annealing conditions: XRD, AFM, FESEM and EDS analyses. *Mater. Chem. Phys.* **2018**, *214*, 402–420. [CrossRef]
28. Franklin, J.B.; Zou, B.; Petrov, P.; McComb, D.W.; Ryan, M.P.; McLachlan, M.A. Optimised pulsed laser deposition of ZnO thin films on transparent conducting substrates. *J. Mater. Chem.* **2011**, *21*, 8178. [CrossRef]
29. Fan, H.; Jia, X. Selective detection of acetone and gasoline by temperature modulation in zinc oxide nanosheets sensors. *Solid State Ion.* **2011**, *192*, 688–692. [CrossRef]
30. Mondal, B.; Mandal, S.P.; Kundu, M.; Adhikari, U.; Roy, U.K. Synthesis and characterization of nano–zinc wire using a self designed unit galvanic cell in aqueous medium and its reactivity in propargylation of aldehydes. *Tetrahedron* **2019**, *75*, 4669–4675. [CrossRef]
31. Friedrich, F.; Nickel, N.H. Resonant Raman scattering in hydrogen and nitrogen doped ZnO. *Appl. Phys. Lett.* **2007**, *91*, 111903. [CrossRef]
32. Sann, J.; Stehr, J.; Hofstaetter, A.; Hofmann, D.M.; Neumann, A.; Lerch, M.; Haboek, U.; Hoffmann, A.; Thomsen, C. Zn interstitial related donors in ammonia-treated ZnO powders. *Phys. Rev. B* **2007**, *76*, 195203. [CrossRef]
33. Montenegro, D.N.; Hortelano, V.; Martínez, O.; Martínez-Tomas, M.C.; Sallet, V.; Muñoz-Sanjosed, V.; Jiménez, J. Non-radiative recombination centres in catalyst-free ZnO nanorods grown by atmospheric-metal organic chemical vapour deposition. *J. Phys. D Appl. Phys.* **2013**, *46*, 235302. [CrossRef]
34. Sazanova, T.S.; Mochalov, L.A.; Logunov, A.A.; Fukina, D.G.; Vorotyntsev, I.V. Influence of plasma power on the size distribution of deposited zinc oxide nanorods. *IOP Conf. Ser. Mater. Sci. Eng.* **2021**, *1155*, 12093. [CrossRef]

Article

Role of Alkylamines in Tuning the Morphology and Optical Properties of SnS₂ Nanoparticles Synthesized by via Facile Thermal Decomposition Approach

Rama Gaur ^{1,*}, Syed Shahabuddin ^{1,*}, Irfan Ahmad ² and Nanthini Sridewi ^{3,*}

¹ Department of Chemistry, School of Technology, Pandit Deendayal Energy University, Knowledge Corridor, Raysan, Gandhinagar 382426, Gujarat, India

² Department of Clinical Laboratory Sciences, College of Applied Medical Sciences, King Khalid University, Abha 61421, Saudi Arabia

³ Department of Maritime Science and Technology, Faculty of Defence Science and Technology, National Defence University of Malaysia, Kuala Lumpur 57000, Malaysia

* Correspondence: rama.gaur@sot.pdpu.ac.in (R.G.); syedshahab.hyd@gmail.com or syed.shahabuddin@sot.pdpu.ac.in (S.S.); nanthini@upnm.edu.my (N.S.); Tel.: +91-8585932338 (S.S.); +60-124-675-320 (N.S.)

Abstract: The present study reported the synthesis of SnS₂ nanoparticles by using a thermal decomposition approach using tin chloride and thioacetamide in diphenyl ether at 200 °C over 60 min. SnS₂ nanoparticles with novel morphologies were prepared by the use of different alkylamines (namely, octylamine (OCA), dodecylamine (DDA), and oleylamine (OLA)), and their role during the synthesis was explored in detail. The synthesized SnS₂ nanostructures were characterized using an array of analytical techniques. The XRD results confirmed the formation of hexagonal SnS₂, and the crystallite size varied from 6.1 nm to 19.0 nm and from 2.5 to 8.8 nm for (100) and (011) reflections, respectively. The functional group and thermal analysis confirmed the presence of organics on the surface of nanoparticles. The FE-SEM results revealed nanoparticles, nanoplates, and flakes assembled into flower-like morphologies when dodecylamine, octylamine, and oleylamine were used as capping agents, respectively. The analysis of optical properties showed the variation in the bandgap and the concentration of surface defects on the SnS₂ nanoparticles. The role of alkylamine as a capping agent was explored and discussed in detail in this paper and the mechanism for the evolution of different morphologies of SnS₂ nanoparticles was also proposed.

Keywords: SnS₂ nanoparticles; thermal decomposition; nanoflakes; nanoflowers; capping agent; alkylamines

Citation: Gaur, R.; Shahabuddin, S.; Ahmad, I.; Sridewi, N. Role of Alkylamines in Tuning the Morphology and Optical Properties of SnS₂ Nanoparticles Synthesized by via Facile Thermal Decomposition Approach. *Nanomaterials* **2022**, *12*, 3950. <https://doi.org/10.3390/nano12223950>

Academic Editor: Meiwen Cao

Received: 26 September 2022

Accepted: 3 November 2022

Published: 9 November 2022

Publisher's Note: MDPI stays neutral with regard to jurisdictional claims in published maps and institutional affiliations.



Copyright: © 2022 by the authors. Licensee MDPI, Basel, Switzerland. This article is an open access article distributed under the terms and conditions of the Creative Commons Attribution (CC BY) license (<https://creativecommons.org/licenses/by/4.0/>).

1. Introduction

The growing population around the world arouses energy concerns in all kinds of fields. It took us a long time to realize that “the ultimate source of energy sun is the ultimate source”. The latest estimates by scientists prove that the amount of solar energy the sun gives to the earth in a single day is sufficient to meet the total energy needs of the world for 27 years at the current rate of consumption [1]. We only have to harness a very little fraction of it to meet all our energy needs for all time to come. Extensive research has been made over the years on solar cells to improve their efficiency and augment their commercialization. Hence, a continuous effort has been made in this area and is still being made to achieve maximum efficiency by modulating the materials used as the photoanode. Reports are available on the use of metal selenides as sensitizers and electron acceptors in dye-sensitized solar cells with an enhanced power conversion efficiency of up to 9.49% [2,3]. Owing to the negative traits such as toxicity and instability of selenides, we need to look for alternative inorganic materials as electron acceptors for future solar cells. The use of layered metal sulfides such as MoS₂, SnS₂, and WS₂ is considered a potential candidate

for this purpose [4]. SnS₂ is a moderate band gap semiconductor (2–2.5 eV) with a layered structure. It has been reported to exhibit a CdI₂-type structure, where hexagonally ordered planes of Sn atoms are held between two hexagonally ordered planes of S atoms, and with adjacent sulfur layers [5,6]. It possesses excellent optical and electrical properties and is an important material for optoelectronic devices. Hence, SnS₂ is considered a potential candidate for various applications such as catalysis, solar cells, sensors, photodetectors, lithium and sodium ion batteries, light-emitting diodes, etc. [4–8].

Looking at the synthetic aspects and environmental concerns, SnS₂ is comparatively easy to synthesize and has no toxic effects on the environment. Various methods have been reported for the synthesis of SnS₂ nanoparticles, such as hydrothermal, sol–gel, laser ablation, chemical vapor deposition, etc. [4,9–11]. The reported synthetic approaches involve harsh conditions, high temperatures, long reaction times, and a lack of control over the shape and size of the materials. Alternate approaches such as solvent-assisted thermal decomposition allow the easy and facile synthesis of shape- and size-controlled nanomaterials.

Morphology-dependent studies on nanomaterials have revealed that the same material with different morphologies exhibits significantly different properties [12,13]. Research is being conducted in this direction to tune the morphology and surface characteristics by chemical methods. Researchers have reported different morphologies of SnS₂ such as flakes, nanosheets, worm-like shapes, nanorods, flower-like shapes, nanobelts, etc. [14–19].

Alkylamines have been reported to be an important class of stabilizers during the synthesis of colloidal semiconductor nanocrystals. A series of alkylamines have been reported as stabilizer/capping agents for the preparation of group II–VI and IV–VI nanomaterials [20]. The addition of these alkylamines during the synthesis of semiconductor nanocrystals aids nucleation and affects crystal growth [21]. The role of alkylamines in controlling morphological characteristics has always been debatable. A few reports suggest that the addition of alkylamine retards the kinetics by passivating the crystal surface, hence retarding crystal growth [22,23]. On the other hand, a few reports suggest their role as promoters by enhancing the nucleation kinetics and influencing crystal growth [24–26]. The above reports point towards the chemical interaction of alkylamines with precursor molecules, resulting in a pre-conditioned molecular precursor. Alkylamine-substituted precursors are decomposed to form nanocrystals with defined morphologies and unique optical and structural properties. The preferential adsorption of alkylamines on the surface of nanocrystals results in the accelerated growth of the other planes. The mechanistic insights into the role of alkylamines have been discussed by García-Rodríguez et al. (2014) in their reports [20]. The interaction of alkylamines with the growing crystal is a temperature-dependent phenomenon. The amine adsorption is minimum at low temperatures and is increased with an increase in the reaction temperature. Li et al. (2004) and Pradhan et al. (2007) suggested that alkylamines activate the precursors of ZnSe, ZnS, and CdSe nanocrystals at various reaction temperatures [25,27]. Similarly, Sun et al. reported that dodecylamine increases the rate of consumption of phosphine selenide precursor as well as the rate of CdSe nanocrystal growth [26]. In contrast, Guo et al. suggested that alkylamines decrease their reactivity instead [28]. Mourdikoudis et al. have reviewed oleyamine as a solvent, surfactant, and reducing agent, for the controlled preparation of a wide range of nanomaterials including metal oxides, metal sulfides, noble metals, and alloy nanocrystals [29]. These unique effects of alkylamines significantly improve the aspect of controlled morphology with desired properties.

From the above discussion, it is very clear that alkylamines play an important role during the synthesis by controlling crystal growth. The present paper aimed at exploring the role of alkylamines as a capping agent and their effect on the optical properties and the morphology of SnS₂ nanoparticles. In a continuation of previous work, the authors attempted the synthesis in the presence of different alkylamines (oleylamine, octylamine, and dodecylamine).

2. Experimental Section

2.1. Reagents

Tin(IV) chloride pentahydrate, thioacetamide (Sigma Aldrich® 99%, Ahemdabad, Gujarat, India), diphenyl ether (Sigma Aldrich® 99%, Ahemdabad, Gujarat, India), octylamine (Sigma Aldrich® 99%, Ahemdabad, Gujarat, India), oleylamine (Sigma Aldrich® 99%, Ahemdabad, Gujarat, India), dodecylamine (Sigma Aldrich® 99%, Ahemdabad, Gujarat, India), and Millipore® water were acquired. All the chemicals were used as received. Methanol used during the reaction was distilled before use.

2.2. Synthesis of SnS₂ Nanoparticles

The SnS₂ nanoparticles were synthesized using a simple thermal decomposition approach. In a typical synthesis, 1 mmol of SnCl₄·5H₂O and 1 mmol of CH₃CSNH₂ were added to 10 mL of diphenyl ether in a 50 mL round-bottom flask and were refluxed at 200 °C in the air for 1 h. After the completion of the reaction, a slurry was obtained and cooled to room temperature. A total of 30 mL of methanol was added to the slurry and the precipitate obtained was washed using an excess of methanol. The precipitate was dried overnight at 65 °C under a vacuum. For the preparation of nanoparticles in the presence of capping agents (1 mmol), oleylamine, octylamine, and dodecylamine were added to different reaction setups along with the Sn and S precursors to diphenyl ether in the initial step. The synthetic details and nomenclature of the SnS₂ samples, prepared in the present study, are given in Table 1.

Table 1. Synthetic details, nomenclature, and morphology of all SnS₂ samples.

Sample ID	Capping Agent	Color of the Product	Morphology	Crystallite Size		Sn:S Ratio (EDX)	Overall % Wt. Loss
				(100)	(011)		
S1	–	Dark Green	Flower-like	18.0	5.3	1:1.8	22.90
S2	Dodecylamine	Brown-green	Small nanoparticles	–	–	1:2.1	25.74
S3	Octylamine	Brown-green	Rosette-like morphology	31.5	8.8	1:2.2	21.6
S4	Oleylamine	Olive green	Nanoplates assembled into stacks	17.6	4.2	1:2.1	26.85

To investigate the role of alkylamines in detail, the synthesis was carried out by varying the amount of capping agent used. The results are discussed in Section 3.

2.3. Characterization

The as-prepared SnS₂ samples were characterized using an array of sophisticated characterization techniques. The SnS₂ nanostructure was analyzed for structural, compositional, and morphological characterization. The phase analysis was carried out using powder X-ray diffraction (Bruker AXS-D8 diffractometer, Cu-K_α radiation ($\lambda = 1.5406 \text{ \AA}$); 2θ range 5–90°; scan speed of 1° min^{−1}). The purity and stability of the as-prepared SnS₂ nanoparticles were analyzed by FT-IR spectroscopy (Perkin Elmer Spectrum 2, Mumbai, Maharashtra, India) and thermal gravimetric analysis (EXSTAR TG/DTA instrument (Hyderabad, Telangana, India); heating rate 10°/min, ambient air atmosphere). Optical properties were investigated using a diffuse reflectance spectrophotometer (DRS) (Perkin Elmer, (Ahemdabad, Gujarat, India)) and photoluminescence (PL) spectrophotometer (Perkin Elmer Model, (Ahemdabad, Gujarat, India)) in the wavelength range of 200 nm to 800 nm. The morphology of SnS₂ samples was analyzed using a field emission scanning electron microscope (Carl Zeiss, Bangalore, Karnataka, India) operating at 20 kV and equipped with an energy-dispersive X-ray analysis (EDXA, Bangalore, Karnataka, India) facility. For the FE-SEM analysis, the SnS₂ powders were sprinkled on clean aluminum stubs using conducting carbon tape and were gold coated for 30 s using a sputtering unit.

3. Results and Discussion

3.1. Structure and Phase Analysis

The XRD results for the SnS₂ nanoparticles prepared via the thermal decomposition approach using different capping agents confirmed the formation of hexagonal SnS₂ (JCPDS File No. 83-1705; Berndtite-2T phase) in all the samples (Figure 1). The XRD peaks at the 2θ values of 15.05°, 28.30°, 30.38°, 32.20°, 42.00°, 50.11°, and 52.63° were indexed to (001), (100), (011), (012), (110), and (111) reflections of SnS₂, respectively. It was observed that the XRD pattern for samples S1 and S3 exhibited sharp and well-defined peaks indicating high crystallinity and morphology characteristics that are discussed later in Section 3.4. The presence of two sets of peaks (sharp and broad) in the XRD patterns of S1 and S3 implied that the growth of certain facets was restrained, and that a special morphology was formed [18].

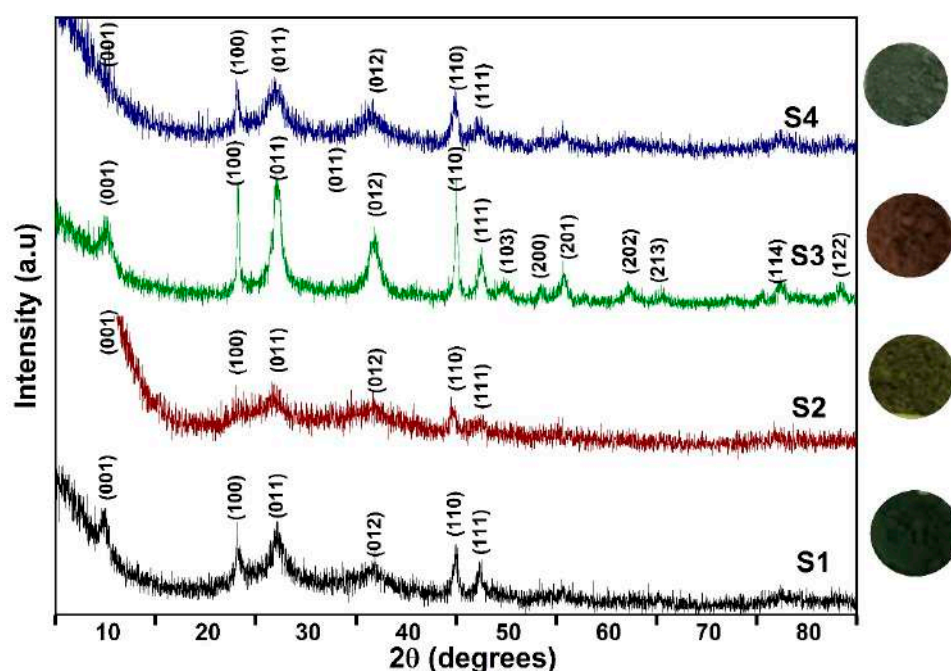


Figure 1. XRD plot of SnS₂ nanoparticles synthesized in the absence and presence of capping agent by thermal decomposition method.

On the other hand, the XRD patterns of samples S2 and S4 exhibited broad and poorly defined peaks, indicating a low crystallinity of the nanoparticles. The crystallite size of SnS₂ was calculated using the Debye–Scherrer formula. The crystallite size varied from 6.1 nm to 19 nm, as calculated using the (100) reflection, and 2.6 nm to 6.6 nm as calculated using the (011) reflection. The presence of the (001) peak in samples S1 and S3 indicated the formation of layered structures. The formation of highly crystalline nanoflakes assembled to form a flower-like structure for samples S1 and S2 was evident from the presence of sharp peaks in the XRD plot. In addition, the low intensity and poorly defined peaks in the XRD pattern pointed towards the formation of nanoparticles and nanoplates for samples S2 and S4.

3.2. Purity and Phase Stability

The purity and phase stability of the as-prepared SnS₂ samples were checked using FT-IR spectroscopy and thermogravimetric analysis (TGA), respectively. Figure 2a shows the FT-IR spectra of the SnS₂ nanoparticles synthesized using different capping agents by the thermal decomposition method. The IR spectra of the SnS₂ nanoparticles showed the presence of bands at around 3400 cm⁻¹ and 1620 cm⁻¹ attributed to stretching and bending vibrations of the hydroxyl group, indicating the presence of physisorbed moisture on the

surface of the SnS₂ nanoparticles [18]. The band at about 3200 cm⁻¹ was attributed to N–H stretching, and the IR bands at around 2920 cm⁻¹, 2840 cm⁻¹, and 1390 cm⁻¹ were ascribed to asymmetric and symmetric stretching and bending of the C–H group, respectively [30]. The bands at around 1260 cm⁻¹, 870 cm⁻¹, and 660 cm⁻¹, were due to asymmetric and symmetric stretching and bending of the C–S group, respectively [31].

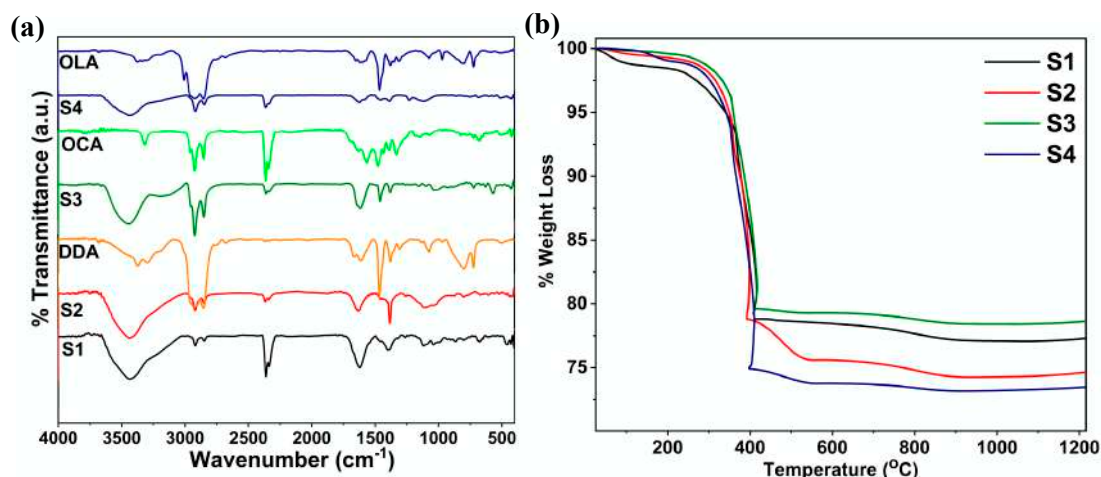


Figure 2. (a) IR and (b) TGA graph of SnS₂ nanoparticles synthesized in the absence and presence of capping agent by thermal decomposition method.

The IR spectra of all the SnS₂ nanoparticles exhibited a band at around 680 cm⁻¹ due to Sn–S stretching. The IR band at around 1110 cm⁻¹ was ascribed to C–N stretching [18]. The assignments of IR peaks for all the SnS₂ samples and capping agents used are listed in Table 2. The shift in the IR band positions confirmed the capping of nanoparticles with the different capping agents used (DDA, OCA, and OLA) on the surface of the SnS₂ nanoparticles.

Table 2. Assignments of IR peaks for the SnS₂ samples and the alkylamines used as capping agents.

S1	S2	(DDA)	S3	(OCA)	S4	(OLA)	Band Assignments
3425	3424	3366	3443	3314	3443	3373 and 3300	$\nu_{as}(\text{NH}_2)$ and $\nu_s(\text{NH}_2)$
3211	–	3292	–	2954	–	3005	$\delta(\text{C-H})$
2920	2914	2923	2923	2923	2920	2950	$\nu_{as}\text{C-H}$
2847	2847	2855	2849	2852	2844	2852	$\nu_s\text{C-H}$
1619	1632	1611	1619	1620	1632	1611	$\delta(\text{NH}_2)$
–	–	1630	–	1638	1592	1620	$\delta(\text{C-C})$
–	–	1461	1461	1477	–	1461	
1392	1384	1378	1380	1388	1384	1376	$\delta(\text{CH}_2)$
1108	–	1303	–	1331	–	1307	
1097	1097	1073	1019	–	–	1070	$\delta(\text{C-N})$
–	–	966	–	–	–	966	$\delta(\text{C-H})$ out of plane mode
–	–	801	–	–	–	801	
–	–	720	720	720	–	720	$\delta(\text{C-C})$
671	671	–	671	–	671	–	Sn–S

The TGA curves (Figure 2b) for all the SnS₂ samples showed a small weight loss of ~1% at around 100 °C due to the loss of physisorbed moisture. The single-step weight loss at around 390 °C was attributed to the phase transformation (oxidation) of SnS₂ to SnO₂ (theoretical weight loss = 17.6%) [32]. The observed weight loss values for S1, S2, S3, and S4 were 19.8%, 20.6%, 20.4% and 24.1%, respectively. The SnS₂ samples (S2, S3,

and S4) prepared using capping agents exhibited marginally higher weight loss compared to those prepared in the absence of any capping agent (S1). This was attributed to the presence of more adsorbed organics on the surface of the SnS₂ nanoparticles (S2, S3, and S4), indicating the presence of capping agents on the SnS₂ nanoparticles. The TGA results were in agreement with the literature reports [18,32].

3.3. Optical Studies

The effect of the use of alkylamines on the optical properties of the SnS₂ nanoparticles was investigated using DRS and PL spectroscopy. Figure 3 shows the DRS and PL spectra for the SnS₂ nanoparticles. The DRS spectra exhibited band gap absorption for the SnS₂ nanoparticles in the range of 400 nm to 550 nm. The PL spectra exhibited an excitonic emission at around 550 nm and a defect emission at around 645 nm. The excitonic emission exhibited a blue shift for samples S1, S3, and S4 with respect to sample S2. The PL results were in agreement with the DRS results. The band gap was estimated from the Tauc plots shown in Figure 4. The band gap was found to vary from 2.31 eV to 3.50 eV. The variation in band gap was attributed to the difference in crystallite size, with sample S1 with the smallest crystallite size exhibiting a band gap of 3.50 eV.

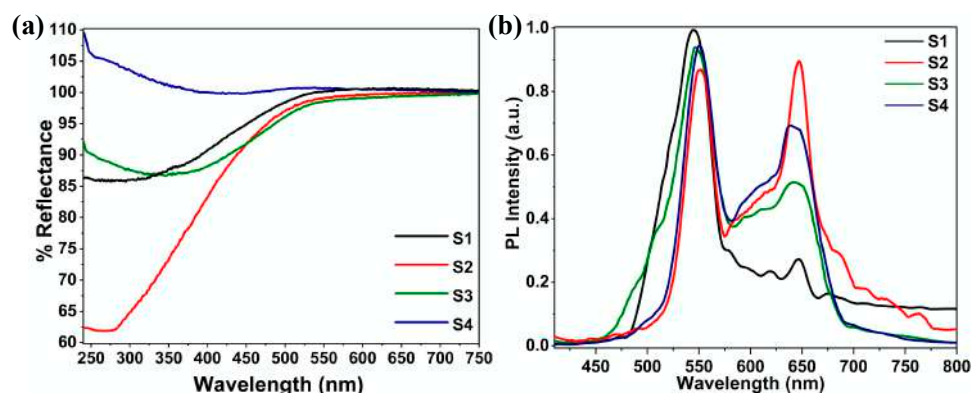


Figure 3. (a) DRS and (b) photoluminescence spectra of SnS₂ nanoparticles synthesized in the absence and presence of capping agent by thermal decomposition method.

Further investigation of the PL spectra indicated an increased concentration of surface defects for samples S2, S3, and S4 when the capping agent was used during the synthesis. The presence of excess surface defects imparted novel characteristics and modifications to the existing properties [33]. The $I_{exc}/I_{defects}$ ratio was found to vary from 2 to 7.3 (Table 3). Sample S2 was observed to exhibit the highest amount of surface defects ($I_{exc}/I_{defects} = 7.3$) and the smallest crystallite size. Alkylamines are reported to play multiple roles as solvent surfactants and reducing agents during the synthesis of nanocrystals [29]. The growth of crystals in the presence of alkylamines results in twinning and stacking during crystal growth resulting in internal defects and influencing the final properties of nanocrystals [34,35].

Table 3. PL peak positions, FWHM, intensity ratio ($I_{excitonic}/I_{defects}$), band gap, and crystallite size of SnS₂ nanoparticles.

Sample ID	Peak Position (nm)		FWHM (nm)	$(I_{excitonic}/I_{defects})$	Band Gap (eV)	Crystallite Size (nm)		Sn:S Ratio
	Excitonic Emission	Defect Emission				(100)	(011)	
S1	544	645	37.5	2	2.86	18.0	5.3	1:1.8
S2	551	645	36.9	7.3	3.50	6.9	2.6	1:2
S3	548	647	53.4	3.6	2.33	7.3	3.0	1:2
S4	551	645	40.7	2.4	2.42	10.3	2.9	1:2

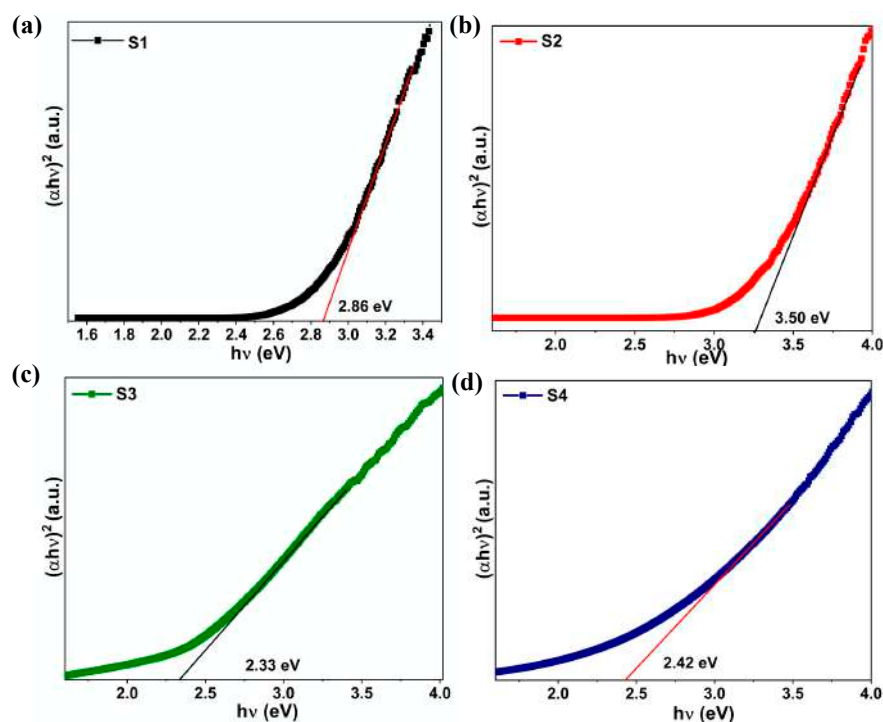


Figure 4. Tauc plot of SnS₂ nanoparticles synthesized in the absence and presence of capping agent by thermal decomposition method.

3.4. Morphological Analysis (FE-SEM and EDX Results)

The SnS₂ nanoparticles synthesized using different capping agents by the thermal decomposition approach were characterized using FE-SEM analysis. Figure 5 shows the FE-SEM images of the SnS₂ nanoparticles prepared in the absence and presence of capping agents such as octylamine, oleylamine, and dodecylamine. The presence of a capping agent played a vital role in influencing the morphology of the resulting nanoparticles. The FE-SEM analysis revealed the formation of a flower-like morphology for the pristine SnS₂ nanoparticles (S1) prepared by the thermal decomposition approach in the absence of a capping agent. A web-like microstructure of SnS₂ with a diameter of 800 nm was observed for Sample S1. The microstructures were formed by the assembly of flake-like nano-building units. The thickness of the flakes ranged from 10 nm to 15 nm.

On the other hand, the SnS₂ nanoparticles synthesized in the presence of capping agents (octylamine, oleylamine, and dodecylamine) exhibited particle-like, twisted-flower-like, and stacked-plate-like morphology, respectively. Sample S2, prepared in the presence of octylamine showed the formation of irregular particles. Sample S3, prepared in the presence of oleylamine, showed the formation of rosette-flower-like morphology. A closer look at the FE-SEM images revealed that the flowers were formed by the twisting and wrapping of linear structures, assembled to form rosette-like structures with a rosette-like morphology with a diameter of 1.2 microns, and the thickness of the linear structure was observed to be around 40 nm. Sample S4, prepared in the presence of dodecylamine, showed the formation of a stack of plate-like structures, or nanoplates assembled into stacks. The diameter of a typical nanoplate was around 250 nm and the thickness were around 30–35 nm.

The composition of all the SnS₂ samples (Sn:S) was analyzed using energy-dispersive X-ray analysis. The weight and atomic percent of Sn and S present in the SnS₂ samples synthesized by the thermal decomposition method are given in Table 1. The EDXA results indicated the presence of tin and sulfur in all the samples, and the Sn:S ratio varied from 1:1.8 to 1:2.2, which was close to the theoretical value (1:2).

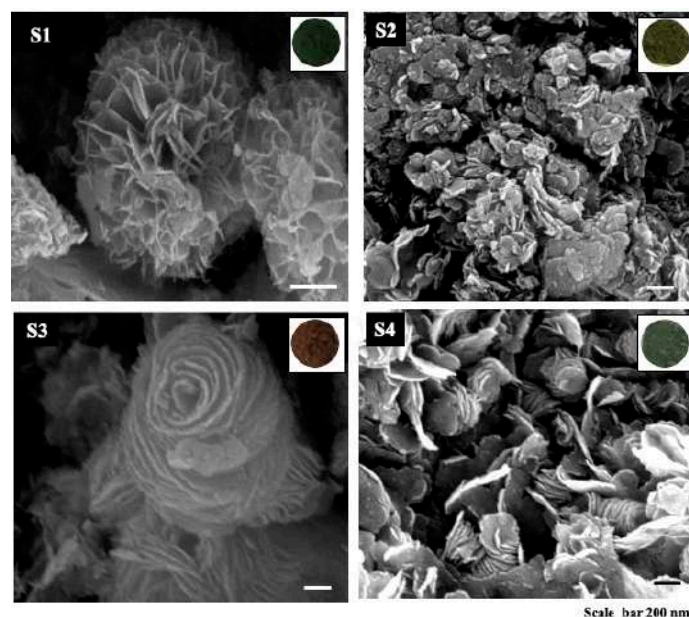


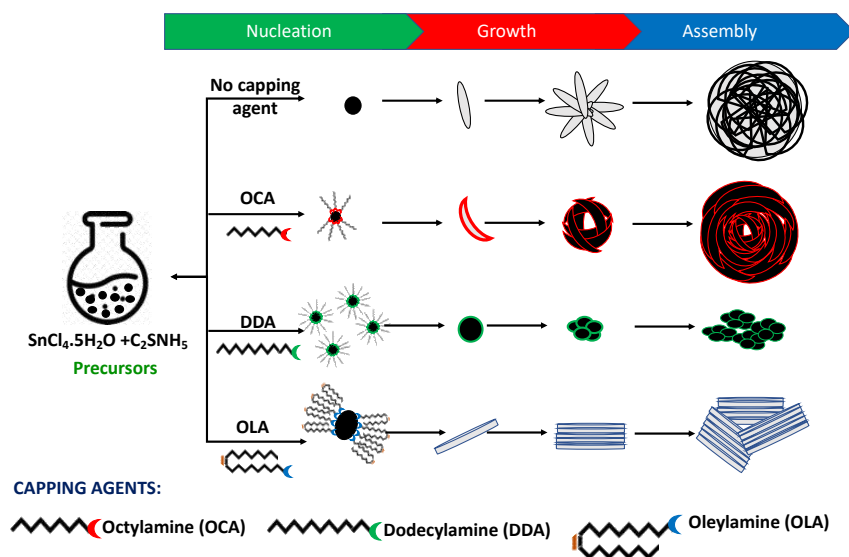
Figure 5. FE-SEM images of SnS₂ nanoparticles (S1–S4) prepared using the thermal decomposition approach in the absence and presence of capping agents. The inset shows the digital images of powder samples.

4. Mechanism for Morphology Evolution (Mechanism of Formation of SnS₂ Nanoparticles with Different Morphologies)

Scheme 1 depicts the proposed mechanism for the formation of SnS₂ nanoparticles with different morphologies using the thermal decomposition approach. The precursors (SnCl₄·5H₂O and CH₃CSNH₂ thioacetamide), when subjected to thermal decomposition, led to the formation of spherical SnS₂ seeds in the initial stage of the reaction. As the reaction proceeded, the nuclei grew to form flakes and strands. The flakes/strands were the primary building blocks for the hierarchical structures and the flakes/strands assembled to form flower-like structures [18]. The presence of capping agents during the thermal decomposition played a vital role in controlling the morphology of SnS₂ resulting in the formation of unique morphologies. Scheme 1 shows that the nuclei or basic building unit of SnS₂ are arranged differently in presence of the different capping agents. The physico-chemical properties of the capping different agents used during the synthesis decided the growth and assembly of the building blocks into nanostructures with a special morphology. The interaction of the surfactant molecule with the crystal seed drastically reduced the generation of nuclei. The reactant molecules then contributed to the characteristic growth of the nanocrystal.

The chain length of alkylamines also plays an important role in controlling the morphology of nanoparticles [21]. It is reported that higher activation energy and low reaction rate of amine with a longer carbon chain leads to the formation of smaller-sized quantum dots due to its higher capping capacity [36,37]. Hence, in this study, the growth was restricted, and this resulted in the formation of irregular particles or anisotropic crystals. Dodecylamine (C12) and oleylamine (C18), due to their longer alkyl(enyl) chains, resulted in the formation of irregular particles and stacks of nanoplates, respectively. On the other hand, octylamine (C8) resulted in the assembly of nuclei strands as a rosette-like morphology. Oleylamine (C18) acted as a surfactant and was adsorbed and subsequently passivated the surface, restricting further growth in planes, and resulting in the formation of nanoplates. The nanoplates were stacked together due to the interaction between the surfactant molecules adsorbed on the surface of the SnS₂ nanoplates. Octylamine (C8) on the other hand, due to its high polarity, led to the fusion of nanoplates in a helical manner, resulting in a flower-like morphology. Long aliphatic chains of dodecylamine

(C12) prevented the assembly and growth of nanoparticles and resulted in the formation of irregular particles.



Scheme 1. Proposed mechanism for the evolution of different morphologies of SnS₂ prepared using thermal decomposition approach in the presence and absence of alkylamines.

5. Conclusions

SnS₂ nanoparticles with different morphologies were successfully synthesized by the thermal decomposition of SnCl₄·5H₂O and thioacetamide in the presence of different surfactants (dodecylamine, octylamine, and oleylamine). The use of alkylamine during the synthesis affected the nucleation and crystal growth and had a great influence on the morphology and optical properties of the SnS₂ nanoparticles. The SnS₂ nanoparticles showed the assembly of flakes into flower-like nanostructures, nanoparticles, and nanoplates stacked together. The formation of characteristic structures had an influence not only on the structural features but also on the optical properties of the SnS₂ nanoparticles. This approach was found to be beneficial for the surfactant-assisted synthesis of SnS₂ nanoparticles with unique morphologies. Alkylamines, due to their multifunctional characteristics, were an integral part of the nanocrystal synthesis. The use of alkylamines during the synthesis not only tailored the morphology but also influenced the properties of the nanomaterials. Thus, it is imperative to explore mechanistic insights into the role of alkylamines in nanocrystal synthesis. The careful optimization of the reaction parameters such as solvents, temperature, surfactants, etc., resulted in nanocrystals with a controlled shape and size for applications in solar cells, catalysis, environmental remediation, etc.

Author Contributions: Formal analysis, Methodology, Investigation, Writing—original draft, Writing—review & editing, R.G.; Funding acquisition, Writing—review & editing, I.A.; Writing—review & editing, S.S.; Funding acquisition, Writing—review & editing, N.S. All authors have read and agreed to the published version of the manuscript.

Funding: The authors would like to thank the Scientific Research Deanship at King Khalid University, Abha, Saudi Arabia through the Large Research Group Project under grant number 9RGP.02/219/43) and the Marine Pollution Special Interest Group, the National Defence University of Malaysia via SF0076-UPNM/2019/SF/ICT/6, for providing research facilities and funding.

Institutional Review Board Statement: Not applicable.

Informed Consent Statement: Not applicable.

Data Availability Statement: The data presented in this study are available on request from the corresponding author.

Acknowledgments: The authors would like to thank the Solar Research and Development Center (SRDC) for FE-SEM characterization and Pandit Deendayal Energy University for providing institutional fellowship, Scientific Research Deanship at King Khalid University, Abha, Saudi Arabia through the Large Research Group Project under grant number 9RGP.02/219/43) and the Marine Pollution Special Interest Group, the National Defence University of Malaysia via SF0076-UPNM/2019/SF/ICT/6, for providing research facilities and funding.

Conflicts of Interest: The authors declare no conflict of interest.

References

1. Shaikh, M.R.S. A review paper on electricity generation from Solar Energy. *Int. J. Res. Appl. Sci. Eng. Technol.* **2017**, *887*, 1884–1889. [CrossRef]
2. Guan, G.; Wu, J.; Huang, J.; Qian, X. Polynary metal selenide CoSe₂/NiSe₂/MoSe₂ porous nanospheres as efficient electrocatalytic materials for high-efficiency dye-sensitized solar cells. *J. Electroanal. Chem.* **2022**, *924*, 116888. [CrossRef]
3. Zhang, T.; Zhang, Q.; Li, Q.; Li, F.; Xu, L. Towards High-Performance Quantum Dot Sensitized Solar Cells: Enhanced Catalytic Activity and Stability of CuCo₂Se₄ Nanoparticles on Graphitic Carbon Nitride G-C₃N₄ Nanosheets. 2022. Available online: https://papers.ssrn.com/sol3/papers.cfm?abstract_id=4211162 (accessed on 1 September 2022).
4. Keshari, A.K.; Kumar, R. Nanostructured MoS₂-, SnS₂-, and WS₂-Based Anode Materials for High-Performance Sodium-Ion Batteries via Chemical Methods: A Review Article. *Energy Technol.* **2021**, *9*, 2100179. [CrossRef]
5. Huang, Y.; Sutter, E.; Sadowski, J.T.; Coflt, M.; Monti, O.L.; Racke, D.A.; Sutter, P. Tin Disulfide: An Emerging Layered Metal Dichalcogenide Semiconductor: Materials Properties and Device Characteristics. *ACS Nano* **2014**, *8*, 10743–10755. [CrossRef]
6. Joseph, A.; Anjitha, C.R.; Aravind, A.; Aneesh, P.M. Structural, optical and magnetic properties of SnS₂ nanoparticles and photo response characteristics of p-Si/n-SnS₂ heterojunction diode. *Appl. Surf. Sci.* **2020**, *528*, 146977. [CrossRef]
7. Dong, W.; Lu, C.; Luo, M.; Liu, Y.; Han, T.; Ge, Y.; Xu, X. Enhanced UV-Vis photodetector performance by optimizing interfacial charge transportation in the heterostructure by SnS and SnSe₂. *J. Colloid Interface Sci.* **2022**, *621*, 374–384. [CrossRef]
8. Sun, Q.; Gong, Z.; Zhang, Y.; Hao, J.; Zheng, S.; Lu, W.; Wang, Y. Synergically engineering defect and interlayer in SnS₂ for enhanced room-temperature NO₂ sensing. *J. Hazard. Mater.* **2022**, *421*, 126816. [CrossRef]
9. Rajwar, B.K.; Sharma, S.K. Chemically synthesized Ti-doped SnS₂ thin films as intermediate band gap material for solar cell application. *Opt. Quantum Electron.* **2022**, *54*, 1–13. [CrossRef]
10. Xu, X.; Xu, F.; Zhang, X.; Qu, C.; Zhang, J.; Qiu, Y.; Wang, H. Laser-Derived Interfacial Confinement Enables Planar Growth of 2D SnS₂ on Graphene for High-Flux Electron/Ion Bridging in Sodium Storage. *Nano-Micro Lett.* **2022**, *14*, 1–16. [CrossRef] [PubMed]
11. Hayashi, K.; Kataoka, M.; Sato, S. Epitaxial Growth of SnS₂ Ribbons on a Au–Sn Alloy Seed Film Surface. *J. Phys. Chem. Lett.* **2022**, *13*, 6147–6152. [CrossRef] [PubMed]
12. Gaur, R. Morphology dependent activity of PbS nanostructures for electrochemical sensing of dopamine. *Mater. Lett.* **2020**, *264*, 127333. [CrossRef]
13. Gaur, R.; Jeevanandam, P. Synthesis and Characterization of Cd_{1-x}Zn_xS (x = 0–1) Nanoparticles by Thermal Decomposition of Bis (thiourea) cadmium–zinc acetate Complexes. *ChemistrySelect* **2016**, *1*, 2687–2697. [CrossRef]
14. Yang, Y.B.; Dash, J.K.; Littlejohn, A.J.; Xiang, Y.; Wang, Y.; Shi, J.; Zhang, L.H.; Kisslinger, K.; Lu, T.M.; Wang, G.C. Large single crystal SnS₂ flakes synthesized from coevaporation of Sn and S. *Cryst. Growth Des.* **2016**, *16*, 961–973. [CrossRef]
15. Huang, L.; Cai, G.; Zeng, R.; Yu, Z.; Tang, D. Contactless Photoelectrochemical Biosensor Based on the Ultraviolet-Assisted Gas Sensing Interface of Three-Dimensional SnS₂ Nanosheets: From Mechanism Reveal to Practical Application. *Anal. Chem.* **2022**, *94*, 9487–9495. [CrossRef]
16. Zou, W.; Sun, L.H.; Cong, S.N.; Leng, R.X.; Zhang, Q.; Zhao, L.; Kang, S.Z. Preparation of worm-like SnS₂ nanoparticles and their photocatalytic activity. *J. Exp. Nanosci.* **2020**, *15*, 100–108. [CrossRef]
17. Sajjad, M.; Khan, Y.; Lu, W. One-pot synthesis of 2D SnS₂ nanorods with high energy density and long term stability for high-performance hybrid supercapacitor. *J. Energy Storage* **2021**, *35*, 102336. [CrossRef]
18. Gaur, R.; Jeevanandam, P. Synthesis of SnS₂ nanoparticles and their application as photocatalysts for the reduction of Cr (VI). *J. Nanosci. Nanotechnol.* **2018**, *18*, 165–177. [CrossRef]
19. Liu, J.; Wen, Y.; van Aken, P.A.; Maier, J.; Yu, Y. In situ reduction and coating of SnS₂ nanobelts for free-standing SnS@ polypyrrole-nanobelt/carbon-nanotube paper electrodes with superior Li-ion storage. *J. Mater. Chem. A* **2015**, *3*, 5259–5265. [CrossRef]
20. García-Rodríguez, R.; Liu, H. Mechanistic insights into the role of alkylamine in the synthesis of CdSe nanocrystals. *J. Am. Chem. Soc.* **2014**, *136*, 1968–1975. [CrossRef]
21. Rempel, J.Y.; Bawendi, M.G.; Jensen, K.F. Insights into the kinetics of semiconductor nanocrystal nucleation and growth. *J. Am. Chem. Soc.* **2009**, *131*, 4479–4489. [CrossRef]
22. Li, F.; Xie, Y.; Hu, Y.; Long, M.; Zhang, Y.; Xu, J.; Qin, M.; Lu, X.; Liu, M. Effects of alkyl chain length on crystal growth and oxidation process of two-dimensional tin halide perovskites. *ACS Energy Lett.* **2020**, *5*, 1422–1429. [CrossRef]

23. Talapin, D.V.; Rogach, A.L.; Kornowski, A.; Haase, M.; Weller, H. Highly luminescent monodisperse CdSe and CdSe/ZnS nanocrystals synthesized in a hexadecylamine-trioctylphosphine oxide-trioctylphosphine mixture. *Nano Lett.* **2001**, *1*, 207–211. [CrossRef] [PubMed]
24. Jose, R.; Zhanpeisov, N.U.; Fukumura, H.; Baba, Y.; Ishikawa, M. Structure-property correlation of CdSe clusters using experimental results and first-principles DFT calculations. *J. Am. Chem. Soc.* **2006**, *128*, 629–636. [CrossRef]
25. Pradhan, N.; Reifsnyder, D.; Xie, R.; Aldana, J.; Peng, X. Surface ligand dynamics in growth of nanocrystals. *J. Am. Chem. Soc.* **2007**, *129*, 9500–9509. [CrossRef] [PubMed]
26. SSun, Z.H.; Oyanagi, H.; Nakamura, H.; Jiang, Y.; Zhang, L.; Uehara, M.; Yamashita, K.; Fukano, A.; Maeda, H. Ligand effects of amine on the initial nucleation and growth processes of CdSe nanocrystals. *J. Phys. Chem. C* **2010**, *114*, 10126–10131. [CrossRef]
27. Li, L.S.; Pradhan, N.; Wang, Y.; Peng, X. High quality ZnSe and ZnS nanocrystals formed by activating zinc carboxylate precursors. *Nano Lett.* **2004**, *4*, 2261–2264. [CrossRef]
28. Guo, Y.; Marchuk, K.; Sampat, S.; Abraham, R.; Fang, N.; Malko, A.V.; Vela, J. Unique challenges accompany thick-shell CdSe/nCdS ($n > 10$) nanocrystal synthesis. *J. Phys. Chem. C* **2012**, *116*, 2791–2800. [CrossRef]
29. Mourdikoudis, S.; Liz-Marzán, L.M. Oleyamine in nanoparticle synthesis. *Chem. Mater.* **2013**, *25*, 1465–1476. [CrossRef]
30. Queiroz, M.F.; Teodosio Melo, K.R.; Sabry, D.A.; Sasaki, G.L.; Rocha, H.A.O. Does the use of chitosan contribute to oxalate kidney stone formation? *Mar. Drugs* **2014**, *13*, 141–158. [CrossRef]
31. Rao, C.N.R.; Venkataraghavan, R.; Kasturi, T.R. Contribution to the infrared spectra of organosulphur compounds. *Can. J. Chem.* **1964**, *42*, 36–42. [CrossRef]
32. Sun, H.; Ahmad, M.; Luo, J.; Shi, Y.; Shen, W.; Zhu, J. SnS₂ nanoflakes decorated multiwalled carbon nanotubes as high performance anode materials for lithium-ion batteries. *Mater. Res. Bull.* **2014**, *49*, 319–324. [CrossRef]
33. Mozetič, M. Surface modification to improve properties of materials. *Materials* **2019**, *12*, 441. [CrossRef] [PubMed]
34. Villaverde-Cantizano, G.; Laurenti, M.; Rubio-Retama, J.; Contreras-Cáceres, R. Reducing Agents in Colloidal Nanoparticle Synthesis—An Introduction. In *Reducing Agents in Colloidal Nanoparticle Synthesis*; Mourdikoudis, S., Ed.; Royal Society of Chemistry: London, UK, 2021; pp. 1–27.
35. Rodrigues, T.S.; Zhao, M.; Yang, T.H.; Gilroy, K.D.; da Silva, A.G.; Camargo, P.H.; Xia, Y. Synthesis of colloidal metal nanocrystals: A comprehensive review on the reductants. *Chemistry* **2018**, *24*, 16944–16963. [CrossRef] [PubMed]
36. Hwang, S.; Choi, Y.; Jeong, S.; Jung, H.; Kim, C.G.; Chung, T.M.; Ryu, B.H. Low temperature synthesis of CdSe quantum dots with amine derivative and their chemical kinetics. *Jpn. J. Appl. Phys.* **2010**, *49*, 05EA03. [CrossRef]
37. Navazi, Z.R.; Nemati, A.; Akbari, H.; Davaran, S. The effect of fatty amine chain length on synthesis process of InP/ZnS quantum dots. *Orient. J. Chem.* **2016**, *32*, 2163–2169. [CrossRef]



Article

Strengthened Optical Nonlinearity of V₂C Hybrids Inlaid with Silver Nanoparticles

Yabin Shao ¹, Qing He ², Lingling Xiang ¹, Zibin Xu ¹, Xiaou Cai ¹ and Chen Chen ^{3,*}

¹ School of Jia Yang, Zhejiang Shuren University, Shaoxing 312028, China; shao_yabin@163.com (Y.S.); melody.xiang@vip.163.com (L.X.); xu_zibin@163.com (Z.X.); cai.xo@163.com (X.C.)

² Collaborative Innovation Center of Steel Technology, University of Science and Technology Beijing, Beijing 100083, China; 123simon@163.com

³ College of Civil Engineering, East University of Heilongjiang, Harbin 150086, China

* Correspondence: chen_chen1600@163.com

Abstract: The investigation of nonlinear optical characteristics resulting from the light–matter interactions of two-dimensional (2D) nano materials has contributed to the extensive use of photonics. In this study, we synthesize a 2D MXene (V₂C) monolayer nanosheet by the selective etching of Al from V₂AlC at room temperature and use the nanosecond Z-scan technique with 532 nm to determine the nonlinear optical characters of the Ag@V₂C hybrid. The z-scan experiment reveals that Ag@V₂C hybrids usually exhibits saturable absorption owing to the bleaching of the ground state plasma, and the switch from saturable absorption to reverse saturable absorption takes place. The findings demonstrate that Ag@V₂C has optical nonlinear characters. The quantitative data of the nonlinear absorption of Ag@V₂C varies with the wavelength and the reverse saturable absorption results from the two-photon absorption, which proves that Ag@V₂C hybrids have great potential for future ultrathin optoelectronic devices.

Keywords: Ag@V₂C MXene; hybrids; Z-scan; nonlinear optical properties

Citation: Shao, Y.; He, Q.; Xiang, L.; Xu, Z.; Cai, X.; Chen, C. Strengthened Optical Nonlinearity of V₂C Hybrids Inlaid with Silver Nanoparticles. *Nanomaterials* **2022**, *12*, 1647. <https://doi.org/10.3390/nano12101647>

Academic Editor: Eric Waclawik

Received: 8 March 2022

Accepted: 6 May 2022

Published: 12 May 2022

Publisher's Note: MDPI stays neutral with regard to jurisdictional claims in published maps and institutional affiliations.



Copyright: © 2022 by the authors. Licensee MDPI, Basel, Switzerland. This article is an open access article distributed under the terms and conditions of the Creative Commons Attribution (CC BY) license (<https://creativecommons.org/licenses/by/4.0/>).

1. Introduction

MXenes [1], 2D transition metal carbides and nitrides, exhibit the outstanding advantages of electrical conductivity, a beneficial elastic modulus and capacitance, an adaptable band gap and optical transparency [2–6]. Nonlinear optical (NLO) properties of MXene have drawn wide attention [7]. Among them, Ti₃C₂Tx is the first and most-studied MXene, and the research has been progressing vigorously regarding the linear optical properties [8–13].

Ti₃C₂Tx thin films was studied by Mochalin and Podila et al., and the findings exhibited a high modulation depth of 50% and high damage thresholds of 70 mJ cm⁻² [11]. Ti₃C₂Tx was synthesized by Wen and Zhang et al. who revealed the Ti₃C₂Tx maximum nonlinear absorption coefficient 10–21 m²/V² had been increased tremendously compared with other 2D materials [12].

Thus far, the linear optical properties have been explored experimentally and theoretically in an extensive way, while little attention has been drawn to V₂CT_x's optical nonlinear features as well as its related applications. The Z-scan technique proposed by Sheik-Bahae et al. is simple and accurate and is widely used to study the nonlinear properties of materials (particularly non-fluorescent) [13].

To achieve the application-oriented demands for MXenes, a large variety of modified techniques have been invented to obtain desired functionalities, such as the previous studies on colloidal solutions of nanoparticles (NPs) hybridized by graphene, TMDs, etc. [14].

Moreover, great breakthroughs have taken place in NLO applications via hybridizing NPs in the past few years in accordance with their defect states, surface control and excellent plasmonic properties [15–17]. In various experiments on its broadband and strong NLO response, V₂CT_x nanosheets, a new member of the MXene family, has drawn extensive

attention due to its novel optical properties. Recent studies have shown that it has very good performance in hybrid mode-locking and good optical nonlinear properties, which indicates its good potential applications in acting as sensors and nonlinear components for lasers [18,19].

2. Materials and Methods

2.1. Preparation of Ag@V₂C Hybrids

First, 400 mesh V₂AlC (1 g) powder (Suzhou Beike Nano Technology Co., Ltd., Suzhou, China) is added slowly to 50% (v/v) HF solution, and it is stirred at room temperature for 90 h [16–18] to ensure the V-Al bonds are completely disconnected from V₂AlC with the V-C bonds intact. Second, to stratify the V₂CT_x, 30 mL tetraethylammonium hydroxide (TMAOH 25% in H₂O) is blended with 1 g multilayer V₂CT_x and sonicated for 30 min at room temperature, and the precipitates are rinsed with deionized water to neutrality (pH ≥ 6). Then, the excess TMAOH is discarded from the product by repeated centrifugation at 3000 rpm. Finally, a 2D monolayer V₂CT_x MXene material is obtained via freeze-drying.

The Ag@V₂C hybrids are made ready by mingling the V₂C hybrid dispersion and AgNO₃ solution. These are shown in Figure 1. First, 3 mL of original V₂C colloidal solution (1 mg/mL) in 30 mL of AgNO₃ solution (1 mg/mL) is re-dispersed, and the mixture is sonicated for 30 min. Then, the obtained colloidal solution of hybrid nanocomposites of Ag@V₂C hybrids is centrifuged at 12,000 rpm for 20 min and re-dispersed in 30 mL deionized water.

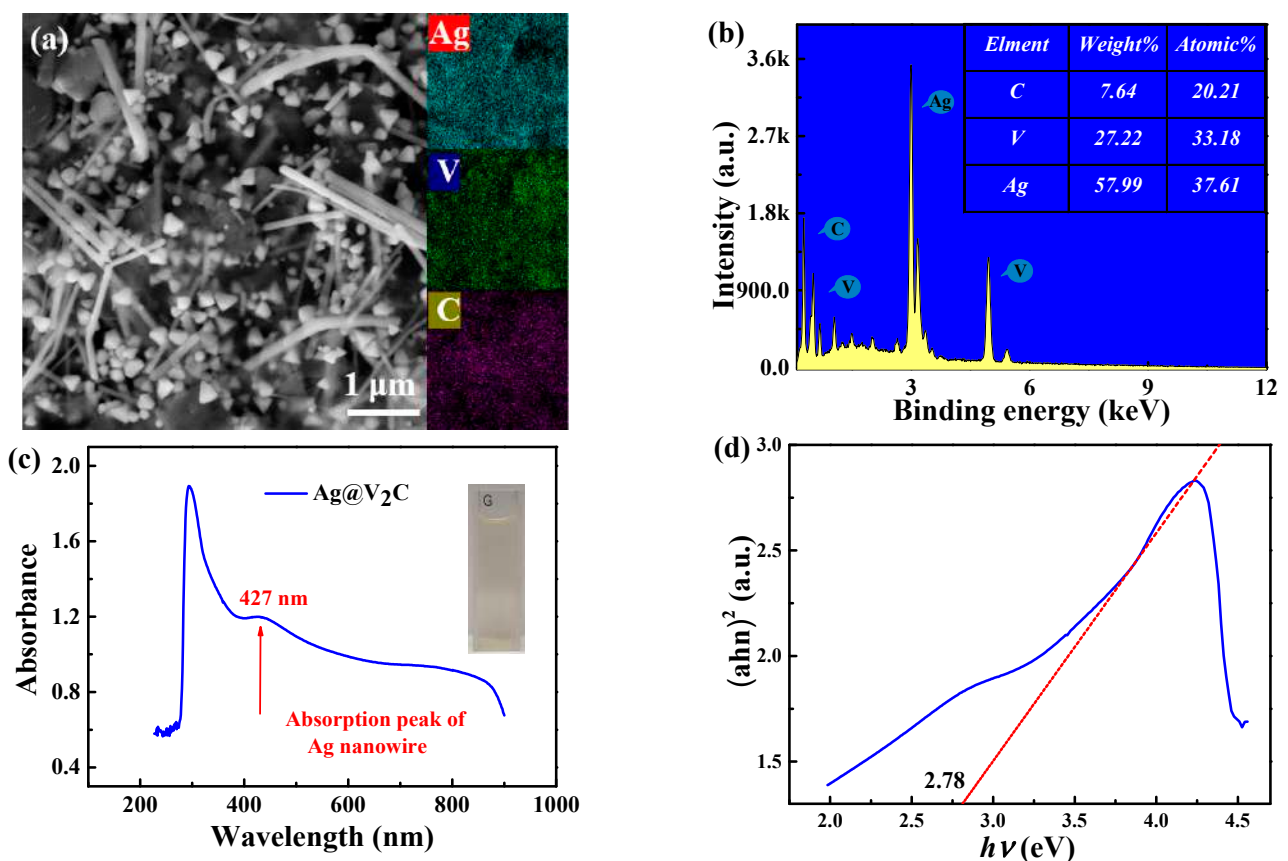


Figure 1. (a) SEM and EDS mappings of Ag V C elements. (b) EDS of Ag@V₂C. The inset is atomic ratios for diverse elements. (c) Optical absorption spectra of Ag@V₂C. (d) Estimation of the band gap of Ag@V₂C.

2.2. Optical Experimental Setup

SEM on a ZEISS Sigma 300 (acceleration voltage: 15 kV, Dublin, CA, USA) was employed to perform the morphological study with a spectrometer (Ocean Optics 4000, CA, USA) to survey the UV–Vis–NIR spectra of monolayer V_2CT_x MXene. To evaluate the NLO features of V_2CT_x MXene flakes nanoparticles, we performed an experiment of a single beam open aperture (OA) Z-scan, with the help of a 6 ns 8 Hz Q-switched Nd:YAG nanosecond pulse laser (Surelite II, Continuum, San Jose, CA, USA) and an optical parametric oscillator (Continuum, APE OPO) to produce lasers beams of diverse wavelengths. In this experiment, the linear transmittance of the V_2CT_x hybrids solution was measured at 500 nm wavelength, and we found that it was 72%.

The laser beam with a waist diameter of 200 μm is focused through a lens with a focal length of 20 cm and projected onto a 2 mm diameter quartz cuvette filled with aqueous dispersion of V_2CT_x monolayer flake nanoparticles. The cuvette is installed on a computer-operated translation motion stage where the transmitted data for every z point is recorded by stored program. Their NLO properties are studied by Z-scan technology under 532 nm nanosecond laser pulses. The findings indicate that the $Ag@V_2CT_x$ has a large nonlinear absorption coefficient.

3. Results

Figure 1a illustrates the typically morphologic multilayer $Ag@V_2C$ with coarse surface and the shape of accordion. The elements mapping data of SEM in combination with EDS illustrates that the Ag, V and C elements are evenly dispersed in the monolayer V_2C . In Figure 1b, the fundamental analysis of $Ag@V_2C$ V_2C , the result of C: V: Ag \approx 2:3:3 is obtained via the energy dispersive X-ray energy spectrum (EDS), while it is impracticable to measure the content of other elements by EDS due to the inadequate content.

In Figure 1c, the linear absorbance spectra of $Ag@V_2C$ is investigated by using ultraviolet visible near infrared spectrophotometer to observe two absorption peaks—that is, 315 and 427 nm. These findings justify that the surface of $Ag@V_2C$ is functionalized with Ag nanoparticles, and the positions of the peaks were predicted by theoretical calculations. In Figure 1d, the estimated band gap value of $Ag@V_2C$ is 2.75–2.80 eV according to Kubelka-Munk’s theory in previous data [19].

Hereinafter are the three different phases. In Figure 2a, the transmittance of $Ag@V_2C$ hybrids remains flat before rising sharply when the Z position approaches zero, and a peak is observed, which reflects the SA property. In Figure 2b, the conversion from SA to RSA is observed. The transmittance goes up to the first peak to indicate SA property and then falls back to a valley to indicate the reverse saturable absorption RSA property when the Z position approaches zero. It then rises again to the second peak and falls back to the flat linear transmittance. In Figure 2c, the laser pulse energy mounts to 681 when a deep valley occurs, which indicates the RSA property. Figure 2a–c, in general, reveals a whole process of NLO properties, including SA, conversion and RSA.

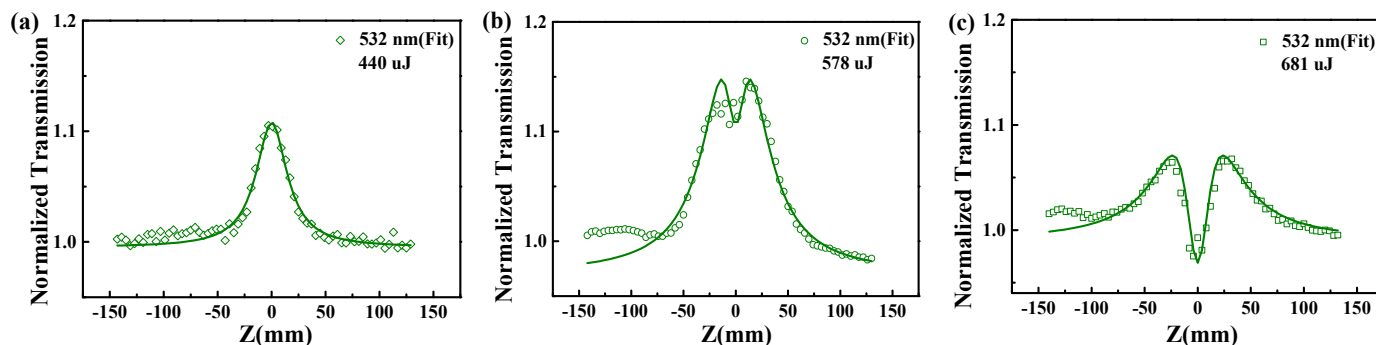


Figure 2. Open aperture Z-scan is conducted at the wavelength of 532 nm and the laser energies at (a) 440 μJ , (b) 578 μJ and (c) 681 μJ to obtain the normalized transmission of V_2CT_x hybrid colloid.

The physical mechanism of NLO properties can be expounded as follows in Figure 3. The above findings are related in the main to the changing energy of incident laser pulse and the nature property of MXene. It is generally believed that nonlinear susceptibility of the material results from intraband transition, interband transition, hot electron excitation and thermal effects. [20]. Specifically, when Ag@V₂C monolayer flakes are at low pulse energy, one photon absorption arises to indicate the SA property [21].

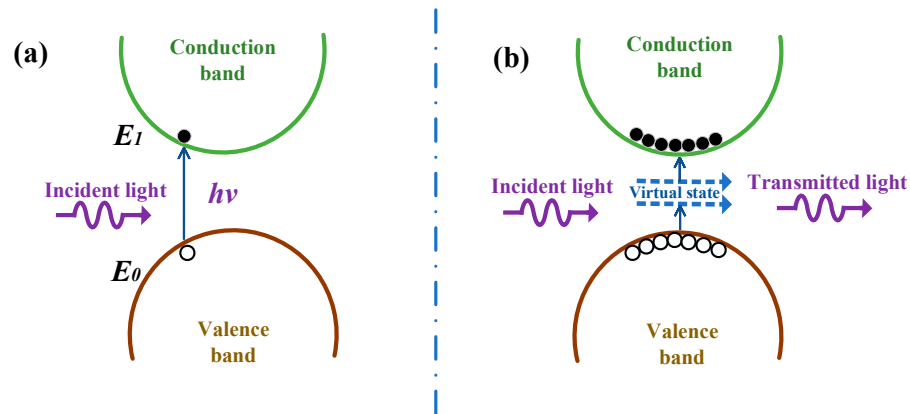


Figure 3. The physical mechanism of the NLO properties of Ag@V₂C monolayer flakes. (a) One photon absorption. (b) Two photon absorption.

Under laser irradiance, as the sample approaches the focal point, the laser energy increases abruptly, and the materials absorbs much incident light pulse when Ag@V₂C monolayer hybrids are pumped into an excited state, leaving a small amount at the ground state. Thus, more light penetrates the sample to make the transmittance higher and SA can be observed [22]. This phenomenon is termed ground-state bleaching of the plasmon band.

To remove the thermal effect’s influence on the possibility of nonlinearity, a laser pulse was set with a short duration and low repetition rate (10 Hz and 6 ns). Moreover, as the incident pulse energy goes up to 1080 μ J, the conversion appears; as it reaches 1380 μ J, RSA occurs. The major causes of RSA may be due to the excited state absorption (ESA) and two-photon absorption (TPA) [23].

The quantitative findings of the Z-scan experiment are as follows. The quantitative relationship between laser energy intensity and optical path length can be expressed as follows [24]:

$$dI = -\alpha I dz \tag{1}$$

In Equation (1), I signifies the laser intensity, z signifies the optical path length, and α signifies the absorption coefficient. The absorption coefficient combining SA and RSA in Ag@V₂C monolayer hybrids is expressed in Equation (2) [25]:

$$\alpha(I) = \frac{\alpha_0}{1 + (I/I_s)} + \beta I \tag{2}$$

Here, α_0 signifies the linear absorption coefficient of Ag@V₂C monolayer hybrids, I signifies the laser intensity, I_s is the saturable intensity, and β is the positive nonlinear absorption coefficient. I in Equation (3) can also be expressed as follows in Equation (3):

$$I = \frac{I_0}{1 + z^2/z_0^2} \tag{3}$$

Therefore, Equation (2) can be reconsidered as:

$$\alpha(I_0) = \frac{\alpha_0}{1 + \frac{I_0}{(1+z^2/z_0^2)I_s}} + \frac{\beta I_0}{1 + z^2/z_0^2} \tag{4}$$

With the help of Equations (1)–(4), the data of normalized transmission in Figure 3 can be fitted. In this way, related parameters are obtained as shown in Table 1.

Table 1. The nonlinear optical parameters of Ag@V₂C monolayer flake hybrids.

λ (nm)	I_0 (W/m ²)	I_s (W/m ²)	β (m/W)
532	1.1×10^{14}	0.61×10^6	-
	1.4×10^{14}	0.82×10^6	
	7.4×10^{13}	0.23×10^6	
			1.12×10^{-10}

To inspect the ultrafast carrier dynamics of Ag@V₂C hybrids, broadband transient absorption was studied. In Figure 4a, TA spectra of Ag@V₂C hybrids are illustrated by 2D map of TA signals that have been achieved temporally and spectrally. A constant pump fluence (6.4×10^3 mW/cm²) and probe beam ranging from 450 to 600 nm are employed to measure broadband TA signals and obtain the 2D color coded maps, cut horizontally through each map five times to obtain five differential absorption spectra at different delay times (0, 3.2, 4.0, 6.6 and 11 ps).

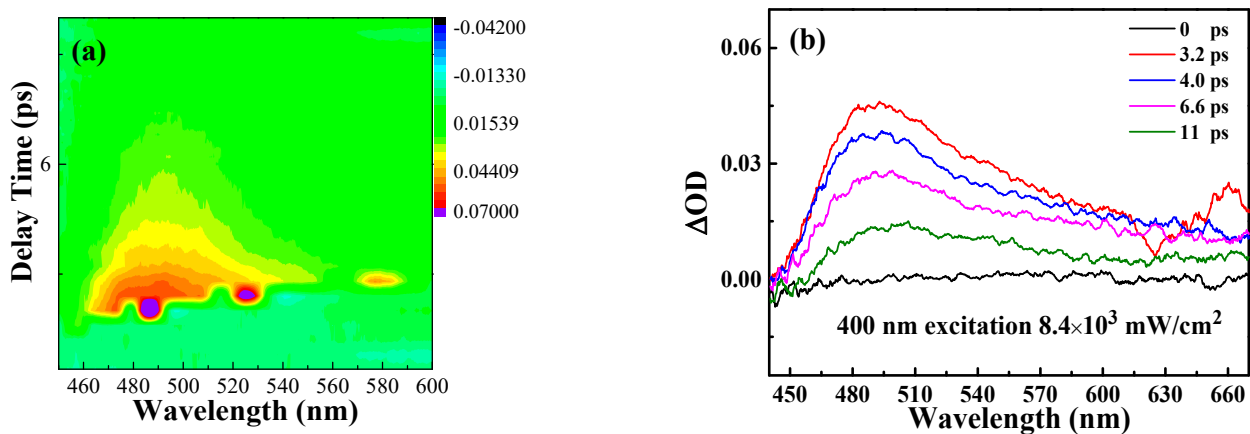


Figure 4. Carrier dynamics (at 400 nm pump) curves for Ag@V₂C. (a) Two-dimensional (2D) mapping of transient absorption spectra pumped at 400 nm with a fluence of 8.4×10^3 mW/cm², (b) Time and wavelength resolved transient absorption data of Ag@V₂C.

In Figure 4b, a positive absorption proves the generation of excited state absorption (ESA) in the spectral region as well as an ultrafast carrier relaxation process within the scale of ps. When the delay time increases, the amplitude of TA spectrum is reduced. The black curve, around the 0 ps delay time, signifies the unexcited Ag@V₂C hybrids. The peak value of Ag@V₂C hybrids, 485 nm, forms when the photo-induced absorption is brought about by the conversion of occupied–unoccupied states, which are found in the Z-scan experiment as RSA [26–28].

Then, the TA signal decays at ~ 13 ps and falls back to zero in the full waveband. The energy of the pump light markedly exceeds the energy bandgap of the Ag@V₂C nanosheet, the former 400 nm (~ 3.10 eV) laser, the latter being ~ 2.78 eV). Hence, with the incident laser pulse working up, electrons are excited and jump back and forth to the conduction band, while the holes remain in the valence band [29].

Soon afterwards is the conversion from electrons to hot electrons through photo-exciting with Fermi–Dirac distribution. The hot carriers will chill down shortly in sync with the decay process through e–e and e–ph diffusion on the conduction band, and with the carrier-phonon dispersing over a few relaxation processes, the hot carriers relax from the conduction band to the valence band and reunite with the holes.

In Figure 5a, the carrier dynamics are inspected at various wavelengths—that is, 480, 495, 515 and 540 nm, as shown in the figure. The optical transmission responses of Ag@V₂C hybrids are composed of two decay processes, a fast and a slow one. Coulomb-induced

hot electrons are excited to be at the core state and be trapped by the surface state before releasing spare energy by dispersing the optical phonons (3.9 ps). The rest of the chilled electrons will experience nonradiative transition to fall back to ground state within 30.1 ps [30,31]. The above-mentioned biexponential decay function is formulated in Equation (3) [32].

$$\frac{\Delta T}{T} = A_1 \exp\left(-\frac{t}{\tau_1}\right) + A_2 \exp\left(-\frac{t}{\tau_2}\right) \quad (5)$$

where A_1 and A_2 signify the amplitudes of the fast, slow decay components, respectively; and τ_1 and τ_2 are the decay lifetimes of each component, correspondingly. The experimental data in Figure 5a justify the formulation of Equation (3) through which the fast and slow decay components, τ_1 and τ_2 , are determined along with the rise of probe wavelengths owing to electrons at the lower energy states that are more apt to be detected and whose number is less likely to decrease than those at higher energy states. Similar properties can be seen in graphite [33].

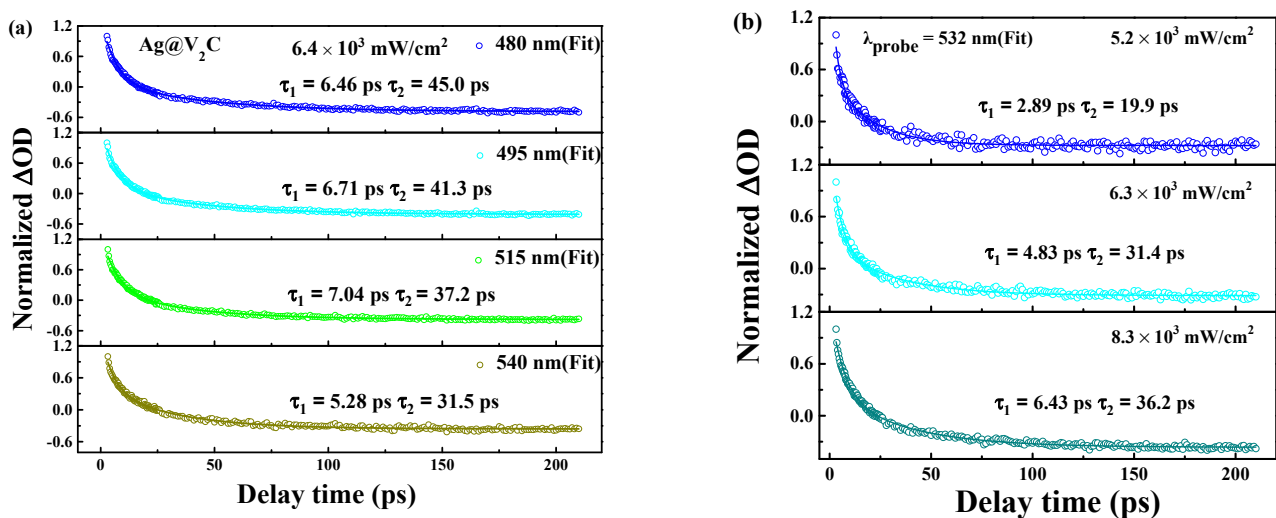


Figure 5. (a) Carrier dynamics (at 400 nm pump) curves for Ag@V₂C nanosheet at various probe wavelengths of 480, 495, 525, 515 and 540 nm, respectively. The scatters are experimental data while the solid lines are theoretical fit generated with pump fluence fixed at 6.4×10^3 mW/cm². (b) Carrier dynamics curves (at 400 nm pump) at different pump fluences 5.2×10^3 , 6.3×10^3 and 8.3×10^3 mW/cm² with a probe wavelength fixed at 532 nm.

The pump fluence effect on carrier dynamics is inspected at the 500 nm probe wavelength. In Figure 5b, the findings of various pump-fluences (5.1×10^3 , 6.4×10^3 and 8.1×10^3 mW/cm²) accord with the results by applying Equation (3) and the corresponding parameters. With the rise of pump fluence, τ_1 goes up from 3.9 to 4.5 ps, and τ_2 goes from 11.1 to 13.2 ps, which is inseparable to the carrier density and its reliance on e–ph coupling [34]).

In brief, the faster decay part of 2D materials follow the principle of e–ph scattering, while the slower part that of ph–ph scattering [35], among which the necessary basis of the electrons’ energy transfer is the electron–phonon interaction [36]. Ultimately, the improved efficiency of electron–phonon interaction promotes the cooling process, or in other words, it is high energy injection that speeds up electron decay. Similar properties can be seen in either quantum dots or 2D films [37–39].

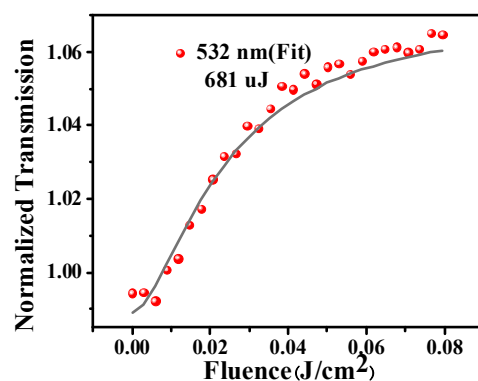
The data shown in Figure 5 can be verified upon checking Equation (3) and please see in Table 2 regarding τ_1 and τ_2 .

Table 2. Carrier dynamics parameters of the Ag@V₂C nanosheet.

	λ (nm)	τ_1 (ps)	τ_2 (ps)
Ag@V ₂ C	470	4.5	33.9
	485	4.6	36.5
	500	4.2	43.1
	520	3.9	45.8
V ₂ C nanosheet	470	3.8	18.0
	485	3.2	27.4
	500	4.6	22.5
	520	4.6	19.9

Resulting from the high density of Ag, those aroused electrons in the CB of Ag@V₂C hybrids tend to move to the d band of Ag atoms until the bleaching effect of VB disappears, which extends the aroused, composite electrons' lifetime and, accordingly, leads to more violent RSA properties [40]. Next, the electrons in the d band become excited functional groups to take in incident light before they move to a higher energy level and lead to an improved RSA effect. Then, the carriers that are excited and dressed with Ag nanoparticles will move from CB of Ti₃C to the sp band of the metal until they reach VB of Ag@V₂C hybrids. Compared with direct decay of pure Ti₃C₂ nanosheet, this takes a longer time scale (50 ps), and thus it enhances the RSA performance. Similar properties can be seen in other 2D materials [41].

Figure 6 exhibits the optical limiting response at 532 nm. With the increase of incident energy, the transmittance increases rapidly at first. When the incident energy continues to increase, the transmittance does not change drastically, which indicates that Ag@V₂C has superior optical limiting ability and can be used to manufacture optical limiting devices.

**Figure 6.** The optical limiting response at 532 nm.

4. Conclusions

Ag@V₂C ultrathin hybrids were synthesized via conventional etching, and remarkable NLO properties of Ag@V₂C hybrids were found through the OA z-scan technique at 532 nm. SA and RSA properties resulted mainly from GSB and TPA. Moreover, femtosecond transient absorption spectroscopy was adopted to inspect the ultrafast dynamics of the specimen, and we found that its decay contained a fast decay component (~4.5 ps) resulting from electron–phonon interactions and a slow component (~40 ps) from phonon–phonon interactions. Additionally, the two decay times increased with the pump fluence. The experiments confirmed that Ag@V₂C hybrids can be used in ultrafast optoelectronics and optical limiters.

Author Contributions: Data curation, C.C.; Funding acquisition, L.X., Z.X. and X.C.; Investigation, Y.S.; Resources, Q.H.; Writing—review and editing, L.X. All authors have read and agreed to the published version of the manuscript.

Funding: The article was supported by the following funds, Natural Science Foundation of Heilongjiang Province (Grant No. LH2021A019), East University of Heilongjiang Scientific Research Fund (Grant Nos. HDFHX210110, 210111, HDFKYTD202105) and Scientific research fund of Zhejiang Shuren University (Grant No. 2021R037).

Institutional Review Board Statement: Not applicable.

Informed Consent Statement: Not applicable.

Data Availability Statement: Data sharing is not applicable to this article.

Conflicts of Interest: The authors declare no conflict of interest.

References

- Naguib, M.; Kurtoglu, M.; Presser, V.; Lu, J.; Niu, J.; Heon, M.; Hultman, L.; Gogotsi, Y.; Barsoum, M.W. Two-dimensional nanocrystals produced by exfoliation of Ti_3AlC_2 . *Adv. Mater.* **2011**, *23*, 4248–4253. [CrossRef] [PubMed]
- Keller, U. Recent developments in compact ultrafast lasers. *Nature* **2003**, *424*, 831–838. [CrossRef] [PubMed]
- Mashtalir, O.; Naguib, M.; Mochalin, V.N.; Dall’Agnese, Y.; Heon, M.; Barsoum, M.W.; Gogotsi, Y. Intercalation and delamination of layered carbides and carbonitrides. *Nat. Commun.* **2013**, *4*, 1716. [CrossRef] [PubMed]
- Lukatskaya, M.R.; Mashtalir, O.; Ren, C.E.; Dall’Agnese, Y.; Rozier, P.; Taberna, P.L.; Naguib, M.; Simon, P.; Barsoum, M.W.; Gogotsi, Y. Cation intercalation and high volumetric capacitance of two-dimensional titanium carbide. *Science* **2013**, *341*, 1502–1505. [CrossRef] [PubMed]
- Shahzad, F.; Alhabeib, M.; Hatter, C.B.; Anasori, B.; Hong, S.M.; Koo, C.M.; Gogotsi, Y. Electromagnetic interference shielding with 2D transition metal carbides (MXenes). *Science* **2016**, *353*, 1137–1140. [CrossRef]
- Peng, Q.; Guo, J.; Zhang, Q.; Xiang, J.; Liu, B.; Zhou, A.; Liu, R.; Tian, Y. Unique lead adsorption behavior of activated hydroxyl group in two-dimensional titanium carbide. *J. Am. Chem. Soc.* **2014**, *136*, 4113–4116. [CrossRef]
- Jhon, Y.I.; Koo, J.; Anasori, B.; Seo, M.; Lee, J.H.; Gogotsi, Y.; Jhon, Y.M. Metallic MXene Saturable Absorber for Femtosecond Mode-Locked Lasers. *Adv. Mater.* **2017**, *29*, 1702496–1702503. [CrossRef]
- Enyashin, A.; Ivanovskii, A. Two-dimensional titanium carbonitrides and their hydroxylated derivatives: Structural, electronic properties and stability of MXenes $\text{Ti}_3\text{C}_{2-x}\text{N}_x(\text{OH})_2$ from DFTB calculations. *J. Solid State Chem.* **2013**, *207*, 42–48. [CrossRef]
- Lashgari, H.; Abolhassani, M.; Boochani, A.; Elahi, S.; Khodadadi, J. Electronic and optical properties of 2D graphene-like compounds titanium carbides and nitrides: DFT calculations. *Solid State Commun.* **2014**, *195*, 61–69. [CrossRef]
- Mauchamp, V.; Bugnet, M.; Bellido, E.P.; Botton, G.A.; Moreau, P.; Magne, D.; Naguib, M.; Cabioch, T.; Barsoum, M.W. Enhanced and tunable surface plasmons in two-dimensional Ti_3C_2 stacks: Electronic structure versus boundary effects. *Phys. Rev. B* **2014**, *89*, 235428. [CrossRef]
- Berdiyev, G. Optical properties of functionalized $\text{Ti}_3\text{C}_2\text{T}_2$ (T=F, O, OH) MXene: First-principles calculations. *AIP Adv.* **2016**, *6*, 055105. [CrossRef]
- Hantanasirisakul, K.; Zhao, M.Q.; Urbankowski, P.; Halim, J.; Anasori, B.; Kota, S.; Ren, C.E.; Barsoum, M.W.; Gogotsi, Y. Fabrication of $\text{Ti}_3\text{C}_2\text{T}_x$ MXene transparent thin films with tunable optoelectronic properties. *Adv. Electron. Mater.* **2016**, *2*, 1600050. [CrossRef]
- Dillon, A.D.; Ghidui, M.J.; Krick, A.L.; Griggs, J.; May, S.J.; Gogotsi, Y.; Barsoum, M.W.; Fafarman, A.T. Highly conductive optical quality solution-processed films of 2D titanium carbide. *Adv. Funct. Mater.* **2016**, *26*, 4162–4168. [CrossRef]
- Kim, I.Y.; Jo, Y.K.; Lee, J.M.; Wang, L.; Hwang, S.-J. Unique Advantages of Exfoliated 2D Nanosheets for Tailoring the Functionalities of Nanocomposites. *J. Phys. Chem. Lett.* **2014**, *5*, 4149–4161. [CrossRef] [PubMed]
- Biswas, S.; Kole, A.K.; Tiwary, C.S.; Kumbhakar, P. Enhanced nonlinear optical properties of graphene oxide–silver nanocomposites measured by Z-scan technique. *RSC Adv.* **2016**, *6*, 10319–10325. [CrossRef]
- Li, Z.; Dong, N.; Cheng, C.; Xu, L.; Chen, M.; Wang, J.; Chen, F. Enhanced nonlinear optical response of graphene by silver-based nanoparticle modification for pulsed lasing. *Opt. Mater. Express* **2018**, *8*, 1368–1377. [CrossRef]
- Yan, X.; Wu, X.; Fang, Y.; Sun, W.; Yao, C.; Wang, Y.; Zhang, X.; Song, Y. Effect of silver doping on ultrafast broadband nonlinear optical responses in polycrystalline Ag-doped InSe nanofilms at near-infrared. *RSC Adv.* **2020**, *10*, 2959–2966. [CrossRef]
- Ma, C.Y.; Huang, W.C.; Wang, Y.Z.; Adams, J.; Wang, Z.H.; Liu, J.; Song, Y.F.; Ge, Y.Q.; Guo, Z.Y.; Hu, L.P.; et al. MXene saturable absorber enabled hybrid mode-locking technology: A new routine of advancing femtosecond fiber lasers performance. *Nanophotonics* **2020**, *9*, 2451–2458. [CrossRef]
- He, Q.; Hu, H.H.; Shao, Y.B.; Zhao, Z.Z. Switchable optical nonlinear properties of monolayer V_2CT_x MXene. *Optik* **2021**, *247*, 167629. [CrossRef]
- Naguib, M.; Gogotsi, Y. Synthesis of Two-Dimensional Materials by Selective Extraction. *Acc. Chem. Res.* **2015**, *48*, 128–135. [CrossRef]
- Jiang, X.; Liu, S.; Liang, W.; Luo, S.; He, Z.; Ge, Y.; Wang, H.; Cao, R.; Zhang, F.; Wen, Q. Broadband nonlinear photonics in few-layer MXene $\text{Ti}_3\text{C}_2\text{T}_x$ (T=F, O, or OH). *Laser Photonics Rev.* **2018**, *12*, 1700229. [CrossRef]
- Dong, Y.; Chertopalov, S.; Maleski, K.; Anasori, B.; Hu, L.; Bhattacharya, S.; Rao, A.M.; Gogotsi, Y.; Mochalin, V.N.; Podila, R. Saturable absorption in 2D Ti_3C_2 MXene thin films for passive photonic diodes. *Adv. Mater.* **2018**, *30*, 1705714. [CrossRef] [PubMed]

23. Wang, J.; Chen, Y.; Li, R.; Dong, H.; Zhang, L.; Lotya, M.; Coleman, J.N.; Blau, W.J. Nonlinear optical properties of graphene and carbon nanotube composites. In *Carbon Nanotubes-Synthesis, Characterization, Applications*; Yellampalli, S., Ed.; IntechOpen: London, UK, 2011.
24. Sheik-Bahae, M.; Said, A.A.; Wei, T.; Hagan, D.J.; Stryland, E.W.V. Sensitive measurement of optical nonlinearities using a single beam. *IEEE J. Quantum Electron.* **1990**, *26*, 760–769. [CrossRef]
25. Wu, W.; Chai, Z.; Gao, Y.; Kong, D.; Wang, Y. Carrier dynamics and optical nonlinearity of alloyed CdSeTe quantum dots in glass matrix. *Opt. Mater. Express* **2017**, *7*, 1547–1556. [CrossRef]
26. Wang, J.; Ding, T.; Wu, K. Charge transfer from n-doped nanocrystals: Mimicking intermediate events in multielectron photocatalysis. *J. Am. Chem. Soc.* **2018**, *140*, 7791–7794. [CrossRef]
27. Lu, S.; Sui, L.; Liu, Y.; Yong, X.; Xiao, G.; Yuan, K.; Liu, Z.; Liu, B.; Zou, B.; Yang, B. White Photoluminescent Ti₃C₂ MXene Quantum Dots with Two-Photon Fluorescence. *Adv. Sci.* **2019**, *6*, 1801470. [CrossRef]
28. Wu, K.; Chen, J.; McBride, J.R.; Lian, T. Efficient hot-electron transfer by a plasmon-induced interfacial charge-transfer transition. *Science* **2015**, *349*, 632–635. [CrossRef]
29. Xie, Z.; Zhang, F.; Liang, Z.; Fan, T.; Li, Z.; Jiang, X.; Chen, H.; Li, J.; Zhang, H. Revealing of the ultrafast third-order nonlinear optical response and enabled photonic application in two-dimensional tin sulfide. *Photonics Res.* **2019**, *7*, 494–502. [CrossRef]
30. Zhang, H. Ultrathin Two-Dimensional Nanomaterials. *ACS Nano* **2015**, *10*, 9451–9469. [CrossRef]
31. Wibmer, L.; Lages, S.; Unruh, T.; Guldi, D.M. Excitons and Trions in One-Photon- and Two-Photon-Excited MoS₂: A Study in Dispersions. *Adv. Mater.* **2018**, *30*, 1706702. [CrossRef]
32. Guo, J.; Shi, R.; Wang, R.; Wang, Y.; Zhang, F.; Wang, C.; Chen, H.; Ma, C.; Wang, Z.; Ge, Y.; et al. Graphdiyne-Polymer Nanocomposite as a Broadband and Robust Saturable Absorber for Ultrafast Photonics. *Laser Photonics Rev.* **2020**, *14*, 1900367–1900378. [CrossRef]
33. Breusing, M.; Ropers, C.; Elsaesser, T. Ultrafast Carrier Dynamics In Graphite. *Phys. Rev. Lett.* **2009**, *102*, 210–213. [CrossRef] [PubMed]
34. Xu, Y.; Jiang, X.-F.; Ge, Y.; Guo, Z.; Zeng, Z.; Xu, Q.-H.; Han, Z.; Yu, X.-F.; Fan, D. Size-dependent nonlinear optical properties of black phosphorus nanosheets and their applications in ultrafast photonics. *J. Mater. Chem. C* **2017**, *5*, 3007–3013. [CrossRef]
35. Gao, L.; Chen, H.; Zhang, F.; Mei, S.; Zhang, Y.; Bao, W.; Ma, C.; Yin, P.; Guo, J.; Jiang, X.; et al. Ultrafast Relaxation Dynamics and Nonlinear Response of Few-Layer Niobium Carbide MXene. *Small Methods* **2020**, *4*, 2000250. [CrossRef]
36. Brongersma, M.L.; Halas, N.J.; Nordlander, P. Plasmon-induced hot carrier science and technology. *Nat. Nanotechnol.* **2015**, *10*, 25–34. [CrossRef]
37. Urayama, J.; Norris, T.B.; Singh, J.; Bhattacharya, P. Observation of Phonon Bottleneck in Quantum Dot Electronic Relaxation. *Phys. Rev. Lett.* **2001**, *86*, 4930–4933. [CrossRef]
38. Wang, J.; Wu, C.; Dai, Y.; Zhao, Z.; Wang, A.; Zhang, T.; Wang, Z.L. Achieving ultrahigh triboelectric charge density for efficient energy harvesting. *Nat. Commun.* **2017**, *8*, 88. [CrossRef]
39. Kameyama, T.; Sugiura, K.; Kuwabata, S.; Okuhata, T.; Tamai, N.; Torimoto, T. Hot electron transfer in Zn–Ag–In–Te nanocrystal–methyl viologen complexes enhanced with higher-energy photon excitation. *RSC Adv.* **2020**, *10*, 16361–16365. [CrossRef]
40. Kalanoor, B.S.; Bisht, P.B.; Akbar, A.S.; Baby, T.T. Optical nonlinearity of silver-decorated graphene. *J. Opt. Soc. Am. B* **2012**, *29*, 669–675. [CrossRef]
41. Yu, Y.; Si, J.; Yan, L.; Li, M.; Hou, X. Enhanced nonlinear absorption and ultrafast carrier dynamics in graphene/gold nanoparticles nanocomposites. *Carbon* **2019**, *148*, 72–79. [CrossRef]



Article

Terahertz Modulation and Ultrafast Characteristic of Two-Dimensional Lead Halide Perovskites

Hongyuan Liu ¹, Xunjun He ^{2,*} , Jie Ren ², Jiuxing Jiang ³, Yongtao Yao ⁴ and Guangjun Lu ^{5,*}¹ School of Computer Science, Harbin University of Science and Technology, Harbin 150080, China² Key Laboratory of Engineering Dielectric and Applications (Ministry of Education), School of Electrical and Electronic Engineering, Harbin University of Science and Technology, Harbin 150080, China³ College of Science, Harbin University of Science and Technology, Harbin 150080, China⁴ National Key Laboratory of Science and Technology on Advanced Composites in Special Environments, Harbin Institute of Technology, Harbin 150080, China⁵ School of Electronic and Information Engineering/School of Integrated Circuits, Guangxi Normal University, Guilin 541004, China

* Correspondence: hexunjun@hrbust.edu.cn (X.H.); lv-guangjun@163.com (G.L.)

Abstract: In recent years, two-dimensional (2D) halide perovskites have been widely used in solar cells and photoelectric devices due to their excellent photoelectric properties and high environmental stability. However, the terahertz (THz) and ultrafast responses of the 2D halide perovskites are seldom studied, limiting the developments and applications of tunable terahertz devices based on 2D perovskites. Here, 2D R-P type (PEA)₂(MA)₂Pb₃I₁₀ perovskite films are fabricated on quartz substrates by a one-step spin-coating process to study their THz and ultrafast characteristics. Based on our homemade ultrafast optical pump–THz probe (OPTP) system, the 2D perovskite film shows an intensity modulation depth of about 10% and an ultrafast relaxation time of about 3 ps at a pump power of 100 mW due to the quantum confinement effect. To further analyze the recombination mechanisms of the photogenerated carriers, a three-exponential function is used to fit the carrier decay processes, obtaining three different decay channels, originating from free carrier recombination, exciton recombination, and trap-assisted recombination, respectively. In addition, the photoconductor changes ($\Delta\sigma$) at different pump–probe delay times are also investigated using the Drude–Smith model, and a maximum difference of 600 S/m is obtained at $\tau_p = 0$ ps for a pump power of 100 mW. Therefore, these results show that the 2D (PEA)₂(MA)₂Pb₃I₁₀ film has potential applications in high-performance tunable and ultrafast THz devices.

Citation: Liu, H.; He, X.; Ren, J.; Jiang, J.; Yao, Y.; Lu, G. Terahertz Modulation and Ultrafast Characteristic of Two-Dimensional Lead Halide Perovskites. *Nanomaterials* **2022**, *12*, 3559. <https://doi.org/10.3390/nano12203559>

Academic Editor: Elias Stathatos

Received: 30 June 2022

Accepted: 7 October 2022

Published: 11 October 2022

Publisher's Note: MDPI stays neutral with regard to jurisdictional claims in published maps and institutional affiliations.



Copyright: © 2022 by the authors. Licensee MDPI, Basel, Switzerland. This article is an open access article distributed under the terms and conditions of the Creative Commons Attribution (CC BY) license (<https://creativecommons.org/licenses/by/4.0/>).

Keywords: 2D R-P type perovskite; OPTP; terahertz modulation; ultrafast characteristics; Drude-Smith model

1. Introduction

In recent years, terahertz (THz) waves have received great attention from various researchers because of their special properties and promising applications in many fields. Currently, THz generators and detectors have been reported and consistently demonstrated, while THz functional devices have faced great challenges due to a lack of the appropriate nature materials [1–3]. THz modulators, as key components of THz communication fields, can modulate the amplitude, phase, and polarization of THz waves by exciting active materials to implement different functions [4–6]. Traditional semiconductors can achieve a high modulation speed among these active materials with ultrafast optical pumping. To achieve a high modulation depth, however, a high power is required to produce photogenerated carriers, thus significantly restricting their application fields [7]. Recently, three-dimensional (3D) organic–inorganic hybrid halide perovskites have achieved unprecedented and rapid developments in the field of photoelectric devices due to their

high absorption efficiency, adjustable energy band, high defect tolerance, and good carrier transport performance [8,9]. However, these conventional 3D halide perovskites are sensitive and unstable to water, light, and heat, meaning that there are high requirements for their preparation and preservation environments, thereby limiting their wide commercial applications [10,11]. For the previously studied $\text{CH}_3\text{NH}_3\text{PbI}_3$ perovskite, for example, the methylamino cation CH_3NH_3^+ (MA) is extremely soluble in water, and thus readily produces PbI_2 in the perovskite, causing irreversible chemical damages [11].

To solve the above issues, a commonly used method is to replace the organic cation in 3D perovskites with a hydrophobic long-chain organic cation to construct the 2D perovskites, thus enhancing the resistance to water molecules and environmental factors (such as ultraviolet rays and heat), and as a result, greatly improving the stability of the organic–inorganic hybrid perovskites [12–17]. Currently, 2D organic–inorganic halide perovskites have been rapidly developed in the field of optoelectronics due to their high stability, tunable photoelectric property, and high quantum efficiency [18–21]. For example, Karunadasa et al. first prepared a 2D organic–inorganic hybrid perovskite solar cell with an active layer of $(\text{PEA})_2(\text{MA})_2\text{Pb}_3\text{I}_{10}$, which can still maintain a high efficiency when placed in an environment with a relative humidity of 52% for 46 days [18]. After that, Sargent et al. designed $(\text{PEA})_2(\text{MA})_{n-1}\text{Pb}_n\text{I}_{n+1}$ ($n > 40$) perovskite systems, which can realize a short-circuit current of up to 19.12 mA/cm^{-2} and conversion efficiency of 15.3% [19]. In 2016, Jinwoo et al. used the $(\text{PEA})_2(\text{MA})_{n-1}\text{Pb}_n\text{Br}_{n+1}$ ($n = 1\text{--}4$) perovskite as a light-emitting layer to prepare high-efficiency quasi-2D light-emitting diodes (LEDs) with a current efficiency of 4.90 cd/A [20]. In 2021, Xu et al. fabricated highly efficient quasi-2D perovskite light-emitting diodes with a maximum brightness of $35,000 \text{ cd/m}^2$ and maximum external quantum efficiency (EQE) of 12.4% [21]. Although 2D perovskites have been extensively studied in photoelectric devices, the THz and ultrafast characteristics of the 2D perovskites are seldom reported, limiting the developments and applications of the tunable and ultrafast THz devices based on 2D perovskites [22].

In this paper, we investigated the THz and ultrafast responses of a 2D $(\text{PEA})_2(\text{MA})_2\text{Pb}_3\text{I}_{10}$ perovskite film to reveal the decay mechanisms of the photogenerated carriers. Firstly, $(\text{PEA})_2(\text{MA})_2\text{Pb}_3\text{I}_{10}$ perovskite films with $n = 3$ (PEA content of 50%) were prepared on the quartz substrates by a one-step spin-coating process. Then, the structural and photoelectric properties of the prepared films were characterized by the scanning electron microscope (SEM), X-ray diffraction (XRD), ultraviolet–visible (UV–vis) spectroscopy, and photoluminescence (PL) technologies, respectively. Next, the THz and ultrafast responses were measured using our homemade ultrafast optical pump–THz probe (OPTP) system, obtaining an intensity modulation depth of about 10% and an ultrafast relaxation time of about 3 ps for the pump power of 100 mW. To further discover the recombination mechanisms of the photogenerated carriers, finally, the decay process of the carriers was fitted using a three-exponential formula. Therefore, the prepared 2D $(\text{PEA})_2(\text{MA})_2\text{Pb}_3\text{I}_{10}$ perovskite has broad application prospects in the design of high-performance tunable and ultrafast THz devices.

2. Structure of 2D Perovskites

Generally, 2D organic–inorganic hybrid perovskites are expressed as $(\text{RNH}_3)_2\text{A}_{n-1}\text{M}_n\text{X}_{3n+1}$ ($n = 1, 2, 3, 4 \dots$), where R is the organic group, and n is the number of the stacked diagonal octahedral layers, namely the number of organic layers. When n is equal to 1 or a finite integer, the $(\text{RNH}_3)_2\text{A}_{n-1}\text{M}_n\text{X}_{3n+1}$ can be considered as a pure-2D or quasi-2D structure, while becoming a 3D structure as $n = \infty$, as shown in Figure 1. Thus, 2D organic–inorganic perovskites can be constructed by replacing the A in 3D structures with the hydrophobic organic macromolecules [20]. Figure 1a shows the structural schematics of the $(\text{PEA})_2(\text{MA})_{n-1}\text{Pb}_n\text{I}_{3n+1}$ perovskites with different PEA percentages, in which the organic and inorganic layers are interbedded with each other, resulting in the formation of a natural multi-quantum well structure, as shown in Figure 1b. Therefore, the 2D organic–inorganic perovskites not only have excellent environmental stability due to the existence of hydrophobic molecules resisting moisture,

light, and heat, but they also have a large exciton binding energy and excellent photoelectric properties due to the presence of the quantum well structure [18,23].

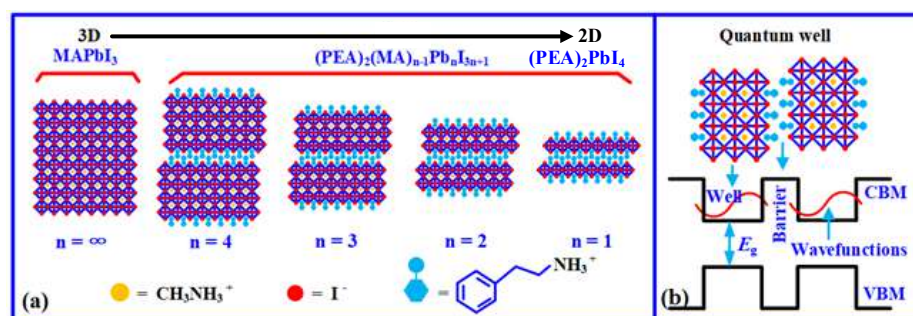


Figure 1. Structural schematic of the perovskites: (a) evolution process of perovskites from 3D to 2D and (b) multi-quantum well structure.

3. Fabrications and Characterization of 2D Perovskite Films

To obtain high-quality 2D perovskite films, it is very important to follow the fabrication procedures to ensure the growth of high-quality grains. Here, a one-step spin-coating process is applied to fabricate 2D perovskite films. Figure 2 shows the fabrication process of the 2D (PEA)₂(MA)₂Pb₃I₁₀ perovskite film. The detailed fabrication steps are as follows: firstly, the MAI and PEA₂I powders are dissolved in a DMF solution at a ratio of 1:1 to form a precursor solution. Then, the precursor solution is deposited on the surface of a 1 cm × 1 cm quartz substrate by the one-step spin-coating process with two consecutive stages (the first stage at 1000 r/min for 10 s, and the second with 3000 r/min for 50 s). Moreover, in the 30 s of the second spin-coating stage, the antisolvent (chlorobenzene) is continuously dripped onto the substrate to quickly form a uniform film. After spin-coating, the fabricated samples are transferred to a hot plate and annealed at 100 °C for 10 min to remove the residual solvents and transit the intermediate solvate phase into the perovskite, finally forming homogeneous 2D (PEA)₂(MA)₂Pb₃I₁₀ perovskite films. All of the fabrication steps are implemented inside a nitrogen-filled glove box at room temperature.

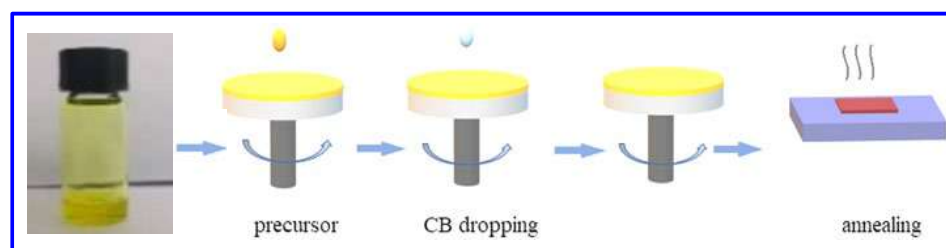


Figure 2. Fabrication process for (PEA)₂(MA)₂Pb₃I₁₀ perovskite film.

To examine the structural morphologies and optical properties of the as-fabricated perovskite films, next, we carried out different measurements and characterizations using SEM, XRD, UV–vis, and PL technologies, as shown in Figure 3. Figure 3a shows an optical microscope image of the 2D (PEA)₂(MA)₂Pb₃I₁₀ perovskite film, which indicates that the perovskite film is very flat and dense owing to the uniform distributions of the precursor solution on the substrate. Figure 3b displays a top-view SEM micrograph of the 2D (PEA)₂(MA)₂Pb₃I₁₀ perovskite film, in which the perovskite appears to have nanorod-like crystalline features at the length scale of hundreds of nanometers and a few pinholes due to tight contact between the grain boundaries. Figure 3c shows an XRD pattern of the perovskite film. In the XRD pattern, there are two diffraction peaks at 14.2° and 28.72°, corresponding to the (111) and (222) crystal planes, respectively, which is consistent with the previously reported crystal plane positions [24]. Moreover, no characteristic peaks associated with PbI₂ or other redundant phases are observed, suggesting that the

fabricated films were fully generated with a high crystallinity. Figure 3d presents the UV–vis absorption and PL emission spectra of the as-grown perovskite film. The PL emission spectrum shows only a PL peak with a full width at half maximum (FWHM) of 47 nm centered near 710 nm, while the absorption spectrum shows that the perovskite film has a broad absorption spectrum with three absorption peaks between 600 and 750 nm, indicating a bandgap of ~ 1.96 eV, as shown in Figure 3e. Moreover, these exciton absorption peaks mainly arise from the low n -member perovskite compounds, demonstrating the presence of 2D perovskites as well as multiphase [25]. In addition, non-zero values of absorbance below the absorption onset are also observed, which is consistent with the fact that the rougher film morphology of perovskites results in a large amount of scattering. Therefore, the above measurement results demonstrate that the as-grown perovskite is a 2D layer structure.

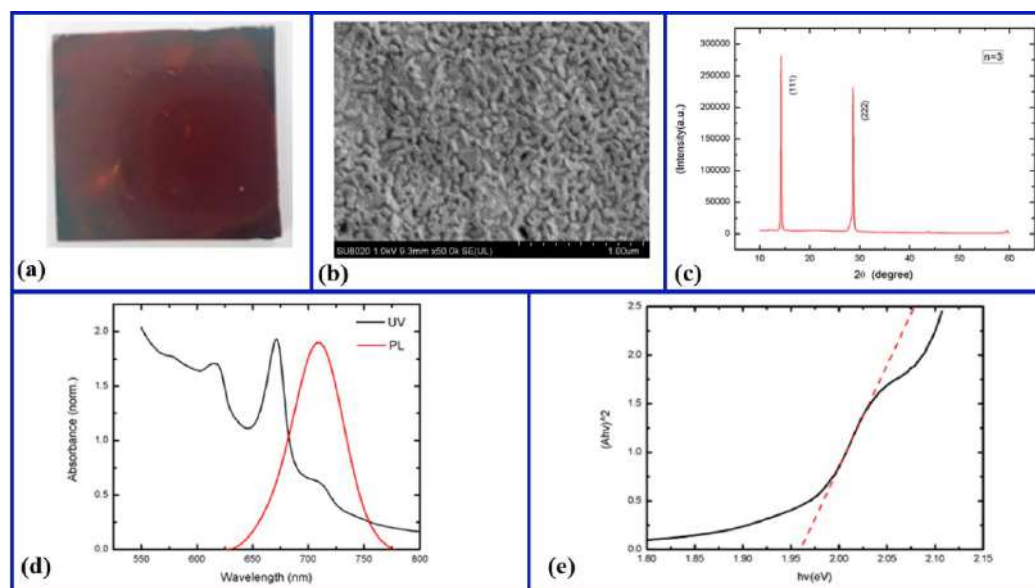


Figure 3. Structural morphologies and optical properties of $(\text{PEA})_2(\text{MA})_2\text{Pb}_3\text{I}_{10}$ perovskite: (a) optical microscope image, (b) SEM image, (c) XRD pattern, (d) absorption profile and PL spectrum, and (e) bandgap extraction.

4. Terahertz and Ultrafast Responses of 2D Perovskite Films

As is well-known, THz waves are very sensitive to changes in external circumstances. When the semiconductor films are pumped by external light, for example, the THz waves passing through them would be modulated due to the existence of photogenerated carriers. Moreover, the more photogenerated carriers, the greater the modulation depth of the device [26]. Thus, the application prospects of the materials can be further developed according to their modulation depths and speeds. A 2D $(\text{PEA})_2(\text{MA})_2\text{Pb}_3\text{I}_{10}$ perovskite is a direct bandgap semiconductor and can absorb the photons with energy larger than its bandgap width when pumped by the external light, producing great photogenerated carriers due to the transition of the electrons as a result. To evaluate the THz modulation depth and ultrafast characteristics of the fabricated 2D perovskite films, we set up an OPTP system mainly consisting of the ZnTe crystal-based THz generation and detection beams and an optical pump beam photoexciting the samples, as shown in Figure 4.

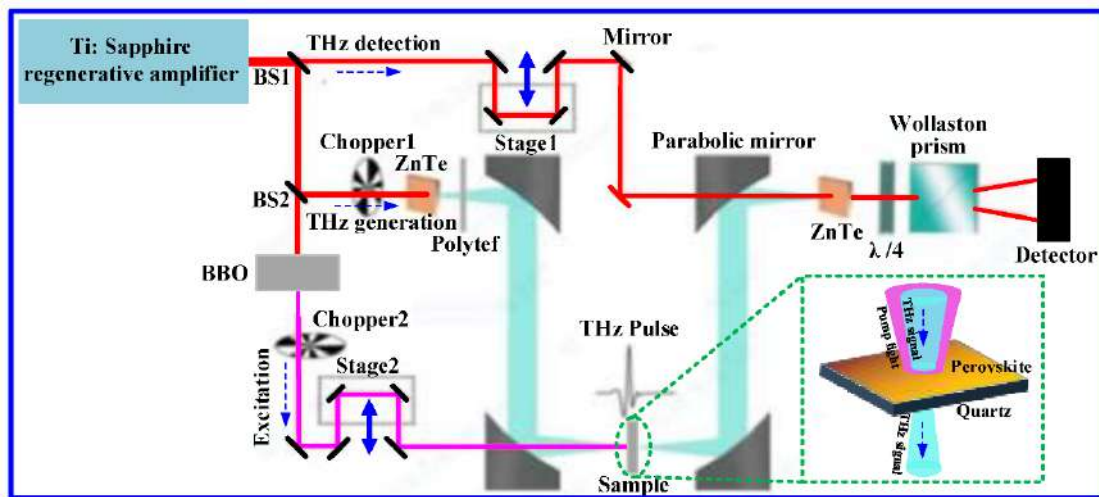


Figure 4. Schematic diagram of the homemade OPTP measurement system.

In this homemade system, an amplified Ti–sapphire laser with a pulse duration of 90 ps, wavelength of 800 nm, spectral width of 28 nm, and repetition rate of 75 MHz is used as the optical source for the generation and detection of the THz signal and the photoexcitation of the samples [27]. The laser output beam is split into three beams, where one beam is employed to excite the ZnTe crystal to generate a THz pulse, the second beam is used to detect the THz pulse via free-space electro–optic sampling in a ZnTe crystal, and the third part is used to generate a frequency-doubled 400 nm pump pulse using a barium borate (BBO) crystal to excite the 2D perovskite sample. Moreover, the 400 nm pump beam has an energy of 3.1 eV higher than the bandgap of 2D perovskites (1.96 eV), which can photoinduced free carriers and excitons. In addition, the diameter of the pump beam is 5 mm, which is larger than the diameter (2 mm) of the focused THz beam to ensure uniform photoexcitation. Thus, the ultrafast response measurements in the OPTP system are carried out by varying the delay time (τ_p) between pump and detection beams using a translational delay stage, while terahertz time-domain spectrum measurements are performed by fixing the pump pulse at the desired position and sampling the THz pulse using another translational delay stage. As a result, the frequency-dependent terahertz spectroscopy can be obtained after the Fourier transform [28].

To examine the THz modulation ability of the fabricated perovskite films, next, the THz time–domain spectra across the sample, fabricated onto a quartz substrate with a thickness of 2 mm, are measured using our OPTP system at different pump powers. The measurement results are shown in Figure 5a, where the gray dotted line is the reference value of the quartz substrate without the perovskite film. There is a significant time delay between the reference and the sample, demonstrating that the perovskite film were fabricated on the substrate. Figure 5b shows the normalized THz transmission spectra of the fabricated sample for different laser excitations, clearly observing a gradual reduction in the THz transmission with the increase in pump power. The change in the transmission spectra can be attributed to the generation of free carriers in the perovskites. For example, in the absence of a pump beam, the carriers in the perovskite are in the thermal balance state, and there is no observed split in the energy level of the perovskite. In this case, the perovskite has a few carriers that can freely move, and thus obtains a transmission intensity of about 90% at 1 THz. Once the perovskite film is pumped with different pump powers. However, the carriers are generated in the perovskite, breaking the thermal equilibrium state of the perovskite. By further increasing the pump power, the numbers of electrons and holes in the conductivity and valence bands of the perovskite can be gradually increased, leading to a reduction in terahertz transmission intensity, achieving a THz intensity change of nearly 5% at 1THz for a pump power of 100 mW.

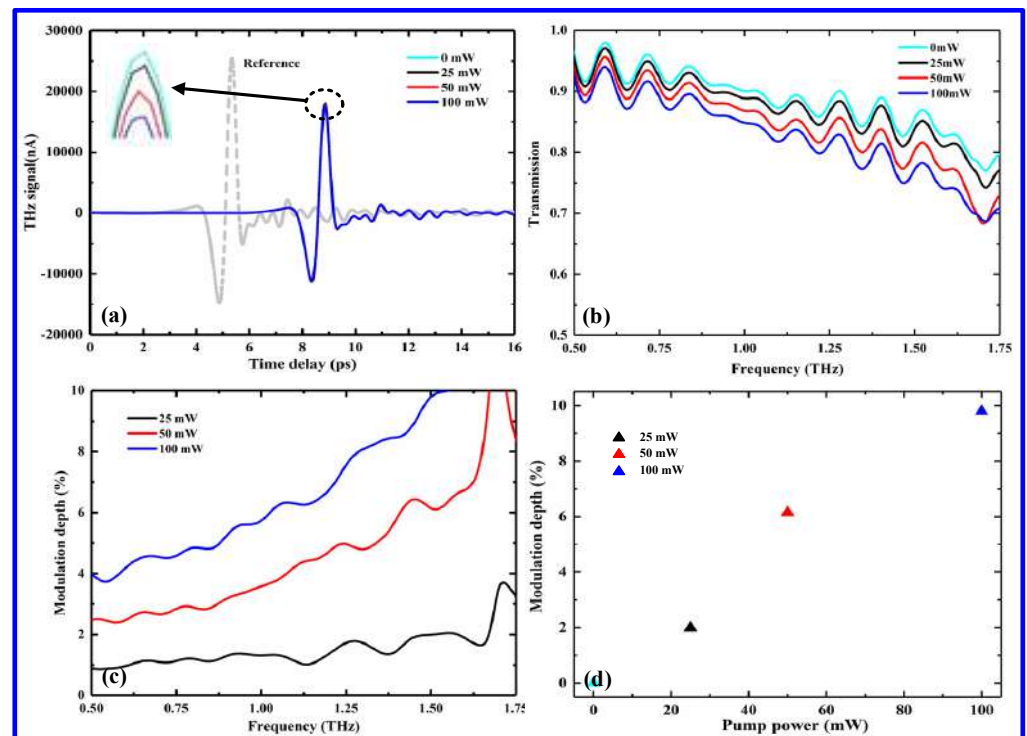


Figure 5. Terahertz performances of the fabricated $(\text{PEA})_2(\text{MA})_2\text{Pb}_3\text{I}_{10}$ perovskite films at different irradiation powers of 25 mW, 50 mW, and 100 mW: (a) terahertz time–domain transmission spectra, in which the inset shows the magnification values at the peak, and the dashed line represents the time-domain transmission spectrum of the reference substrate without perovskite film; (b) terahertz frequency-domain transmission spectra; (c) modulation depth over the broadband range of 0.5–1.75 THz; and (d) modulation depth of different pump powers at 1.5 THz.

To further assess the modulation performance of the $(\text{PEA})_2(\text{MA})_2\text{Pb}_3\text{I}_{10}$ perovskite film, a modulation depth (MD) was introduced to quantify the modulation ability of the perovskite film at different irradiation powers, which can be expressed as

$$MD = \frac{\int P_{laser-off}(\omega)d\omega - \int P_{laser-on}(\omega)d\omega}{P_{laser-off}(\omega)} \quad (1)$$

where $P_{laser-on}(\omega)$ and $P_{laser-off}(\omega)$ represent the THz amplitudes as the laser pump beam is turned on and off, respectively [29]. As shown in Figure 5c,d, the intensity modulation depth of the fabricated 2D $(\text{PEA})_2(\text{MA})_2\text{Pb}_3\text{I}_{10}$ perovskite films is gradually enhanced with the increase in pump power, showing a linear increase for different pump powers. The maximum intensity MD is found to be about 10% at 1.5 THz for the pump power of 100 mW. Moreover, the lower MD can be further improved by increasing the pump power. Therefore, the $(\text{PEA})_2(\text{MA})_2\text{Pb}_3\text{I}_{10}$ perovskite is demonstrated as a promising material that can implement a highly efficient THz modulation.

Next, to explore the ultrafast relaxation response of the photogenerated carriers, the homemade OPTP system is used to monitor the dynamic decay process of the photogenerated carriers by varying the relative delay time (τ_p) between the pump and detection beams. In this experiment, the sample is excited by a femtosecond laser beam with a 400 nm wavelength at the normal incidence, and the probing THz electric field vector is parallel to the plane of the surface of the sample [30]. Following photoexcitation, generally, the relative change in the THz electric field is proportional to the photoinduced conductivity of the pumped material due to the presence of free charges. Thus, the dynamics of charge carriers are manifested as the photoinduced THz transmission changes ($-\Delta T/T_0$) in the samples at the peak of the THz pulse as a function of pump–probe delay. Figure 6 shows

the transient THz transmission dynamics following the photoexcitation of the prepared 2D (PEA)₂(MA)₂Pb₃I₁₀ perovskite film for a range of pump powers. In these experimental results, it is noted that the nonequilibrium carriers relax at ultrafast speeds, fully recovering the equilibrium state within a dozen picosecond time scale for the pump power of 25 mW. Moreover, the fast relaxation becomes increasingly significant with the increase in the pump power, indicating that the 2D (PEA)₂(MA)₂Pb₃I₁₀ perovskite has potential application prospects in ultrafast THz devices. This ultrafast phenomenon can be attributed to the inherent multi-quantum well structure in the 2D perovskites.

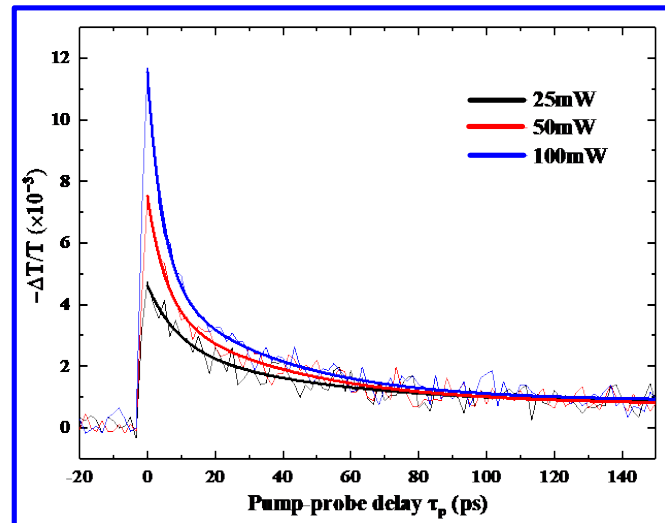


Figure 6. Carrier transient dynamics of 2D (PEA)₂(MA)₂Pb₃I₁₀ perovskite film at different pump powers (The thin and thick solid curves correspond to the measured and fitted results).

To further understand the ultrafast relaxation dynamics of the 2D (PEA)₂(MA)₂Pb₃I₁₀ perovskite, a triexponential decay function is used to fit the measured THz transient dynamics at different pump powers, extracting the carrier lifetimes of the ultrafast processes to discover the recombination channels of the photoexcited free carriers and excitons. Thus, the triexponential decay function is given by the following express [31]

$$f(t) = A_1 e^{-\frac{t}{\tau_1}} + A_2 e^{-\frac{t}{\tau_2}} + A_3 e^{-\frac{t}{\tau_3}} \quad (2)$$

where τ_1 , τ_2 , and τ_3 are the lifetimes of different relaxation processes, respectively. A_1 , A_2 , and A_3 are the corresponding coefficients of each lifetime component, which determine the weights of the decaying and nondecaying components separately. By fitting the measured THz transient changes obtained using our OPTP system, the lifetimes are extracted for different pump powers, as summarized in Table 1. As observed in Table 1, the lifetimes of the three components are $\tau_1 \sim 10$ ps, $\tau_2 \sim 33$ ps, and $\tau_3 \sim 2$ ns for a pump power of 25 mW, respectively. With the increase in the pump power, the initial fast relaxation process becomes faster, while the slow process becomes slower, obtaining $\tau_1 \sim 3$ ps, $\tau_2 \sim 18$ ps, and $\tau_3 \sim 6$ ns for the pump power of 100 mW as a result. These results indicate that such a decay process usually involves three recombination pathways: monomolecular recombination, bimolecular recombination, and Auger recombination [32]. At a lower pump power, the photogenerated carrier relaxations are dominated by the monomolecular decay (τ_3), corresponding to the slow process, whereas at a higher pump power, the recombination channels are dominated by the bimolecular decay (τ_2) and Auger decay (τ_1), corresponding to the fast process. Thus, the monomolecular decay component observed at a lower pump power arises most likely from trap-assisted recombinations, depending on the trap cross-section, energetic depth, density, and distribution. For higher pump power, the bimolecular decay originates from the overlaps of electron and hole wavefunctions,

while the Auger process results from the exciton–exciton scatterings, where the excitons are localized inside the QW structures, providing an additional channel for the fast relaxation of free carriers [30].

Table 1. Extracted lifetimes of different pump powers by the triexponential fitting.

Power	25 mW	50 mW	100 mW
τ_1 (ps)	10 ± 0.2	6 ± 0.2	3 ± 0.1
τ_2 (ps)	32 ± 0.8	30 ± 0.9	18 ± 1.2
τ_3 (ps)	1830 ± 30	3341 ± 50	5854 ± 50

To gain further insights into the ultrafast relaxation behaviors with three exponential decay components (τ_1 , τ_2 , and τ_3), the spectral dispersions of the THz photoinduced conductivity ($\Delta\sigma$) at different pump–probe delay times (τ_p) were derived from the measured THz transmission transient dynamics using the following expression [33]:

$$\Delta\sigma(\omega, \tau_p) \approx -\frac{n+1}{Z_0} \frac{\Delta T(\omega, \tau_p)}{T(\omega, \tau_p)} / d \text{ [S/m]} \quad (3)$$

where n is the refractive index of the quartz substrate, whose value is 1.95 at the terahertz range; $Z_0 = 377 \Omega$ is the impedance of free space; and d is the thickness of the perovskite film.

Figure 7a shows a typical trace of THz transmission for the pump power of 100 mW, which reveals the transient dynamics of free carriers and excitons in the 2D perovskite film, as discussed above. Figure 7b displays the THz electric field changes at different pump–probe delay times, as shown in Figure 7a (blue, red, and black solid curves correspond to τ_p of 0, 5, and 113 ps, respectively, in which the ΔE is enlarged by over ten times for clarity), while Figure 7c displays the changes in the THz photoconductivity extracted using the corresponding THz electric field changes, which is shown by scattered points. It is noted that the variations of the THz intensity and photoconductivity are increasingly weakened with the increase in the pump–probe delay time. For example, at $\tau_p = 0$ ps, the photogenerated carriers start to decay and relax quickly, and THz intensity and conductivity exhibit maximal changes due to the existence of abundant photogenerated carriers. As τ_p is increased from 0 to 5.0 ps, the change in THz intensity and conductivity is gradually decreased due to the recombination of the photogenerated carriers. At $\tau_p = 113$ ps, however, the system is almost restored to the initial balanced state, and the photogenerated carriers have been fully recombined, leading to the minimal change of the THz intensity and conductivity. Such a change trend can be attributed to the change in the photoinduced free carry density [34]. In addition, the Drude–Smith model is used to further fit the extracted photoinduced THz conductivities (solid curves of Figure 7c), and the corresponding deviations are shown in Figure 7d. It is noticed that in the early process, the extracted photoinduced THz conductivities show a considerable disparity from the Drude–Smith model due to the complicated THz responses, as shown in the top row of Figure 7d. Such a remarked deviation can result from the contributions of both the charge carrier transport and exciton–phonon scattering [35]. For the slow decay process ($\tau_p = 113$ ps), however, the extracted values agree well with the fitting values (see the bottom row of Figure 7d), indicating a primary contribution from the defect trapping process [36].

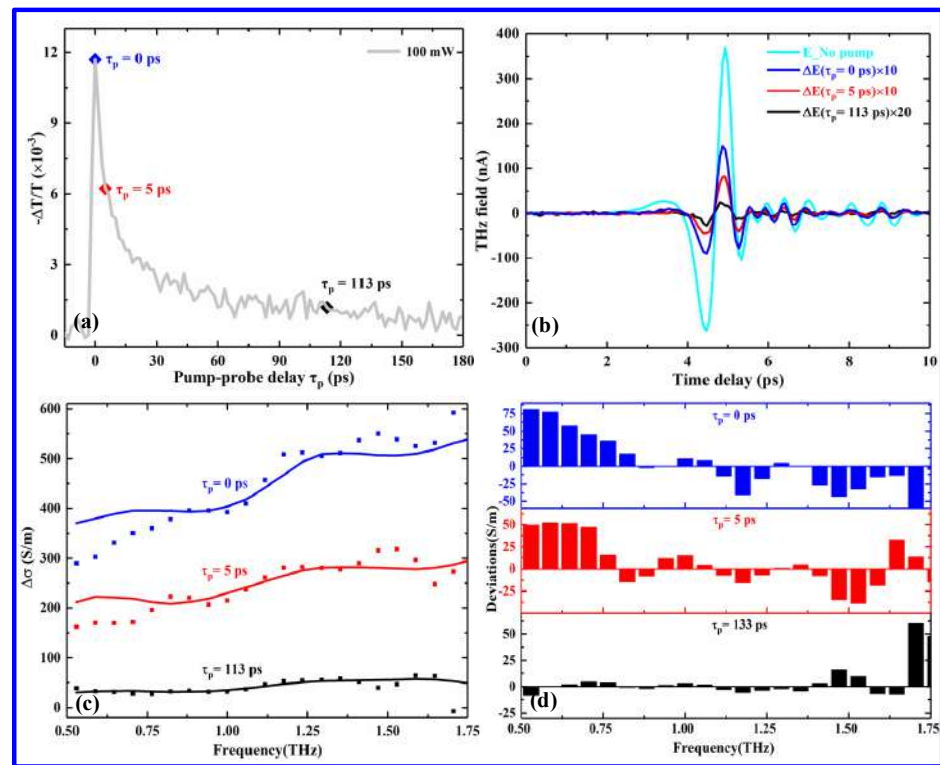


Figure 7. Changes in the THz transmission field, and photoinduced conductivity of the (PEA)₂(MA)₂Pb₃I₁₀ film at a pump power of 100 mW: (a) THz transmission change at different pump–probe delay times, (b) THz field change at $\tau_p = 0, 5$ and 113.3 ps, (c) THz photoinduced conductivity changes at $\tau_p = 0, 5$ and 113.3 ps, and (d) deviations between the extracted and fitted photoinduced conductivities.

5. Conclusions

In summary, we prepared the (PEA)₂(MA)₂Pb₃I₁₀ perovskite films by a one-step spin-coating process and characterized them by different measuring methods. The SEM, XRD, UV–vis, and PL measurements demonstrate that the as-grown (PEA)₂(MA)₂Pb₃I₁₀ perovskite films are a 2D layer structure. The OPTP measurements show that the 2D (PEA)₂(MA)₂Pb₃I₁₀ perovskite film can achieve an MD of up to 10% at 1.5 THz and an ultrafast relaxation time of about 3ps at an illumination power of 100 mW. Moreover, the fitting results obtained by a three-exponential function reveal that the decay mechanism involves the monomolecular, bimolecular, and Auger recombination processes, corresponding to the free carrier relaxation, exciton recombination, and trap-assisted recombination, respectively. In addition, the changes in the photogenerated conductivity at different pump–probe delay times were extracted and fitted using the measured THz transient dynamics and the Drude-Smith model, respectively, obtaining a maximum change of 600 S/m at $\tau_p = 0$ ps. Therefore, these results show that the 2D (PEA)₂(MA)₂Pb₃I₁₀ film has potential applications in high-performance tunable and ultrafast THz devices.

Author Contributions: Conceptualization, X.H., J.R. and H.L.; methodology, H.L. and J.R.; validation, H.L. and G.L.; resources, X.H. and G.L.; data curation, J.J. and Y.Y.; writing—original draft preparation, H.L., J.R. and G.L.; writing—review and editing, J.R., X.H. and G.L.; visualization, Y.Y.; supervision, X.H.; project administration, J.J.; funding acquisition, X.H. and G.L. All authors have read and agreed to the published version of the manuscript.

Funding: The work is supported by the National Natural Science Foundation of China (Nos. 62075052), the Science Foundation of the National Key Laboratory of Science and Technology on Advanced Composites in Special Environments (JCKYS2020603C009 and 6142905212711), and the Natural Science Foundation of Heilongjiang Province (LH2019F022).

Institutional Review Board Statement: Not applicable.

Informed Consent Statement: Not applicable.

Data Availability Statement: Data is contained within the article.

Conflicts of Interest: The authors declare no conflict of interest.

References

- Wang, L.; Zhang, Y.; Guo, X.; Chen, T.; Liang, H.; Hao, X.; Hou, X.; Kou, W.; Zhao, Y.; Zhou, T.; et al. A review of THz modulators with dynamically tunable metasurfaces. *Nanomaterials* **2019**, *9*, 965. [CrossRef] [PubMed]
- Edmund, L. Terahertz applications: A source of fresh hope. *Nat. Photonics* **2007**, *1*, 257–258.
- Chen, H.T.; Padilla, W.J.; Zide, J.M.O.; Gossard, A.C.; Taylor, A.J.; Averitt, R.D. Active terahertz metamaterial devices. *Nature* **2006**, *444*, 597–600. [CrossRef] [PubMed]
- Rahm, M.; Li, J.S.; Padilla, W.J. THz wave modulators: A brief review on different modulation techniques. *J. Infrared Millim. Terahertz Waves* **2013**, *34*, 1–27. [CrossRef]
- Kleine-Ostmann, T.; Pierz, K.; Hein, G.; Dawson, P.; Koch, M. Audio signal transmission over THz communication channel using semiconductor modulator. *Electron. Lett.* **2004**, *40*, 124–126. [CrossRef]
- Qiao, J.; Wang, S.; Wang, Z.; He, C.; Zhao, S.; Xiong, X.; Zhang, X.; Tao, X.; Wang, S.L. Ultrasensitive and broadband all-optically controlled THz modulator based on MoTe₂/Si van der Waals heterostructure. *Adv. Opt. Mater.* **2020**, *8*, 2000160. [CrossRef]
- Ono, M.; Hata, M.; Tsunekawa, M.; Nozaki, K.; Sumikura, H.; Chiba, H.; Notomi, M. Ultrafast and energy-efficient all-optical switching with graphene-loaded deep-subwavelength plasmonic waveguides. *Nat. Photonics* **2020**, *14*, 37–43. [CrossRef]
- Solanki, A.; Yadav, P.; Turner-Cruz, S.H.; Lim, S.S.; Saliba, M.; Sum, T.C. Cation influence on carrier dynamics in perovskite solar cells. *Nano Energy* **2019**, *58*, 604–611. [CrossRef]
- Kojima, A.; Teshima, K.; Shirai, Y.; Miyasaka, T. Organometal halide perovskites as visible-light sensitizers for photovoltaic cells. *J. Am. Chem. Soc.* **2009**, *131*, 6050–6051. [CrossRef]
- Rong, Y.; Liu, L.; Mei, A.; Li, X.; Han, H. Beyond efficiency: The challenge of stability in mesoscopic perovskite solar cells. *Adv. Energy Mater.* **2015**, *5*, 1501066. [CrossRef]
- Wang, Z.; Shi, Z.; Li, T.; Chen, Y.; Huang, W. Stability of perovskite solar cells: A prospective on the substitution of the A cation and X anion. *Angew. Chem. Int. Ed.* **2017**, *56*, 1190–1212. [CrossRef]
- Lai, H.; Kan, B.; Liu, T.; Zheng, N.; Xie, Z.; Zhou, T.; Wan, X.; Zhang, X.D.; Liu, Y.S.; Chen, Y. Two-dimensional Ruddlesden–Popper perovskite with nanorod-like morphology for solar cells with efficiency exceeding 15%. *J. Am. Chem. Soc.* **2018**, *140*, 11639–11646. [CrossRef]
- Tsai, H.; Nie, W.; Blanco, J.C.; Stoumpos, C.C.; Asadpour, R.; Harutyunyan, B.; Neukirch, A.J.; Verduzco, R.; Kanatzidis, M.G.; Mohite, A.D.; et al. High-efficiency two-dimensional Ruddlesden–Popper perovskite solar cells. *Nature* **2016**, *536*, 312–316. [CrossRef]
- Chen, Y.; Sun, Y.; Peng, J.; Tang, J.; Zheng, K.; Liang, Z. 2D Ruddlesden–Popper perovskites for optoelectronics. *Adv. Mater.* **2018**, *30*, 1703487. [CrossRef]
- Ren, H.; Yu, S.; Chao, L.; Xia, Y.; Sun, Y.; Zuo, S.; Li, F.; Niu, T.; Zhang, L.; Chen, Y.; et al. Efficient and stable Ruddlesden–Popper perovskite solar cell with tailored interlayer molecular interaction. *Nat. Photonics* **2020**, *14*, 154–163. [CrossRef]
- Zhao, T.; Chueh, C.C.; Chen, Q.; Rajagopal, A.; Jen, A.K.-Y. Defect passivation of organic-inorganic hybrid perovskites by diammonium iodide toward high-performance photovoltaic devices. *ACS Energy Lett.* **2016**, *1*, 757–763. [CrossRef]
- Niu, T.; Ren, H.; Wu, B.; Xia, Y.; Xie, X.; Yang, Y.; Gao, X.; Chen, Y.; Huang, W. Reduced-dimensional perovskite enabled by organic diamine for efficient photovoltaics. *J. Phys. Chem. Lett.* **2019**, *10*, 2349–2356. [CrossRef]
- Smith, I.C.; Hoke, E.T.; Solis-Ibarra, D.; McGehee, M.D.; Karunadasa, H.I. A layered hybrid perovskite solar-cell absorber with enhanced moisture stability. *Angew. Chem. Int. Ed.* **2014**, *53*, 11232–11235. [CrossRef]
- Quan, L.N.; Yuan, M.; Comin, R.; Voznyy, O.; Bearegard, E.M.; Hoogland, S.; Buin, A.; Kirmani, A.R.; Zhao, K.; Amassian, A.; et al. Ligand-stabilized reduced-dimensionality perovskites. *J. Am. Chem. Soc.* **2016**, *138*, 2649–2655. [CrossRef]
- Byun, J.; Cho, H.; Wolf, C.; Jang, M.; Sadhanala, A.; Friend, R.H.; Yang, H.; Lee, T. Efficient visible quasi-2D perovskite light-emitting diodes. *Adv. Mater.* **2016**, *28*, 7515–7520. [CrossRef]
- Xu, Q.; Wang, R.; Jia, Y.L.; He, X.; Deng, Y.; Yu, F.; Zhang, Y.; Ma, X.; Chen, P.; Zhang, Y.; et al. Highly efficient quasi-two dimensional perovskite light-emitting diodes by phase tuning. *Organ. Electron.* **2021**, *98*, 106295. [CrossRef]
- Stoumpos, C.C.; Cao, D.H.; Clark, D.J.; Young, J.; Rondinelli, J.M.; Jang, J.I.; Hupp, J.T.; Kanatzidis, M.G. Ruddlesden–Popper hybrid lead iodide perovskite 2D homologous semiconductors. *Chem. Mater.* **2016**, *28*, 2852–2867. [CrossRef]
- Milot, R.L.; Sutton, R.J.; Eperon, G.E.; Haghighirad, A.A.; Hardigree, J.M.; Miranda, L.; Snaith, H.J.; Johnston, M.B.; Herz, L.M. Charge-carrier dynamics in 2D hybrid metal-halide perovskites. *Nano Lett.* **2016**, *16*, 7001–7007. [CrossRef]
- Shang, Q.; Wang, Y.; Zhong, Y.; Mi, Y.; Qin, L.; Zhao, Y.; Qiu, X.; Liu, X.; Zhang, Q. Unveiling structurally engineered carrier dynamics in hybrid quasi-two-dimensional perovskite thin films toward controllable emission. *J. Phys. Chem. Lett.* **2017**, *8*, 4431–4438. [CrossRef]

25. Zheng, Y.; Deng, H.; Jing, W.; Li, C. Bandgap energy tuning and photoelectrical properties of self-assembly quantum well structure in organic-inorganic hybrid perovskites. *Acta Phys. Sin.* **2011**, *60*, 2433. [CrossRef]
26. Yan, H.J.; Ku, Z.L.; Hu, X.F.; Zhao, W.; Zhong, M.; Zhu, Q.; Lin, X.; Jin, Z.; Ma, G. Ultrafast terahertz probes of charge transfer and recombination pathway of CH₃NH₃PbI₃ perovskites. *Chin. Phys. Lett.* **2018**, *35*, 028401. [CrossRef]
27. Molis, G.; Adomavicius, R.; Krotkus, A.; Bertulis, K.; Giniunas, L.; Pocius, J.; Danielius, R. Terahertz time-domain spectroscopy system based on femtosecond Yb: KGW laser. *Electron. Lett.* **2007**, *43*, 1. [CrossRef]
28. Nuss, M.C.; Orenstein, J. Terahertz time-domain spectroscopy. In *Millimeter and Submillimeter Wave Spectroscopy of Solids, Topics in Applied Physics*; Springer: Berlin/Heidelberg, Germany, 1998; Volume 74, pp. 7–50.
29. Lee, K.S.; Kang, R.; Son, B.; Kim, D.; Yu, N.; Ko, D.K. Characterization of optically-controlled terahertz modulation based on a hybrid device of perovskite and silicon. In *Proceedings of the Conference on Lasers and Electro-Optics/Pacific Rim*, Singapore, 31 July–4 August 2017; p. s1712.
30. Wehrenfennig, C.; Eperon, G.E.; Johnston, M.B.; Snaith, H.J.; Herz, L.M. High charge carrier mobilities and lifetimes in organolead trihalide perovskites. *Adv. Mater.* **2014**, *26*, 1584–1589. [CrossRef] [PubMed]
31. Qin, Z.; Zhang, C.; Chen, L.; Wang, X.; Xiao, M. Charge carrier dynamics in sn-doped two-dimensional lead halide perovskites studied by terahertz spectroscopy. *Front. Energy Res.* **2021**, *9*, 658270. [CrossRef]
32. Johnston, M.B.; Herz, L.M. Hybrid perovskites for photovoltaics: Charge-carrier recombination, diffusion, and radiative efficiencies. *Acc. Chem. Res.* **2016**, *49*, 146–154. [CrossRef] [PubMed]
33. Chanana, A.; Liu, X.; Zhang, C.; Vardeny, Z.V.; Nahata, A. Ultrafast frequency-agile terahertz devices using methylammonium lead halide perovskites. *Sci. Adv.* **2018**, *4*, eaar7353. [CrossRef]
34. Lin, D.; Ma, L.; Ni, W.; Wang, C.; Zhang, F.; Dong, H.; Gurzadyan, G.G.; Nie, Z. Unveiling hot carrier relaxation and carrier transport mechanisms in quasi-two-dimensional layered perovskites. *J. Mater. Chem. A* **2020**, *8*, 25402–25410. [CrossRef]
35. Blancon, J.C.; Tsai, H.; Nie, W.; Stoumpos, C.C.; Pedesseau, L. Extremely efficient internal exciton dissociation through edge states in layered 2D perovskites. *Science* **2017**, *355*, 1288–1292. [CrossRef]
36. Delport, G.; Chehade, G.; Lédée, F.; Diab, H.; Milesi-Brault, C.; Trippé-Allard, G.; Even, J.; Lauret, J.; Deleporte, E.; Garrot, D. Exciton–exciton annihilation in two-dimensional halide perovskites at room temperature. *J. Phys. Chem. Lett.* **2019**, *10*, 5153–5159. [CrossRef]



Article

Zirconia-Doped Methylated Silica Membranes via Sol-Gel Process: Microstructure and Hydrogen Permselectivity

Lintao Wang and Jing Yang *

School of Urban Planning and Municipal Engineering, Xi'an Polytechnic University, Xi'an 710048, China; wanglt912@163.com

* Correspondence: jingy76@163.com; Tel.: +86-29-62779357

Abstract: In order to obtain a steam-stable hydrogen permselectivity membrane, with tetraethylorthosilicate (TEOS) as the silicon source, zirconium nitrate pentahydrate ($Zr(NO_3)_4 \cdot 5H_2O$) as the zirconium source, and methyltriethoxysilane (MTES) as the hydrophobic modifier, the methyl-modified ZrO_2 - SiO_2 (ZrO_2 - $MSiO_2$) membranes were prepared via the sol-gel method. The microstructure and gas permeance of the ZrO_2 - $MSiO_2$ membranes were studied. The physical-chemical properties of the membranes were characterized by Fourier transform infrared spectroscopy (FTIR), X-ray photoelectron spectroscopy (XPS), X-ray diffraction (XRD), transmission electron microscopy (TEM), scanning electron microscope (SEM), and N_2 adsorption-desorption analysis. The hydrogen permselectivity of ZrO_2 - $MSiO_2$ membranes was evaluated with Zr content, temperature, pressure difference, drying control chemical additive (glycerol) content, and hydrothermal stability as the inferred factors. XRD and pore structure analysis revealed that, as n_{Zr} increased, the $MSiO_2$ peak gradually shifted to a higher 2θ value, and the intensity gradually decreased. The study found that the permeation mechanism of H_2 and other gases is mainly based on the activation-diffusion mechanism. The separation of H_2 is facilitated by an increase in temperature. The ZrO_2 - $MSiO_2$ membrane with $n_{Zr} = 0.15$ has a better pore structure and a suitable ratio of micropores to mesopores, which improved the gas permselectivities. At 200 °C, the H_2 permeance of $MSiO_2$ and ZrO_2 - $MSiO_2$ membranes was 3.66×10^{-6} and 6.46×10^{-6} mol·m⁻²·s⁻¹·Pa⁻¹, respectively. Compared with the $MSiO_2$ membrane, the H_2/CO_2 and H_2/N_2 permselectivities of the ZrO_2 - $MSiO_2$ membrane were improved by 79.18% and 26.75%, respectively. The added amount of glycerol as the drying control chemical additive increased from 20% to 30%, the permeance of H_2 decreased by 11.55%, and the permselectivities of H_2/CO_2 and H_2/N_2 rose by 2.14% and 0.28%, respectively. The final results demonstrate that the ZrO_2 - $MSiO_2$ membrane possesses excellent hydrothermal stability and regeneration capability.

Citation: Wang, L.; Yang, J. Zirconia-Doped Methylated Silica Membranes via Sol-Gel Process: Microstructure and Hydrogen Permselectivity. *Nanomaterials* **2022**, *12*, 2159. <https://doi.org/10.3390/nano12132159>

Academic Editor: Jürgen Eckert

Received: 19 May 2022

Accepted: 20 June 2022

Published: 23 June 2022

Publisher's Note: MDPI stays neutral with regard to jurisdictional claims in published maps and institutional affiliations.



Copyright: © 2022 by the authors. Licensee MDPI, Basel, Switzerland. This article is an open access article distributed under the terms and conditions of the Creative Commons Attribution (CC BY) license (<https://creativecommons.org/licenses/by/4.0/>).

Keywords: microporous membrane; H_2 permselectivity; zirconia-doped SiO_2 membrane; hydrothermal stability; regeneration

1. Introduction

It is well-known that hydrogen is a clean energy source [1]. At present, there are many ways to obtain H_2 , but the biggest problem preventing its commercialization is the purification and separation of H_2 . The purification of H_2 can be achieved in three main ways: pressure swing adsorption, cryogenic distillation, and membrane separation [2,3]. Although pressure swing adsorption and cryogenic distillation can be operated commercially, the economic benefits are low. The main commercial application of membranes in gas separation is the separation of hydrogen from nitrogen, methane, and argon in an ammonia sweep gas stream. In the past few years, hundreds of new polymer materials have been reported, and only eight or nine polymer materials have been used to make gas separation membrane bases. Surprisingly few of them were used to make industrial membranes [4]. Membrane separation technology is also one of the most promising hydrogen purification

methods. At high temperatures, the H₂ separation membrane has attracted much attention in the application of membrane reactors, for example, in the steam reforming of natural gas. The characteristics of lower energy consumption and investment cost, as well as simple operation, have made the membrane separation method widely concerned. Compared to other techniques of hydrogen purification, the membrane separation method offers more energy efficiency and environmental friendliness. The quality of the separation membrane directly affects the separation performance. Therefore, it is very necessary to choose suitable materials to prepare efficient and stable membrane materials [5].

In recent years, research on hydrogen separation membranes has mainly focused on molecular sieves, alloys, and microporous silica [6–9]. Prominently, silica membranes have received extensive attention for H₂ separation due to their advantages such as high permselectivity and considerable thermal stability [10]. Amorphous silica membranes derived from sol-gel and chemical vapor deposition (CVD) methods received an enormous amount of attention [11,12]. They have a stable chemical structure and molecular sieve mechanism, which can separate hydrogen across a broad temperature range [13]. However, silica membranes have demonstrated poor steam and thermal stability. Due to the hydrophilic nature of silica membranes, if they are frequently exposed to humid, low-temperature atmospheres, the flux and permselectivity of H₂ will largely be reduced [14,15]. The study found that the addition of hydrophobic groups can reduce the affinity of silica for water and improve gas permselectivity [15]. At this stage, methyl, vinyl, perfluorodecalin, etc., are often used in the hydrophobic modification of gas permeation separation in silica membrane, and the effect of increasing the hydrothermal stability is obvious [16]. Wei et al. [17] prepared perfluorodecyl hydrophobically modified silica membranes. The results demonstrated that the addition of perfluorodecyl made the modified silica membrane change from hydrophilic to hydrophobic. The membrane exhibited excellent hydrothermal stability at 250 °C and a water vapor molar ratio of 5%. Debarati et al. [18] hydrophobically modified the surface of ceramic membranes with polydimethylsiloxane to achieve a contact angle of 141°. It shows that the surface of the ceramic membrane with the methyl group is highly hydrophobic. Somayeh et al. [19] also demonstrated that vinyl-modified silica particles can improve the hydrophobic properties of the membrane.

It is well-known that the addition of metal oxides (such as TiO₂ [20,21], Al₂O₃ [22,23], Fe₂O₃ [24], CoO [25], and ZrO₂ [26,27]) can not only enhance the hydrothermal stability of the membrane, but also further improve the antifouling ability and performance of the membrane. This indicates that the incorporation of metal oxides can form mixed oxide network structures that are more stable than amorphous silica materials [28,29]. In particular, ZrO₂ is an excellent transition metal oxide, which is often utilized in studies of gas membrane separation. Li et al. [30] prepared a zirconia membrane via the polymeric sol-gel method, which possessed H₂ permeance of about $5 \times 10^{-8} \text{ mol}\cdot\text{m}^{-2}\cdot\text{s}^{-1}\cdot\text{Pa}^{-1}$, H₂/CO₂ permselectivity of 14, and outstanding hydrothermal stability under a steam pressure of 100 KPa. Gu et al. [31] used the sol-gel method to prepared the microporous zirconia membrane. After being treated with 0.50 mol·L⁻¹ of H₂SO₄, the hydrogen permeance was $(2.8 \text{ to } 3.0) \times 10^{-6} \text{ mol}\cdot\text{Pa}^{-1}\cdot\text{m}^{-2}\cdot\text{s}^{-1}$. The H₂ permselectivities of the equimolar binary system were 6 and 9, respectively. Doping ZrO₂ in the SiO₂ matrix can improved the hydrophobicity and hydrothermal stability of the membrane matrix, and further enhance the gas permeability. Numerous studies have been carried out on ZrO₂-doped silica materials/membranes. According to mesoporous stabilized zirconia intermediate layers, Gestel et al. [32] revealed a much better membrane setup. For various CO₂/N₂ combinations, the as-prepared membrane demonstrated permselectivities of 20–30 and CO₂ permeances of 1.5 to 4 m³/(m²·h·bar). Ahn et al. [33] prepared a silica-zirconia membrane with hydrogen permselectivity on a porous alumina support using tetraethyl orthosilicate (TEOS) and tert-butanol zirconium (IV) under 923 K conditions by chemical vapor deposition. The H₂ permeance of the obtained membrane was $3.8 \times 10^{-7} \text{ mol}\cdot\text{m}^{-2}\cdot\text{s}^{-1}\cdot\text{Pa}^{-1}$, and the permselectivities for CO₂ and N₂ were 1100 and 1400, respectively. Hove et al. [34] compared the gas permeation properties of a hybrid silica (BTESE) membrane, Zr-doped BTESE

membrane, and silica membrane before and after hydrothermal treatment under the same circumstances. At 100 °C, the hybrid silica membrane and Zr-doped BTESE membrane maintained good hydrothermal stability, while the silica membrane lost selectivity for all the studied gases. After hydrothermal treatment at 200 or 300 °C, the CO₂ permeance of the Zr-doped BTESE membrane decreased significantly, and the H₂/CO₂ permselectivity increased significantly, by 65.71%. So far, many scholars have demonstrated the effect of different conditions during preparation on the properties of zirconia-doped silica materials/membranes. The influence of the Zr/Si molar ratio on the microstructure of the membrane and the permeability of the gas is crucial. Unfortunately, there are few reports in this regard. Furthermore, the effects of methyl modification on the microstructure and steam stability of ZrO₂-SiO₂ membranes were rarely described in papers. Some scholars have found that adding a drying control chemical additive (DCCA) in the process of preparing the membrane via the sol-gel method can effectively reduce the uneven shrinkage of the membrane during the heating process and during the calcining process [35], and improve the gas permselectivity of the membrane.

In this paper, methyl-modified ZrO₂-SiO₂ (ZrO₂-MSiO₂) materials/membranes with various Zr/Si molar ratios (n_{Zr}) were fabricated. Glycerol was chosen to be the DCCA. The impact of n_{Zr} on the microstructures and H₂ permselectivities of ZrO₂-MSiO₂ membranes was thoroughly addressed. The water vapor stability of ZrO₂-MSiO₂ membranes was investigated further by comparing the gas permeability characteristics of the ZrO₂-MSiO₂ membranes before and after steam treatment. The heat regeneration performance of ZrO₂-MSiO₂ membranes was also investigated.

2. Materials and Methods

2.1. Preparation of MSiO₂ Sols

The MSiO₂ sols were prepared by tetraethylorthosilicate (TEOS, purchased from Xi'an chemical reagent Co., Ltd., Xi'an, China) as a silica source, methyltriethoxysilane (MTES, purchased from Hangzhou Guibao Chemical Co., Ltd., Hangzhou, China) as a hydrophobic modified agent, anhydrous ethanol (EtOH, purchased from Tianjin Branch Micro-Europe Chemical Reagent Co., Ltd., Tianjin, China) as a solvent, and nitric acid (HNO₃, purchased from Sichuan Xilong Reagent Co., Ltd., Chengdu, China) as a catalyst. To begin, TEOS, MTES, and EtOH were completely combined in a three-necked flask using a magnetic stirrer. The flask was correctly immersed in an ice-water combination. The solution was then agitated for 50 min using a magnetic stirrer to ensure thorough mixing. The H₂O and HNO₃ combination was then dropped into the mixture while it was still being stirred. The reaction mixture was then agitated in a three-necked flask at a constant temperature of 60 °C for 3 h to yield the MSiO₂ sol.

2.2. Preparation of ZrO₂ Sols

In a three-necked flask, 0.6 M zirconium nitrate pentahydrate (Zr(NO₃)₄·5H₂O, purchased from Tianjin Fuchen Chemical Reagent Co., Ltd., Tianjin, China) and 0.2 M oxalic acid (C₂H₂O₄·2H₂O, purchased from Tianjin HedongHongyan Chemical Reagent Co., Ltd., Tianjin, China) solutions were combined at a molar ratio of 4.5:1.0 and agitated. The aforementioned mixture was then treated with 35% (*v/v*) glycerol (GL, purchased from Tianjin Kemiou Chemical Reagent Co., Ltd., Tianjin, China), and stirring was maintained in a water bath at 50 °C for 3 h to yield the ZrO₂ sols.

2.3. Preparation of ZrO₂-MSiO₂ Sols

The ZrO₂ sols were aged for 12 h at 25 °C. The ZrO₂ sols and EtOH were then added to the MSiO₂ sols and stirred for 60 min to create the required ZrO₂-MSiO₂ sols. The n_{Zr} ratio was 0, 0.08, 0.15, 0.3, and 0.05. The ZrO₂-MSiO₂ sols were diluted three times with ethanol after 12 h. GL was used as a drying control agent at 0%, 10%, 20%, and 30% (DCCA). After 60 min of stirring, ZrO₂-MSiO₂ sols with varied GL contents were obtained.

2.4. Preparation of ZrO_2 - $MSiO_2$ Materials

The ZrO_2 - $MSiO_2$ sols were then placed individually in petri plates for gelation at 30 °C. The gel materials were ground and pulverized with a mortar, and then calcined at a heating rate of 0.5 °C·min⁻¹ at 400 °C for 2 h under nitrogen atmosphere protection, and then cooled down naturally. The ZrO_2 - $MSiO_2$ materials with different n_{Zr} were prepared. The ZrO_2 - $MSiO_2$ materials with $n_{Zr} = 0$ are also referred to as “ $MSiO_2$ ” materials.

2.5. Preparation of ZrO_2 - $MSiO_2$ Membranes

The ZrO_2 - $MSiO_2$ membranes were coated on top of composite interlayers supported by porous α -alumina discs. The discs are 5 mm-thick and 30 mm in diameter, with a porosity of 40% and an average pore size of 100 nm. ZrO_2 - $MSiO_2$ membranes were effectively prepared by dip-coating the substrates in three-fold ethanol-diluted silica sol for 7 s, then drying and calcining them. Each sample was dried at 30 °C for 3 h before being calcined at 400 °C in a temperature-controlled furnace in a N_2 environment with a ramping rate of 0.5 °C·min⁻¹ and a dwell period of 2 h. The dip-coating-drying-calcining process was repeated three times. Figure 1 demonstrates the preparation process of the ZrO_2 - $MSiO_2$ materials/membranes. The ZrO_2 - $MSiO_2$ membranes with $n_{Zr} = 0$ are also referred to as “ $MSiO_2$ ” membranes.



Figure 1. Schematic diagram of the preparation of ZrO_2 - $MSiO_2$ materials/membranes.

2.6. Steam Treatment and Regeneration of ZrO_2 - $MSiO_2$ Membranes

The ZrO_2 - $MSiO_2$ membranes were subjected to a 7-day steam stability test in which they were placed into saturated steam at 25 °C. After steam treatment, for thermal regeneration of ZrO_2 - $MSiO_2$ membranes, they were processed at a calcination temperature of 350 °C, with the same calcination technique as before. The gas permeances of ZrO_2 - $MSiO_2$ membranes were investigated after steam treatment and regeneration, respectively.

2.7. Characterizations

Using Fourier transform infrared spectroscopy, the functional groups of ZrO_2 - $MSiO_2$ materials were characterized (FTIR, Spotlight 400 and Frontier, PerkinElmer Corporation, Waltham, MA, USA), and the wavelength measuring range was 400 to 4000 cm⁻¹ using the KBr compression technique. Using a Rigaku D/max-2550pc X-ray diffractometer (XRD, Rigaku D/max-2550pc, Hitachi, Tokyo, Japan) with $CuK\alpha$ radiation at 40 kV and 40 mA, the ZrO_2 - $MSiO_2$ materials' phase structure was found. The X-ray photoelectron spectra (XPS) were acquired on a K-Alpha X-ray photoelectron spectroscope from Thermo Fisher Scientific with $AlK\alpha$ excitation and were calibrated regarding the signal of adventitious carbon (XPS, ESCALAB250xi, Thermo Scientific, Waltham, MA, USA). The binding energy estimates

were derived using the C (1s) line at 284.6 eV as the reference point. Transmission electron microscopy (TEM, JEM 2100F, JEOL, Tokyo, Japan) was utilized to investigate the ZrO₂-MSiO₂ powders' crystallization. Operating at 5 kV, scanning electron microscopy (SEM, JEOL JSM-6300, Hitachi, Tokyo, Japan) was utilized to study the surface morphologies of the ZrO₂-MSiO₂ membranes. N₂ adsorption–desorption measurements were conducted using an automated Micromeritics, ASAP2020 analyzer (ASAP 2020, Micromeritics, Norcross, GA, USA). The ZrO₂-MSiO₂ materials' BET surface area, pore volume, and pore size distribution were determined.

Figure 2 is a schematic of the experimental setup used to evaluate the performance of single gas permeation. Prior to the experiment, the pressure and temperature were set to the desired values for thirty minutes to allow the gas permeation to stabilize. The permeation properties of MSiO₂ and ZrO₂-MSiO₂ membranes were evaluated using H₂, CO₂, and N₂. The gas permeability was determined based on the outlet gas flow. The gas permselectivity values (ideal permselectivities) were calculated by the permeance ratio between two gases.

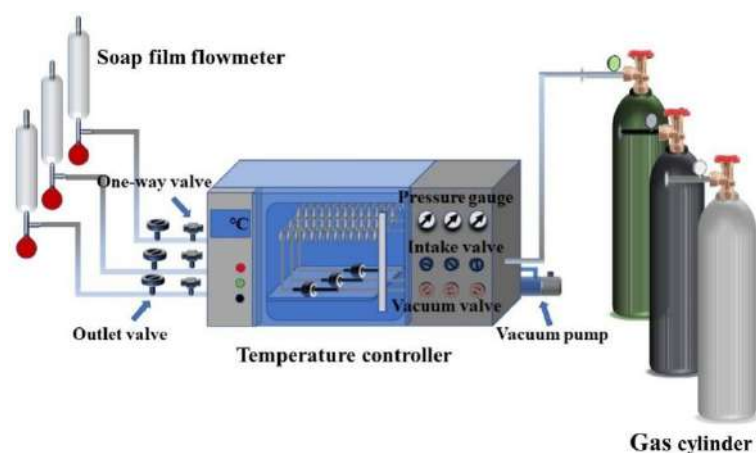


Figure 2. Single gas permeation experiment device diagram.

3. Results

3.1. Chemical Structure Analysis

FTIR spectra were used to investigate the functional groups of ZrO₂-MSiO₂ materials. The FTIR spectra of ZrO₂-MSiO₂ materials containing various n_{Zr} contents are displayed in Figure 3. The absorption peak at around 3448 cm⁻¹ was assigned to the stretching and bending vibration of the -OH group from the absorbed water. The absorption peak at 1630 cm⁻¹ corresponds to Si-OH and Zr-OH on the surface of ZrO₂-MSiO₂ materials [36]. The antisymmetric stretching vibration absorption peak -CH₃ at 2985 cm⁻¹ was mainly from unhydrolyzed TEOS and MTES. The absorption peak at 1278 cm⁻¹ was attributed to the Si-CH₃ group. It is also the main hydrophobic functional group of the membrane. The absorption peak observed at 1050 cm⁻¹ was attributed to the Si-O-Si bond [37]. Compared with the materials with $n_{Zr} = 0$, the materials with $n_{Zr} = 0.08$ –0.5 all showed a new absorption peak at the wavenumber of 448 cm⁻¹. This was related to the formation of Zr-O bonds [38]. Meanwhile, with the increase of n_{Zr} , the peak at 1050 cm⁻¹ shifted to around 1100 cm⁻¹. This may be ascribed to the fact that partial substitution of Zr atoms for Si atoms in the Si-O-Si network to form Zr-O-Si bonds occurred [39], breaking the symmetry of SiO₂ and leading to the shift of peak positions. However, there was no obvious Zr-O-Si bond in the FTIR spectrum of ZrO₂-MSiO₂ materials due to the overlap of the Zr-O-Si bond with Si-O-Si [40]. Furthermore, the decrease in the intensity of the silanol band at 779 and 835 cm⁻¹ with increasing n_{Zr} could be attributed to the substitution of Si-OH bonds by Zr-O-Si bonds [41]. It demonstrates the formation of Zr-O-Si bonds in the produced materials.

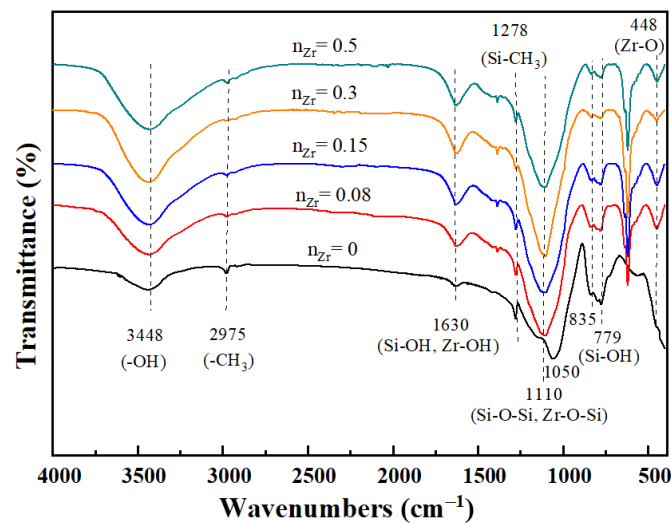


Figure 3. FTIR spectra curves of $\text{ZrO}_2\text{-MSiO}_2$ materials with various n_{Zr} .

3.2. Phase Structure Analysis

The XRD patterns of the $\text{ZrO}_2\text{-MSiO}_2$ materials with varied n_{Zr} are presented in Figure 4. The peaks of amorphous SiO_2 were concentrated at $2\theta = 23.1^\circ$ [42]. The SiO_2 peak moved progressively towards higher 2θ values as n_{Zr} rose, and it slowly dropped in intensity. This is attributable to the replacement of the portion of silicon atoms by the inserted Zr atoms, producing Zr-O-Si bonds, resulting in a drop in the SiO_2 concentration. The peaks corresponding to a crystalline tetragonal structure of zirconia are clearly apparent in the $\text{ZrO}_2\text{-MSiO}_2$ materials with $n_{\text{Zr}} = 0.15\text{--}0.5$. The (101), (112), and (202) reflection planes of the body-centered ZrO_2 (t- ZrO_2) tetragonal phase were ascribed to the large diffraction peaks occurring at 60.2° , 50.7° , and 30.2° , respectively (JCPDS No. 79-1771). XRD analysis demonstrated that with the growth of the Zr concentration, the peak intensity corresponding to t- ZrO_2 progressively increased. In other words, the content of t- ZrO_2 increased with the growth in Zr content. Combined with the FTIR analysis, the Zr element in $\text{ZrO}_2\text{-MSiO}_2$ materials may exist in the form of Zr-O-Si bonds and t- ZrO_2 .

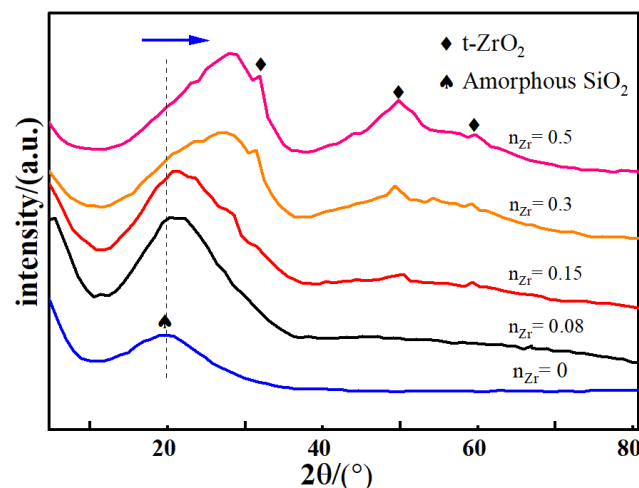


Figure 4. XRD patterns of $\text{ZrO}_2\text{-MSiO}_2$ materials with various n_{Zr} .

To further investigate the presence of Zr and Si species in the $\text{ZrO}_2\text{-MSiO}_2$ materials, the XPS measurement was conducted. The survey XPS spectrum of $\text{ZrO}_2\text{-MSiO}_2$ material with $n_{\text{Zr}} = 0.15$ is shown in Figure 5. Figure 5 demonstrates that C, O, Si, and Zr elements are present in the $\text{ZrO}_2\text{-MSiO}_2$ material, which indicates the successful incorporation of Zr into the silica frameworks. Figure 6 presents the Si 2p and Zr 3d XPS spectra of the

ZrO₂-MSiO₂ sample with $n_{Zr} = 0.15$. In Figure 6a, the peaks at the binding energies of 102.8 and 104.7 eV correspond to Si-C and Si-O bonds, respectively. In Figure 6b, the peaks at 186.6 and 183.3 eV correspond to the Zr-O 3d_{3/2} and Zr-O 3d_{5/2} peaks, respectively.

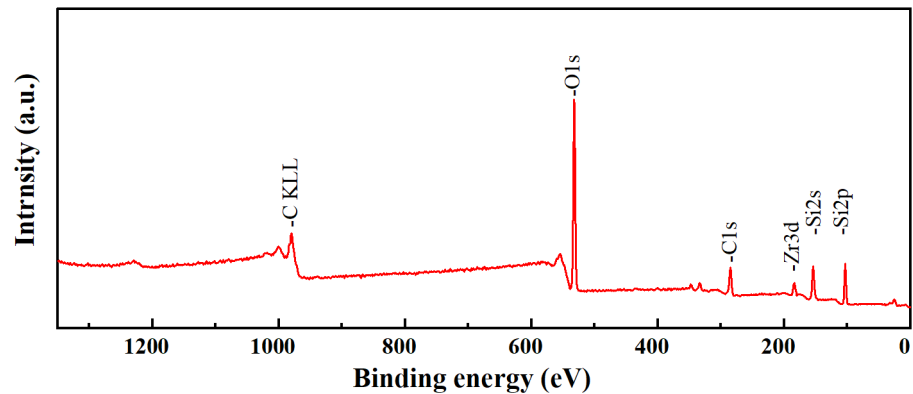


Figure 5. The survey XPS spectrum of ZrO₂-MSiO₂ materials.

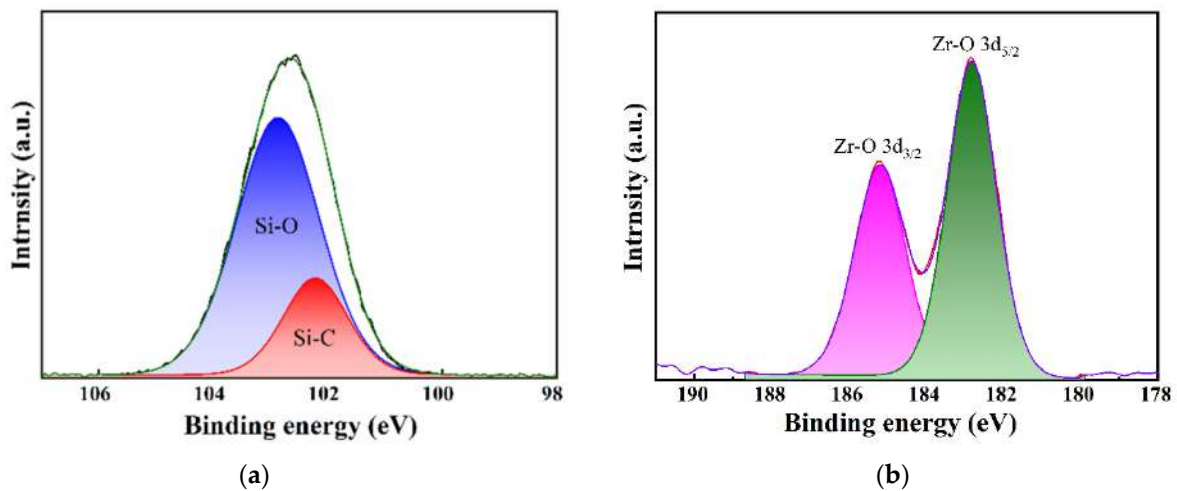


Figure 6. XPS peak decomposition for the (a) Si 2p and (b) Zr 3d photoelectron peaks of the ZrO₂-MSiO₂ materials.

3.3. TEM Analysis

The TEM micrographs of the ZrO₂-MSiO₂ material with $n_{Zr} = 0$ and 0.15 at 400 °C under nitrogen atmosphere are illustrated in Figure 7. Figure 7a depicts that the silica particles in MSiO₂ materials are amorphous, while in Figure 7b, a small amount of particles with darker color appear and are mixed in the silica skeleton, which may be due to the presence of t-ZrO₂. Overall, the ZrO₂-MSiO₂ materials with $n_{Zr} = 0.15$ still maintained the amorphous state.

3.4. Pore Structure Analysis

The N₂ adsorption-desorption isotherm of the ZrO₂-MSiO₂ materials with various n_{Zr} are shown in Figure 8a. According to the Brunauer-DeMing-DeMing-Teller (BDDT) classification, the ZrO₂-MSiO₂ materials showed a type I adsorption isotherm, while $n_{Zr} = 0$ indicated the formation of microporous structures. The isotherms for the four samples ($n_{Zr} = 0.08$ –0.5) all showed a similar trend, which could be categorized as type IV isotherms. However, the shapes of the hysteresis loops for the four samples were different, implying the variation of pore structures. A significant proportion of adsorption occurred in the range of low relative pressure, $P/P_0 < 0.1$, indicating that the materials contain a large quantity of micropores. The shape of the hysteresis loop of the ZrO₂-MSiO₂ materials

with $n_{Zr} = 0.5$ was altered, indicating the presence of larger mesopores or macropores. In addition, the distributions of pore size for all samples are depicted in Figure 8b. It is found that the samples with $n_{Zr} = 0.08$ – 0.5 showed a broader pore size distribution and a larger mean pore size than the samples with $n_{Zr} = 0$. The conclusion was also confirmed by the pore structure parameters of ZrO_2 -MSiO₂ materials with various n_{Zr} in Table 1. The average pore size, BET specific surface area, and total pore volume of the ZrO_2 -MSiO₂ materials gradually increased with $n_{Zr} = 0.08$ and 0.15 , and the pore size distribution became wider. However, the total pore volume of the ZrO_2 -MSiO₂ materials with $n_{Zr} = 0.3$ and 0.5 decreased instead. The fact is that the bond length of Zr-O (1.78 Å) was slightly longer than that of Si-O (1.64 Å) [43]. Figure 9 shows the molecular structure models of MSiO₂, ZrO_2 -MSiO₂, and t- ZrO_2 crystallites, respectively. Hence, the formation of Zr-O-Si bonds contributes to the formation of pores. With the increase of Zr content, more and more t- ZrO_2 crystallites were formed and distributed in the framework of MSiO₂ materials, and the internal pore structure of the ZrO_2 -MSiO₂ materials was hindered from shrinking and pore collapse, resulting in the decrease of the BET surface area and pore volume. From Table 1, it can be seen that the ZrO_2 -MSiO₂ materials with $n_{Zr} = 0.15$ had the maximal total pore volume ($0.43 \text{ cm}^3 \cdot \text{g}^{-1}$), BET surface area ($616.77 \text{ m}^2 \cdot \text{g}^{-1}$), and the minimum mean pore size (2.19 nm).

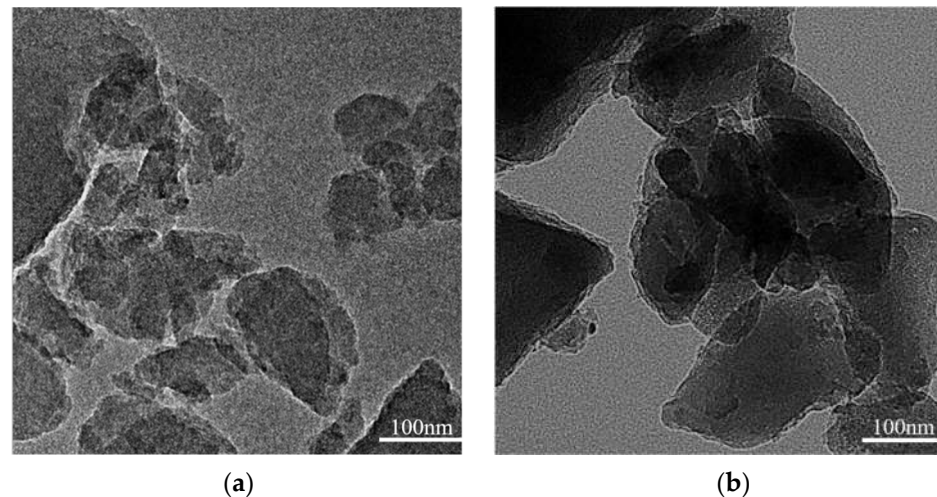


Figure 7. TEM images of ZrO_2 -MSiO₂ materials with $n_{Zr} =$ (a) 0 and (b) 0.15.

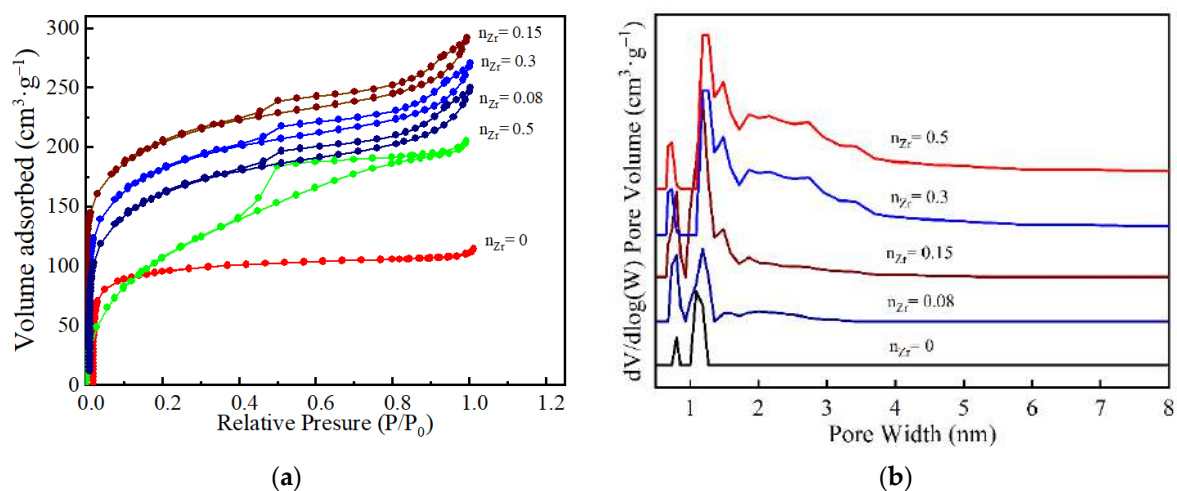


Figure 8. (a) The nitrogen adsorption-desorption isotherms and (b) the corresponding pore size distribution curves for the ZrO_2 -MSiO₂ materials with various n_{Zr} .

Table 1. Pore structure parameters of the ZrO₂-MSiO₂ materials with various n_{Zr} .

n_{Zr}	BET Surface Area (m ² ·g ⁻¹)	Average Pore Size (nm)	V _{total} (STP) (cm ³ ·g ⁻¹)	V _{micro} (STP) (cm ³ ·g ⁻¹)	V _{micro} /V _{total} (%)
0	389.38	1.75	0.23	0.15	65.22
0.08	579.96	2.08	0.37	0.13	35.14
0.15	616.77	2.19	0.43	0.12	27.91
0.3	606.35	2.35	0.41	0.09	21.95
0.5	545.32	3.58	0.38	0.08	21.05

**Figure 9.** Molecular structural models of MSiO₂, ZrO₂-MSiO₂, and t-ZrO₂.

3.5. Gas Permselectivity Analysis

3.5.1. The Influence of n_{Zr}

Figure 10 depicts the influence of n_{Zr} on the gas permeabilities and H₂ permselectivities of ZrO₂-MSiO₂ membranes with varying n_{Zr} and 0% DCCA addition at 25 °C and 0.1 MPa. In Figure 10a, with the increase of n_{Zr} , the H₂, CO₂, and N₂ permeances of the samples increased until $n_{Zr} = 0.15$, and then decreased. Compared with the MSiO₂ membranes ($n_{Zr} = 0$), the H₂, CO₂, and N₂ permeance of the ZrO₂-MSiO₂ membranes with $n_{Zr} = 0.15$ increased by 50.95%, 26.74%, and 36.36%, respectively. From the pore structure analysis (Table 1), the overall pore volumes of the ZrO₂-MSiO₂ membranes grew somewhat with increasing n_{Zr} until $n_{Zr} = 0.15$, and then decreased, which can explain why the ZrO₂-MSiO₂ membranes with $n_{Zr} = 0.15$ had the highest permeance to each gas. For the same membrane, the order of gas molecular permeance is H₂ > CO₂ > N₂. Gas permeance decreased with increasing d_k (0.289, 0.33, and 0.364 nm, respectively), indicating that all membranes exhibited molecular sieve properties. However, when $n_{Zr} \geq 0.15$, the permeance of CO₂ decreased more closely to that of N₂. This behavior was related to the fact that following heat treatment at 400 °C, the Zr-O-Si bonds and t-ZrO₂ crystallites generated in the ZrO₂-SiO₂ membranes will generate a significant number of Brønsted acid sites. High acidity leads to a reduction in the affinity of the membranes for CO₂, hence lowering the CO₂ permeance [44].

It can be observed from Figure 10b that compared with MSiO₂ membranes, the H₂/CO₂ and H₂/N₂ permselectivities of ZrO₂-MSiO₂ membranes with $n_{Zr} = 0.15$ increased by 22.93% and 33.04%, respectively. Combined with the previous characterization test, it was found that the ZrO₂-MSiO₂ membranes with $n_{Zr} = 0.15$ had a good pore structure, which is beneficial to improve the permselectivity of gas. In addition, the acidic sites formed by the ZrO₂-MSiO₂ membranes reduced the affinity of the membranes for CO₂ and helped to separate it from H₂. However, the permselectivities of ZrO₂-MSiO₂ membranes after $n_{Zr} = 0.15$ showed a decreasing trend. Compared with the ZrO₂-MSiO₂ membranes with $n_{Zr} = 0.15$, the H₂/CO₂ and H₂/N₂ permselectivities of the membranes with $n_{Zr} = 0.5$ decreased by 9.35% and 20.15%, respectively. As a result, just because the n_{Zr} concentration is larger, it does not indicate that the separation effect is better. Since the Zr-O and Si-O

bonds in zirconium-substituted siloxane rings are longer than in pure siloxane rings, for the $\text{ZrO}_2\text{-MSiO}_2$ membranes with $n_{\text{Zr}} = 0.5$, the number of siloxane rings containing Zr increased, and the pore size of the membranes became larger. Meanwhile, a large number of $t\text{-ZrO}_2$ crystals were produced, which led to the shrinkage of the pore structure inside the membranes and the collapse of the pores, resulting in the decrease of the permselectivities of the membranes.

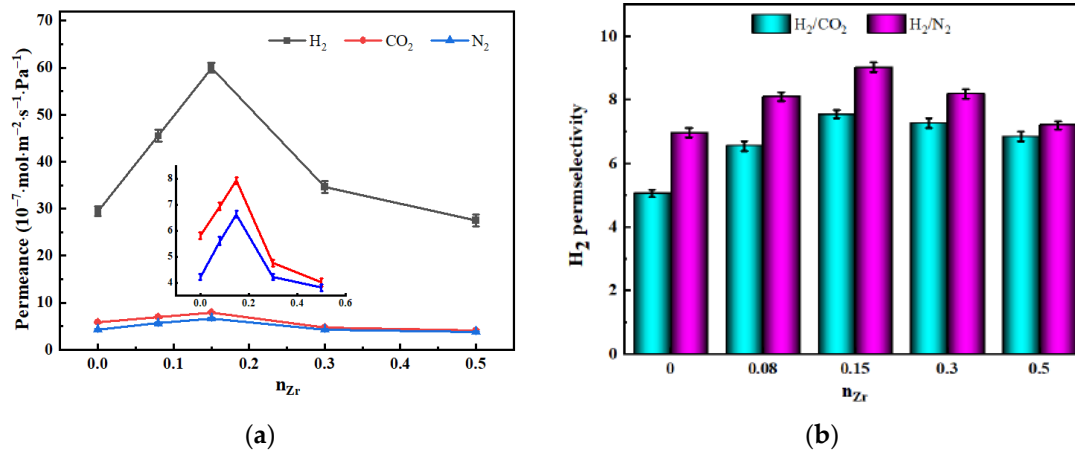


Figure 10. (a) Gas permeance and (b) H_2 permselectivities of $\text{ZrO}_2\text{-MSiO}_2$ membranes with various n_{Zr} and 0% DCCA addition at a pressure difference of 0.1 MPa and 25 °C.

SEM images of surface topography for MSiO_2 and $\text{ZrO}_2\text{-MSiO}_2$ ($n_{\text{Zr}} = 0.15$) membranes calcined at 400 °C are shown in Figure 11. Compared to the MSiO_2 membranes, the particle size and distribution of the $\text{ZrO}_2\text{-MSiO}_2$ membranes were more uniform, the membranes' surfaces had no obvious defects, and the surface was uniform and smooth. The particle size of MSiO_2 membranes was between 1.1 and 5.8 nm, while the particle size of $\text{ZrO}_2\text{-MSiO}_2$ membranes was between 1.3 and 8.9 nm. The formed $\text{ZrO}_2\text{-MSiO}_2$ membranes with a smooth surface and uniform membrane pores were more conducive to the gas permselectivity.

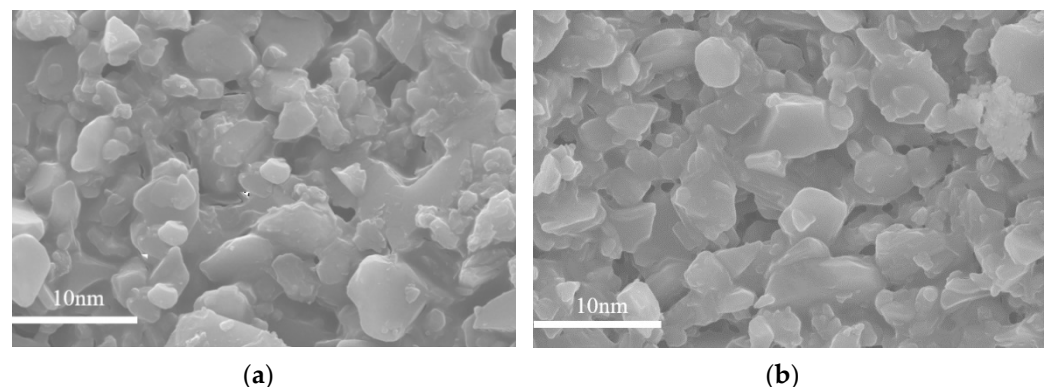


Figure 11. SEM images of surface topography for (a) MSiO_2 and (b) $\text{ZrO}_2\text{-MSiO}_2$ ($n_{\text{Zr}} = 0.15$) membranes with 0% DCCA addition calcined at 400 °C.

3.5.2. The Influence of Temperature

The permeances and permselectivities of the MSiO_2 and $\text{ZrO}_2\text{-MSiO}_2$ ($n_{\text{Zr}} = 0.15$) membranes with 0% DCCA addition at a pressure difference of 0.1 MPa and temperature changing from 25 to 200 °C are shown in Figure 12. Obviously, with the increasing temperature, the permeance of H_2 of MSiO_2 and $\text{ZrO}_2\text{-MSiO}_2$ membranes increased gradually, as seen in Figure 12a. From 25 to 200 °C, the H_2 permeance of MSiO_2 and $\text{ZrO}_2\text{-MSiO}_2$ membranes rose by 19.66% and 7.12%, respectively, demonstrating that the H_2 permeation

behavior in the two membranes followed the activated diffusion transport mechanism. In contrast, the permeabilities of CO₂ and N₂ were similar to the Knudsen diffusion trend, whereby both slightly decreased. The CO₂ permeance of MSiO₂ and ZrO₂-MSiO₂ membranes decreased by 31.46% and 30.20% from 25 to 200 °C, respectively, and the N₂ permeance decreased by 18.60% and 29.98%, respectively. The major explanations for the decrease in CO₂ and N₂ permeance were the violent movement of molecules and the rise in the mean free path as temperature increased.

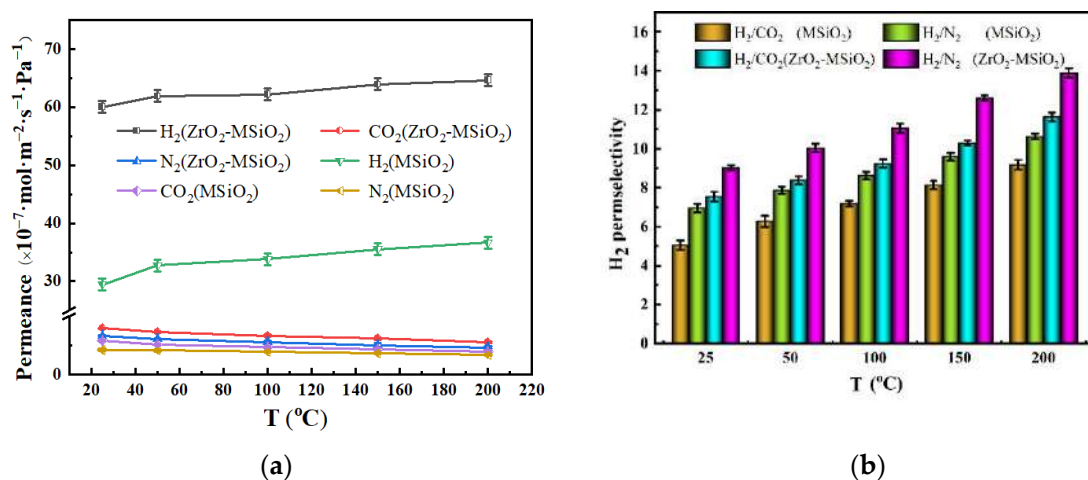


Figure 12. Influence of temperature on the (a) gas permeances and (b) H₂ permselectivities of MSiO₂ and ZrO₂-MSiO₂ ($n_{Zr} = 0.15$) membranes with 0% DCCA addition at a pressure difference of 0.1 MPa.

In Figure 12b, it can be seen that the permselectivities in the membranes gradually increased with the increase of temperature. At 200 °C, compared with the MSiO₂ membranes, the H₂/CO₂ and H₂/N₂ permselectivities of the ZrO₂-MSiO₂ membranes increased by 21.11% and 23.34%, respectively. The above results show that the ZrO₂-MSiO₂ membranes had better permselectivity and permeance of H₂ than the MSiO₂ membranes under the same conditions.

Combined with the preceding studies, it was determined that a rise in temperature facilitated the separation of H₂ and that the separation process of H₂ from CO₂ and N₂ is dominated by activation diffusion, which is described by the Arrhenius equation [45]:

$$P = P_0 \exp\left(-\frac{E_a}{RT}\right) \quad (1)$$

In Formula (1), P is the permeation rate, E_a is the apparent activation energy, and P_0 is a constant, which depends on the pore wall–gas molecule interaction, gas selective layer thickness, and pore shape and tortuosity [46]. For linear fitting, $1000/RT$ was used as the abscissa and $\ln P$ as the ordinate, and the slope of the fitting equation might be used to obtain the apparent activation energy. Figure 13 depicts the Arrhenius fitting diagrams for the three gases.

Figure 13 demonstrates that the apparent activation energy of H₂ is positive, while that of various other gases is negative. This is related to the gas-activated transport behavior, whereby there are two parallel transmission channels for gas through the membrane: one is through selective micropores, with gas transport processed by a thermally activated surface diffusion mechanism in the micropore state [47], and the other is through larger pores [48]. The activation energies for CO₂ and N₂ are negative, indicating that there are permeation pathways large enough in these types of membranes to allow the diffusion of these larger gas. It is generally believed that E_a is composed of two parts [46], the adsorption heat, Q_{st} , of gas on the surface of the membrane and the activation energy, E_m , of gas flowing through the solid surface. The larger the E_m is, the harder it is for the gas to diffuse, E_a

$= E_m - Q_{st}$. Arrhenius equation parameter values are shown in Table 2. Table 2 shows that the E_m values of the gases in the ZrO₂-MSiO₂ membrane are all less than those in the MSiO₂ membrane. It shows that the structure of ZrO₂-MSiO₂ membranes is not as dense as that of MSiO₂ membranes. This is in good accordance with the N₂ adsorption–desorption results. This finding also shows that ZrO₂ doping successfully diminishes the densification of the SiO₂ network. The higher porosity of the ZrO₂-MSiO₂ membranes allows the gas to cross the membrane pore barrier using their kinetic energy. Therefore, the gas (H₂, CO₂, and N₂) permeance of ZrO₂-MSiO₂ membranes is higher than that of MSiO₂ membranes.

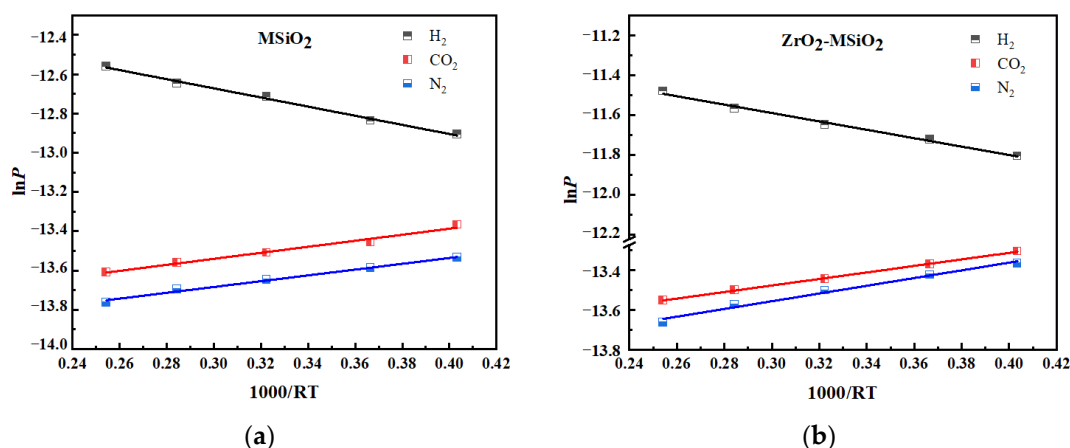


Figure 13. Arrhenius plots of different gases of (a) MSiO₂ and (b) ZrO₂-MSiO₂ ($n_{Zr} = 0.15$) membranes.

Table 2. Arrhenius equation parameter values of MSiO₂ and ZrO₂-MSiO₂ ($n_{Zr} = 0.15$) membranes.

Membrane	Gases	E_a (kJ·mol ⁻¹)	Q_{st} (kJ·mol ⁻¹)	E_m (kJ·mol ⁻¹)
MSiO ₂	H ₂	2.32	6.00	8.32
	CO ₂	−1.53	24.00	22.47
	N ₂	−1.48	18.00	16.52
ZrO ₂ -MSiO ₂	H ₂	2.10	6.00	8.10
	CO ₂	−1.64	24.00	22.36
	N ₂	−1.94	18.00	16.06

Table 3 displays the E_a of H₂, pore diameter, H₂ permeance, and H₂ permselectivities for several membranes/films prepared by other researchers. It is challenging to concurrently enhance the membranes' permselectivity and gas permeability, as seen in Table 3. Generally, the larger the average pore size of the membrane, the higher the permeance to H₂, which is accompanied by a smaller E_a . Meanwhile, the E_a of H₂ is related to the interaction of H₂ with the membrane pore wall. It can be seen from Table 3 that the as-prepared ZrO₂-MSiO₂ membrane has a large H₂ permselectivity compared to other membranes.

Table 3. E_a of H₂, pore diameter, H₂ permeance, and H₂ permselectivities for various membranes/films prepared by other researchers.

Type	Temperature/Pressure	E_a of H ₂ (kJ·mol ⁻¹)	Pore Diameter (nm)	H ₂ Permeance (mol·m ⁻² ·s ⁻¹ ·Pa ⁻¹)	H ₂ Permselectivities	
					H ₂ /CO ₂	H ₂ /N ₂
SiO ₂ [49]	200 °C, 2 bar	-	0.30–0.54	4.62×10^{-7}	3.7	10.5
ZIF-7-SiO ₂ [50]	200 °C	-	5	8×10^{-7}	8.78	11.8
Pd-SiO ₂ [51]	200 °C, 0.3 MPa	-	0.57	7.26×10^{-7}	4.3	14
ZrO ₂ [52]	350 °C	-	4.95	5.3×10^{-8}	14.3	3.1
ZrO ₂ -SiO ₂ [27]	550 °C	7.0	0.165	1.8×10^{-7}	-	-
BTDA-DDS polyimide [53]	30 °C, 5 MPa	-	-	2.52×10^{-9}	5.16	193.21
Cellulose acetate [54]	25 °C, 1 bar	-	-	3.55×10^{-9}	-	30.3
ZrO ₂ -MSiO ₂ *	200 °C, 0.1 MPa	2.10	2.19	6.46×10^{-6}	11.64	13.88

* In this work.

3.5.3. The Influence of Pressure Difference

Figure 14 illustrates the effect of pressure difference on the gas permeances and H_2 permselectivities of $MSiO_2$ and ZrO_2 - $MSiO_2$ ($n_{Zr} = 0.15$) membranes at 200 °C with 0% DCCA addition. In Figure 14a, it can be observed that the H_2 permeance of the ZrO_2 - $MSiO_2$ membranes with $n_{Zr} = 0.15$ improved with the increase of the pressure difference, and the pressure dependence increased. However, the H_2 permeance of $MSiO_2$ membranes remained basically unchanged. The $MSiO_2$ and ZrO_2 - $MSiO_2$ membranes increased their H_2 permeance by 2.16% and 19.96%, respectively, when the pressure was increased from 0.10 to 0.40 MPa. In Figure 14b, the H_2 permselectivities of $MSiO_2$ membranes did not change significantly, and the H_2/CO_2 and H_2/N_2 permselectivities decreased by 5.27% and 1.12%, respectively. However, the H_2 permselectivities of the ZrO_2 - $MSiO_2$ membranes with $n_{Zr} = 0.15$ changed greatly, where the H_2/CO_2 and H_2/N_2 permselectivities decreased by 22.04% and 21.12%, respectively. Clearly, it can be seen that the permselectivity of the ZrO_2 - $MSiO_2$ membranes was reduced more than that of the $MSiO_2$ membranes, that is, the pressure had a relatively small effect on the gas permeation of the $MSiO_2$ membranes. This phenomenon is attributed to the relatively dense $MSiO_2$ membranes with micropores as the main component. With the increase of the pressure difference between the two sides of the membranes, the power of the gas passing through the ZrO_2 - $MSiO_2$ membranes increased, making it easier for the gas to pass through the mesopores or even the macropores, which has a greater impact on the permselectivity of the membranes. At the same time, it is shown that the H_2 diffusion mechanism of ZrO_2 - $MSiO_2$ membranes was different from that of $MSiO_2$ membranes due to the influence of doping ZrO_2 . The gas transport in the ZrO_2 - $MSiO_2$ membranes follows the surface diffusion mechanism. In addition, when the pressure difference increased to 0.4 MPa, the permselectivities of H_2/CO_2 and H_2/N_2 were still higher than their respective Knudsen diffusion (4.69 and 3.74, respectively), indicating that they still have good gas permeation performance under high pressure.

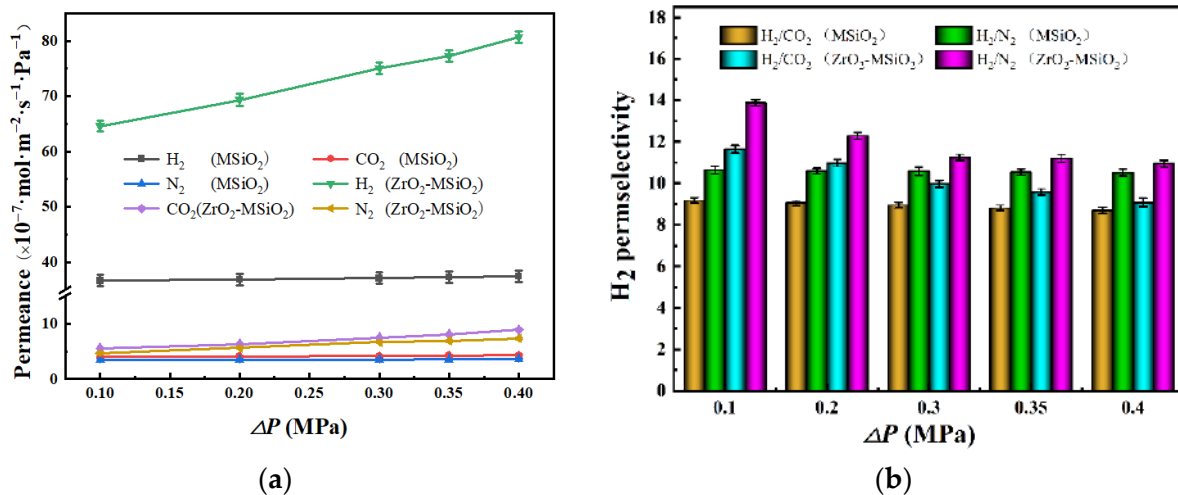


Figure 14. Influence of pressure difference on the (a) gas permeances and (b) H_2 permselectivities of $MSiO_2$ and ZrO_2 - $MSiO_2$ ($n_{Zr} = 0.15$) membranes with 0% DCCA addition at 200 °C.

3.5.4. The Influence of the DCCA

Comparing and analyzing the previous results, it was found that the addition of DCCA (glycerol) by the sol-gel method can effectively reduce the uneven shrinkage of the membrane when it is heated during firing. The gas permeances and H_2 permselectivities of ZrO_2 - $MSiO_2$ membranes ($n_{Zr} = 0.15$) with various DCCA additions at 200 °C and 0.1 MPa are shown in Figure 15.

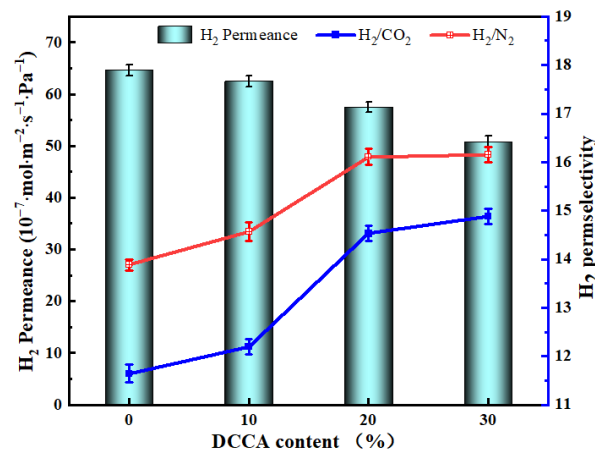


Figure 15. H₂ permeances and permselectivities of ZrO₂-MSiO₂ membranes ($n_{Zr} = 0.15$) with various DCCA additions at 200 °C and 0.1 MPa.

Figure 15 demonstrates that the H₂ permeance of the ZrO₂-MSiO₂ membranes reduced by 21.30% as the DCCA addition increased from 0 to 30%. The permselectivities of H₂/CO₂ and H₂/N₂ increased by 21.77% and 14.07%, respectively. However, compared with the 20% membranes, the H₂/CO₂ and H₂/N₂ permselectivities of the membranes with the addition of 30% only increased by 2.14% and 0.28%, respectively. Figure 16 shows the relationship between DCCA (GL) contents and $F_{H_2} \times \alpha_{H_2}$ (F_{H_2} is the H₂ permeance, α_{H_2} is the permselective of H₂). It was clearly observed that the addition of DCCA from 0 to 20% enhanced the $F_{H_2} \times \alpha_{H_2}$ value, and after more than 20%, the $F_{H_2} \times \alpha_{H_2}$ value showed a lower level. This is attributed to the fact that the addition of glycerol will gradually surround the sol particles, reduce the agglomeration caused by the collision of the colloid particles, accelerate the creation of the sol-gel network, and improve the stability of the sol structure [52]. In addition, the membrane layer collapsed and cracked easily during the drying and calcination processes, and the addition of glycerol can effectively reduce the liquid–gas surface tension to a certain extent, thereby protecting the gel skeleton from deformation [55]. However, the particles of the sol were surrounded by steric effects when too much GL was added, making the sol sticky and difficult to dry to form a membrane. The extension of the drying time makes the cross-linking of the sol more thorough and eventually leads to the densification of the membrane, which is not conducive to gas separation. From the above point of view, the membranes with 20% DCCA addition were the more worthy choice.

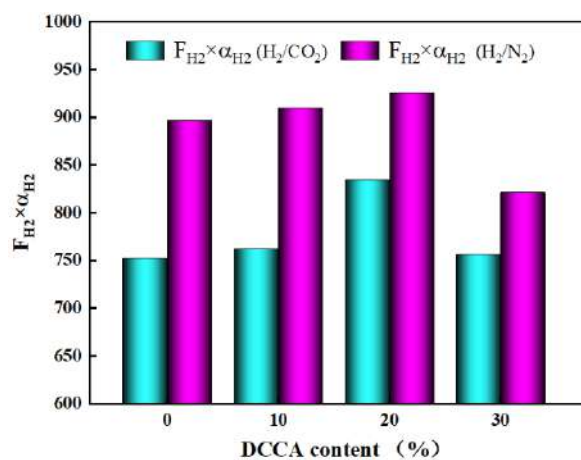


Figure 16. The relationship between DCCA addition and $F_{H_2} \times \alpha_{H_2}$.

3.5.5. Steam Treatment and Regeneration Analysis

Figure 17 shows the effects of steam treatment and thermal regeneration on the gas permeances (H_2 , CO_2 , and N_2) and H_2 permselectivities of $MSiO_2$ and ZrO_2 - $MSiO_2$ ($n_{Zr} = 0.15$) membranes with 0% DCCA addition at a pressure difference of 0.1 MPa and 25 °C. The permeances of H_2 , CO_2 , and N_2 for $MSiO_2$ and ZrO_2 - $MSiO_2$ membranes appear to have reduced after steam treatment. After steam aging for 7 days, the permeance of H_2 for $MSiO_2$ and ZrO_2 - $MSiO_2$ membranes dropped by 20.63% and 3.70%, respectively, as compared to untreated fresh samples, and the permselectivities of H_2/CO_2 and H_2/N_2 for $MSiO_2$ membranes decreased by 1.59% and 1.04%, respectively, whereas those of ZrO_2 - $MSiO_2$ membranes increased by 0.09% and 0.43%, respectively.

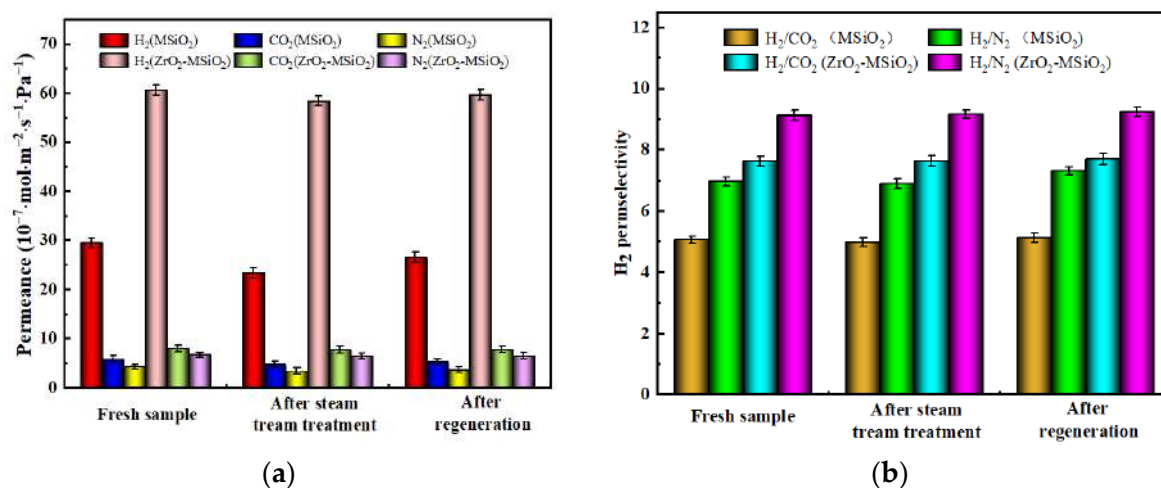


Figure 17. Effect of hydrothermal conditions on the (a) gas permeances and (b) H_2 permselectivities of $MSiO_2$ and ZrO_2 - $MSiO_2$ ($n_{Zr} = 0.15$) membranes with 0% DCCA addition at a pressure difference of 0.1 MPa and 25 °C.

The gas permeances (H_2 , CO_2 , and N_2), as well as the permselectivities of H_2/CO_2 and H_2/N_2 for two membranes, all exhibit an increased trend after regeneration by calcination at 350 °C. However, as compared to untreated fresh samples, the H_2 permeances of $MSiO_2$ and ZrO_2 - $MSiO_2$ membranes after regeneration dropped by 9.96% and 1.65%, respectively, whereas the permselectivities of H_2/CO_2 and H_2/N_2 for $MSiO_2$ membranes improved by 1.12% and 4.71%, respectively, and those for ZrO_2 - $MSiO_2$ membranes increased by 0.08% and 1.21%, respectively. The decrease in gas permeances in both membranes suggests that membrane pore shrinking occurs after calcination at 350 °C. Lower permeance and greater permselectivities are produced as a result of the smaller pores. This is attributed to the partial Zr atoms replacing the Si atoms in Si-O-Si to form more stable Zr-O-Si bonds, which further improves the hydrothermal stability of the membrane material. Therefore, the above results indicated that the ZrO_2 - $MSiO_2$ membranes had a better hydrothermal stability and reproducibility than $MSiO_2$ membranes.

4. Conclusions

The ZrO_2 - $MSiO_2$ membranes were manufactured to enhance the steam stability and H_2 permselectivity of SiO_2 membranes. It was found that with the increase of ZrO_2 content, the pore size distribution of the materials became wider and the average pore size increased, indicating that the doping of ZrO_2 had the effect of expanding the pores. The ZrO_2 - $MSiO_2$ membranes with $n_{Zr} = 0.15$ had a good pore structure and suitable micropore/mesoporous ratio, which is beneficial to improve the permeance of natural gas. At 200 °C, the H_2/CO_2 and H_2/N_2 permselectivities of ZrO_2 - $MSiO_2$ membranes were 79.18% and 26.75% greater than those of $MSiO_2$ membranes, respectively. Furthermore, when the pressure was increased to 0.4 MPa, the permselectivities were still higher than their respective Knudsen

diffusion, indicating that they still had good gas permeance at high pressure. With the addition of DCCA from 20% to 30%, the H_2/CO_2 and H_2/N_2 permselectivities of ZrO_2 - $MSiO_2$ membranes only increased by 2.14% and 0.28%, respectively, and the $F_{H_2} \times \alpha_{H_2}$ value with 20% addition was the highest. In conclusion, it is worthwhile to choose 20% GL as the DCCA addition for ZrO_2 - $MSiO_2$ membranes. Compared with the untreated fresh sample, after 7 days of water vapor aging, the permeance of ZrO_2 - $MSiO_2$ membranes to H_2 decreased by only 3.70%, and the permselectivities of H_2/CO_2 and H_2/N_2 increased by only 0.09% and 0.43%, respectively. After regeneration at 350 °C, the H_2 permeance of the ZrO_2 - $MSiO_2$ membranes decreased by 1.65%, and the permselectivities of H_2/CO_2 and H_2/N_2 increased by 0.08% and 1.21%. It is enough to show that the prepared ZrO_2 - $MSiO_2$ membranes had a good hydrothermal stability and certain regeneration performance. In the future, the influence of high temperature (for example, ≥ 300 °C) and mixed gases on the gas permeances and permselectivities of ZrO_2 - $MSiO_2$ membranes should be explored, which is important to the practical engineering applications.

Author Contributions: Conceptualization, L.W. and J.Y.; writing—original draft preparation, L.W. and J.Y.; funding acquisition, J.Y. All authors have read and agreed to the published version of the manuscript.

Funding: This work was supported by the Scientific Research Project of Shaanxi province of China (2022SF-287) and the Scientific Research Project of Shaanxi Education Department, China (19JC017).

Institutional Review Board Statement: Not applicable.

Informed Consent Statement: Not applicable.

Data Availability Statement: Not applicable.

Conflicts of Interest: The authors declare no conflict of interest.

References

- Nazir, H.; Louis, C.; Jose, S.; Prakash, J.; Muthuswamy, N.; Buan, M.E.; Flox, C.; Chavan, S.; Shi, X.; Kauranen, P.; et al. Is the H_2 economy realizable in the foreseeable future? Part I: H_2 production methods. *Int. J. Hydrogen Energy* **2020**, *45*, 13777–13788. [CrossRef]
- Nordio, M.; Wassie, S.A.; Van Sint Annaland, M.; Tanaka, D.A.P.; Sole, J.L.V.; Gallucci, F. Techno-economic evaluation on a hybrid technology for low hydrogen concentration separation and purification from natural gas grid. *Int. J. Hydrogen Energy* **2020**, *46*, 23417–23435. [CrossRef]
- Cai, L.; Cao, Z.; Zhu, X.; Yang, W. Improved hydrogen separation performance of asymmetric oxygen transport membranes by grooving in the porous support layer. *Green Chem. Eng.* **2020**, *2*, 96–103. [CrossRef]
- Lv, B.; Luo, Z.; Deng, X.; Chen, J.; Fang, C.; Zhu, X. Study on dry separation technology of a continuous gas-solid separation fluidized bed with a moving scraper ()—Separation performance. *Powder Technol.* **2021**, *377*, 565–574. [CrossRef]
- Koutsonikolas, D.E.; Pantoleontos, G.; Karagiannakis, G.; Konstandopoulos, A.G. Development of H_2 selective silica membranes: Performance evaluation through single gas permeation and gas separation tests. *Sep. Purif. Technol.* **2021**, *264*, 118432. [CrossRef]
- Wu, R.; Yue, W.; Li, Y.; Huang, A. Ultra-thin and high hydrogen permeable carbon molecular sieve membrane prepared by using polydopamine as carbon precursor. *Mater. Lett.* **2021**, *295*, 129863. [CrossRef]
- Singla, S.; Shetti, N.P.; Basu, S.; Mondal, K.; Aminabhavi, T.M. Hydrogen production technologies—Membrane based separation, storage and challenges. *J. Environ. Manag.* **2022**, *302*, 113963. [CrossRef]
- Yan, E.; Huang, H.; Sun, S.; Zou, Y.; Chu, H.; Sun, L. Development of Nb-Ti-Co alloy for high-performance hydrogen separating membrane. *J. Membr. Sci.* **2018**, *565*, 411–424. [CrossRef]
- Farina, L.; Santucci, A.; Tosti, S. Plasma Enhancement Gases separation via ceramic porous membranes for plasma exhaust processing system of DEMO. *Fusion Eng. Des.* **2021**, *169*, 112484. [CrossRef]
- Zhang, D.; Zhang, X.; Zhou, X.; Song, Y.; Jiang, Y.; Lin, B. Phase stability and hydrogen permeation performance of $BaCo_{0.4}Fe_{0.4}Zr_{0.1}Y_{0.1}O_{3-\delta}$ ceramic membranes. *Ceram. Int.* **2021**, *48*, 9946–9954. [CrossRef]
- Bakoglidis, K.D.; Palisaitis, J.; Dos Santos, R.B.; Rivelino, R.; Persson, P.O.; Gueorguiev, G.K.; Hultman, L. Self-Healing in Carbon Nitride Evidenced As Material Inflation and Superlubric Behavior. *ACS Appl. Mater. Interfaces* **2018**, *10*, 16238–16243. [CrossRef]
- Kakanakova-Georgieva, A.; Gueorguiev, G.; Sangiovanni, D.G.; Suwannaharn, N.; Ivanov, I.G.; Cora, I.; Pécz, B.; Nicotra, G.; Giannazzo, F. Nanoscale phenomena ruling deposition and intercalation of AlN at the graphene/SiC interface. *Nanoscale* **2020**, *12*, 19470–19476. [CrossRef] [PubMed]

13. Thirumal, V.; Yuvaakkumar, R.; Kumar, P.S.; Ravi, G.; Keerthana, S.P.; Velauthapillai, D. Facile single-step synthesis of [email-protected] hybrid nanocomposite by CVD method to remove hazardous pollutants. *Chemosphere* **2021**, *286*, 131733. [CrossRef] [PubMed]
14. Kanezashi, M.; Asaeda, M. Hydrogen permeation characteristics and stability of Ni-doped silica membranes in steam at high temperature. *J. Membr. Sci.* **2006**, *271*, 86–93. [CrossRef]
15. Rosli, A.; Ahmad, A.L.; Low, S.C. Anti-wetting polyvinylidene fluoride membrane incorporated with hydrophobic polyethylene-functionalized-silica to improve CO₂ removal in membrane gas absorption. *Sep. Purif. Technol.* **2019**, *221*, 275–285. [CrossRef]
16. Yang, J.; Chen, J. Hydrophobic modification and silver doping of silica membranes for H₂/CO₂ separation. *J. CO₂ Util.* **2013**, *3–4*, 21–29. [CrossRef]
17. Wei, Q.; Ding, Y.L.; Nie, Z.R.; Liu, X.G.; Li, Q.Y. Wettability, pore structure and performance of perfluorodecyl-modified silica membranes. *J. Membr. Sci.* **2014**, *466*, 114–122. [CrossRef]
18. Mukherjee, D.; Kar, S.; Mandal, A.; Ghosh, S.; Majumdar, S. Immobilization of tannery industrial sludge in ceramic membrane preparation and hydrophobic surface modification for application in atrazine remediation from water. *J. Eur. Ceram. Soc.* **2019**, *39*, 3235–3246. [CrossRef]
19. Karimiab, S.; Mortazavia, Y.; Khodadadia, A.A.; Holmgrenb, A.; Korelskiyc, D.; Hedlund, J. Functionalization of silica membranes for CO₂ separation. *Sep. Purif. Technol.* **2020**, *235*, 116207. [CrossRef]
20. Khan, A.A.; Maitlo, H.A.; Khan, I.A.; Lim, D.; Zhang, M.; Kim, K.-H.; Lee, J.; Kim, J.-O. Metal oxide and carbon nanomaterial based membranes for reverse osmosis and membrane distillation: A comparative review. *Environ. Res.* **2021**, *202*, 111716. [CrossRef]
21. Kurt, T.; Topuz, B. Sol-gel Control on Mixed Network Silica Membranes for Gas Separation. *Sep. Purif. Technol.* **2020**, *255*, 117654. [CrossRef]
22. Zhang, Y.; Huang, B.; Mardkhe, M.K.; Woodfield, B.F. Thermal and hydrothermal stability of pure and silica-doped mesoporous aluminas. *Microporous Mesoporous Mater.* **2019**, *284*, 60–68. [CrossRef]
23. Gu, Y.; Hacırlıoğlu, P.; Oyama, S.T. Hydrothermally stable silica–alumina composite membranes for hydrogen separation. *J. Membr. Sci.* **2008**, *310*, 28–37. [CrossRef]
24. Teo, H.T.; Siah, W.R.; Yuliati, L. Enhanced adsorption of acetylsalicylic acid over hydrothermally synthesized iron oxide-mesoporous silica MCM-41 composites. *J. Taiwan Inst. Chem. Eng.* **2016**, *65*, 591–598. [CrossRef]
25. Uhlmann, D.; Smart, S.; da Costa, J.C.D. H₂S stability and separation performance of cobalt oxide silica membranes. *J. Membr. Sci.* **2011**, *380*, 48–54. [CrossRef]
26. Chang, C.H.; Gopalan, R.; Lin, Y.S. A comparative study on thermal and hydrothermal stability of alumina, titania and zirconia membranes. *J. Membr. Sci.* **1994**, *91*, 27–45. [CrossRef]
27. Yoshida, K.; Hirano, Y.; Fujii, H.; Tsuru, T.; Asaeda, M. Hydrothermal stability and performance of silica-zirconia membranes for hydrogen separation in hydrothermal conditions. *J. Chem. Eng. Jpn.* **2001**, *34*, 523–530. [CrossRef]
28. Díez, B.; Roldán, N.; Martín, A.; Sotro, A.; Perdigón-Melón, J.; Arsuaga, J.; Rosal, R. Fouling and biofouling resistance of metal-doped mesostructured silica/polyethersulfone ultrafiltration membranes. *J. Membr. Sci.* **2017**, *526*, 252–263. [CrossRef]
29. Wang, L.; Yang, J.; Mu, R.; Guo, Y.; Hou, H. Sol-Gel Processed Cobalt-Doped Methylated Silica Membranes Calcined under N₂ Atmosphere: Microstructure and Hydrogen Perm-Selectivity. *Materials* **2021**, *14*, 4188. [CrossRef]
30. Li, L.; Hong, Q. Gas separation using sol-gel derived microporous zirconia membranes with high hydrothermal stability. *Chin. J. Chem. Eng.* **2015**, *23*, 1300–1306. [CrossRef]
31. Gu, Y.; Kusakabe, K.; Morooka, S. Sulfuric acid-modified zirconia membrane for use in hydrogen separation. *Sep. Purif. Technol.* **2001**, *24*, 489–495. [CrossRef]
32. Van Gestel, T.; Velterop, F.; Meulenberg, W.A. Zirconia-supported hybrid organosilica microporous membranes for CO₂ separation and pervaporation. *Sep. Purif. Technol.* **2020**, *259*, 118114. [CrossRef]
33. Ahn, S.J.; Takagaki, A.; Sugawara, T.; Kikuchi, R.; Oyama, S.T. Permeation properties of silica-zirconia composite membranes supported on porous alumina substrates. *J. Membr. Sci.* **2017**, *526*, 409–416. [CrossRef]
34. Hove, M.T.; Luiten-Olieman, M.; Huiskes, C.; Nijmeijer, A.; Winnubst, L. Hydrothermal stability of silica, hybrid silica and Zr-doped hybrid silica membranes. *Purif. Technol.* **2017**, *189*, 48–53. [CrossRef]
35. Goswami, K.P.; Pugazhenth, G. Effect of binder concentration on properties of low-cost fly ash-based tubular ceramic membrane and its application in separation of glycerol from biodiesel. *J. Clean. Prod.* **2021**, *319*, 128679. [CrossRef]
36. Pan, G.S.; Gu, Z.H.; Yan, Z.; Li, T.; Hua, G.; Yan, L. Preparation of silane modified SiO₂ abrasive particles and their Chemical Mechanical Polishing (CMP) performances. *Wear* **2011**, *273*, 100–104. [CrossRef]
37. Azmiyawati, C.; Niami, S.S.; Darmawan, A. Synthesis of silica gel from glass waste for adsorption of Mg²⁺, Cu²⁺, and Ag⁺ metal ions. *IOP Conf. Ser. Mater. Sci. Eng.* **2019**, *509*, 012028. [CrossRef]
38. Sumanjit; Rani, S.; Mahajan, R.K. Equilibrium, kinetics and thermodynamic parameters for adsorptive removal of dye Basic Blue 9 by ground nut shells and Eichhornia. *Arab. J. Chem.* **2016**, *9*, S1464–S1477. [CrossRef]
39. Xiong, R.; Li, X.; Ji, H.; Sun, X.; He, J. Thermal stability of ZrO₂–SiO₂ aerogel modified by Fe(III) ion. *J. Sol-Gel Sci. Technol.* **2014**, *72*, 496–501. [CrossRef]
40. Del Monte, F.; Larsen, W.; Mackenzie, J.D. Chemical Interactions Promoting the ZrO₂ Tetragonal Stabilization in ZrO₂–SiO₂ Binary Oxides. *J. Am. Ceram. Soc.* **2010**, *83*, 1506–1512. [CrossRef]

41. Wang, W.; Zhou, J.; Wei, D.; Wan, H.; Zheng, S.; Xu, Z.; Zhu, D. ZrO₂-functionalized magnetic mesoporous SiO₂ as effective phosphate adsorbent. *J. Colloid Interface Sci.* **2013**, *407*, 442–449. [CrossRef] [PubMed]
42. Musić, S.; Filipović-Vinceković, N.; Sekovanić, L. Precipitation of amorphous SiO₂ particles and their properties. *Braz. J. Chem. Eng.* **2011**, *28*, 89–94. [CrossRef]
43. Zheng, W.; Bowen, K.H.; Li, J.; Dabkowska, I.; Gutowski, M. Electronic structure differences in ZrO₂ vs. HfO₂. *J. Phys. Chem. A* **2005**, *109*, 11521–11525. [CrossRef] [PubMed]
44. Kazunari, K.; Jyunichi, I.; Hideaki, M.; Satoshi, F. Evaluation of hydrogen permeation rate through zirconium pipe. *Nucl. Mater. Energy* **2018**, *16*, 12–18.
45. Lin, R.B.; Xiang, S.; Xing, H.; Zhou, W.; Chen, B. Exploration of porous metal–organic frameworks for gas separation and purification. *Coord. Chem. Rev.* **2017**, *378*, 87–103. [CrossRef]
46. Hong, Q.; Chen, H.; Li, L.; Zhu, G.; Xu, N. Effect of Nb content on hydrothermal stability of a novel ethylene-bridged silsesquioxane molecular sieving membrane for H₂/CO₂ separation. *J. Membr. Sci.* **2012**, *S421–S422*, 190–200.
47. Boffa, V.; Blank, D.; Elshof, J. Hydrothermal stability of microporous silica and niobia–silica membranes. *J. Membr. Sci.* **2008**, *319*, 256–263. [CrossRef]
48. Liu, L.; Wang, D.K.; Martens, D.L.; Smart, S.; da Costa, J.C.D. Binary gas mixture and hydrothermal stability investigation of cobalt silica membranes. *J. Membr. Sci.* **2015**, *493*, 470–477. [CrossRef]
49. Qureshi, H.F.; Nijmeijer, A.; Winnubst, L. Influence of sol–gel process parameters on the micro-structure and performance of hybrid silica membranes. *J. Membr. Sci.* **2013**, *446*, 19–25. [CrossRef]
50. He, D.; Zhang, H.; Ren, Y.; Qi, H. Fabrication of a novel microporous membrane based on ZIF-7 doped 1,2-bis(triethoxysilyl)ethane for H₂/CO₂ separation. *Microporous Mesoporous Mater.* **2022**, *331*, 111674. [CrossRef]
51. Song, H.; Zhao, S.; Lei, J.; Wang, C.; Qi, H. Pd-doped organosilica membrane with enhanced gas permeability and hydrothermal stability for gas separation. *J. Mater. Sci.* **2016**, *51*, 6275–6286. [CrossRef]
52. Beyler, A.P.; Boye, D.M.; Hoffman, K.R.; Silversmith, A.J. Fluorescence enhancement in rare earth doped sol-gel glass by N,N dimethylformamide as a drying control chemical additive. *Phys. Procedia* **2011**, *13*, 4–8. [CrossRef]
53. García, M.G.; Marchese, J.; Ochoa, N.A. Aliphatic–aromatic polyimide blends for H₂ separation. *Int. J. Hydrogen Energy* **2010**, *35*, 8983–8992. [CrossRef]
54. Nikolaeva, D.; Azcune, I.; Tanczyk, M.; Warmuzinski, K.; Jaschik, M.; Sandru, M.; Dahl, P.I.; Genua, A.; Lois, S.; Sheridan, E.; et al. The performance of affordable and stable cellulose-based poly-ionic membranes in CO₂/N₂ and CO₂/CH₄ gas separation. *J. Membr. Sci.* **2018**, *564*, 552–561. [CrossRef]
55. Chen, F.; Ji, Z.; Qi, Q. Effect of liquid surface tension on the filtration performance of coalescing filters. *Sep. Purif. Technol.* **2019**, *209*, 881–891. [CrossRef]



Article

Maxwell Nanofluids: FEM Simulation of the Effects of Suction/Injection on the Dynamics of Rotatory Fluid Subjected to Bioconvection, Lorentz, and Coriolis Forces

Liaqat Ali ^{1,*} , Abdul Manan ² and Bagh Ali ³ ¹ School of Sciences, Xi'an Technological University, Xi'an 710021, China² Department of Physics and Mathematics, Faculty of Sciences, Superior University, Lahore 54000, Pakistan³ Department of Computer Science and Information Technology, Faculty of Sciences, Superior University, Lahore 54000, Pakistan

* Correspondence: liaqat@xatu.edu.cn

Abstract: In this study, the relevance of Lorentz and Coriolis forces on the kinetics of gyratory Maxwell nanofluids flowing against a continually stretched surface is discussed. Gyrotactic microbes are incorporated to prevent the bioconvection of small particles and to improve consistency. The nanoparticles are considered due to their valuable properties and ability to enhance thermal dissipation, which is important in heating systems, advanced technology, microelectronics, and other areas. The main objective of the analysis is to enhance the rate of heat transfer. An adequate similarity transformation is used to convert the primary partial differential equations into non-linear dimensionless ordinary differential equations. The resulting system of equations is solved using the finite element method (FEM). The increasing effects of the Lorentz and Coriolis forces induce the velocities to moderate, whereas the concentration and temperature profiles exhibit the contrary tendency. It is observed that the size and thickness of the fluid layers in the axial position increase as the time factor increases, while the viscosity of the momentum fluid layers in the transverse path decreases as the time factor decreases. The intensity, temperature, and velocity variances for the suction scenario are more prominent than those for the injection scenario, but there is an opposite pattern for the physical quantities. The research findings are of value in areas such as elastomers, mineral productivity, paper-making, biosensors, and biofuels.

Keywords: Maxwell nanofluid; finite element analysis; suction/injection; grid independence analysis; Coriolis force

Citation: Ali, L.; Manan, A.; Ali, B. Maxwell Nanofluids: FEM Simulation of the Effects of Suction/Injection on the Dynamics of Rotatory Fluid Subjected to Bioconvection, Lorentz, and Coriolis Forces. *Nanomaterials* **2022**, *12*, 3453. <https://doi.org/10.3390/nano12193453>

Academic Editor: Henrich Frielinghaus

Received: 27 August 2022

Accepted: 20 September 2022

Published: 2 October 2022

Publisher's Note: MDPI stays neutral with regard to jurisdictional claims in published maps and institutional affiliations.



Copyright: © 2022 by the authors. Licensee MDPI, Basel, Switzerland. This article is an open access article distributed under the terms and conditions of the Creative Commons Attribution (CC BY) license (<https://creativecommons.org/licenses/by/4.0/>).

1. Introduction

The heat and mass transfer analysis of the non-Newtonian hydrodynamic boundary layer flow phenomenon has attracted the interest of many researchers due to the enormous number of potential applications in engineering and industry. The well-known Newtonian liquids (liquids with a sequential strain-stress correlation) basic theory is incapable of elucidating the fluids' internal microstructure. Non-Newtonian liquids (liquids with a sequential strain-stress correlation) include quince paste, animal blood, cement sludges, esoteric lubricating oils, effluent slurry, and liquids containing synthetic polymer additives. One such rate-type non-Newtonian fluid model is called the Maxwell nanofluid model which predicts the stress relaxation time. The extensive choice of methodological and engineering applications associated with Maxwell nanofluids, such as biochemical, gasoline, polymer, and nutrition release, has motivated many investigators to scrutinize the features of Maxwell nanofluids with respect to numerous geometrical and substantial limitations. The convective Maxwell hybrid nanofluid stream in a sturdy channel was studied using the Laplace transform strategy [1], whereby the authors developed a solution to dynamical problems involving Maxwell fluid fractionally. The Caputo fractional differential function

was used for the energy dissipation assessment of hydromagnetic Maxwell nanofluid flow over an elongating penetrable surface with Dufour and Soret ramifications. Jawad et al. [2] used HAM to procure estimated analytical results. Jamshed [3] exploited the Keller box technique (KBT) to investigate the fluidity of an mhd Maxwell nanofluid over a non-linearly elongating sheet in terms of viscous dissipation and entropy propagation. Ali et al. [4] investigated buoyant, induced transitory bio-convective Maxwell nanofluid spinning three-dimensional flows over the Riga surface for chemically reactive and activating energy using a finite element stratagem. Dulal et al. [5] presented results of a study on mhd radiative heat transfer of nanofluids induced by a plate through a porous medium with chemical reaction. Very recently, various authors have explored boundary layer Maxwell nanofluid flow past a different geometric environment. These include Ahmed et al. [6], who reported on mixed convective 3D flow over a vertical stretching cylinder with a shooting technique, Gopinath et al. [7] who explored convective-radiative boundary layer flow of nanofluids with viscous-Ohmic dissipation, Bilal et al. [8] who presented the significance of the Coriolis force on the dynamics of the Carreau–Yasuda rotating nanofluid subject to gyrotactic microorganisms, Ahmed [9] who investigated the effect of a heat source on the stagnation point fluid flow via an elongating revolving plate using a numerical approach, M. Bilal [10] who used the HAM technique to investigate chemically reactive impacts on magnetised nanofluid flow over a rotary pinecone, Amirsom et al. [11] who estimated the influence of bioconvection on three-dimensional nanofluid flow induced by a bi-axial stretching sheet, Prabhavathi et al. [12] who used FEM to investigate CNT nanofluid flow through a cone with thermal slip scenarios, Zohra et al. [13] who used mhd micropolar fluid bio-nanoconvective Navier slip flow in a stretchable horizontal channel, and Gopinath et al. [14] who reported on diffusive mhd nanofluid flow past a non-linear stretching/shrinking sheet with viscous-Ohmic dissipation and thermal radiation.

Nanofluids are fluids that incorporate an appropriate distribution of metal and metallic nanoparticles at the nano size and are engineered to perform specific functions [15–18]. The literature suggests that the presence of nanoparticles in a base fluid has a significant impact on the thermophysical properties of the fluid, particularly those fluids with inadequate permittivity characteristics based on theoretical and experimental investigations [19–21]. Applications in virtually every field of engineering and science relating to convective nanofluid heat transfer flow have stimulated the interest of many scientists and engineers. These include the use of diamond and silica nanoparticles to enhance the electrical characteristics of lubricants, the use of liquids containing nanoparticles to absorb sunlight in solar panels, and exploitation of the antimicrobial properties of zinc and titanium oxide particles for biomedical engineering applications, such as drug delivery and pharmacological treatment [22–25].

The bioconvection phenomenon occurs as a result of the existence of a density gradient in the flow field. Consequently, the movement of particles at the macroscopic level enhances the density stratification of the base liquid in one direction. The presence of gyrotactic microorganisms in nanofluid flow has attracted the interest of many researchers due to their potential application in relation to enzyme function, bio-sensors, biotechnology, drug delivery, and biofuels. These applications have motivated researchers to undertake numerical studies on bioconvective nanofluid flow with microorganisms in different flow field geometries. Chu et al. [26] investigated bioconvective Maxwell nanofluid flow using a reversible, regularly pivoting sheet in the presence of non-linear radiative and heat emitter influences using a homotopy analysis method. Sreedevi et al. [27] investigated the influence of Brownian motion and thermophoresis on Maxwell three-dimensional nanofluid flow over a stretching sheet with thermal radiation. Rao et al. [28] explored bioconvection in conventional reactive nanofluid flow over a vertical cone with gyrotactic microorganisms embedded in a permeable medium. Awais Ali et al. [29], using an Adams–Bash strategy (ABS), statistically explored the Lie group, to investigate bio-convective nanofluid supporting and opposing flow with motile microorganisms. To determine the Arrhenius activation energy of bio-convective nanofluid flow through a stretchable surface, Paluru [30] undertook a heat and mass transfer analysis of MWCNT-kerosene nanofluid flow over a wedge with

thermal radiation. Transient bio-convective Carreau nanofluid flow with gyrotactic microorganisms past a horizontal slender stretching sheet was considered by Elayarani et al. [31] to investigate heat and mass transfer effects in the presence of thermal radiation, multi-slip conditions, and magnetic fields by employing the ANFIS (adaptive neuro-fuzzy inference system) model. Bagh et al. [32] reported on the g-jitter impact on magnetohydrodynamic non-Newtonian fluid over an inclined surface by applying a finite element simulation. Umar et al. [33] investigated the optimized Cattaneo–Christov heat and mass transference flow of bio-convective Carreau nanofluid with microorganisms, influenced by a longitudinal straining cartridge with convective limitations. Al-Hussain [34] developed an analytical model based on the Cattaneo–Christov transit law for a bio-convective magnetic nanofluid stream via a whirling cone immersed in an asymmetric penetrable surface in the context of cross-diffusion, Navier-slip, and Stefan blowing effects.

The careful review of the literature detailed above shows that little attention has been paid to the self-motile denitrifying microbes contained in Maxwell nanofluid spinning flows through an elongating sheet under an externally applied magnetic field. To the best of our knowledge, none of the studies cited has considered the interpreted problem. Consequently, the main objective of this study was to explore the mass and heat transfer impacts on transitory hydromagnetic Maxwell spinning nanofluid 3D radiative flow comprising microbes and suction/injection processes. Many authors [35–37] have examined mhd nanofluid flow using different numerical techniques. Here, the flow-governing associated non-linear PDEs are computed using a finite volume technique [38,39] by adopting a weighted residual strategy. The varied flow field properties for a variety of substantial factors are explained and illustrated graphically. The computing results generated using Matlab source code were validated against previous studies and determined to show acceptable consistency. The values of the friction factor, Nusselt, and Sherwood numbers are simulated and addressed in tabulated form. The computational evaluation can be used for gasoline, polymers, precise nutrition release, engine lubricants, paint rheology, biosensors, medicine delivery, and biofuels.

Research Queries

The following research questions are addressed in this study:

1. What effects do relaxation of the Deborah number, the Coriolis effect, and an applied magnetic field force have on the hydrodynamics of heat flux, fluid viscosity, and concentration level variances using injection/suction?
2. What impact do Brownian motion and thermophoresis have on heat and mass transfer rates and the skin friction factor for suction/injection?
3. How do Brownian motion, the relaxation Deborah number, and time-dependent factors impact on the temperature profile?
4. What is the bioconvection impact on the motile dispersal function with suction/injection?

2. Mathematical Geometry

The transitory magneto-hydrodynamic 3D rotational flow of Maxwell nanofluid over a bidirectional elongating surface is investigated. Figure 1 depicts the fluid dynamic layout and coordinate structure of the articulated problem, with the flow, constrained to $z \geq 0$. With a rotational consistent velocity Ω , the nanofluid flow rotates around the z-axis. When $z = t = 0.0$, the sheet is extended along the x-axis having $u_w = \tilde{a}x$ velocity. In the axial direction, a static and uniform magnetic field of magnitude B_0 is implemented. An induced magnetic Reynolds number leads to a reduced magnetic field, which results in minimal Hall current and Ohmic inefficiency [40]. To avoid causing sedimentation, gyrotactic microbes are utilized to maintain convective stability. The external temperature and intensity are signified by T_∞ , and C_∞ , N_∞ , respectively, while the temperature and intensity at the surface are represented by T_w , and C_w , N_w , respectively. For the current elaborated problem, $V = (u_1(x, y, z), u_2(x, y, z), u_3(x, y, z))$ is assumed to be the velocity

field. The equations of mass conservation, linear moments, temperature, and concentrations are formulated as a result of the preceding assertions [41–43]:

$$\partial_x u_1 + \partial_y u_2 + \partial_z u_3 = 0 \tag{1}$$

$$\rho_{nf}(\partial_t u_1 + u_1 \partial_x u_1 + u_2 \partial_y u_1 + u_3 \partial_z u_1 - 2\Omega u_2 + \lambda_1 \varrho_{u_1}) = -\partial_x p + \mu_{nf} \partial_{zz} u_1 - \sigma_{nf} B_0^2 u_1 \tag{2}$$

$$\rho_{nf}(\partial_t u_2 + u_1 \partial_x u_2 + u_2 \partial_y u_2 + u_3 \partial_z u_2 - 2\Omega u_1 + \lambda_1 \varrho_{u_2}) = -\partial_y p + \mu_{nf} \partial_{zz} u_2 - \sigma_{nf} B_0^2 u_2 \tag{3}$$

$$\rho_{nf}(\partial_t u_3 + u_1 \partial_x u_3 + u_2 \partial_y u_3 + u_3 \partial_z u_3) = -\partial_z p + \mu_{nf} \partial_{zz} u_3 \tag{4}$$

$$\partial_t T + u_1 \partial_x T + u_2 \partial_y T + u_3 \partial_z T = \alpha_{nf} \partial_{zz} T + \tau^* \left\{ D_b \partial_z C \partial_z T + \frac{D_T}{T_\infty} (\partial_z T)^2 \right\} \tag{5}$$

$$\partial_t C + u_1 \partial_x C + u_2 \partial_y C + u_3 \partial_z C = D_b \partial_{zz} C + \frac{D_T}{T_\infty} \partial_{zz} T \tag{6}$$

$$\partial_t N + u_1 \partial_x N + u_2 \partial_y N + u_3 \partial_z N + \frac{bWc}{(C_w - C_\infty)} [\partial_z (N \partial_z C)] = D_m \partial_{zz} N \tag{7}$$

where,

$$\varrho_{u_1} = \left\{ u_1^2 \partial_{xx} u_1 + u_2^2 \partial_{yy} u_1 + u_3^2 \partial_{zz} u_1 + 2u_1 u_2 \partial_{xy} u_1 + 2u_2 u_3 \partial_{yz} u_1 + 2u_1 u_3 \partial_{xz} u_1 - 2\Omega(u_1 \partial_x u_2 + u_2 \partial_y u_2 + u_3 \partial_z u_2) + 2\Omega(u_2 \partial_x u_1 - u_1 \partial_y u_1) \right\},$$

$$\varrho_{u_2} = \left\{ u_1^2 \partial_{xx} u_2 + u_2^2 \partial_{yy} u_2 + u_3^2 \partial_{zz} u_2 + 2u_1 u_2 \partial_{xy} u_2 + 2u_2 u_3 \partial_{yz} u_2 + 2u_1 u_3 \partial_{xz} u_2 - 2\Omega(u_1 \partial_x u_1 + u_2 \partial_y u_1 + u_3 \partial_z u_1) + 2\Omega(u_2 \partial_x u_2 - u_1 \partial_y u_2) \right\}$$

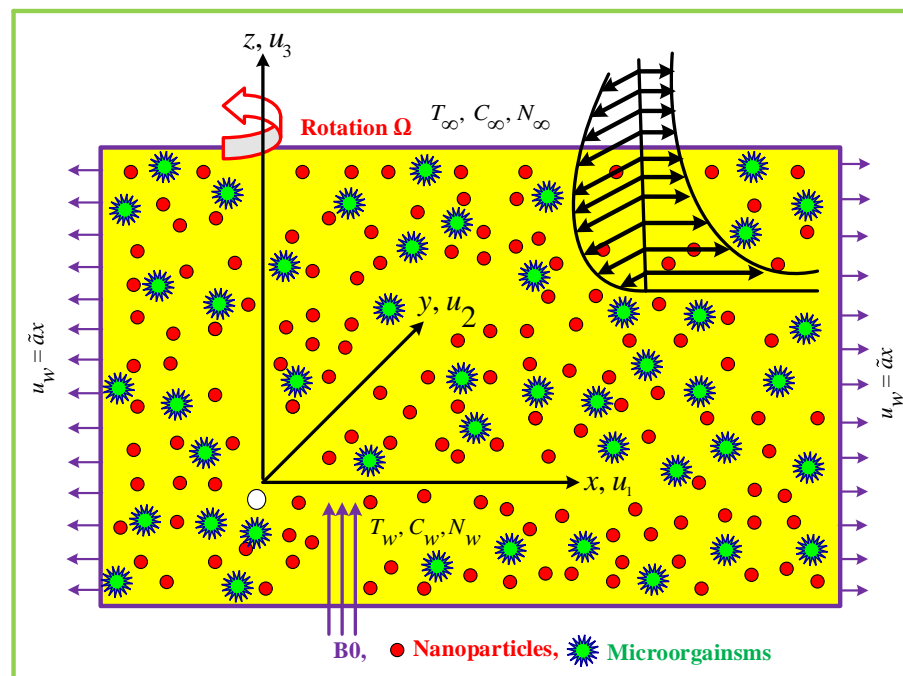


Figure 1. Flow Sketch.

Here, (C, N, T) represent the nanoparticle density, micro-organism concentration, and fluid temperature, (D_b, D_T, D_m) are the Brownian motion, thermophoresis and microorganism diffusion; $(\lambda_1, \rho_{n_f}, \mu_{n_f}, \alpha_{n_f})$ are, respectively, the relaxation time, density, dynamic viscosity, and thermal diffusivity of the nanofluid. The boundary conditions are [44,45]:

$$t < 0 : u_1 = 0, u_2 = 0, u_3 = 0, C = (C_\infty), N = (N_\infty), T = (T_\infty) \tag{8}$$

$$t \geq 0 : u_1 = a(x), u_3 = -w_0, u_2 = 0, C = (C_w), N = (N_w), T = (T_w), \text{ when } z = 0 \tag{9}$$

$$t \geq 0 : u_1 \rightarrow 0, u_2 \rightarrow 0, C \rightarrow C_\infty, N \rightarrow N_\infty, T \rightarrow T_\infty, \text{ when } z \rightarrow \infty. \tag{10}$$

The following similarity transforms are used to alleviate the complexity of the articulated problem as [41,44]:

$$\left. \begin{aligned} \Gamma = \tilde{a}t, u_1 = \tilde{a}x \frac{\partial F(\zeta, \eta)}{\partial \eta}, u_2 = \tilde{a}xG(\zeta, \eta), u_3 = -\sqrt{\tilde{a}v\zeta}F(\zeta, \eta), \zeta = 1 - e^{-\Gamma}, \eta = \sqrt{\frac{\tilde{a}xz^2}{\zeta\nu}} \\ C = (C_w - C_\infty)\Phi(\zeta, \eta) + C_\infty, N = (N_w - N_\infty)\chi(\zeta, \eta) + N_\infty, T = (T_w - T_\infty)\theta(\zeta, \eta) + T_\infty \end{aligned} \right\} \tag{11}$$

In the context of Equation (11), Equation (1) is justified, and Equations (2)–(10) are transmuted into the non-linear PDEs illustrated below in (ζ, η) form:

$$F''' + \frac{\eta}{2}F'' - \frac{\zeta\eta}{2}F'' + \zeta\{FF'' - F'^2 - M^2F' + 2\lambda G + \beta\zeta u_1\} - \zeta(1 - \zeta) \frac{\partial F'}{\partial \zeta} = 0 \tag{12}$$

$$G'' + \frac{\eta}{2}G' - \frac{\zeta\eta}{2}G' + \zeta\{FG' - 2\lambda F' - M^2G - F'G + \beta\zeta u_2\} - \zeta(1 - \zeta) \frac{\partial G}{\partial \zeta} = 0 \tag{13}$$

$$\theta'' - \frac{\eta}{2}(\zeta - 1)Pr\theta' + \zeta PrF\theta' + N_b Pr\theta\Phi + N_t Pr\theta'^2 - \zeta(1 - \zeta)Pr \frac{\partial \theta}{\partial \zeta} = 0 \tag{14}$$

$$\Phi'' + 0.5\eta Le(1 - \zeta)\Phi' + Le\zeta F\Phi' + N_t N_b^{-1}\theta'' - \zeta(1 - \zeta)Le \frac{\partial \Phi}{\partial \zeta} = 0 \tag{15}$$

$$\chi'' + \frac{Lb}{2}(1 - \zeta)Lb\chi' + \zeta LbF\chi' - Pe\Phi''(\delta_1 + \chi) + Pe\chi'\Phi' = Lb\zeta(1 - \zeta) \frac{\partial \chi}{\partial \zeta} \tag{16}$$

$$\left. \begin{aligned} F(\zeta, \eta) = \Gamma, F'(\zeta, \eta) = \theta(\zeta, \eta) = 1, G(\zeta, \eta) = 0, \Phi(\zeta, \eta) = \chi(\zeta, \eta) = 1, \zeta \geq 0, \text{ when } \eta = 0 \\ F'(\zeta, \eta) \rightarrow 0, \theta(\zeta, \eta) \rightarrow 0, G(\zeta, \eta) \rightarrow 0, \Phi(\zeta, \eta) \rightarrow 0, \chi(\zeta, \eta) \rightarrow 0, \zeta \geq 0, \text{ when } \eta \rightarrow \infty \end{aligned} \right\} \tag{17}$$

where $\zeta_{u_1} = 2FF'F'' - F^2F''' - 2\lambda FG'$, $\zeta_{u_2} = 2FF'G' - F^2G'' - 2\lambda F'^2 + 2\lambda FF'' - 2\lambda G^2$, and primes ($'$, $''$, $'''$) denote the derivatives w.r.t (η) . Here rotation, magnetized, Prandtl and Lewis numbers, Brownian factor, bioconvection Lewis number, thermophoresis, Peclet number, relaxation Deborah number, microorganism concentration difference, and suction/injection are, respectively, $\lambda, M, Pr, Le, N_b, Lb, N_t, Pe, \beta, \delta_1$, and Γ factors are described as:

$$\lambda = \frac{\Omega}{a}, M = \sqrt{\frac{\sigma_{n_f} B_0^2}{\rho_f \tilde{a}}}, Pr = \frac{\nu}{\alpha_{n_f}}, Le = \frac{\nu}{D_B}, Lb = \frac{\nu}{D_m}, N_b = \tau\nu^{-1}D_B(C_w - C_\infty), \\ N_t = \frac{D_T(\tau T_w - \tau T_\infty)}{\nu T_\infty}, \beta = \lambda_1 a, Pe = \frac{bW_c}{D_m}, \delta_1 = \frac{N_\infty}{N_w - T_\infty}, \Gamma = \frac{w_0}{\sqrt{\tilde{a}\nu\zeta}}.$$

The physical quantities (Sherwood, Nusselt) numbers, and the coefficient of skin friction are expressed here as:

$$Nu_x = \frac{xq_w}{\kappa(T_w - T_\infty)}, Shr = \frac{xq_m}{D_B(C_w - C_\infty)}, C_{f_x} = \frac{\tau_w^x}{\rho u_1^2}, C_{f_y} = \frac{\tau_w^y}{\rho u_1^2}. \tag{18}$$

here, the skin friction tensors at the wall are represented as $\tau_w^x = \mu \left(\frac{\partial u_1}{\partial z} \right)_{z=0}$ (along the x-axis) and $\tau_w^y = \mu \left(\frac{\partial u_2}{\partial z} \right)_{z=0}$ (along the y-axis), the heat flux, and the mass at the surface is $qm = -D_B \left(\frac{\partial C}{\partial z} \right)_{z=0}$, and $qw = -\kappa \left(\frac{\partial T}{\partial z} \right)_{z=0}$. Taking Equation (11), we get:

$$\begin{cases} C_{f_x} Re_x^{1/2} = \frac{F''(0)}{\sqrt{\zeta}}, C_{f_y} Re_x^{1/2} = \frac{G'(0)}{\sqrt{\zeta}}, \\ Nu_x Re_x^{1/2} = -\frac{[\theta'(0)]}{\sqrt{\zeta}}, Shr_x Re_x^{1/2} = -\frac{[\Phi'(0)]}{\sqrt{\zeta}}. \end{cases} \tag{19}$$

3. Computational Procedure

The finite element analysis (FEA) is a computational approach for discovering numerical approximations to ODEs and PDEs with complicated boundary conditions. This is an efficient approach for resolving technological problems, especially those involving fluid diversities. This methodology represents an excellent numerical strategy for solving a variety of real-world problems, particularly for heat transfer via fluids and biomaterials [46]. Reddy [47,48] presents a layout of the Galerkin finite element methodology (GFEM), summarizing the main elements of this methodology. This methodology is an unparalleled computational methodology in the field of engineering, is valuable for evaluating integral governing equations incorporating fluid diversities, and is an extremely effective methodology for resolving numerous non-linear problems [49–51]. To evaluate the set of Equations (12)–(16) along the boundary condition (17), firstly, we assume:

$$F' = P \tag{20}$$

The system of Equations (12)–(17) reduced as:

$$P'' - \frac{\eta}{2}(\zeta - 1)P' + \zeta(FP' - P^2 + 2\lambda G - M^2P + \beta(2FPP' - F^2P'' - 2\beta FG')) = \zeta \frac{\partial P}{\partial \zeta} - \zeta^2 \frac{\partial P}{\partial \zeta} \tag{21}$$

$$\begin{aligned} G'' + \frac{1}{2}(1 - \zeta)\eta G' + \zeta(FG' + \beta(2FPG' - F^2G'' - 2\lambda P^2 + 2\beta FP' - 2\beta G^2)) \\ - PG - 2\beta P = -\zeta^2 \frac{\partial(G)}{\partial \zeta} + \zeta \frac{\partial(G)}{\partial \zeta} \end{aligned} \tag{22}$$

$$\theta'' - \frac{\eta}{2}(\zeta - 1)Pr\theta' + Pr\zeta F\theta' + Pr\theta'(N_b\Phi' + N_t\theta') = Pr\zeta(1 - \zeta) \frac{\partial \theta}{\partial \zeta} \tag{23}$$

$$\Phi'' + \frac{\eta}{2}Le(1 - \zeta)\Phi' + Le\zeta F\Phi' + N_t N_b^{-1} \theta'^2 = \zeta(1 - \zeta)Le \frac{\partial \Phi}{\partial \zeta} \tag{24}$$

$$\chi'' + \frac{Lb}{2}(1 - \zeta)\eta\chi' + \zeta LbF\chi' - Pe\Phi''(\delta_1 + \chi) + Pe\chi'\Phi' = Lb\zeta(1 - \zeta) \frac{\partial \chi}{\partial \zeta} \tag{25}$$

$$\left. \begin{aligned} F(\zeta, \eta) = \Gamma, G(\zeta, \eta) = 0, P(\zeta, 0) = \theta(\zeta, \eta) = \Phi(\zeta, \eta) = \chi(\zeta, \eta) = 1, \zeta \geq 0, \text{ at } \eta = 0 \\ P(\zeta, \eta) \rightarrow 0, G(\zeta, \eta) \rightarrow 0, \theta(\zeta, \eta) \rightarrow 0, \Phi(\zeta, \eta) \rightarrow 0, \chi(\zeta, \eta) \rightarrow 0, \zeta \geq 0, \text{ as } \eta \rightarrow \infty \end{aligned} \right\} \tag{26}$$

For numerical calculation, the plate length has been specified as $\zeta = 1.0$ and the thickness as $\eta = 5.0$. The Equations (20)–(25) have a variational form that can be represented as:

$$\int_{\Omega_e} w_{f_1} \{F' - P\} d\Omega_e = 0 \tag{27}$$

$$\int_{\Omega_e} w_{f_2} \left\{ P'' + \frac{1}{2}(1 - \zeta)\eta P' + \zeta(FP' - P^2 + 2\lambda P - M^2P + \beta(2FPP' - F^2P'' - 2\lambda FG')) - \zeta(1 - \zeta) \frac{\partial P}{\partial \zeta} \right\} d\Omega_e = 0 \tag{28}$$

$$\int_{\Omega_e} w_{f_3} \left\{ G'' + \frac{1}{2}(1 - \zeta)\eta G' + \zeta(FG' + \beta(2FPG' - F^2G'' - 2\lambda P^2 + 2\lambda FP' - 2\lambda G^2)) - PG - 2\lambda P + (\zeta - 1)\zeta \frac{\partial(G)}{\partial \zeta} \right\} d\Omega_e = 0 \tag{29}$$

$$\int_{\Omega_e} w_{f_4} \left\{ \theta'' + \frac{Pr}{2}(1 - \zeta)\eta\theta' + Pr\zeta F\theta' + N_b Pr\theta'\Phi' + N_t Pr(\theta')^2 - Pr\zeta(1 - \zeta) \frac{\partial\theta}{\partial \zeta} \right\} d\Omega_e = 0 \tag{30}$$

$$\int_{\Omega_e} w_{f_5} \left\{ \Phi'' - \frac{\eta}{2} Le(\zeta - 1)\Phi' + Le(\zeta F\Phi' + \frac{N_t}{LeN_b}(\theta'')^2 + (\zeta - 1)\zeta \frac{\partial\Phi}{\partial \zeta}) \right\} d\Omega_e = 0 \tag{31}$$

$$\int_{\Omega_e} w_{f_6} \left\{ \chi'' + \frac{Lb}{2}(1 - \zeta)\eta\chi' + \zeta LbF\chi' - Pe \left(\Phi''(\delta_1 + \chi) + \chi'\Phi' \right) - \zeta(1 - \zeta)Lb \frac{\partial\chi}{\partial \zeta} \right\} d\Omega_e = 0. \tag{32}$$

Here w_{f_s} ($s = 1, 2, 3, 4, 5, 6$) stand for trial functions. Let the domain (Ω_e) be divided into 4-nodded elements. The associated approximations of the finite element are:

$$F = \sum_{j=1}^t [\hat{F}_j Y_j(\zeta, \eta)], P = \sum_{j=1}^t [\hat{P}_j Y_j(\zeta, \eta)], G = \sum_{j=1}^t [\hat{G}_j Y_j(\zeta, \eta)], \theta = \sum_{j=1}^t [\hat{\theta}_j Y_j(\zeta, \eta)], \Phi = \sum_{j=1}^t [\hat{\Phi}_j Y_j(\zeta, \eta)]. \tag{33}$$

here, Y_j ($j = 1, 2, 3, 4$) and $t = 4$ For Ω_e , the linear-interpolation key functions are defined as follows:.

$$\left. \begin{aligned} Y_1 &= \frac{(\zeta_{e+1} - \zeta)(\eta_{e+1} - \eta)}{(\zeta_{e+1} - \zeta_e)(\eta_{e+1} - \eta_e)}, Y_2 = \frac{(\zeta - \zeta_e)(\eta_{e+1} - \eta)}{(\zeta_{e+1} - \zeta_e)(\eta_{e+1} - \eta_e)} \\ Y_3 &= \frac{(\zeta - \zeta_e)(\eta - \eta_e)}{(\zeta_{e+1} - \zeta_e)(\eta_{e+1} - \eta_e)}, Y_4 = \frac{(\zeta_{e+1} - \zeta)(\eta - \eta_e)}{(\zeta_{e+1} - \zeta_e)(\eta_{e+1} - \eta_e)} \end{aligned} \right\} \tag{34}$$

Therefore, the stiffness element matrix, matrix of unknowns and the force vector/matrix for the finite element model are followed as:

$$\begin{bmatrix} [L^{11}] & [L^{12}] & [L^{13}] & [L^{14}] & [L^{15}] & [L^{16}] \\ [L^{21}] & [L^{22}] & [L^{23}] & [L^{24}] & [L^{25}] & [L^{26}] \\ [L^{31}] & [L^{32}] & [L^{33}] & [L^{34}] & [L^{35}] & [L^{36}] \\ [L^{41}] & [L^{42}] & [L^{43}] & [L^{44}] & [L^{45}] & [L^{46}] \\ [L^{51}] & [L^{52}] & [L^{53}] & [L^{54}] & [L^{55}] & [L^{56}] \\ [L^{61}] & [L^{62}] & [L^{63}] & [L^{64}] & [L^{65}] & [L^{66}] \end{bmatrix} \begin{bmatrix} \{F\} \\ \{P\} \\ \{G\} \\ \{\theta\} \\ \{\Phi\} \\ \{\chi\} \end{bmatrix} = \begin{bmatrix} \{R_1\} \\ \{R_2\} \\ \{R_3\} \\ \{R_4\} \\ \{R_5\} \\ \{R_6\} \end{bmatrix} \tag{35}$$

where $[L_{mn}]$ and $[R_m]$ ($m, n = 1, 2, 3, 4, 5, 6$) are expressed as:

$$\begin{aligned}
 L_{ij}^{11} &= \int_{\Omega_e} Y_i \frac{dY_j}{d\eta} d\Omega_e, L_{ij}^{12} = - \int_{\Omega_e} Y_i Y_j d\Omega_e, L_{ij}^{13} = L_{ij}^{14} = L_{ij}^{15} = L_{ij}^{21} = L_{ij}^{24} = L_{ij}^{25} = L_{ij}^{26} = 0, \\
 L_{ij}^{22} &= - \int_{\Omega_e} \frac{dY_i}{d\eta} \frac{dY_j}{d\eta} d\Omega_e + \frac{1}{2}(1-\zeta)\eta \int_{\Omega_e} Y_i \frac{dY_j}{d\eta} d\Omega_e + \zeta \int_{\Omega_e} \bar{F} Y_i \frac{dY_j}{d\eta} d\Omega_e - \zeta \int_{\Omega_e} \bar{P} Y_i Y_j d\Omega_e - \zeta(1-\zeta) \int_{\Omega_e} Y_i \frac{dY_j}{d\zeta} d\Omega_e \\
 &+ 2\beta\zeta \int_{\Omega_e} \bar{F} \bar{P} Y_i \frac{dY_j}{d\eta} d\Omega_e + \beta\zeta \int_{\Omega_e} \bar{F}^2 \frac{dY_i}{d\eta} \frac{dY_j}{d\eta} d\Omega_e - M^2\zeta \int_{\Omega_e} Y_i Y_j d\Omega_e, L_{ij}^{23} = 2\lambda\zeta \int_{\Omega_e} Y_i Y_j d\Omega_e \\
 &- 2\beta\lambda \int_{\Omega_e} \zeta \bar{F} Y_i \frac{dY_j}{d\eta} d\Omega_e, L_{ij}^{31} = L_{ij}^{34} = L_{ij}^{35} = L_{ij}^{36} = 0, L_{ij}^{32} = 2\lambda\zeta \int_{\Omega_e} Y_i Y_j d\Omega_e - 2\lambda\beta \int_{\Omega_e} \zeta \bar{F} Y_i \frac{dY_j}{d\eta} d\Omega_e, \\
 L_{ij}^{33} &= - \int_{\Omega_e} \frac{dY_i}{d\eta} \frac{dY_j}{d\eta} d\Omega_e + \frac{1}{2}(1-\zeta)\eta \int_{\Omega_e} Y_i \frac{dY_j}{d\eta} d\Omega_e + \zeta \int_{\Omega_e} \bar{F} Y_i \frac{dY_j}{d\eta} d\Omega_e - \zeta \int_{\Omega_e} \bar{P} Y_i Y_j d\Omega_e - \zeta(1-\zeta) \int_{\Omega_e} Y_i \frac{dY_j}{d\zeta} d\Omega_e \\
 &+ 2\beta\zeta \int_{\Omega_e} \bar{F} \bar{P} Y_i \frac{dY_j}{d\eta} d\Omega_e + \beta\zeta \int_{\Omega_e} \bar{F}^2 \frac{dY_i}{d\eta} \frac{dY_j}{d\eta} d\Omega_e - 2\lambda\beta \int_{\Omega_e} \zeta \bar{G} Y_i Y_j d\Omega_e, L_{ij}^{41} = L_{ij}^{42} = L_{ij}^{43} = 0, \\
 L_{ij}^{44} &= - \int_{\Omega_e} \frac{dY_i}{d\eta} \frac{dY_j}{d\eta} d\Omega_e + \frac{Pr}{2}(1-\zeta)\eta \int_{\Omega_e} Y_i \frac{dY_j}{d\eta} d\Omega_e + Pr\zeta \int_{\Omega_e} \bar{F} Y_i \frac{dY_j}{d\eta} d\Omega_e + PrN_b \int_{\Omega_e} \bar{\Phi}' Y_i \frac{dY_j}{d\eta} d\Omega_e \\
 &+ PrN_t \int_{\Omega_e} \bar{\theta}' Y_i \frac{dY_j}{d\eta} d\Omega_e - Pr\zeta(1-\zeta) \int_{\Omega_e} Y_i \frac{dY_j}{d\zeta} d\Omega_e, L_{ij}^{45} = L_{ij}^{46} = L_{ij}^{51} = L_{ij}^{52} = L_{ij}^{53} = L_{ij}^{56} = 0, \\
 L_{ij}^{54} &= - \frac{N_t}{N_b} \int_{\Omega_e} \frac{dY_i}{d\eta} \frac{dY_j}{d\eta} d\Omega_e, L_{ij}^{55} = - \int_{\Omega_e} \frac{dY_i}{d\eta} \frac{dY_j}{d\eta} d\Omega_e + \frac{Le}{2}(1-\zeta)\eta \int_{\Omega_e} Y_i \frac{dY_j}{d\eta} d\Omega_e + Le\zeta \int_{\Omega_e} \bar{F} Y_i \frac{dY_j}{d\eta} d\Omega_e \\
 &- Le\zeta(1-\zeta) \int_{\Omega_e} Y_i \frac{dY_j}{d\zeta} d\Omega_e, L_{ij}^{61} = L_{ij}^{62} = L_{ij}^{63} = L_{ij}^{64} = 0, \\
 L_{ij}^{65} &= -Pe\delta_1 \int_{\Omega_e} \frac{dY_i}{d\eta} \frac{dY_j}{d\eta} d\Omega_e, L_{ij}^{66} = - \int_{\Omega_e} \frac{dY_i}{d\eta} \frac{dY_j}{d\eta} d\Omega_e + \frac{Lb}{2}(1-\zeta)\eta \int_{\Omega_e} Y_i \frac{dY_j}{d\eta} d\Omega_e + Lb\zeta \int_{\Omega_e} \bar{F} Y_i \frac{dY_j}{d\eta} d\Omega_e \\
 &- Pe \int_{\Omega_e} \bar{\Phi}' Y_i \frac{dY_j}{d\eta} d\Omega_e - Pe \int_{\Omega_e} \bar{\Phi}'' Y_i d\varphi_j d\Omega_e - Lb\zeta(1-\zeta) \int_{\Omega_e} Y_i \frac{dY_j}{d\zeta} d\Omega_e,
 \end{aligned}$$

and

$$\begin{aligned}
 R_i^1 &= \Gamma, R_i^2 = - \oint_{\Gamma_e} Y_i n_\eta \frac{\partial P}{\partial \eta} ds, R_i^3 = - \oint_{\Gamma_e} Y_i n_\eta \frac{\partial G}{\partial \eta} ds, R_i^4 = - \oint_{\Gamma_e} Y_i n_\eta \frac{\partial \theta}{\partial \eta} ds, \\
 R_i^5 &= - \oint_{\Gamma_e} Y_i n_\eta \frac{\partial \Phi}{\partial \eta} ds - \frac{Nt}{Nb} \oint_{\Gamma_e} Y_i n_\eta \frac{\partial \theta}{\partial \eta} ds, R_i^6 = - \oint_{\Gamma_e} Y_i n_\eta \frac{\partial \chi}{\partial \eta} ds. \tag{36}
 \end{aligned}$$

Here, $\bar{F} = \sum_{j=1}^t (\bar{F}_j Y_j)$, $\bar{G} = \sum_{j=1}^t (\bar{G}_j Y_j)$, $\bar{P} = \sum_{j=1}^t (\bar{P}_j Y_j)$, $\bar{\theta}' = \sum_{j=1}^t (\bar{\theta}'_j Y_j)$, and $\bar{\Phi}' = \sum_{j=1}^t (\bar{\Phi}'_j Y_j)$ are key values that are probably supposed to be renowned. In order to linearize the acquired 61,206 equations with the 10^{-5} needed precision, we perform six function evaluations at each node.

4. Results and Discussion

This section describes through FE analysis how suction/injection impacts the mechanisms of a Maxwell spinning fluid when it is impacted by the Coriolis effect, magneto-hydrodynamic effects, and micro-organisms. Three different patterns of arcs are mapped on fluctuating values of the intravenous injection/suction (Γ) factor for every figure

for these significant quantities, as follows: ($\Gamma = -0.2$) (suction), ($\Gamma = 0.0$) (static), and ($\Gamma = 0.2$) (injection). The following are the predefined values for the parameters involved: $\beta = 0.1$, $\lambda = 1.0 = M$, $N_b = 0.2 = N_t$, $Le = 10$, $Pr = Lb = 5.0$, $Pe = 0.5$, $\delta_1 = 0.2$. An analysis of mesh separation is executed to show that the finite element simulations are accurate. The entire zone is split into various grid concentrations of mesh sizes, and there is no further modification after (100×100) has been observed, so all simulations are based on this mesh size (Table 1). For distinctive scenarios, comparisons with previous research are provided in Tables 2 and 3 to determine the remedy methodology’s accuracy. In certain restrictive instances, it is observed that the existing mathematical evaluations correlate very well with the current investigation. The friction coefficient, as well as the axial and transverse indications $-F''(0)$, $-G(0)$, are calculated using finite element analysis and are summarized in Table 2 for various values of the rotatory factor (λ) = 0.0, 1.0, 2.0, 5.0 when (ζ) = 1. The table shows that the computational findings achieved are consistent with the results reported by [52,53]. Furthermore, in Table 3, the Nusselt quantity $-\theta(0)$ outputs are consistent with those reported by Bagh et al. [54] and Mustafa et al. [55], who present FEA findings for a variety of values β , λ , Pr , and determine that they are satisfactorily correlated. As a result, certainty in statistical computing is increased, and it is confirmed that the finite element evaluations obtained using the Matlab program show a strong rate of convergence.

Table 1. Meshing analysis for various mesh dimensions when $\zeta = 1.0$.

Grid Size	$-F''(\zeta, 0)$	$-G'(\zeta, 0)$	$-\theta'(\zeta, 0)$	$-\Phi'(\zeta, 0)$	$-\chi'(\zeta, 0)$
15 × 15	1.7050	0.6876	0.6954	3.7399	4.5771
40 × 40	1.6946	0.6764	0.7399	3.4025	4.8073
70 × 70	1.6935	0.6742	0.7538	3.3371	4.7750
100 × 100	1.6932	0.6736	0.7556	3.3265	4.7565
120 × 120	1.6931	0.6736	0.7558	3.3264	4.7562

Table 2. Assessment of $-F''(0)$ and $-G'(0)$ for different values of λ when $\zeta = 1$ and other parameters are fixed at zero.

λ	Ali [52]		Wang [53]		Present Results	
	$-F''(0)$	$-G'(0)$	$-F''(0)$	$-G'(0)$	$-F''(0)$	$-G'(0)$
0	01.00000	00.00000	01.0000	00.0000	01.00000	00.00000
1	01.32501	00.83715	01.3250	00.8371	01.32501	00.83715
2	01.65232	01.28732	01.6523	01.2873	01.65232	01.28732
5	02.39026	02.15024	–	–	02.39026	02.15024

Table 3. Assessment of $\{-\theta'(0)\}$ at $\zeta = 1$ at various values of Pr , λ and other parameters are fixed at zero.

Pr	β	λ	Ali [54]	Shafique [55]	Present Results (FEM)
1.0	0.20	0.2	00.546683	00.54670	00.5466828
–	0.40	–	00.528090	00.52809	00.5280903
–	0.60	–	–	00.51009	00.5100870
–	0.80	–	00.492547	00.49255	00.4925468

4.1. Variations of Velocity Profiles

Figures 2–5 illustrate the primary and secondary velocity dispersion for various values of the magnetism factor, rotating factor, unsteady factor, and meditation Deborah quantity. Figure 2a,b illustrates the effect of various values of the magnetism factor on the velocity profiles $G'(\zeta, \eta)$ and $F'(\zeta, \eta)$. The presence of frictional factors in the context of a Lorentz effect is caused by the incorporation of a stimulating external magnetization and results in the transverse momentum declines shown in Figure 2a, whereas the axial momentum exhibits

an inverse relation, as shown in Figure 2b. The axial $F'(\zeta, \eta)$ and transverse $G'(\zeta, \eta)$ for various rotating parametric inputs are shown in Figure 3a,b. Figure 3a shows that the Coriolis force causes the transverse momentum to decrease for increasing values of the rotation factor, whereas Figure 3b demonstrates the reverse effect. Figure 4a,b show that the size and thickness of the momentum fluid layers in the axial position increase as the time factor increases, while the viscosity of the momentum fluid layers in the transverse path decreases as the time factor decreases. As a result, it is clear that the unsteadiness factor is crucial for influencing the transverse momentum. Physically, a reduced quantity of fluids is pinched axially with the enhanced viscoelastic effects and fluid is pushed away in a radial direction. Figure 5a,b shows that the Deborah quantity is (β) over the velocity profiles for various values of the tranquility factor. The presence of thermoelastic impacts in the context of delivering the best results in a deflation of the building of transverse momentum is shown in Figure 5a, whereas the tangential momentum exhibits an inverse correlation, as shown in Figure 5b. The increasing relative strength of the rheological effect is associated with a higher meditation quantity, resulting in a decrease in velocity. Additionally, these graphs demonstrate that the $F'(\zeta, \eta)$ profile decreases with increase in $\Gamma = 0.2$ (injection), but is significantly increased when $\Gamma = -0.2$ (suction).

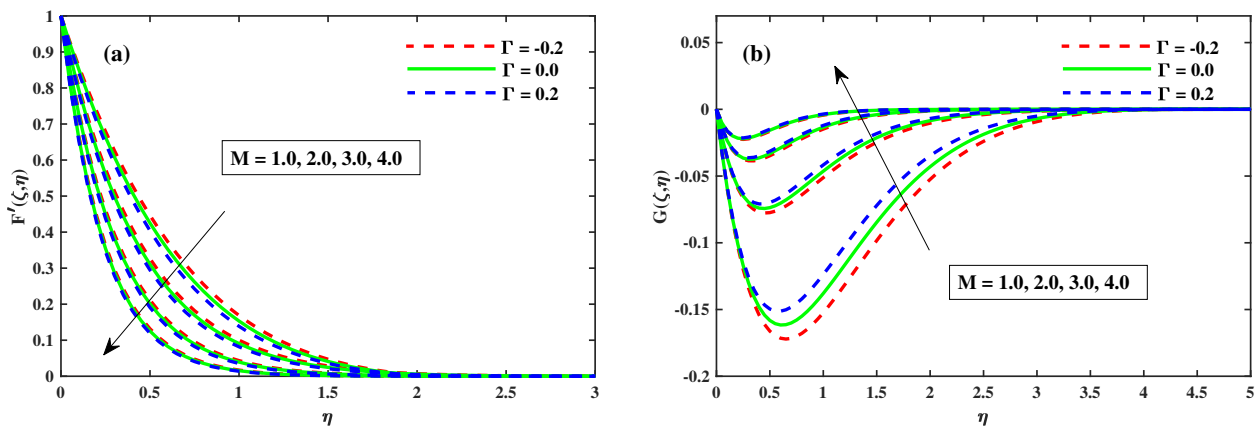


Figure 2. Influence of M on G along y -direction in (b), and F' along x -direction in (a) when $\zeta = 1$.

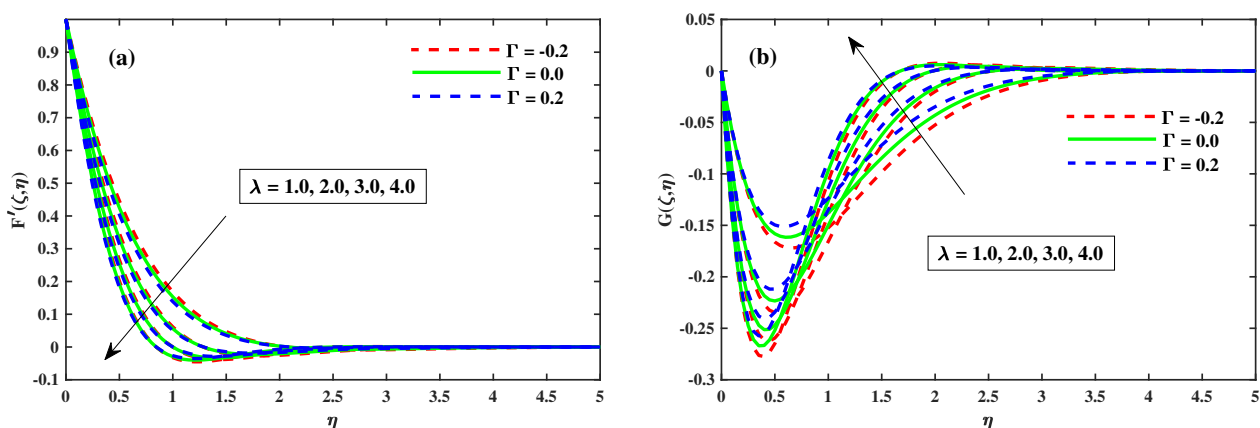


Figure 3. Influence of λ on G along y -direction in (b) and F' along x -direction in (a) when $\zeta = 1$.

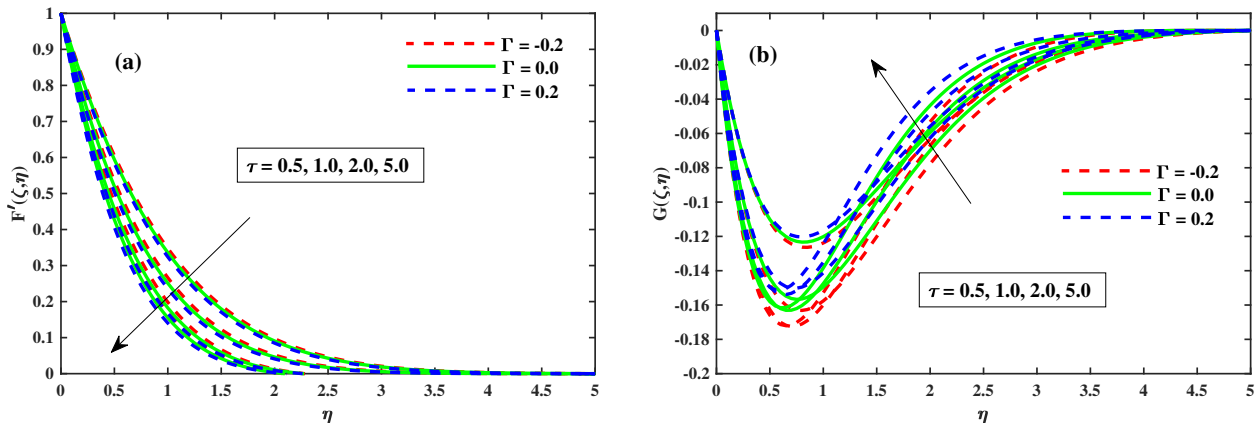


Figure 4. Influence of τ on G along y-direction in (b) and F' along x-direction in (a) when $\zeta = 1$.

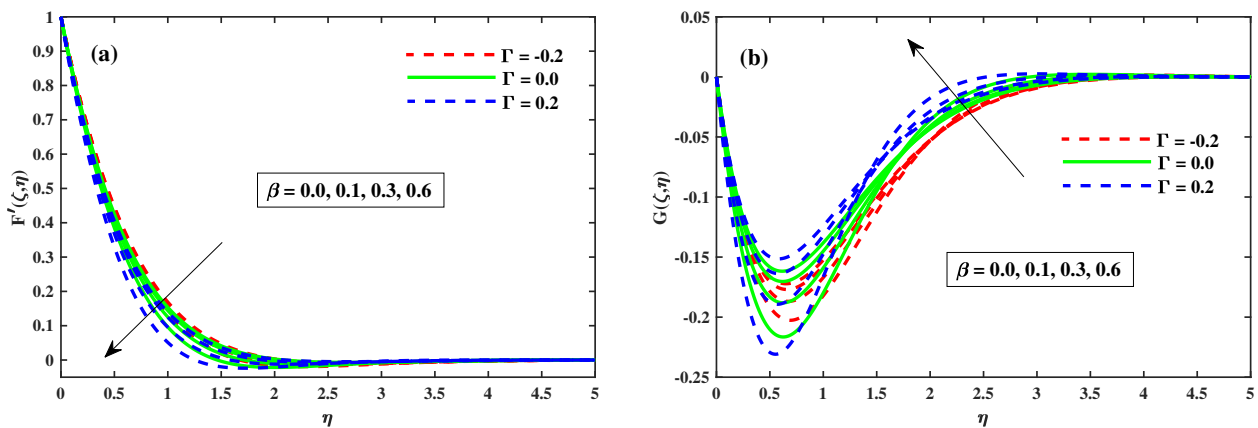


Figure 5. Influence of β on G along y-direction in (b) and F' along x-direction in (a) when $\zeta = 1$.

Figure 6a,b shows the graphics of $C_{f_x} \sqrt{Re_x}$ (friction factor) across the transverse and $C_{f_y} \sqrt{Re_x}$ (axial direction) closer to the surface for the $\zeta(0 : 0.2 : 1)$ spectrum and for $M(1 : 1 : 5)$. As shown in Figure 6a, increasing $\zeta(0 \rightarrow 1)$ gradually increases the spread of $(C_{f_x} \sqrt{Re_x})$ until no significant difference is observed. In contrast, the $(C_{f_x} \sqrt{Re_x})$ value adjacent to the plate substrate decreases significantly when M is increased. Figure 6b shows that when boosting $\zeta(0 \rightarrow 1)$, the spread of $(C_{f_x} \sqrt{Re_x})$ changes steadily up to a consistent rate, and then there is no significant variation, whereas M continues to increase. A large discrepancy in values adjacent to the surface of the sheet, $(C_{f_y} \sqrt{Re_x})$ can be observed. Physically, the application of a magnetic field normal to the direction of fluid flow gives rise to a force known as Lorentz force. Figure 7a,b shows that the dispersion of $(C_{f_x} \sqrt{Re_x})$ tends to increase at a consistent rate up to a certain point, after which no significant variation for enhancing $\zeta(0 \rightarrow 1)$ occurs. When λ increases, however, there is a substantial decrease in $(C_{f_x} \sqrt{Re_x})$. When $\zeta(0 \rightarrow 1)$ is enhanced, the dissemination of $(C_{f_x} \sqrt{Re_x})$ is substantially decreased until no significant change is detected, as shown in Figure 7b, while λ is increased. Furthermore, it is apparent from these infographics that the basic values of $(C_{f_x} \sqrt{Re_x})$ and $(C_{f_y} \sqrt{Re_x})$ for the scenario of $\Gamma = 0.2$ (injection) are smaller than those for the scenario of $\Gamma = -0.2$ (suction).

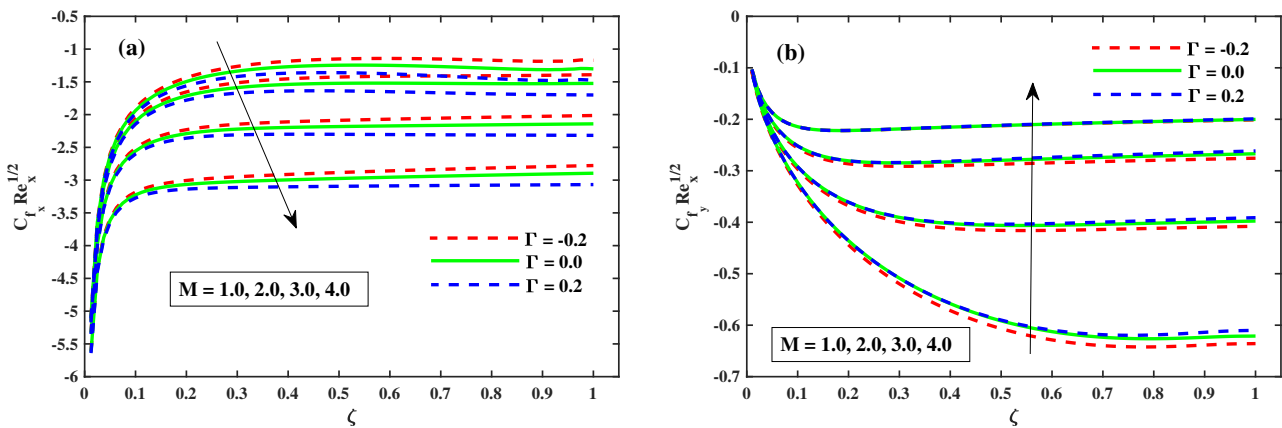


Figure 6. Influence of M on $Cf_x Re_x^{1/2}$ along x-direction in (a), and $Cf_y Re_y^{1/2}$ along y-direction in (b).

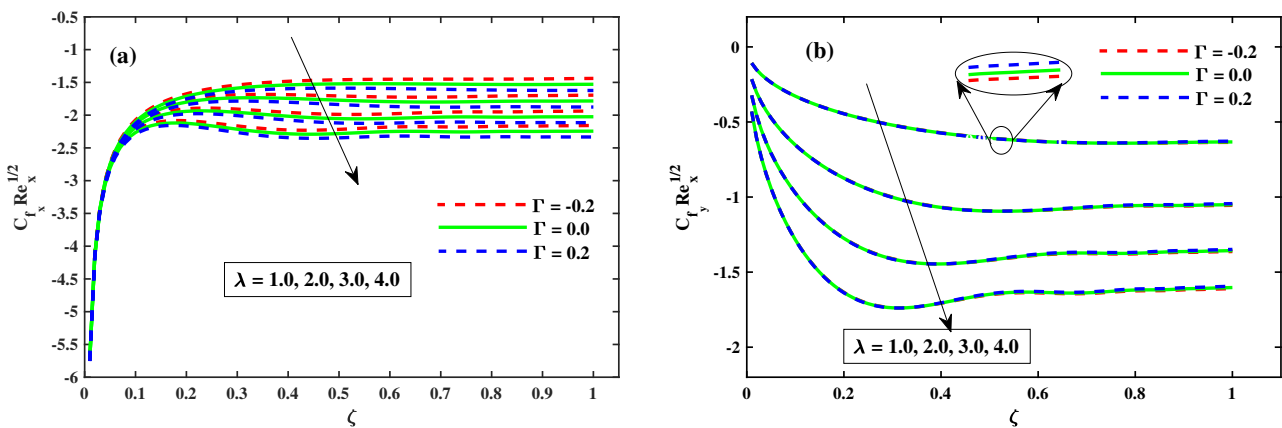


Figure 7. Impact of λ of $Cf_x Re_x^{1/2}$ along x-direction in (a), and $Cf_y Re_y^{1/2}$ along y-direction in (b).

4.2. Temperature Profiles

Figures 8–10 illustrate the $\theta(\zeta, \eta)$ dissemination when varying the factors involved. The thermal configurations in Figure 8 are enhanced by the magnetic field factor. The cumulative induced resultant force, also known as the resistor Lorentz force, governs the flow momentum between the externally applied magnetic effect and the inner electromagnetic force, as shown in Figure 8a, whereas the wall thickness of the heat transfer performance increases with increasing λ , as shown in Figure 8b. Figure 8a,b show how the thermophoretic factor (N_t) and the Brownian motion factor (N_b) affect the temperature profile. The dispersion of the temperature profile appears to grow as N_b and N_t inclines. Physically, N_t apply a force on the neighbour particles, the force moving the particles from a hot region to a cold region. Figure 10a,b show the impact of (β) and the time-dependent (τ) on the temperature profile. The tranquility of Deborah's number and the unsteady factor are enhanced, as are the $\theta(\zeta, \eta)$ profiles. Furthermore, it can be seen from these graphs that the temperature decreases with the intensity of $\Gamma = 0.2$ (injection), while increasing with the $\Gamma = -0.2$ (suction) factor. Illustrations of the Nusselt quantity ($Nu_x Re_x^{1/2}$) at $(0.1 : 0.1 : 0.3) N_t \& N_b$ for $M \& \lambda$ are shown in Figure 11a,b. The dispersion of $(Nu_x \sqrt{Re_x})$ decreases subsequently as M and λ are accelerated. For increasing values of $N_t \& N_b$, a substantial deterioration in $(Nu_x \sqrt{Re_x})$ occurs close to the panel substrate. Additionally, the figure indicates that for $\Gamma = 0.2$ (injection) there is a relatively large quantity of $(Nu_x \sqrt{Re_x})$.

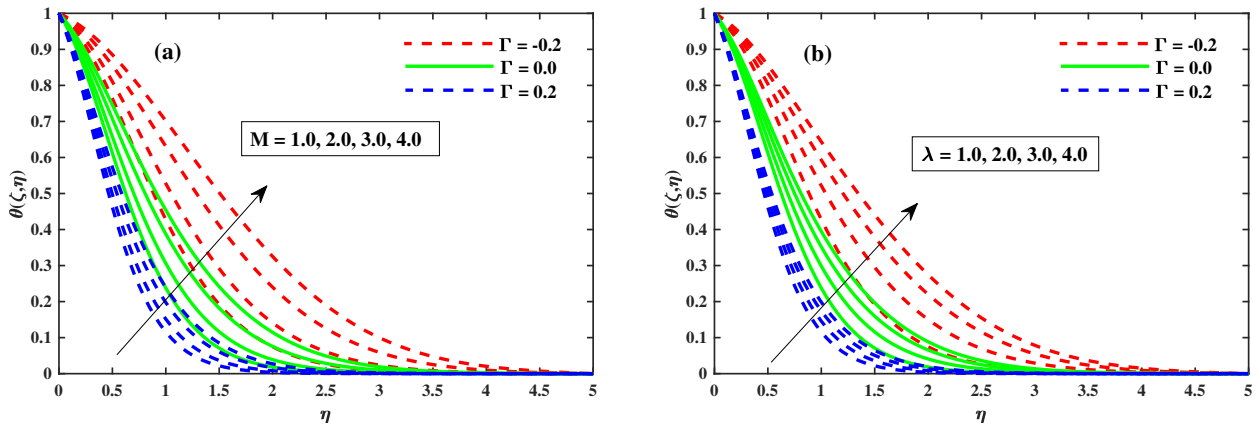


Figure 8. Variation of $\theta(\zeta, \eta)$ for M in (a) and for λ in (b) when $\zeta = 1$.

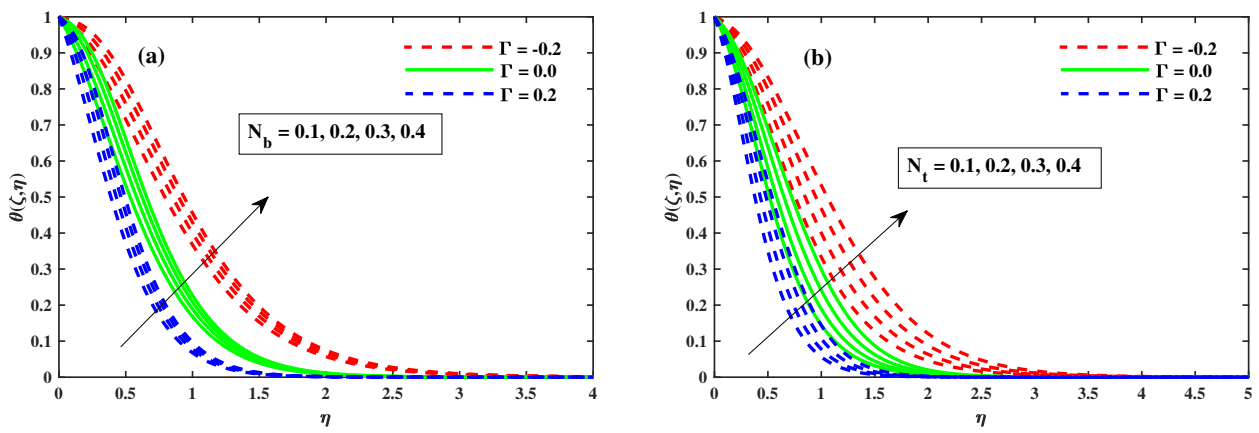


Figure 9. Influence of N_b in (a) and N_t in (b) on the temperature profiles.

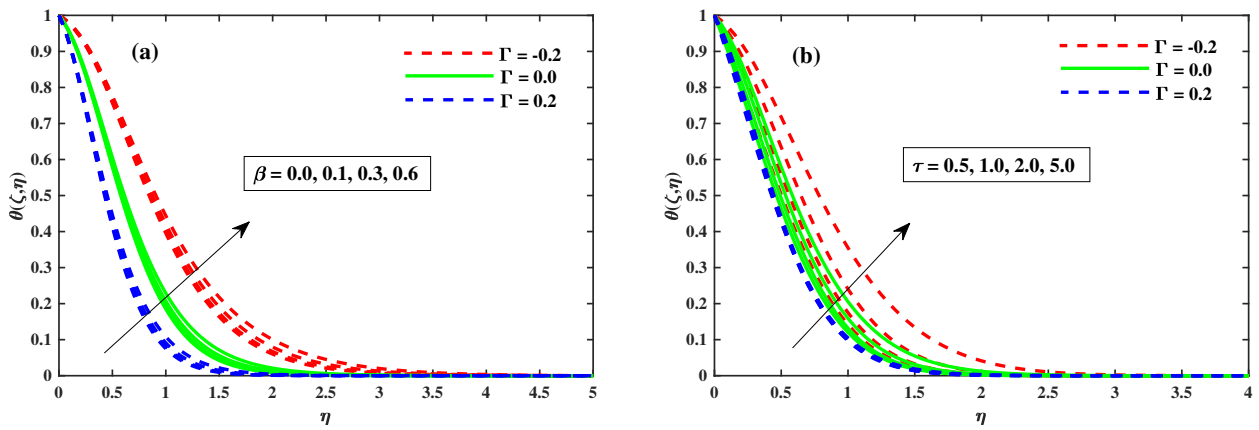


Figure 10. The variation of temperature against β in (a) and for τ in (b).

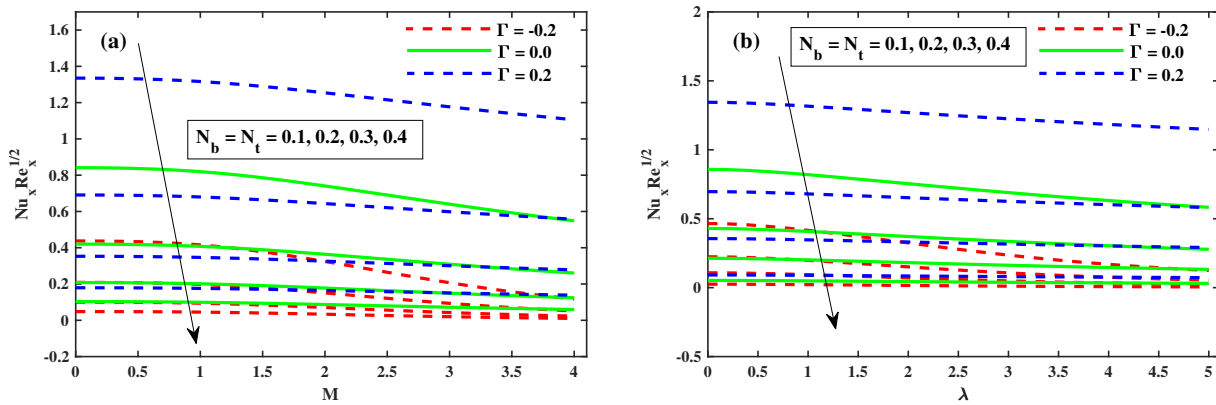


Figure 11. The variation of Nusselt number with N_b, N_t against M in (a) and against λ in (b).

4.3. Concentration Distributions

Figure 12a,b illustrates that $\Phi(\zeta, \eta)$ varies with the magnetic M , the rotating factor λ , the Lewis Le , and the Deborah number (β). The concentration profiles are augmented as the magnetic field, rotating field, and relaxation Deborah parameters are enhanced, as illustrated in Figures 12a,b and 13b, respectively. Furthermore, Figure 13a demonstrates that deterioration in the organism’s density increases the Lewis number Le . Physically, a high Lewis number corresponds to a low mass diffusivity, causing the species concentration in the nanofluid to decrease. Figure 14a,b show the progressive behavioural patterns of the local Sherwood number ($Shr_x \sqrt{Re_x}$) at $(0.1 : 0.1 : 0.3) Nt \& Nb$ for $M(0 : 1 : 5) \& \lambda(0 : 1 : 5)$. The dispersion of ($Shr_x \sqrt{Re_x}$) is reduced as M and λ are increased. In the case of enhancing $Nt \& Nb$, however, a conflicting pattern is observed, and the $\Gamma = 0.2$ (injection) scenario is higher ($Shr_x \sqrt{Re_x}$) than the $\Gamma = -0.2$ (suction) specific case. Figures 15 and 16a,b show $\chi(\zeta, \eta)$ for variation in M , the rotating parameter λ , the bioconvection Lewis number Lb , and the Peclet number (Pe). The microbe dispersion profile is intensified as the magnetic factor M and rotation factor λ inputs increase, and it notably tumbles in the context of the bioconvection Lewis number Lb and the Peclet number (Pe) (see Figure 16a,b). Furthermore, it can be seen in the infographics that the microbe dispersion profile $\chi(\zeta, \eta)$ decreases when the $\Gamma = 0.2$ (injection) parameter is used, but it is fractionally increased when the $\Gamma = -0.2$ (suction) factor is used. Figure 17a,b shows the trend in the microbe concentration quantity $Re_x^{1/2} N_x$ for $M(0 : 1 : 5) \& \lambda(0 : 1 : 5)$ at $Nt \& Nb(0.1 : 0.1 : 0.3)$, respectively. The $Re_x^{1/2} N_x$ decreases as M and λ increase, whereas the $Re_x^{1/2} N_x$ increases as $Nt \& Nb$ increase. It is also observed that for $\Gamma = 0.2$ (injection), $Re_x^{1/2} N_x$ is higher than for $\Gamma = -0.2$ (suction).

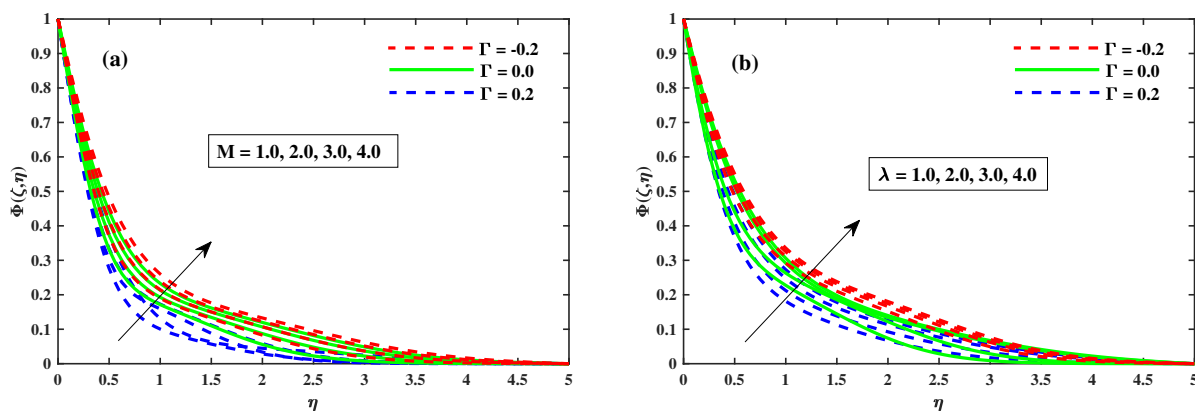


Figure 12. Variation in $\Phi(\zeta, \eta)$ for M in (a) and for λ in (b) when $\zeta = 1$.

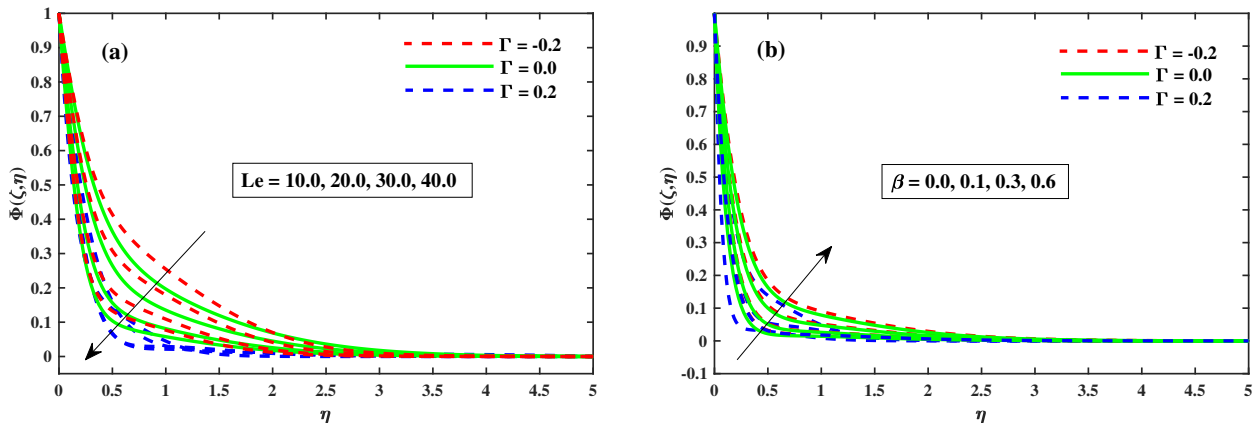


Figure 13. The variation in $\Phi(\zeta, \eta)$ against Le in (a) and for β in (b).

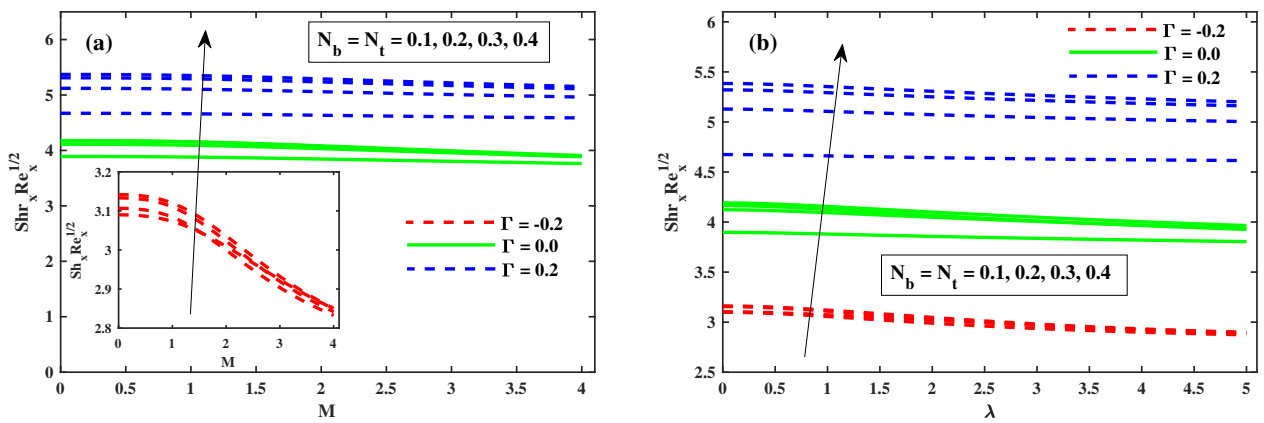


Figure 14. The effect of N_b, N_t for M in (a) and for λ in (b) on Sherwood number.

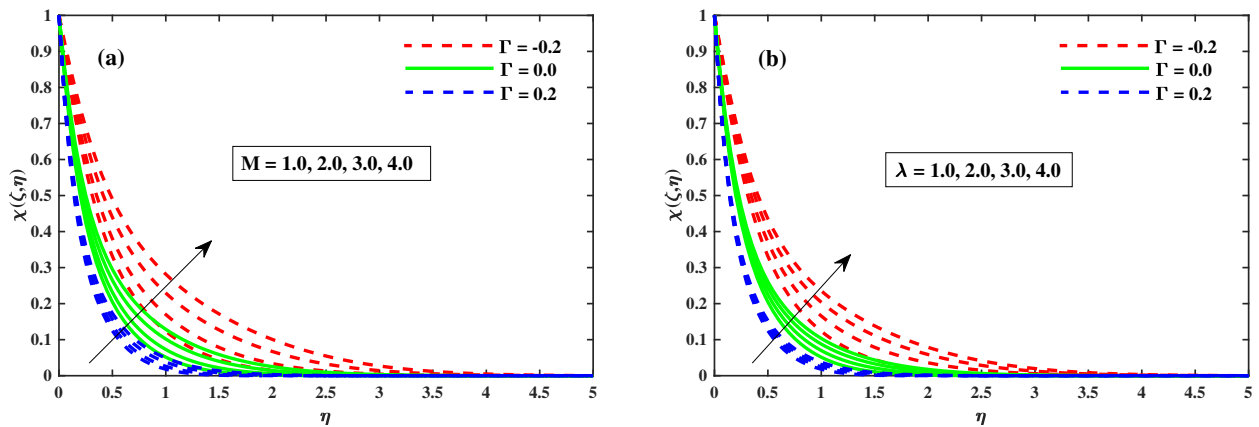


Figure 15. Influence of M in (a) and λ in (b) on $\chi(\zeta, \eta)$ when $\zeta = 1$.

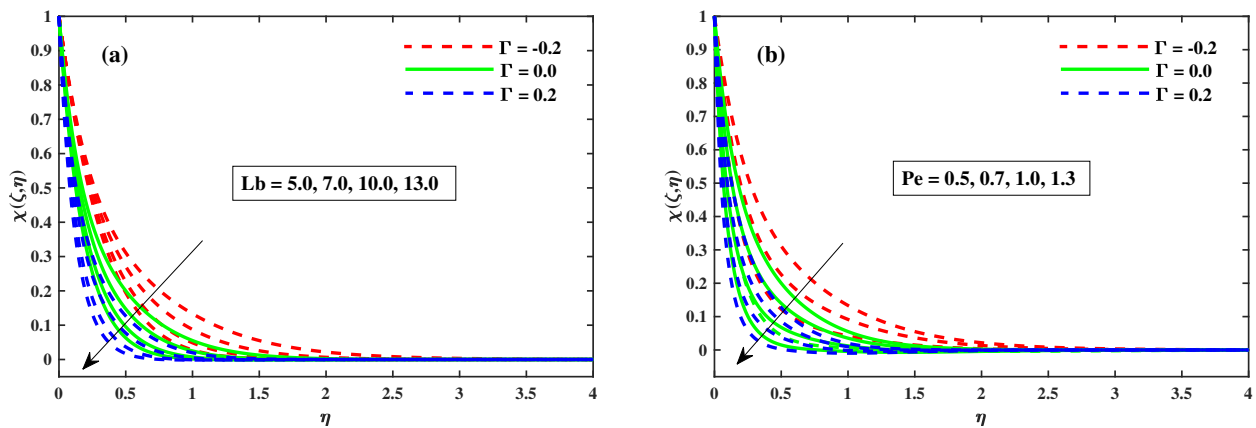


Figure 16. Impact of Lb in (a) and Pe in (b) on $\chi(\zeta, \eta)$ at $\zeta = 1$.

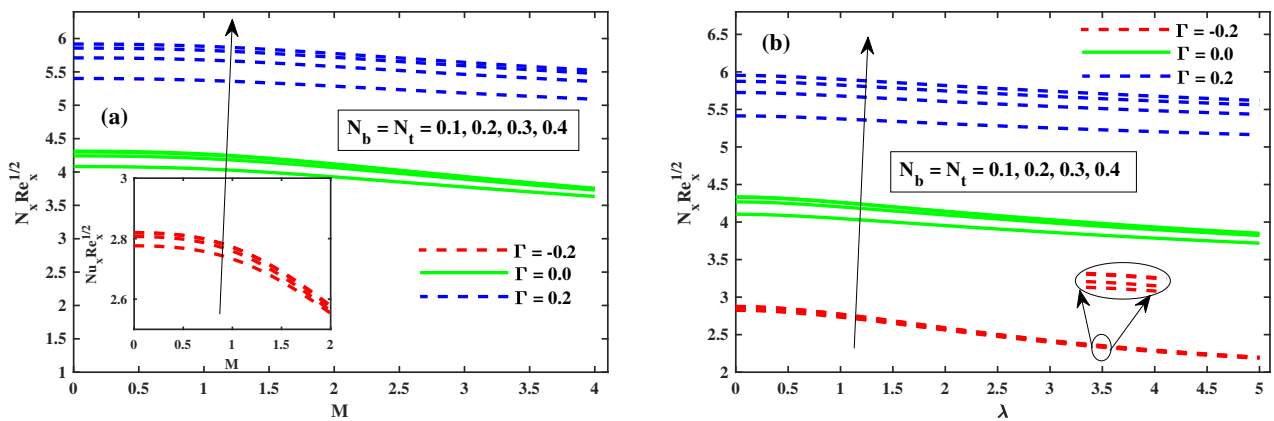


Figure 17. Fluctuation in $N_x Re_x^{1/2}$ for N_b, N_t , along M in (a) and along λ in (b).

5. Concluding Remarks

In this article, a finite element simulation was exploited to investigate Maxwell nanofluid flows over a bidirectional elongating surface with bio-convection, suction/injection, Coriolis, and Lorentz forces for three-dimensional spinning flow. Based on the results, the following inferences can be made:

1. Increase in the Coriolis and Lorentz's forces has a decreasing impact on the velocity magnitude, and
 - has a significant influence on the temperature dispersion and concentration.
 - intensifies the impact of $Cf_x Re_x^{1/2}$.
 - the Coriolis force causes the transverse momentum to decrease for increasing values of the rotation factor.
 - with the infusion capability, the velocity, temperature, and concentration components are reduced.
2. It is becoming increasingly evident that the simultaneous enhancement of Brownian and thermophoresis factors has a negative effect on the distribution of temperature, and
 - a declining impact on $Nu_x Re_x^{1/2}$, and positive effects on $Shr_x Re_x^{1/2}$.
 - injection is associated with a larger amount in $Nu_x Re_x^{1/2}$.
 - the injection case has a larger $Shr_x Re_x^{1/2}$ and $Re_x^{1/2} N_x$ compared to the suction case.

- the wall thickness of the heat transfer performance increases with increasing rotating parameter.
3. Higher input to the relaxation Deborah number and the unsteady parameter has a negative impact on the magnitude of the primary and secondary velocity, but
 - has substantial consequences for temperature dispersion.
 - for tiny particles, the volume fraction shows rising effects with higher relaxation Deborah number.
 4. Motile microorganism viscosity reduces in the context of augmented bioconvection Peclet and Lewis numbers

This study has involved an analysis of the parameters that their impact on dynamic of fluid flow problems and can be extended in future to include Blasius and Sakiadis flow, and Darcy–Forchheimer and thermoelastic Jeffrey nanofluids.

Author Contributions: L.A. writing—original draft preparation, resources, formal analysis, validation, project administration; A.M. review and editing, investigation and B.A. thoroughly checked the mathematical modeling, corrections, validation. All authors finalized the manuscript after its internal evaluation. All authors have read and agreed to the published version of the manuscript.

Funding: This work is supported by the Xi’an Technological University, with scientific research start-up fund (Grant No. 0853-302020678) in support of this research project.

Data Availability Statement: Not applicable.

Acknowledgments: This work is supported by Xi’an Technological University. The authors would like to acknowledge and express their gratitude to the School of Sciences for their continuous support to work at Xi’an Technological University, Xi’an, China.

Conflicts of Interest: The authors declare no conflict of interest.

Nomenclature

The following abbreviations are used in this manuscript:

T	Non-dimensional temperature, K	T_w	Temperature at surface, K
T_∞	Temperature away from the surface, K	σ	Conductivity of fluid
D_T	Thermophoretic dispersion	U_w	Velocity, s^{-1}
Cf_x	Skin friction at x-direction	C_p	Specific heat
Cf_y	Skin friction at y-direction	B_0	Magnetic field strength
Nu_x	Nusselt number	ρ_f	Density of fluid, Kgm^{-3}
ν_f	Kinematic viscosity of fluid, $m^{-2}s^{-1}$	M	Magnetic parameter
C_p	Specific heat at constant pressure, $JKg^{-1}K^{-1}$	Ω	Rotating parameter
Pe	Peclet number	W_c	Optimum cell swimming
Re_x	Local Reynold number	f	Base fluid
β	Deborah number	Γ	Suction/injection
D_B	Brownian diffusion coefficient	Pr	Prandtl number
Nb	Brownian motion parameter	q_w	Surface heat flux, Wm^{-2}
N	Intensity of microbes	Le	Lewis number
ρ_p	Nanoparticle density	Nt	Thermophoresis parameter
τ_w	External heat transfer factor	Le	Lewis number

References

1. Ali, R.; Asjad, M.I.; Aldalbahi, A.; Rahimi-Gorji, M.; Rahaman, M. Convective flow of a Maxwell hybrid nanofluid due to pressure gradient in a channel. *J. Therm. Anal. Calorim.* **2020**, *43*, 1319–1329. [CrossRef]
2. Jawad, M.; Saeed, A.; Gul, T. Entropy Generation for MHD Maxwell Nanofluid Flow Past a Porous and Stretching Surface with Dufour and Soret Effects. *Braz. J. Phys.* **2021**, *13*, 469–480. [CrossRef]
3. Jamshed, W. Numerical investigation of MHD impact on maxwell nanofluid. *Int. Commun. Heat Mass Transf.* **2021**, *120*, 104973. [CrossRef]
4. Ali, L.; Ali, B.; Ghori, M.B. Melting effect on Cattaneo–Christov and thermal radiation features for aligned MHD nanofluid flow comprising microorganisms to leading edge: FEM approach. *Comput. Math. Appl.* **2022**, *109*, 260–269. [CrossRef]

5. Pal, D.; Mandal, G. Magneto-hydrodynamic nonlinear thermal radiative heat transfer of nanofluids over a flat plate in a porous medium in existence of variable thermal conductivity and chemical reaction. *Int. J. Ambient. Energy* **2021**, *42*, 1167–1177. [CrossRef]
6. Ahmed, A.; Khan, M.; Ahmed, J. Mixed convective flow of Maxwell nanofluid induced by vertically rotating cylinder. *Appl. Nanosci.* **2020**, *10*, 5179–5190. [CrossRef]
7. Pal, D.; Mandal, G. Hydromagnetic convective–radiative boundary layer flow of nanofluids induced by a non-linear vertical stretching/shrinking sheet with viscous–Ohmic dissipation. *Powder Technol.* **2015**, *279*, 61–74. [CrossRef]
8. Ahmad, B.; Ahmad, M.O.; Ali, L.; Ali, B.; Hussein, A.K.; Shah, N.A.; Chung, J.D. Significance of the Coriolis force on the dynamics of Carreau–Yasuda rotating nanofluid subject to Darcy–forchheimer and gyrotactic microorganisms. *Mathematics* **2022**, *10*, 2855. [CrossRef]
9. Ahmed, J.; Khan, M.; Ahmad, L. Stagnation point flow of Maxwell nanofluid over a permeable rotating disk with heat source/sink. *J. Mol. Liq.* **2019**, *287*, 110853. [CrossRef]
10. Bilal, S.; Ur Rehman, K.; Mustafa, Z.; Malik, M. Maxwell nanofluid flow individualities by way of rotating cone. *J. Nanofluids* **2019**, *8*, 596–603. [CrossRef]
11. Amirson, N.A.; Uddin, M.; Basir, M.F.M.; Ismail, A.; Beg, O.A.; Kadir, A. Three-dimensional bioconvection nanofluid flow from a bi-axial stretching sheet with anisotropic slip. *Sains Malays.* **2019**, *48*, 1137–1149. [CrossRef]
12. Prabhavathi, B.; Reddy, P.S.; Vijaya, R.B. Heat and mass transfer enhancement of SWCNTs and MWCNTs based Maxwell nanofluid flow over a vertical cone with slip effects. *Powder Technol.* **2018**, *340*, 253–263. [CrossRef]
13. Zohra, F.T.; Uddin, M.J.; Ismail, A.I. Magneto-hydrodynamic bio-nanoconvective Navier slip flow of micropolar fluid in a stretchable horizontal channel. *Heat Transf. Res.* **2019**, *48*, 3636–3656. [CrossRef]
14. Pal, D.; Mandal, G. Double diffusive magneto-hydrodynamic heat and mass transfer of nanofluids over a nonlinear stretching/shrinking sheet with viscous–Ohmic dissipation and thermal radiation. *Propuls. Power Res.* **2017**, *6*, 58–69. [CrossRef]
15. Ali, B.; Ali, L.; Abdal, S.; Asjad, M.I. Significance of Brownian motion and thermophoresis influence on dynamics of Reiner–Rivlin fluid over a disk with non-Fourier heat flux theory and gyrotactic microorganisms: A Numerical approach. *Phys. Scr.* **2021**, *96*, 94001. [CrossRef]
16. Mandal, G.; Pal, D. Entropy generation analysis of radiated magneto-hydrodynamic flow of carbon nanotubes nanofluids with variable conductivity and diffusivity subjected to chemical reaction. *J. Nanofluids* **2021**, *10*, 491–505. [CrossRef]
17. Ali, L.; Liu, X.; Ali, B.; Din, A.; Al Mdallal, Q. The function of nanoparticle’s diameter and Darcy–Forchheimer flow over a cylinder with effect of magnetic field and thermal radiation. *Case Stud. Therm. Eng.* **2021**, *28*, 101392. [CrossRef]
18. Mandal, G. Convective–radiative heat transfer of micropolar nanofluid over a vertical non-linear stretching sheet. *J. Nanofluids* **2016**, *5*, 852–860. [CrossRef]
19. Sreedevi, P.; Reddy, P.S.; Chamkha, A.J. Magneto-hydrodynamics heat and mass transfer analysis of single and multi-wall carbon nanotubes over vertical cone with convective boundary condition. *Int. J. Mech. Sci.* **2018**, *135*, 646–655. [CrossRef]
20. Ali, L.; Liu, X.; Ali, B. Finite Element Analysis of Variable Viscosity Impact on MHD Flow and Heat Transfer of Nanofluid Using the Cattaneo–Christov Model. *Coatings* **2020**, *10*, 395. [CrossRef]
21. Uddin, M.; Kabir, M.; Bég, O.A.; Alginahi, Y. Chebyshev collocation computation of magneto-bioconvection nanofluid flow over a wedge with multiple slips and magnetic induction. *Proc. Inst. Mech. Eng. Part N J. Nanomater. Nanoeng. Nanosyst.* **2018**, *232*, 109–122. [CrossRef]
22. Rout, B.; Mishra, S.; Thumma, T. Effect of viscous dissipation on Cu-water and Cu-kerosene nanofluids of axisymmetric radiative squeezing flow. *Heat Transf. Res.* **2019**, *48*, 3039–3054. [CrossRef]
23. Sheri, S.R.; Thumma, T. Numerical study of heat transfer enhancement in MHD free convection flow over vertical plate utilizing nanofluids. *Ain Shams Eng. J.* **2018**, *9*, 1169–1180. [CrossRef]
24. Thumma, T.; Mishra, S. Effect of viscous dissipation and Joule heating on magneto-hydrodynamic Jeffery nanofluid flow with and without multi slip boundary conditions. *J. Nanofluids* **2018**, *7*, 516–526. [CrossRef]
25. Bég, O.A.; Kabir, M.N.; Uddin, M.J.; Izani Md Ismail, A.; Alginahi, Y.M. Numerical investigation of Von Karman swirling bioconvective nanofluid transport from a rotating disk in a porous medium with Stefan blowing and anisotropic slip effects. *Proc. Inst. Mech. Eng. Part C J. Mech. Eng. Sci.* **2021**, *235*, 3933–3951. [CrossRef]
26. Chu, Y.M.; Aziz, S.; Khan, M.I.; Khan, S.U.; Nazeer, M.; Ahmad, I.; Tlili, I. Nonlinear radiative bioconvection flow of Maxwell nanofluid configured by bidirectional oscillatory moving surface with heat generation phenomenon. *Phys. Scr.* **2020**, *95*, 105007. [CrossRef]
27. Sreedevi, P.; Reddy, P.S. Combined influence of Brownian motion and thermophoresis on Maxwell three-dimensional nanofluid flow over stretching sheet with chemical reaction and thermal radiation. *J. Porous Media* **2020**, *4*, 23. [CrossRef]
28. Rao, M.V.S.; Gangadhar, K.; Chamkha, A.J.; Surekha, P. Bioconvection in a Convective Nanofluid Flow Containing Gyrotactic Microorganisms over an Isothermal Vertical Cone Embedded in a Porous Surface with Chemical Reactive Species. *Arab. J. Sci. Eng.* **2021**, *46*, 2493–2503. [CrossRef]
29. Awais, M.; Awan, S.E.; Raja, M.A.Z.; Parveen, N.; Khan, W.U.; Malik, M.Y.; He, Y. Effects of Variable Transport Properties on Heat and Mass Transfer in MHD Bioconvective Nanofluid Rheology with Gyrotactic Microorganisms: Numerical Approach. *Coatings* **2021**, *11*, 231. [CrossRef]

30. Sreedevi, P.; Sudarsana Reddy, P. Heat and mass transfer analysis of MWCNT-kerosene nanofluid flow over a wedge with thermal radiation. *Heat Transf.* **2021**, *50*, 10–33. [CrossRef]
31. Elayarani, M.; Shanmugapriya, M.; Kumar, P.S. Intensification of heat and mass transfer process in MHD Carreau nanofluid flow containing gyrotactic microorganisms. *Chem. Eng. Process. Process. Intensif.* **2021**, *160*, 108299. [CrossRef]
32. Ali, B.; Raju, C.; Ali, L.; Hussain, S.; Kamran, T. G-Jitter impact on magnetohydrodynamic non-Newtonian fluid over an inclined surface: Finite element simulation. *Chin. J. Phys.* **2021**, *71*, 479–491. [CrossRef]
33. Farooq, U.; Waqas, H.; Khan, M.I.; Khan, S.U.; Chu, Y.M.; Kadry, S. Thermally radioactive bioconvection flow of Carreau nanofluid with modified Cattaneo-Christov expressions and exponential space-based heat source. *Alex. Eng. J.* **2021**, *60*, 3073–3086. [CrossRef]
34. Alhussain, Z.A.; Renuka, A.; Muthamilselvan, M. A magneto-bioconvective and thermal conductivity enhancement in nanofluid flow containing gyrotactic microorganism. *Case Stud. Therm. Eng.* **2021**, *23*, 100809. [CrossRef]
35. Sreedevi, P.; Reddy, P.S. Effect of SWCNTs and MWCNTs Maxwell MHD nanofluid flow between two stretchable rotating disks under convective boundary conditions. *Heat Transf. Res.* **2019**, *48*, 4105–4132. [CrossRef]
36. Ali, L.; Wu, Y.J.; Ali, B.; Abdal, S.; Hussain, S. The crucial features of aggregation in TiO₂-water nanofluid aligned of chemically comprising microorganisms: A FEM approach. *Comput. Math. Appl.* **2022**, *123*, 241–251. [CrossRef]
37. Kumar, P.; Poonia, H.; Ali, L.; Areekara, S. The numerical simulation of nanoparticle size and thermal radiation with the magnetic field effect based on tangent hyperbolic nanofluid flow. *Case Stud. Therm. Eng.* **2022**, *37*, 102247. [CrossRef]
38. Sheri, S.R.; Thumma, T. Heat and mass transfer effects on natural convection flow in the presence of volume fraction for copper-water nanofluid. *J. Nanofluids* **2016**, *5*, 220–230. [CrossRef]
39. Ali, L.; Liu, X.; Ali, B.; Mujeed, S.; Abdal, S.; Mutahir, A. The Impact of Nanoparticles Due to Applied Magnetic Dipole in Micropolar Fluid Flow Using the Finite Element Method. *Symmetry* **2020**, *12*, 520. [CrossRef]
40. Ali, B.; Rasool, G.; Hussain, S.; Baleanu, D.; Bano, S. Finite element study of magnetohydrodynamics (MHD) and activation energy in Darcy–Forchheimer rotating flow of Casson Carreau nanofluid. *Processes* **2020**, *8*, 1185. [CrossRef]
41. Abbas, Z.; Javed, T.; Sajid, M.; Ali, N. Unsteady MHD flow and heat transfer on a stretching sheet in a rotating fluid. *J. Taiwan Inst. Chem. Eng.* **2010**, *41*, 644–650. [CrossRef]
42. Babu, M.J.; Sandeep, N. 3D MHD slip flow of a nanofluid over a slendering stretching sheet with thermophoresis and Brownian motion effects. *J. Mol. Liq.* **2016**, *222*, 1003–1009. [CrossRef]
43. Hayat, T.; Muhammad, T.; Shehzad, S.; Alsaedi, A. Three dimensional rotating flow of Maxwell nanofluid. *J. Mol. Liq.* **2017**, *229*, 495–500. [CrossRef]
44. Ali, B.; Hussain, S.; Nie, Y.; Hussein, A.K.; Habib, D. Finite element investigation of Dufour and Soret impacts on MHD rotating flow of Oldroyd-B nanofluid over a stretching sheet with double diffusion Cattaneo Christov heat flux model. *Powder Technol.* **2021**, *377*, 439–452. [CrossRef]
45. Rosali, H.; Ishak, A.; Nazar, R.; Pop, I. Rotating flow over an exponentially shrinking sheet with suction. *J. Mol. Liq.* **2015**, *211*, 965–969. [CrossRef]
46. Ali, B.; Hussain, S.; Nie, Y.; Ali, L.; Hassan, S.U. Finite element simulation of bioconvection and cattaneo-Christov effects on micropolar based nanofluid flow over a vertically stretching sheet. *Chin. J. Phys.* **2020**, *68*, 654–670. [CrossRef]
47. Reddy, J.N. *Solutions Manual for an Introduction to the Finite Element Method*; McGraw-Hill: New York, NY, USA, 1993; p. 41.
48. Jyothi, K.; Reddy, P.S.; Reddy, M.S. Carreau nanofluid heat and mass transfer flow through wedge with slip conditions and nonlinear thermal radiation. *J. Braz. Soc. Mech. Sci. Eng.* **2019**, *41*, 415. [CrossRef]
49. Ali, B.; Nie, Y.; Khan, S.A.; Sadiq, M.T.; Tariq, M. Finite Element Simulation of Multiple Slip Effects on MHD Unsteady Maxwell Nanofluid Flow over a Permeable Stretching Sheet with Radiation and Thermo-Diffusion in the Presence of Chemical Reaction. *Processes* **2019**, *7*, 628. [CrossRef]
50. Ali, L.; Ali, B.; Liu, X.; Ahmed, S.; Shah, M.A. Analysis of bio-convective MHD Blasius and Sakiadis flow with Cattaneo-Christov heat flux model and chemical reaction. *Chin. J. Phys.* **2021**, *12*, 554–571. [CrossRef]
51. Ibrahim, W.; Gadisa, G. Finite Element Method Solution of Boundary Layer Flow of Powell-Eyring Nanofluid over a Nonlinear Stretching Surface. *J. Appl. Math.* **2019**, *2019*. [CrossRef]
52. Ali, B.; Naqvi, R.A.; Ali, L.; Abdal, S.; Hussain, S. A Comparative Description on Time-Dependent Rotating Magnetic Transport of a Water Base Liquid With Hybrid Nano-materials Over an Extending Sheet Using Buongiorno Model: Finite Element Approach. *Chin. J. Phys.* **2021**, *70*, 125–139. [CrossRef]
53. Wang, C. Stretching a surface in a rotating fluid. *Z. Angew. Math. Phys. ZAMP* **1988**, *39*, 177–185. [CrossRef]
54. Ali, B.; Nie, Y.; Hussain, S.; Manan, A.; Sadiq, M.T. Unsteady magneto-hydrodynamic transport of rotating Maxwell nanofluid flow on a stretching sheet with Cattaneo–Christov double diffusion and activation energy. *Therm. Sci. Eng. Prog.* **2020**, *20*, 100720. [CrossRef]
55. Shafique, Z.; Mustafa, M.; Mushtaq, A. Boundary layer flow of Maxwell fluid in rotating frame with binary chemical reaction and activation energy. *Results Phys.* **2016**, *6*, 627–633. [CrossRef]



Article

Natural Gas Storage Filled with Peat-Derived Carbon Adsorbent: Influence of Nonisothermal Effects and Ethane Impurities on the Storage Cycle

Andrey V. Shkolin ^{1,2,*} , Evgeny M. Strizhenov ^{1,2} , Sergey S. Chugaev ^{1,2} , Ilya E. Men'shchikov ² , Viktoriia V. Gaidamavichute ², Alexander E. Grinchenko ² and Anatoly A. Zherdev ¹

¹ Research Institute of Power Engineering, Bauman Moscow State Technical University, Baumanskaya 2-ya str. 5, 105005 Moscow, Russia

² Frumkin Institute of Physical Chemistry and Electrochemistry, Russian Academy of Sciences, Leninskii Prospect, 31, Build. 4, 119071 Moscow, Russia

* Correspondence: shkolin@phyche.ac.ru

Abstract: Adsorbed natural gas (ANG) is a promising solution for improving the safety and storage capacity of low-pressure gas storage systems. The structural–energetic and adsorption properties of active carbon ACPK, synthesized from cheap peat raw materials, are presented. Calculations of the methane–ethane mixture adsorption on ACPK were performed using the experimental adsorption isotherms of pure components. It is shown that the accumulation of ethane can significantly increase the energy capacity of the ANG storage. Numerical molecular modeling of the methane–ethane mixture adsorption in slit-like model micropores has been carried out. The molecular effects associated with the displacement of ethane by methane molecules and the formation of a molecule layered structure are shown. The integral molecular adsorption isotherm of the mixture according to the molecular modeling adequately corresponds to the ideal adsorbed solution theory (IAST). The cyclic processes of gas charging and discharging from the ANG storage based on the ACPK are simulated in three modes: adiabatic, isothermal, and thermocontrolled. The adiabatic mode leads to a loss of 27–33% of energy capacity at 3.5 MPa compared to the isothermal mode, which has a 9.4–19.5% lower energy capacity compared to the thermocontrolled mode, with more efficient desorption of both methane and ethane.

Keywords: mixture adsorption; nanoporous carbon; natural gas storage; methane; ethane; heat of adsorption; cyclic adsorption; ideal adsorbed solution theory; numerical molecular simulation; molecular dynamic

Citation: Shkolin, A.V.; Strizhenov, E.M.; Chugaev, S.S.; Men'shchikov, I.E.; Gaidamavichute, V.V.; Grinchenko, A.E.; Zherdev, A.A. Natural Gas Storage Filled with Peat-Derived Carbon Adsorbent: Influence of Nonisothermal Effects and Ethane Impurities on the Storage Cycle. *Nanomaterials* **2022**, *12*, 4066. <https://doi.org/10.3390/nano12224066>

Academic Editor: Meiwen Cao

Received: 24 October 2022

Accepted: 16 November 2022

Published: 18 November 2022

Publisher's Note: MDPI stays neutral with regard to jurisdictional claims in published maps and institutional affiliations.



Copyright: © 2022 by the authors. Licensee MDPI, Basel, Switzerland. This article is an open access article distributed under the terms and conditions of the Creative Commons Attribution (CC BY) license (<https://creativecommons.org/licenses/by/4.0/>).

1. Introduction

Natural gas as one of the most common, cheap, and environmentally friendly fuels may in the near future become the main energy source for countries adhering to the principles of sustainable development. However, based on the experience of countries using natural gas as the main energy source for domestic consumption, it can be noted that among the main difficulties on the way to a large-scale energy transition to natural gas is the issue of gas delivery and back-up storage close to the consumer. The energy crisis in Europe in 2021–2022 has highlighted the importance of building an appropriate gas infrastructure with back-up storage to mitigate problems with gas supplies and uneven consumption. In addition, the events of 26 September 2022 on the Nord Stream gas pipelines also exposed the security problem of the existing gas infrastructure.

In recent years, the development of adsorbed natural gas (ANG) systems has been considered the most promising solution to improve the safety [1,2] and capacity of a low-pressure gas storage system [3]. However, there are several well-known difficulties that prevent ANG large-scale implementation: high requirements for the adsorbent, stability,

uniformity and reproducibility of its adsorption properties; the exothermic nature of adsorption, leading to predominantly negative thermal effects, which should be compensated for during charging and discharging, and to an increase in the duration of these processes [4]; and a decrease in storage efficiency due to the accumulation of C_{2+} hydrocarbon impurities during cyclic operation [5].

The study of the impurities' influence on the efficiency of adsorption gas storage is presented in the scientific literature much less often than studies on the thermal effects. This is mainly due to the complexity and laboriousness of conducting a cyclic experiment. A study [6] showed that when using natural gas with a methane content of about 92.18% mol., after 700 natural gas charging cycles, corresponding to about 250,000 km of vehicle mileage, the efficiency of the storage system drops by 50% due to the accumulation of impurity hydrocarbons C_{2+} . The ethane accumulation ended around cycle 30, but the efficiency continued to decline through 700 cycles due to the accumulation of heavier hydrocarbons. In [6], an adsorption layer with high thermal conductivity due to expanded natural graphite (ENG) was used, which together with a water thermostat significantly reduced the thermal effects in the charging and discharging processes. The authors of [7] supplied gas in the radial direction from the central collector (pipes with 40 channels) to reduce the heterogeneity of thermal effects. The work used natural gas with a methane content of 90.68% mol. After 10 cycles (the study included 30 cycles in total), the charging mass of gas decreased by 20%, and the discharging mass of gas by only 2% compared with the first cycle: according to the authors, the loss in discharging due to the accumulation of impurities fully appeared already from the first cycle and subsequently weakly changed. In [8], the cyclic process of charging and discharging gas from an ANG tank at room temperature on commercial activated carbon Maxsorb MSC-30 was studied. When charging natural gas with 85.45% mol. methane, the gravimetric excess adsorption decreased to 33% after 100 cycles and continued to slowly decrease until it reached 25% by the 1000th cycle. Volumetric storage capacity decreased to 50% after the first 100 cycles and remained constant thereafter. The authors showed that periodic regeneration by degassing at 400 °C for 2 h makes it possible to remove impurities and reactivate active carbon. These works were not aimed to investigate the combined effect of the impurity accumulation and the thermal control of the adsorber or the thermal effects of adsorption. In [9], the method of mathematical modeling was used to study the cyclic processes of charging and discharging natural gas containing 88% mol. methane for two limit cases: isothermal and adiabatic. The authors noted that non-isothermal effects in the adiabatic process can be more negative to the performance of the gas charging–discharging cycle than the presence of impurities in natural gas. In the case of the adiabatic process using natural gas with impurities, the accumulation efficiency decreased by 37–40%. However, the authors noted that they limited themselves to only C_1 – C_4 hydrocarbons, excluding the accumulation of heavier hydrocarbons from the model. The authors of [10] studied the effect of impurities in natural gas (methane content 90.58% mol.) in a full-size system with and without thermal control (heating during discharging). It was found that for 20 cycles without thermal control, the useful volumetric storage capacity decreased by 16%, and the amount of gas discharged by 10%. However, with the use of thermal management, efficiency losses have been reduced to 7% and 5%, respectively, due to more efficient ethane removal. However, thermal control showed no significant improvement in reducing the accumulation of hydrocarbons heavier than C_2H_6 , which continued to displace methane and ethane from the system.

In this paper, we study the properties of active carbon synthesized from cheap peat raw materials, its properties for adsorption of methane and ethane, the two main components of natural gas, and their mixture adsorption by the methods of the ideal adsorbed solution theory (IAST) and molecular modeling. The cyclic mode of charging and discharging of a model scaled natural gas storage equipped with a synthesized adsorbent is also considered, and the effect of ethane accumulation and thermal control of the system on the higher heating value (HHV) of the discharged gas is shown.

2. Materials and Methods

2.1. Adsorbent and Adsorbed Gases

High purity methane (99.99%) and ethane (99.95%) produced by Linde Gas was used in adsorption data experiments. The properties of gases and their mixtures were determined using the CoolProp program [11] using NIST data.

High-moor peat of the wood group with a high degree of metamorphism was used as a raw material for the synthesis of the adsorbent.

The synthesis of nanoporous activated carbon ACPK from peat with a decomposition degree of more than 50% (H8 and higher on the Von Post scale) consisted of the stage of raw material preparation, carbonization without oxygen, thermochemical activation, washing, and drying. Thermochemical activation makes it possible to obtain a more uniform structure of narrow micropores.

The stage of preparation of raw materials included the processing and drying of peat, followed by grinding and sieving to separate the required fraction up to 2 mm in size. The carbonization stage was carried out in a muffle furnace without access to oxygen at a temperature of 800 °C with a heating rate of 10 °C/min. For activation, aqueous mixtures of carbonizate and KOH activator were prepared in ratios of 1:2, which were placed in a steel crucible and then in a furnace. Thermochemical activation was carried out at a temperature of 900 °C at a heating rate of 10 °C/min. After reaching the required temperature, the samples were kept for 1 h. After cooling the samples to ambient temperature, the samples were washed with distilled water to pH 8 and dried in an oven for 24 h at a temperature of 110 °C.

2.2. Characterization

The surface morphology and elemental composition of ACPK were examined by scanning electron microscopy (SEM) using a Quanta 650 FEG microscope (FEI Company, Hillsboro, OR, USA) equipped with an Oxford Energy Dispersive X-ray (EDX) detector operating at 15 kV accelerating voltage.

To study the phase composition of the studied adsorbent and the initial assessment of their physicochemical and adsorption properties, an X-ray powder diffraction study was carried out using an Empyrean Panalytical diffractometer in the range of scattering angles 2θ from 10 to 120°.

To evaluate the structural characteristics of the adsorbent, we used the small-angle X-ray scattering (SAXS) method on a SAXSess diffractometer (Anton Paar). Monochromatic radiation was obtained using a Cu-K α filter ($\lambda = 0.154$ nm), and scattering was recorded on a two-dimensional Imaging Plate detector.

These methods provide a comprehensive understanding of the carbon framework and a primary understanding of the porous structure of the synthesized material ACPK. The detailed porous structure of ACPK was examined by N₂ adsorption–desorption isotherms at 77 K, which were performed on a Quantachrome Autosorb iQ multifunctional surface area analyzer. The specific volume of micropores W_0 (cm³·g^{−1}), standard characteristic energy of adsorption E_0 (kJ·mol^{−1}), and effective half-width of micropores x_0 (nm) were calculated by the Dubinin–Radushkevich (D-R) equation [12,13]. The Brunauer–Emmett–Teller (BET) method [14] using the criteria for microporous adsorbents [15] was also applied to evaluate the specific surface area, S_{BET} (cm²·g^{−1}). The Kelvin equation [16] was used to calculate the specific surface area of mesopores, S_{ME} (cm²·g^{−1}), respectively. The specific mesopore volume was calculated as $W_{\text{ME}} = W_{\text{S}} - W_0$, where W_{S} (cm³·g^{−1}) is the total pore volume obtained from the nitrogen adsorption at the relative pressure $P/P_{\text{S}} = 0.99$. The pore size distribution function in ACPK was calculated using the Quenched Solid Density Functional Theory (QSDFT) developed for micro-mesoporous adsorbents [17].

2.3. Single-Component Adsorption

Single-component adsorption isotherms of C₂H₆ and CH₄ were collected on purpose-designed adsorption benches, the schemes of which are reported in the previous works [18–20].

Methane adsorption was studied at temperatures of 213, 243, 273, 293, 333, and 393 K at pressures up to 20 MPa. Ethane adsorption was studied at temperatures of 273, 293, 313, and 333 K at pressures up to 120 kPa. The selected measurement ranges cover the most common field of practical application of ANG systems. Before gas adsorption measurements, the degas process was carried out under vacuum at 250 °C for 6 h.

Adsorption at temperatures different from the experimental ones was determined by the property of the linearity of the isosteres in the $\ln P-1/T$ coordinates, which in turn were plotted from the experimental isotherms (at least three points). To expand the pressure range of the calculated isotherms, an additional extrapolation was carried out according to the equations that best describe the experimental adsorption isotherms: the Sips and the theory of volume filling of micropores (TVFM) equations [21]. The TVFM equation was used in the subcritical region, and the Sips equation in the supercritical. The study of the thermodynamic functions of the adsorption process was carried out using Bakaev's approach [22–24], which is based on the method of changing variables to establish a, P, T (adsorption, pressure, and temperature, respectively) parameters of adsorption equilibrium in a wide range of pressures and temperatures, taking into account the nonideality of the gas phase in a thermodynamic system defined in accordance with the Guggenheim approach [25].

2.4. Mixture Adsorption Calculation

To determine the mixture adsorption of methane and ethane by the IAST method [26–28], the system of equations was solved:

$$\frac{\pi}{RT} = \int_0^{P_i^*} \frac{a_i^*}{P_i} dP_i \quad (1)$$

$$PY_i = P_i^* X_i \quad (2)$$

$$\sum_{i=1}^N X_i = 1 \quad (3)$$

$$\frac{1}{a_\Sigma} = \sum_{i=1}^N \frac{X_i}{a_i^*}, \quad (4)$$

where π is the spreading pressure, (Pa); T is the temperature, (K); R is the universal gas constant, (J/(mol K)); a_i^* is the adsorption of the pure component i of the mixture, (mmol/g), at T and the equilibrium pressure of the gas phase P_i^* (Pa), which corresponds to π ; X_i is the mole fraction of component i in the adsorbed phase; Y_i is the mole fraction of component i in the gas phase; a_Σ is the adsorption of the mixture in mmol/g at its equilibrium pressure P , (Pa).

The integral reduced (to the mass of the adsorbent) enthalpy of the mixed adsorbate was calculated as the sum of the integral reduced enthalpies of the adsorbate components at spreading pressure π and, accordingly, a_i^* , corrected for the actual filling of the pore with this component a_i :

$$h_a = \sum_{i=1}^N \frac{h_i(a_i^*, T)}{a_i^*} a_i = \sum_{i=1}^N h_i(a_i^*, T) \frac{X_i \cdot a_\Sigma}{a_i^*}, \quad (5)$$

where h_i is the integral reduced (to the mass of the adsorbent) enthalpy of the pure component i of the adsorbate at adsorption a_i^* and temperature T , (J/kg).

2.5. Molecular Modeling

The adsorption of a methane–ethane mixture was modeled by molecular dynamics using the Dynamic software module from the Tinker molecular modeling software package [29]. To reduce the cost of computer time, the universal atom–atom force field OPLSAA was used [30], which simulates the total interaction potential. It was shown in [31] that

among the existing universal potentials, this force field is best suited for describing model adsorption systems consisting of carbon structures and hydrocarbon molecules.

The simulation was carried out in the canonical (N, V, T are the number of molecules, volume, and temperature, respectively) ensemble. The simulation cell was a parallelepiped. Its height corresponded to the width of the pore plus 2 radii of carbon atoms. Micropores with a width in the range from 0.6 to 1.8 nm with a step of 0.2 nm were studied. The selected range of micropore widths corresponds to the most common widths for industrial carbon adsorbents. The walls of micropore are formed by single-layer graphene. The side faces of the simulation cell were 10 nm. The edges of the simulation cell are limited by periodic boundary conditions. The temperature of the numerical experiment was 293 K. Andersen's thermostat was used to thermostat the simulation system [32]. Studies of the molecular dynamics trajectory were carried out in the time interval 2×10^{-9} s. The elementary step of integrating the equation of motion was 10^{-15} s. Averaging of the system parameters for processing the results of a numerical experiment was carried out every 10^{-12} s. The time to reach the equilibrium states of the studied systems was estimated from the change in the total energy with time; it was no more than 10^{-9} s.

2.6. Adsorption Storage

The paper considers a model of an adsorption storage with a volume of 1 m^3 , limited by an aluminum shell. The calculation uses 5005-H18 alloy, which has average characteristics for aluminum alloys and is comparable in strength to popular stainless steels. With a shell mass of 250 kg or 500 kg, the maximum safe pressure inside is 5.0 and 10.0 MPa, respectively, however, taking into account possible temperature changes during gas storage, charging should be limited to pressures of 3.5 and 7.0 MPa, respectively. The storage is completely filled with a monolith adsorbent formed from ACPK active carbon and a polymeric binder with mass fractions of 95% and 5%, respectively. The density of the monolith adsorbent in the dried state is 720 kg/m^3 (corresponds to the indicators achieved in practice). The storage model is lumped, zero-dimensional, with a uniform distribution of temperatures, pressure, and adsorption of each component of the mixture.

A simplified scheme of the adsorption storage is shown in Figure 1. The storage can consist of several tanks A1 . . . AN, charging up to a pressure of 3.5 or 7.0 MPa (before the pressure regulator PR1) using a compressor C1 or directly from the gas pipeline, while the temperature of the supplied gas is constant (in all calculations 293 K). Gas is supplied to the consumer at a pressure of 0.1 MPa (after the PR2 regulator); if necessary, the pressure of the gas supplied to the consumer is increased using the C2 compressor. Constant pressure at the inlet (before PR1) and outlet (after PR2) allows us to assume that no technical work is done on the system, and the change in the enthalpy of the adsorption storage occurs due to the enthalpy of the inlet or outlet gas and heat supply or removal. The model is based on the assumption that there is no natural heat exchange with the environment: heat flow only occurs forcibly and is controlled using the TCU—thermal control unit. In practice, thermal control is provided using built-in heat exchangers [22,33,34] or gas circulation through the adsorbent bed with cooling/heating in an external heat exchanger [35–37].

The paper analyzes the cyclic charging and discharging processes in the adsorption storage in three different modes:

- (a) in “isothermal” mode, which can be oriented as a base case;
- (b) in a mode without heat exchange with the environment, which can be considered conditionally “adiabatic” (if we do not take into account the mass transfer due to the charging and discharging of gas);
- (c) in “thermo-controlled” mode with cooling at gas charging and heating at gas discharging. In terms of temperature change, this mode is opposite to the “adiabatic” mode.

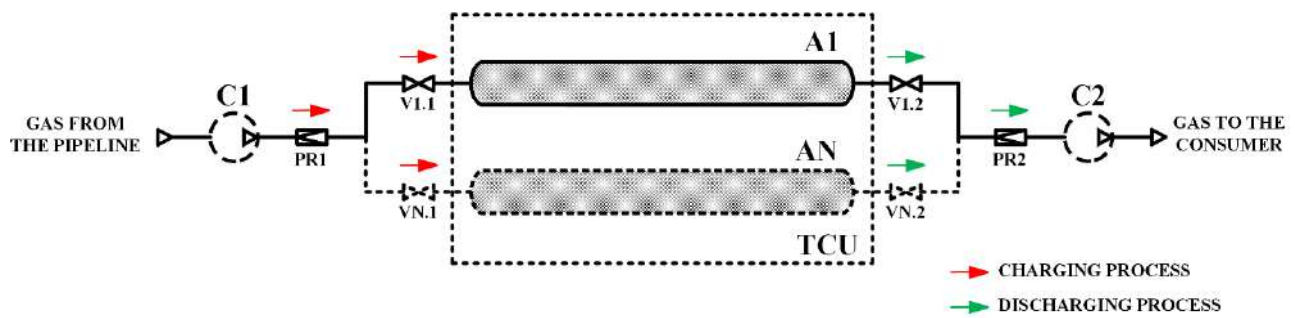


Figure 1. Scheme of the adsorption storage. C1, C2—natural gas compressors; A1 ... AN—ANG storage systems (adsorption tanks); TCU—thermal control unit; V1.1 ... VN.1 and V1.2 ... VN.2—stop valves; PR1–2—pressure regulators.

Cycling calculations are based on the heat balance of the system and the mass balance for each component.

The mass of each component of the mixture in the adsorption storage is determined by the expression, (kg):

$$M_i = (\rho_p(1 - x_b)a_i\mu_i + Y_{mi}\varepsilon\rho_{g\Sigma})V_s, \quad (6)$$

where ρ_p is the packing density of the adsorbent, (kg/m^3); $x_b = 0.05$ is the mass fraction of the polymer binder; μ_i is the molar mass of component i , (kg/mol); $\rho_{g\Sigma}$ is the density of the gas phase as a mixture, (kg/m^3) at pressure P and temperature T in storage; ε is the porosity, the fraction of space free for the gas phase; Y_{mi} is the mass fraction of component i in the gas phase; V_s is the volume of adsorption storage, (m^3).

The enthalpy of the entire storage is the sum of the enthalpies of its individual components, (J):

$$H_\Sigma = (h_a\rho_p(1 - x_b) + h_{g\Sigma}\varepsilon\rho_{g\Sigma})V_s + H_b + H_s, \quad (7)$$

where $h_{g\Sigma}$ is the specific enthalpy of the gas phase as a mixture, (J/kg); H_b is the enthalpy of the binder, (J); H_s —is the enthalpy of the storage metal shell, (J).

3. Results and Discussion

3.1. Characterization

ACPK carbon adsorbent is made from highly decomposed peat, the content of carbon and mineral impurities in which can vary over a wide range. As a result, the adsorbent is heterogeneous in content. Part of the carbon remained in its original form of large nanocrystals of ordered graphite, for which narrow reflections (002), (10), (100), (004), and (11) are characteristic, Figure 2. An increase in the background to small angles indicates the content of high-carbon radicals of the amorphous phase in the structure of the adsorbent. In addition to reflexes related to graphite deposits, a number of extraneous peaks are also observed, indicating the presence of mineral inclusions.

Based on the experimental data of SAXS (Figure 3), for the region of inhomogeneities III (1–2 nm), which correspond to scattering in micropores, the radius of gyration (inertia) R_G was calculated using the method in [38]. This integral parameter conditionally characterizes the average sizes of micropores, and thus is most indicative in the analysis of the porous structure of carbon adsorbents [39]. Based on the obtained values of R_G , the sizes of model micropores of different shaped adsorbents were determined: spherical R_S and cylindrical R_T . The results of determining the parameters of the model adsorbent pores and gyration radius are shown in Table 1.

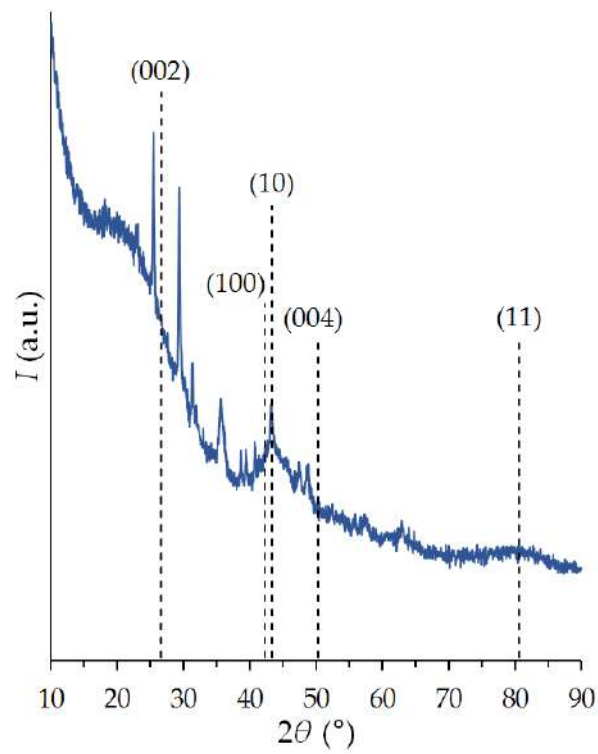


Figure 2. X-ray diffraction pattern of the carbon adsorbent ACPK. Graphite reflections are (002), (10), (100), (004), and (11).

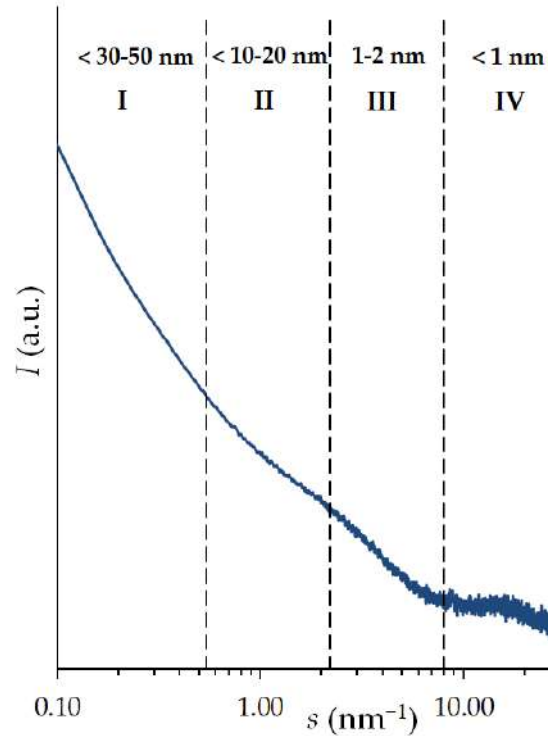
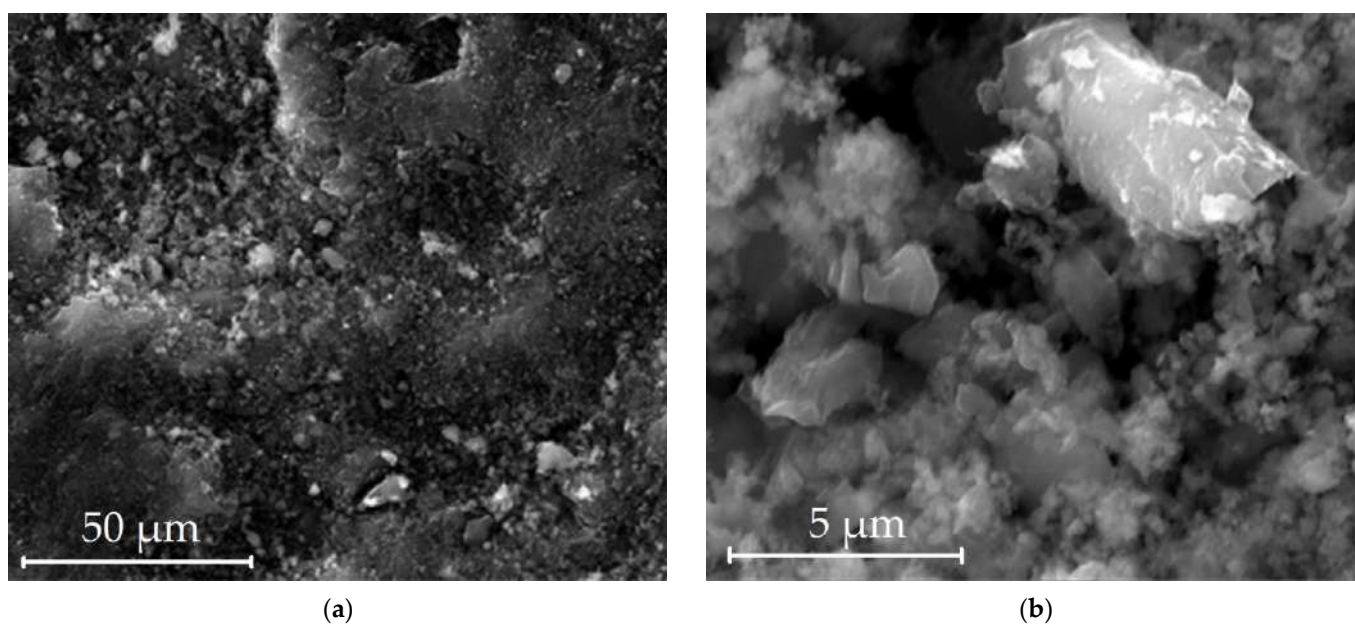


Figure 3. Dependence of the small-angle X-ray scattering intensity on the carbon adsorbent ACPK on the scattering vector at small and medium angles. I–IV are the characteristic X-ray scattering data areas used to obtain the structural parameters of the adsorbents.

Table 1. Parameters of the microporous structure of the ACPK carbon adsorbent calculated from SAXS data for various pore models.

Pore Model	Spherical		Cylindrical	
	R_G	R_S , nm	R_G	R_T , nm
Model characteristics ACPK	0.40	0.52	0.22	0.31

Pictures of the surface by scanning electron microscopy (SEM) are shown in Figure 4. The structure of the adsorbent has a granular type, and an inhomogeneous appearance in shape and size. In places, grains of a layered type are observed, similar to carbon graphite.

**Figure 4.** Electron microscopy images of the surface of the adsorbent from peat raw material ACPK: 50 μm (a); 5 μm (b).

The presence of a large number of mineral impurities on the surface of the adsorbent is probably due to the fact that the raw in the form of fossil peat and coal dust contains a significant proportion of various elements. High content of impurities, up to 13.3% wt. (Table 2), may qualitatively indicate that the contribution to the energetics of adsorption of peat coals is made by surface chemistry, and not only by the width of micropores and their size distribution.

Table 2. Elemental chemical composition of the ACPK surface.

Content	C	O	Other Impurities
% at.	75.6	18.3	6.1
% wt.	65.6	21.1	13.3

Adsorption–desorption isotherms of standard nitrogen vapor at 77 K of the studied adsorbent are shown in Figure 5. As follows from Figure 5, the isotherm in the coordinates $a = f(P/P_S)$ has an L-shaped form of type I [40] in the initial region of the isotherm up to 0.3 P/P_S , which indicates the presence of a developed volume of micropores in the porous structure of the adsorbent. At pressures close to the saturated vapor pressure, the adsorption–desorption isotherms show a capillary-condensation hysteresis loop of the H4 type [40], which is characteristic of a mesoporous structure.

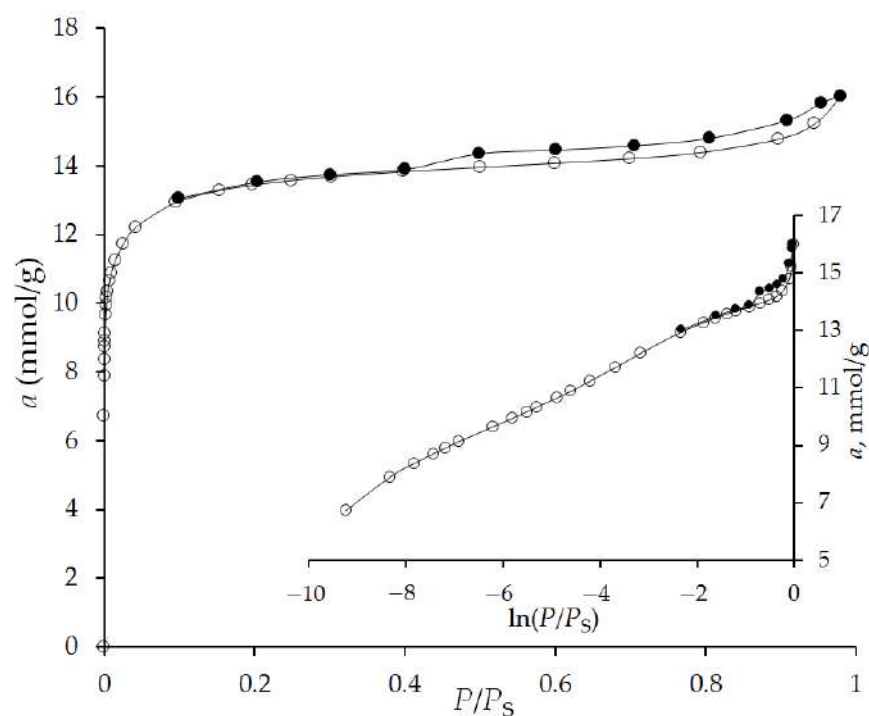


Figure 5. Adsorption (light symbols) and desorption (solid symbols) isotherms of nitrogen on the microporous carbon adsorbent ACPK at 77 K in linear and semi-logarithmic coordinates. Lines–spline approximation.

Table 3 presents the parameters of the porous structure of the ACPK adsorbent. As follows from Table 3, the mesopore volume of the adsorbent is about 25% of the total pore volume, and the mesopore surface is 40 m²/g. Thus, the adsorbent contains a significant proportion of mesopores, the adsorption of gases in which must be taken into account.

Table 3. Parameters of the porous structure of the carbon nanoporous adsorbent ACPK.

Method	BET	TVFM	TVFM	TVFM	TVFM	TVFM	BET	QSDFT
Adsorbent	$S_{\text{BET}}, \text{m}^2/\text{g}$	$W_0, \text{cm}^3/\text{g}$	x_0, nm	$E_{0(\text{N}_2)}, \text{kJ/mol}$	$W_{\text{S}}, \text{cm}^3/\text{g}$	$W_{\text{ME}}, \text{cm}^3/\text{g}$	$S_{\text{ME}}, \text{m}^2/\text{g}$	$r_{\text{max}}, \text{nm}$
ACPK	1105	0.44	0.52	7.63	0.56	0.12	40	0.59

To estimate the size distribution of micropores, we used the approach of the density functional theory QSDFT for a spherical pore model as the most probable pore model for a given adsorbent according to X-ray diffraction data. The distribution curves of micropores by size $dW_0/dd = f(d)$ are shown in Figure 6. The maximum on the micropore size distribution curve corresponds to $r_{\text{max}} = 0.56 \text{ nm}$.

The pore parameters determined from the results of XRD (Table 1) coincide with the determination by the TVFM [41] (Figure 5, Table 3) and are close to the pore size distribution determined by the QSDFT method (Figure 6, Table 3). In this case, the adsorbent has a second, less pronounced maximum on the distribution curve, with a radius corresponding to the distribution maximum of 0.92 nm. The ratio of pore volumes for the two distribution maxima is about 75/25% for narrow and wide pores, respectively.

3.2. Equilibrium Adsorption Tests

Methane adsorption on ACPK was measured in the temperature range from 213 to 393 K, and ethane in the temperature range from 273 to 333 K. The results are shown in Figure 7. The isotherms of both gases are type I isotherms [40]. At a pressure of 3.5 MPa and 293 K, the adsorption of methane on the synthesized adsorbent ACPK is 6.55 mmol/g or 10.5% wt., and at a pressure of 7.0 MPa and 293 K, respectively, 7.80 mmol/g

and 12.5% wt. These adsorption properties make it possible to use this adsorbent for the purpose of methane (natural gas) storage, but under the condition of a high packing density of the adsorbent, for example in the form of monoliths [34,42–45].

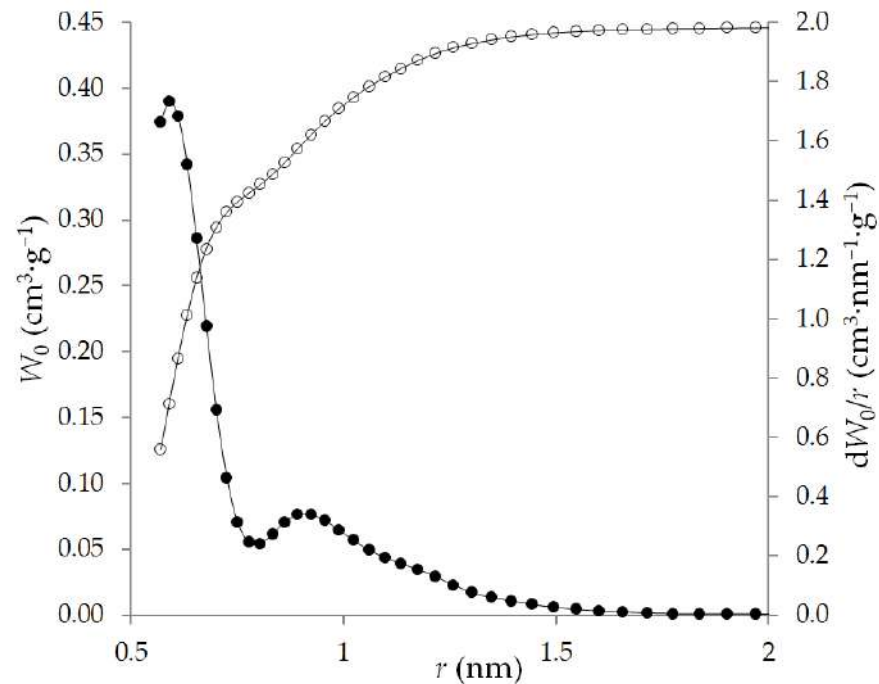


Figure 6. The QSDFT cumulative W_0 (light symbols) and differential dW_0/r (dark symbols) pore volume distributions calculated for ACPK from the nitrogen adsorption at 77 K for a sphere pore model.

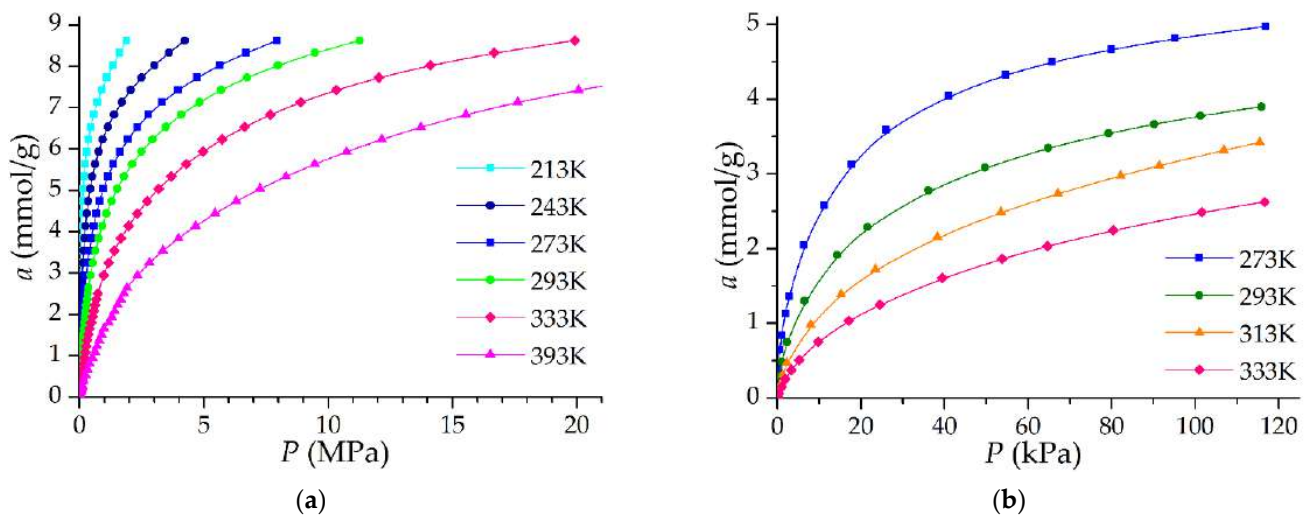


Figure 7. Adsorption isotherms of methane (a) and ethane (b) on the ACPK adsorbent. Symbols are an experiment. The lines are a spline approximation.

Figure 8 shows the dependence of the differential molar isosteric heat of adsorption of methane and ethane on the nanoporous carbon adsorbent ACPK at a temperature of 293 K. The plotting area for C_2H_6 is limited by the area of reliable experimental measurements of adsorption with the possibility of isostere linearization by at least three points. Heat is determined without taking into account adsorption-stimulated and thermal deformation. The value of carbon adsorbents deformation under the described conditions does not exceed 0.3–0.4%, while the contribution of deformation to the heat of adsorption at a temperature of 293 K does not exceed 2–5% [23,46,47]. The absence of an abrupt jump in the heats of

adsorption in the initial region of filling indicates a weak inhomogeneity of the adsorbent sorption surface. A barely noticeable extremum at 0.2 mmol/g is observed on ethane, but this is probably due to experimental errors due to the proximity to the boundary of the measurement region. Otherwise, the dependences of the heats of adsorption of methane and ethane in the studied area repeat the shape of each other.

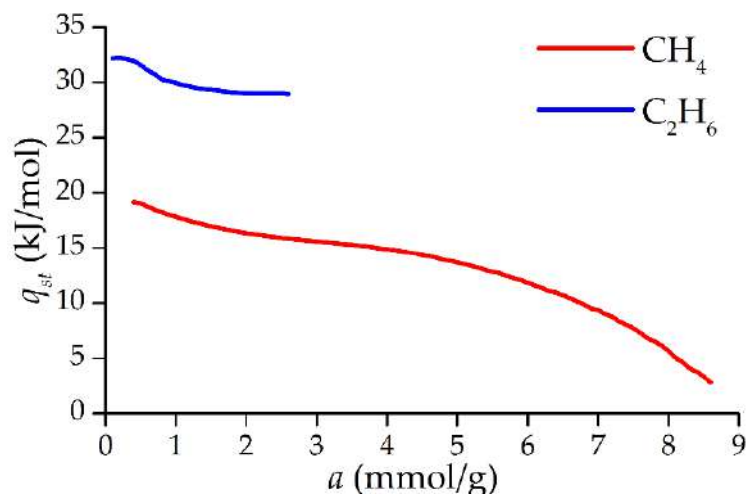


Figure 8. Differential molar isosteric heat of adsorption of methane and ethane on the microporous carbon adsorbent ACPK at a temperature of 293 K, determined from experimental data.

3.3. Mixture Adsorption

The IAST results of determining the adsorption of a mixture and individual components in a mixture of CH₄ and C₂H₆ are shown in Figure 9. With a content of 2% mol. ethane in the gas phase, its contribution to the total adsorption is much more significant: from 14.7% mol. at 3.5 MPa and 333 K up to 23.8% mol. when the temperature decreases to 273 K. At the same time, methane remains the main adsorbed gas in the entire considered pressure range from 0.05 to 7 MPa. At a content of 10% mol. ethane in the gas phase, the situation is reversed: ethane is adsorbed in even larger quantities than methane at a temperature of 273 K (59.5% mol. of ethane in the total adsorption at 3.5 MPa) to approximately equal adsorption with methane at a temperature of 333 K.

It is obvious that such active absorption of ethane can adversely affect the active capacity of the adsorption storage due to the fact that ethane is less efficiently desorbed upon depressurization compared to methane. On the other hand, as can be seen from Figure 9, the total molar adsorption of the mixture varies slightly with a change in the ethane content in the gas phase, however, the higher heating value of 1 mol of ethane is 75% higher than that of methane. Thus, the energy capacity of the adsorption storage increases with an increase in the ethane concentration: at a pressure of 3.5 MPa and 293 K, the higher heating value of the adsorbate at an ethane concentration of 10% mol. in the gas phase is 8.57 MJ per 1 kg of adsorbent, while in the case of pure methane this heat is 5.84 MJ/kg—1.47 times less—while the higher heating value of the gas phase differs by only 7.5%. In some cases, this effect can be useful; for example, by integrating the storage into a flowing gas pipeline network: the storage capacity will increase significantly due to the capture of ethane and heavy hydrocarbons from the flow. However, the extraction of this excess energy is complex due to the difficulty of extracting ethane (and other heavy hydrocarbons, if present in natural gas). The advantages and disadvantages of the presence of impurity hydrocarbons in natural gas depend on the form of the gas charging and discharging processes organization.

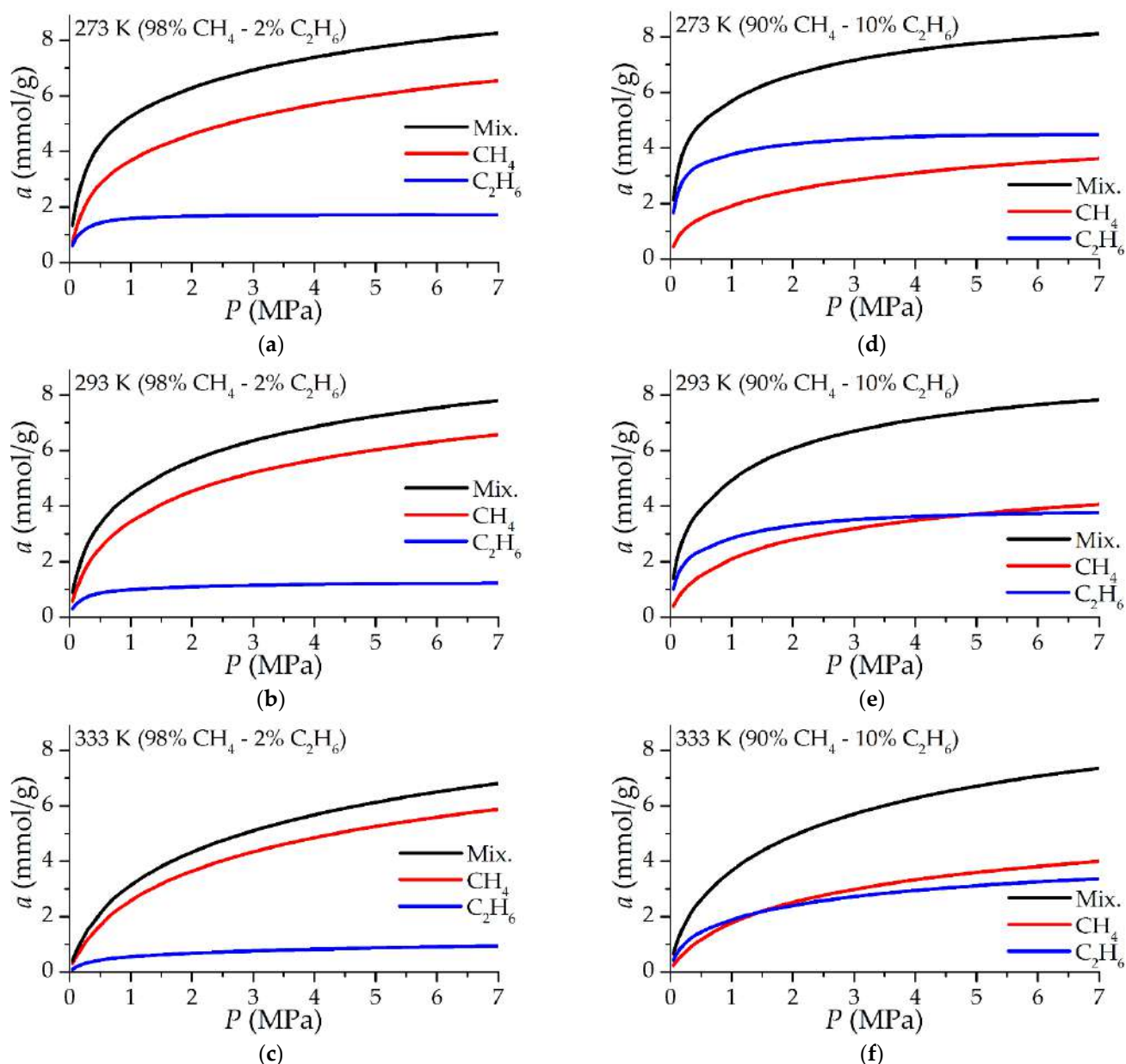


Figure 9. Equilibrium adsorption of a binary mixture of methane and ethane depending on the pressure of a gas mixture with a molar content of 2% (a–c) and 10% (d–f) ethane at temperatures of 273 K (a,d), 293 K (b,e), 333 K (c,f). The calculation method is IAST using experimental isotherms of pure components.

3.4. Molecular Modeling

For a more detailed understanding of the mechanism of mixture adsorption of methane and ethane, a numerical simulation in model pores of a carbon adsorbent of various widths H_5 from 0.6 to 1.8 nm with a step of 0.2 nm was performed using the molecular dynamics method. For the study, a slit-like micropore model was used as it is one of the most common models for the formation of pores in carbon adsorbents. [48,49]. Carbon adsorbents, in general, consist of an ordered part of carbon crystallites and an amorphous part of high-carbon radicals [50]. The ratio of the amorphous and crystalline parts of carbon is determined by the raw and carbonization conditions. When using organic carbon-containing raw materials, the structure of crystallites resembles graphite, but they themselves are packed less regularly in the volume of carbon. At the same time, an increase in activation leads to a decrease in the fraction of crystallites and an increase in

the amorphous fraction. The amorphous part may contain micropores of various shapes, including those close to spherical. According to the results of the adsorbent structure study (Tables 1 and 3 and Figure 6), the ACPK adsorbent contains a significant part of amorphous carbon with a pore shape close to spherical. On the other hand, X-ray diffraction analysis (Figure 2) revealed the presence of peak characteristics of graphite-like microporous structures. Thus, the use of the slit-like micropores of graphite-like crystallites model of a carbon adsorbent in a numerical simulation is legitimate. A numerical experiment was carried out for a mixture 95% CH₄ and 5% C₂H₆. The temperature of the experiments was 293 K. The concentration of the mixture for the study was selected based on the data on the average concentration of C₂₊ hydrocarbons.

Figure 10 shows the dependencies of the probability of the mass center location of a methane or ethane molecule in a pore for various pore widths and their filling. In the process of adsorption, for narrow pores 0.6, 0.8, and 1 nm wide, the concentration displacement of ethane is shown. For pores with a width of 1 nm, close to the size of ACPK micropores according to X-ray diffraction analysis (Table 1) and the first maximum on the QSDFT pore size distribution curve (Figure 6), the mixture is almost completely sorbed in the pore at low fillings (up to 100 molecules in the modeling system), forming molecular complexes near the graphene walls, Figure 10a. Figure 10a shows that the centers of mass of ethane molecules are shifted relative to the centers of mass of methane molecules, which can be explained by the fact that linear ethane molecules tend to occupy a perpendicular position to the micropore walls. With an increase in the number of molecules in the simulation system, methane molecules completely fill the molecular complexes located in the potential minima of the model micropore near the graphene surface, displacing ethane molecules outside the pore, Figure 10b.

For micropores with a width of more than 1.2 nm, the effect of concentration displacement is not observed. Figure 10c,d show the simulation results for a wide model micropore with a width of 1.8 nm, which is close in value to the wide ACPK pores corresponding to the second distribution maximum in Figure 6. At low fillings, the behavior of adsorbate molecules is similar to that observed in narrow pores, but at high fillings, ethane molecules are present in the micropore, forming a “layered” structure with methane molecules, while ethane molecules are displaced from molecular complexes closer to the center of the micropore.

Figure 11 shows instantaneous snapshots of the molecular dynamics trajectory of the simulation system for micropores of different widths. These images clearly demonstrate the dependences shown in Figure 10, while expanding our understanding of the behavior of methane and ethane molecules in a micropore. Thus, in a narrow micropore 1.0 nm wide, sorbed ethane molecules are located closer to the edges of graphenes, Figure 11a, probably due to the predominant interaction of methane molecules with each other in the field of dispersion forces of the adsorbent than the interactions of methane–ethane. As a result, ethane molecules are forced out of the narrow micropore.

In the case of a wide pore 1.8 nm wide, the situation is different: Figure 11b shows that methane and ethane molecules together form molecular complexes in accordance with Figure 10c. With further filling of a wide micropore, ethane is not completely displaced from the pore, Figure 11c: in the center of the micropore, the density of molecules is low, which allows two more layers of ethane molecules and even a third layer of methane between them to be accommodated, Figure 10d.

Figure 12 shows the dependence of the number of adsorbed methane and ethane molecules on the number of molecules in the ratio of 95% methane and 5% ethane in simulation cells with a width of 1.0 nm and 1.8 nm at a constant temperature of 293 K, the molecular adsorption isotherm of the mixture.

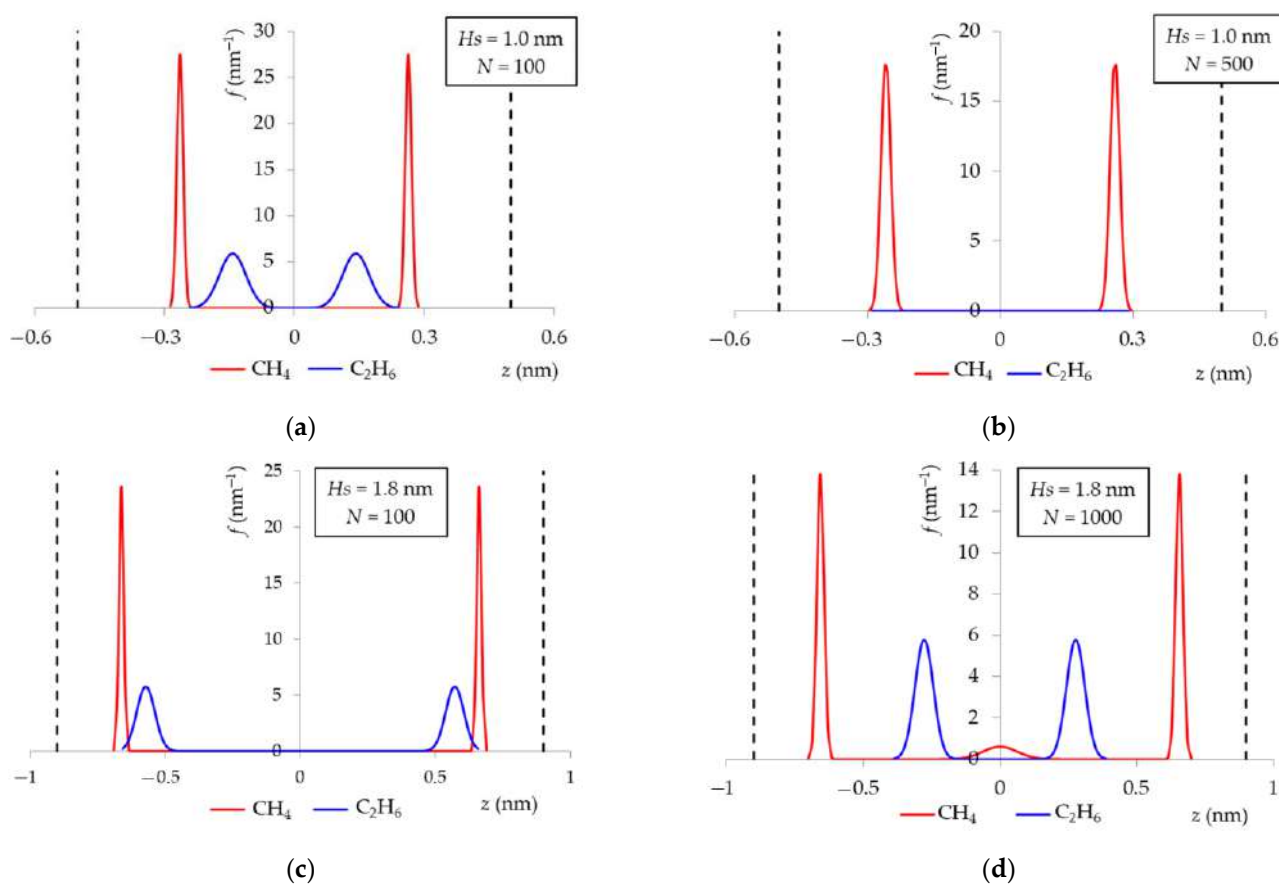


Figure 10. Probability density of the mass center location of a methane and ethane molecule in a model pore of a carbon adsorbent with a width of $H_s = 1.0$ nm (a,b) and 1.8 nm (c,d) for different numbers of molecules N in the simulation cell, corresponding to the region of averages (a,c) and maximum (b,d) fillings of micropores. The number of molecules of the mixture N (the ratio of the molecules number of methane and ethane is 95:5) in the modeling system, pcs: 100 (a); 500 (b); 100 (c); 1000 (d). The temperature is 293 K. The ordinate axis intersects the abscissa axis at point $z = 0$, corresponding to the symmetry plane of the pore. The dotted line is the boundary of the model micropore.

In a narrow micropore 1.0 nm wide, Figure 12a, in the region of up to 100 molecules (95 methane molecules and 5 ethane molecules), a classical increase in the amount of adsorbed methane and ethane is observed in the system. Moreover, almost all ethane molecules and most of the methane molecules in this region from the free phase enter the micropore. With an increase in the number of molecules in the simulation system, the number of ethane molecules in the pore gradually decreases due to its displacement by methane. At 160 molecules of the mixture (an instantaneous snapshot was presented in Figure 11a) in the simulation system, ethane is completely displaced by methane from micropores: an interesting behavior is observed that if there are ethane molecules in the free phase (analogue of the gas phase), they are not in the adsorption pore. This behavior is probably explained by the difference in size and shape of methane and ethane molecules. Small and spherically symmetric methane molecules fill the micropore into two adsorption layers, forming a more energetically favorable state of the adsorbate than ethane molecules, which, due to their linear shape, tend to occupy a perpendicular position in the narrow micropore and thereby prevent the formation of the second adsorption layer. Figure 12b shows the results of modeling the mixture adsorption in wider pores, using the example of a micropore 1.8 nm wide. In this case, ethane adsorption continuously increased as the number of molecules in the system increased. From the previously considered

Figures 10 and 11, it is already known that ethane is not completely replaced by methane in a wide pore.

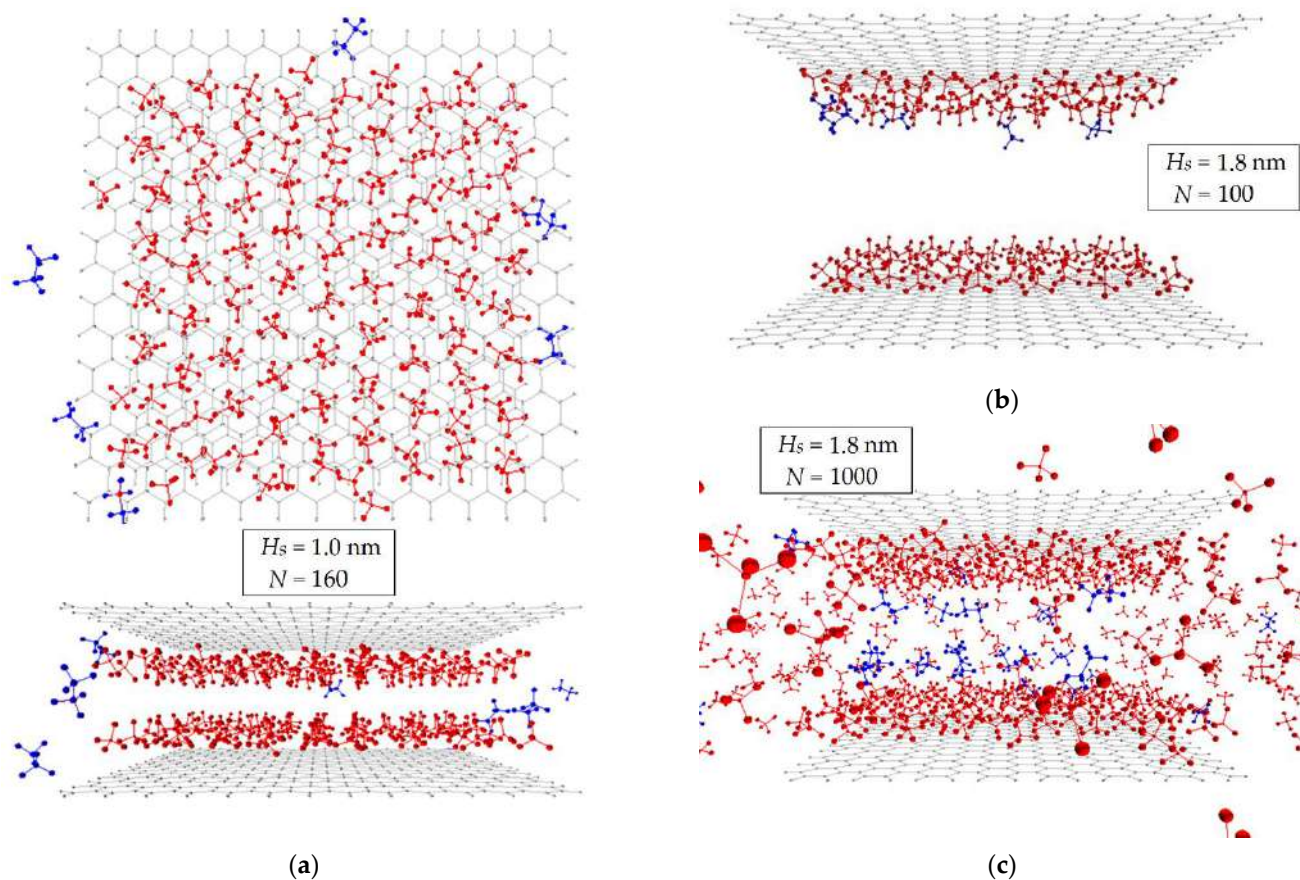


Figure 11. Instantaneous snapshot of the molecular dynamics trajectory of a simulation system consisting of two graphenes at a distance of $H_S = 1.0$ nm (a) and 1.8 nm (b,c) at different numbers of N molecules (the ratio of the number of molecules of methane and ethane is 95:5) in simulation cell: 160 (a); 100 (b); 1000 (c). The bonds of atoms forming graphene are indicated by solid lines. Atoms are shown as unscalable red (methane) and blue (ethane) spheres.

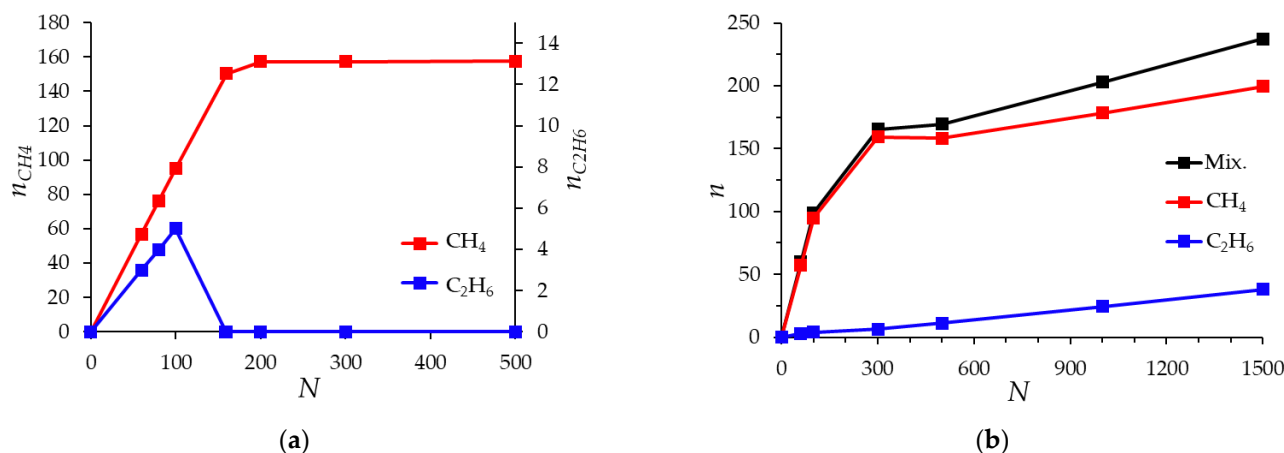


Figure 12. Dependence of the number of adsorbed molecules n of methane CH_4 and ethane C_2H_6 and their total number (Mix.) on the number of molecules in the simulation cell N (ratio of the number of molecules of methane and ethane 95:5) for a pore with a width of 1.0 nm (a) and 1.8 nm (b). The temperature is 293 K.

The obvious differences between the molecular isotherms shown in Figure 12 and the adsorption isotherms of the mixture calculated using the IAST model (Figure 9) are explained by the fact that the IAST method is based on the isotherms of the pure components, which are in fact integral isotherms over all pores of a real adsorbent with a wide pore size distribution. Figure 13 shows an attempt by the authors to evaluate the integral adsorption isotherm of a mixture obtained by summarizing molecular isotherms for pores of various widths, the weight contribution of which is determined by the share of pores of the corresponding width in the pore size distribution defined by the QSDFT method (Figure 6) for the ACPK adsorbent. As can be seen from Figure 13, the integral molecular adsorption isotherms of the mixture and their components behave similarly to the isotherms calculated using the IAST model: thus, the adsorption of ethane in a wide range of fillings (from 100 to 500 molecules) changes relatively weakly, similar to the saturation of ethane in Figure 9. This is due to the simultaneous decrease and increase in the amount of sorbed ethane in pores of various sizes. A direct comparison of the integral molecular isotherm and IAST isotherms is difficult due to the correct consideration of the free (gas) phase, as well as differences in the pore structure of the real and model adsorbent, due to the presence of a significant fraction of the amorphous carbon phase in the structure of the real adsorbent.

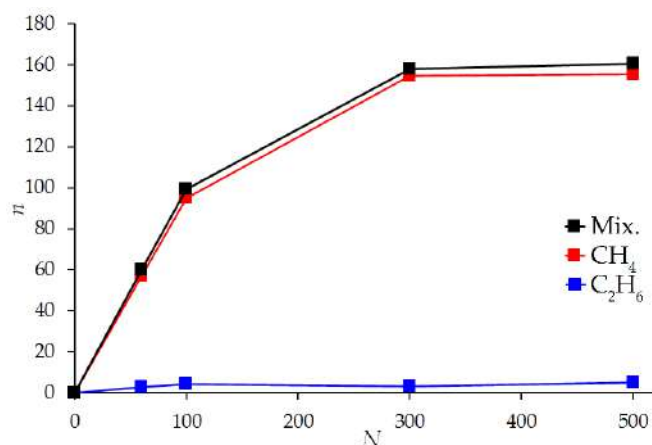


Figure 13. Integral dependence of the number of adsorbed molecules n of methane CH_4 and ethane C_2H_6 and their total number Mix. on the number of molecules N (ratio of the number of molecules of methane and ethane 95:5) in an array of simulation cells, quantitatively corresponding to the pore size distribution of the ACPK adsorbent. The temperature is 293 K.

Despite the fact that the IAST model and the molecular model can produce results similar in form, it is obvious that some molecular features of the filling of micropores of different sizes with certain substances cannot be taken into account in principle by the IAST model, even when applying this model to a specific model micropore. For example, the case of a slit-like micropore 1.0 nm wide: the adsorption of pure methane and ethane in it is not equal to zero, but the mixture adsorption, according to the results of molecular modeling, can lead to the complete displacement of one of the components, which is not observed in the IAST model.

3.5. Cycles in Adsorption Natural Gas Storage

To assess the influence of thermal effects and the presence of impurities (ethane in a binary mixture with methane), modeling of cyclic processes of gas charging and discharging was performed using the IAST method. Idle time and gas storing processes have been eliminated, charging starts immediately after discharging, and vice versa. In the initial state, the adsorption storage is filled with pure methane at a pressure of 0.1 MPa and a temperature of 293 K. The storage is charged up to 3.5 or 7.0 MPa. The supplied gas has a pressure of 3.5 or 7.0 MPa, respectively, and a temperature of 293 K. Gas leaves the

storage under variable conditions corresponding to the conditions in the storage. Since in the considered zero-dimensional model (with lumped parameters) all processes are in equilibrium and there is no natural heat exchange with the environment, the time factor does not play a significant role. The time scale is replaced by the gas exchange scale: the total mass of gas entering and exiting the storage. If we assign certain flow rates for gas charging and discharging, then such a gas exchange scale is definitely translated into a time scale, but this does not play a role for the analysis of cycles.

Figure 14 shows the results of modeling the first 50 cycles of “adiabatic” (without heat exchange with the environment and thermal control) charging up to 3.5 MPa with gas containing 98% mol. methane and 2% mol. ethane and gas discharging up to 0.1 MPa from storage. The gradual cooling of the storage under “adiabatic” conditions is explained by mass exchange with the external environment: the incoming gas at a temperature of 293 K is colder than the outgoing gas in the first cycles, which ultimately leads to the stabilization of the storage temperature below the initially set 293 K. Despite the very low content of ethane in the inlet gas, it accumulates in the system until the outlet gas has, on average, the same concentration of ethane as the inlet gas. Therefore, in the first approximation, the effect of ethane can be estimated from the equilibrium adsorption isotherms of the mixture shown in Figure 9. However, it should be taken into account that the molar fraction of ethane changes during the process. The share of ethane in the adsorbate after 50 cycles reaches 41.5% mol. at the end of discharging (at the minimum pressure in the system) and about 21.5% mol. at the end of charging (at maximum pressure in the system). At the end of 50 cycles shown in Figure 14, the periodic mode is not yet steady. The periodic mode can be considered established approximately around 110 cycles of adiabatic charging and discharging, when the difference in the amount of charged and discharged ethane differs by less than 1%, and this error becomes comparable with the mathematical errors of the model itself.

To assess the effect of impurities in fuel storage systems, it should be taken into account that both considered gases are combustible and targeted. Therefore, the influence of impurities should be assessed from the position of loss in the energy capacity of the storage. The same approach makes it possible to take into account the thermal effects of adsorption and desorption, which are expressed in a lower active storage capacity. The usual approach to assessing the active capacity of an adsorption storage in terms of volume (m^3 of gas per m^3 of volume) is incorrect, since 1 m^3 of ethane under normal conditions (101,325 Pa and 293.15 K) has the higher heating value by 76% more than 1 m^3 of methane. The assessment by weight can be considered justified: the difference in the combustion energy of 1 kg of methane and ethane is only 7%, which with ethane content up to 10% mol. leads to a mass combustion energy range of 54.9–55.5 MJ/kg.

Figure 15 shows the dependencies of the higher heating value of the discharging gas by cycles for various types of charging up to a pressure of 3.5 MPa and discharging up to 0.1 MPa: “adiabatic”, “isothermal”, which is not ideal, but convenient as a reference point, and “thermocontrolled”, the opposite of adiabatic, i.e., with cooling when charging up to 293 K and heating when discharging gas up to 333 K. The adiabatic mode significantly reduces the active energy capacity of the storage: by 27–33% compared to the isothermal process with the same composition of the supplied gas; this is the influence of the thermal effects of adsorption and desorption. Surprisingly, in the adiabatic mode, the accumulation of ethane has practically no effect on the active energy capacity of the storage (compared to operation on pure methane): losses in methane are compensated over time by a large amount of ethane released. The “harmful” accumulation of ethane is more noticeable in isothermal and thermocontrolled modes: over time, the active energy capacity of the storage decreases to a certain steady-state value. In isothermal mode 2% mol. the concentration of ethane in the gas supplied leads to a loss of efficiency of 5.7%, and at a concentration of 10% mol. losses already 16.6%. The accumulation of ethane has a greater effect on the isothermal mode.

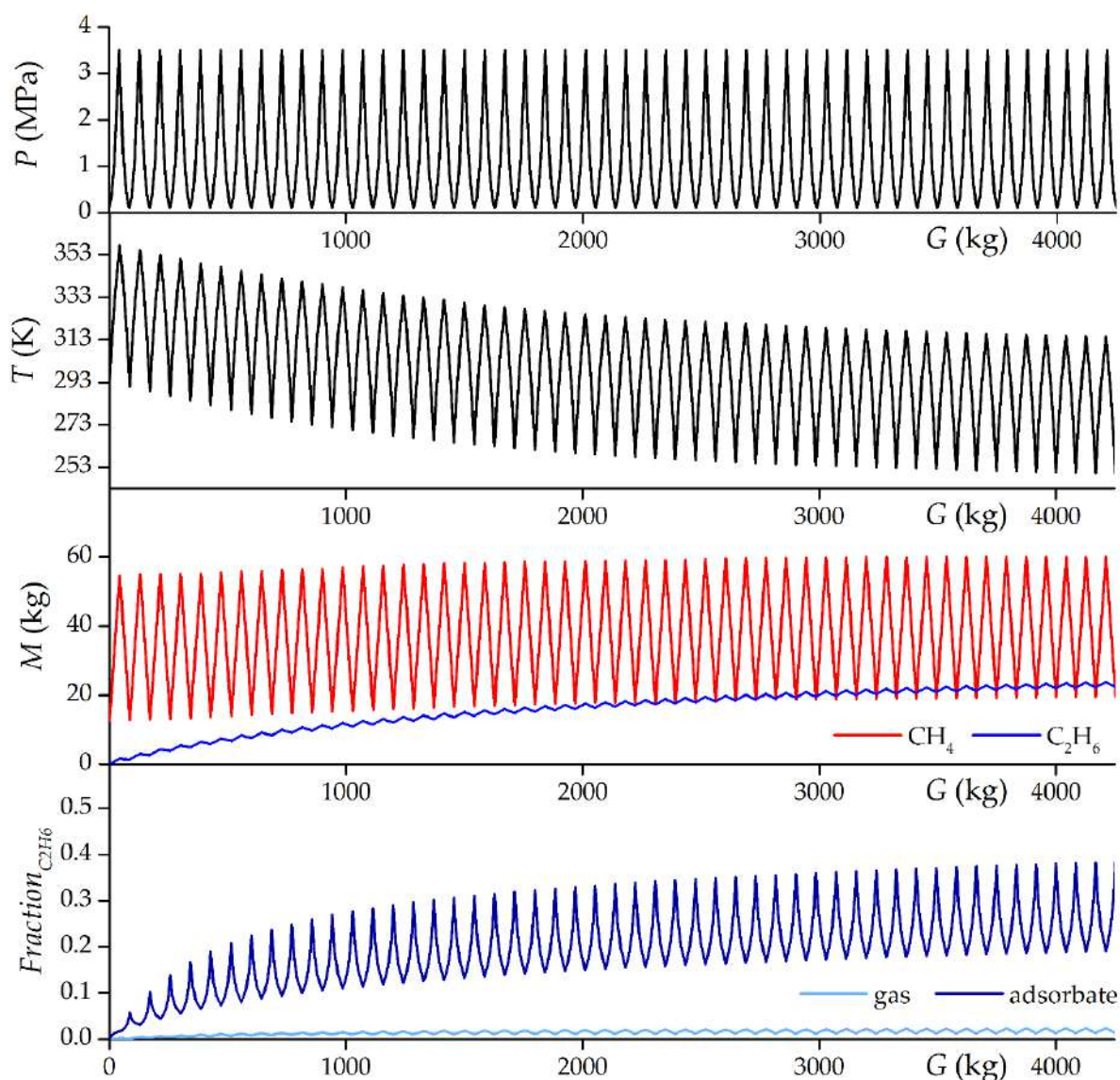


Figure 14. Dependencies of pressure, temperature, and mass of methane and ethane in the adsorption storage with a volume of 1 m^3 based on ACPK adsorbent and the mole fraction of ethane in the gas and adsorbed phases in the “adiabatic” cyclic charging/discharging process and supplied gas with 98% mol. methane and 2% mol. ethane using the IAST simulation results from the cumulative gas exchange since the beginning of the simulation. The first 50 cycles are shown.

The advantages of the thermocontrolled mode in the energy storage capacity compared to the isothermal mode depend on the composition of the supplied gas: with a large number of cycles, the advantage is 9.4% on pure methane (due to a higher temperature at the end of the discharging process), 11.7% at 2% mol. fraction of ethane in the gas supplied to the system, and 19.5% at 10% mol. Fraction of ethane, i.e., the temperature-controlled mode allows for more efficient removal of ethane and contributes to a reduction in its accumulation. It can also be seen from Figure 15 that thermocontrolling reduces the duration of reaching a stable periodic mode compared to the isothermal mode, while the opposite adiabatic mode can be unstable for quite a long time. The greater the proportion of impurities in the incoming gas, the faster a stable periodic process comes in isothermal and thermocontrolled modes: impurities accumulate faster to a steady value. In general, about 20 cycles in all considered modes are sufficient to achieve an approximately steady value of the combustion energy, however, the accumulation of ethane in the considered processes continues after 20 cycles.

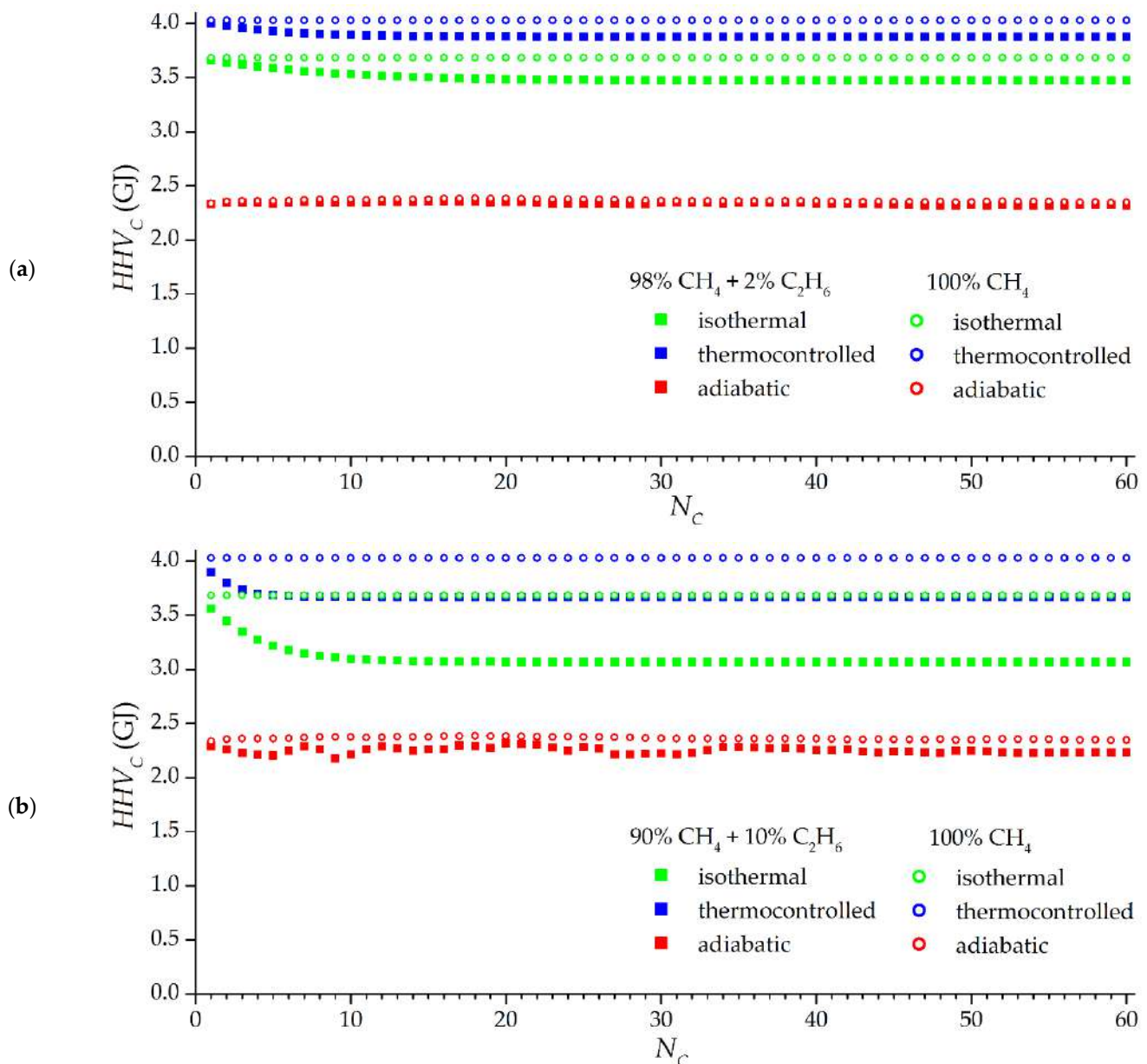


Figure 15. Dependence of the higher heating value of the mixed gas leaving for one cycle from a storage with a volume of 1 m³ based on the ACPK adsorbent, on the cycle number. Filled dots correspond to mixtures: 98% mol. methane and 2% mol. ethane (a); 90% mol. methane and 10% mol. ethane (b). Empty points correspond to pure methane.

These results are adequately consistent with the publications reviewed in the introduction. In most studies, the noticeable effect of ethane, which is the main impurity of natural gas, ended approximately in the region of 10–30 cycles [6,7,10]. In terms of the effect on the active capacitance, the results are also close to those published earlier: in [7], the effect of 10.3% mol. impurities (not only ethane) led to a loss of 20% capacity, and in [10] the effect of 10.4% mol. impurities to losses of 16%, which correlates with the simulation results. In general, such an approach can be considered justified, at least as a first approximation.

Figure 16 shows the dependencies of the steady-state values of the active energy capacity of the adsorption and conventional gas storage for one charging and discharging cycle on the ethane content in the supplied gas for different modes. As the ethane content increases, the energy capacity of the gas storage increases by increasing the density of the mixture—or by increasing the average molar energy of combustion. The efficiency of the

adsorption storage, on the contrary, decreases. It is likely that there is a certain concentration of ethane at which adsorption storage will no longer provide an advantage over conventional gas storage. In Figure 16, this is clearly seen at a pressure of 7.0 MPa: with an ethane fraction of 10% mol. adsorption storage, which gives only a small advantage in active energy capacity compared to conventional gas storage: 29% in isothermal mode, although with pure methane the advantage is 71%. At a pressure of 3.5 MPa, the advantage of the adsorption storage is more obvious: even in the low-efficiency adiabatic mode, the energy capacity is higher than that of the conventional gas storage, and in the thermocontrolled mode, the active energy capacity is 2.5 times greater at an ethane concentration in the gas of 10% mol. and three times greater when operating on pure methane.

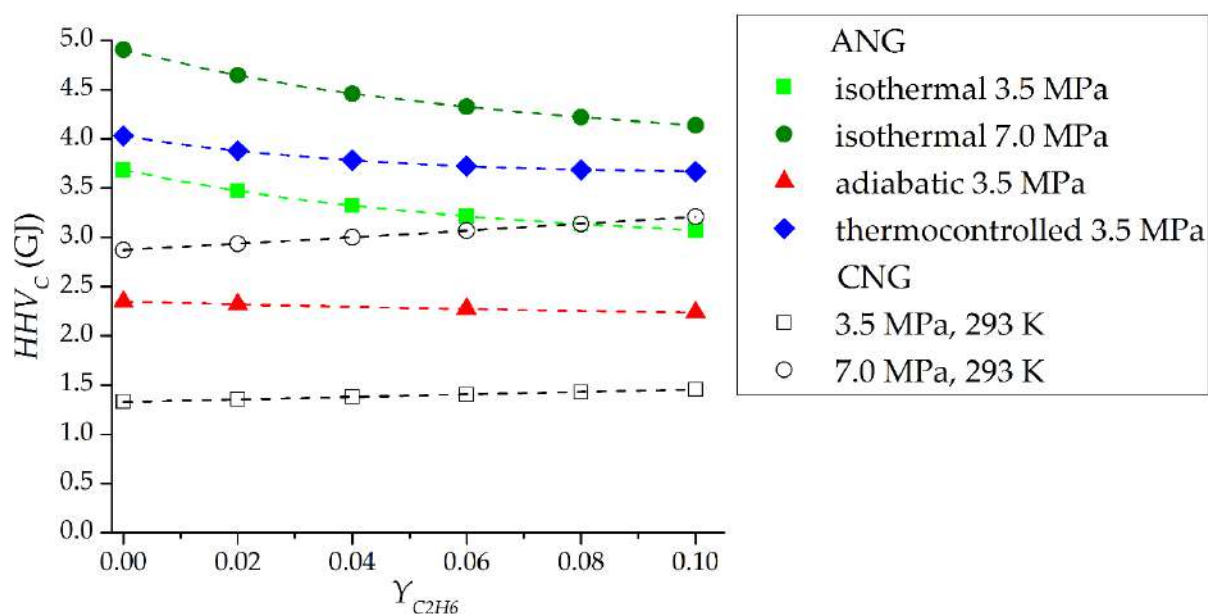


Figure 16. Dependence of the active energy capacity of the gas leaving the storage with a volume of 1 m^3 for 1 cycle based on ACPK adsorbent based on the results of modeling cyclic processes. ANG is the adsorption gas storage. CNG is the conventional gas storage in the “isothermal” mode, without taking into account non-equilibrium intake/exhaust processes.

The simulation results show that the area of effective application of adsorption storages on real natural gas with impurities is smaller than in the case of analyzing their operation on pure methane. Ignoring impurities during the design phase of the adsorption storage can lead to high and unrealistic expectations and will negatively affect real work. It should be noted that the dealing with impurities is possible not only due to the thermal management analyzed in the article, but also using various scheme solutions of the adsorption storage tank.

4. Conclusions

Synthesis of active carbon ACPK from peat raw materials was carried out. The resulting adsorbent has a wide pore size distribution with maxima in the region of a pore radius of 0.59 (main extremum) and 0.92 nm (secondary). The specific volume of micropores is $0.44 \text{ cm}^3/\text{g}$ with a total pore volume of $0.56 \text{ cm}^3/\text{g}$. The adsorption of methane at 3.5 MPa and 293 K was 10.5% wt., which makes it possible to use this adsorbent for the purpose of methane storage under the condition of a high packing density of the adsorbent—for example, in the form of monoliths. Theoretical studies of a binary mixture of methane–ethane (with an ethane content of up to 10 mol.) adsorption were carried out by the IAST method based on experimental adsorption isotherms of pure components. It is shown that at a pressure of 3.5 MPa and 293 K, the higher heating value of the accumulated adsorbate at an ethane concentration of 10% mol. in the gas phase is 8.57 MJ per 1 kg of

adsorbent, while in the case of pure methane this heat is 5.84 MJ/kg, 1.47 times less. Thus, capturing ethane (and other heavy hydrocarbons), for example, from a flowing natural gas stream can significantly increase the capacity of the adsorption storage, provided that the accumulated gases can later be recovered.

Numerical molecular modeling of the methane–ethane mixture adsorption in slit-like model micropores of various widths from 0.6 to 1.8 nm at a temperature of 293 K was carried out. It is shown that this mixture is characterized by the appearing characteristic molecular effects: the displacement of ethane by methane molecules from narrow 1.0 nm-wide micropores, as well as the formation of obvious layers of methane and ethane in wide micropores 1.8 nm wide. However, the integral molecular adsorption isotherm of the mixture, which includes adsorption in pores of various sizes, corresponding to the result of the QSDFT method, is similar in shape to the adsorption isotherm, determined by the IAST method. Thus, various molecular effects observed in individual model micropores together result in the classical adsorption isotherm.

Since the results of numerical molecular modeling showed no contradictions with the IAST model, this approach was used to simulate the cyclic processes of gas charging and discharging from a 1 m³ adsorption storage filled with ACPK adsorbent. Three modes of operation were analyzed: adiabatic, isothermal, and thermocontrolled, which is the opposite of adiabatic. The results of the study showed that in the adiabatic mode, the accumulation of ethane can continue up to about 110 cycles, although the accumulation itself had very little effect on the higher heating value of the gas discharging in the cycle. To a much greater extent, the thermal effects of adsorption themselves were influential, reducing the energy capacity by 27–33%. The thermocontrolled process showed significant efficiency compared to the isothermal one: if on pure methane the advantage in energy capacity was 9.4%, then at 10% mol. ethane the share advantage increased by 19.5% due to a more efficient ethane recovery. Thus, thermal management (heating during discharging) of the adsorption storage is a viable way not only to directly increase the amount of outgoing gas, but also an effective means of dealing with the accumulation of ethane. The analysis of the active energy capacity of the adsorption storage in comparison with a conventional gas one showed that at a relatively high pressure of 7.0 MPa, the capacity of the adsorption storage is 71% higher in the isothermal mode on pure methane and only 29% higher when operating on natural gas with a content of 10% mol. ethane. Thus, it is not enough to evaluate the efficiency of the adsorption storage solely for pure methane; it is necessary to take into account the actual composition of the gas. At a pressure of 3.5 MPa, the efficiency of the adsorption storage is significantly higher than that of the conventional gas storage, especially in the thermocontrolled mode: the active energy capacity is 2.5 times higher at an ethane concentration in the gas of 10% mol. and three times higher when operating on pure methane.

Author Contributions: Conceptualization, A.V.S., E.M.S. and A.A.Z.; methodology, A.V.S., I.E.M. and E.M.S.; software, E.M.S.; validation, S.S.C., A.V.S. and V.V.G.; formal analysis, I.E.M., S.S.C. and A.A.Z.; investigation, I.E.M., A.V.S., E.M.S., S.S.C., V.V.G. and A.E.G.; resources, A.V.S., I.E.M. and A.A.Z.; data curation, A.V.S. and I.E.M.; writing—original draft preparation, E.M.S., S.S.C., A.V.S., I.E.M. and V.V.G.; writing—review and editing, E.M.S., S.S.C., A.V.S. and I.E.M.; visualization, E.M.S., S.S.C., V.V.G. and A.E.G.; supervision, A.A.Z. and A.V.S.; project administration, A.V.S. and A.A.Z.; funding acquisition, A.V.S. All authors have read and agreed to the published version of the manuscript.

Funding: The research was supported by a grant from the Russian Science Foundation (project No. 20-19-00421).

Data Availability Statement: Not applicable.

Conflicts of Interest: The authors declare no conflict of interest. The funders had no role in the design of the study; in the collection, analyses, or interpretation of data; in the writing of the manuscript, or in the decision to publish the results.

References

1. Golovoy, A. Sorbent-containing storage systems for natural gas powered vehicles. *SAE Technical Paper* **1983**, 831070, 39–46.
2. Chugaev, S.S.; Strizhenov, E.M.; Zherdev, A.A.; Kuznetsov, R.A.; Podchufarov, A.A.; Zhidkov, D.A. Fire- and explosion-safe low-temperature filling of an adsorption natural gas storage system. *Chem. Pet. Eng.* **2017**, *52*, 846–854. [CrossRef]
3. Tsivadze, A.Y.; Aksyutin, O.E.; Ishkov, A.G.; Men'Shchikov, I.E.; Fomkin, A.A.; Shkolin, A.V.; Khozina, E.V.; Grachev, V.A. Porous carbon-based adsorption systems for natural gas (methane) storage. *Russ. Chem. Rev.* **2018**, *87*, 950–983. [CrossRef]
4. Biloe, S.; Goetz, V.; Mauran, S. Dynamic discharge and performance of a new adsorbent for natural gas storage. *AIChE J.* **2001**, *47*, 2819–2830. [CrossRef]
5. Mota, J.P.B. Impact of gas composition on natural gas storage by adsorption. *AIChE J.* **1999**, *45*, 986–996. [CrossRef]
6. Pupier, O.; Goetz, V.; Fiscal, R. Effect of cycling operations on an adsorbed natural gas storage. *Chem. Eng. Process.* **2005**, *44*, 71–79. [CrossRef]
7. Rios, R.B.; Bastos-Neto, M.; Amora, M.R., Jr.; Torres, A.E.B.; Azevedo, D.C.S.; Cavalcante, C.L., Jr. Experimental analysis of the efficiency on charge/discharge cycles in natural gas storage by adsorption. *Fuel* **2011**, *90*, 113–119. [CrossRef]
8. Romanos, J.; Rash, T.; Dargham, S.A.; Prosniewski, M.; Barakat, F.; Pfeifer, P. Cycling and regeneration of adsorbed natural gas in microporous materials. *Energy Fuels* **2017**, *31*, 14332–14337. [CrossRef]
9. Walton, K.S.; LeVan, M.D. Natural gas storage cycles: Influence of nonisothermal effects and heavy alkanes. *Adsorption* **2006**, *12*, 227–235. [CrossRef]
10. Prosniewski, M.; Rash, T.; Romanos, J.; Gillespie, A.; Stalla, D.; Knight, E.; Smith, A.; Pfeifer, P. Effect of cycling and thermal control on the storage and dynamics of a 40-L monolithic adsorbed natural gas tank. *Fuel* **2019**, *244*, 447–453. [CrossRef]
11. Bell, I.H.; Wronski, J.; Quoilin, S.; Lemort, V. Pure and pseudo-pure fluid thermophysical property evaluation and the open-source thermophysical property library CoolProp. *Ind. Eng. Chem. Res.* **2014**, *53*, 2498–2508. [CrossRef] [PubMed]
12. Dubinin, M.M.; Radushkevich, L.V. Equation of the characteristic curve of activated charcoal. *Proc. Acad. Sci. Phys. Chem. Sect. USSR* **1947**, *55*, 331–333.
13. Dubinin, M.M. Physical adsorption of gases and vapors in micropores. *Prog. Surf. Membr. Sci.* **1975**, *9*, 1–70.
14. Brunauer, S.; Emmett, P.H.; Teller, E. Adsorption of gases in multimolecular layers. *J. Am. Chem. Soc.* **1938**, *60*, 309–319. [CrossRef]
15. Rouquerol, J.; Llewellyn, P.; Rouquerol, F. Is the BET equation applicable to microporous adsorbents? *Stud. Surf. Sci. Catal.* **2007**, *160*, 49–56.
16. Gregg, S.J.; Sing, K.S.W. *Adsorption, Surface Area and Porosity*; Academic Press: London, UK; New York, NY, USA, 1982.
17. Neimark, A.V.; Lin, Y.; Ravikovitch, P.I.; Thommes, M. Quenched solid density functional theory and pore size analysis of micro-mesoporous carbons. *Carbon* **2009**, *47*, 1617–1628. [CrossRef]
18. Shkolin, A.V.; Fomkin, A.A. Measurement of carbon-nanotube adsorption of energy-carrier gases for alternative energy systems. *Meas. Tech.* **2018**, *61*, 395–401. [CrossRef]
19. Fomkin, A.A.; Shkolin, A.V.; Men'shchikov, I.E.; Pulin, A.L.; Pribylov, A.A.; Smirnov, I.A. Measurement of adsorption of methane at high pressures for alternative energy systems. *Meas. Tech.* **2016**, *58*, 1387–1391. [CrossRef]
20. Pribylov, A.A.; Serpinski, V.V.; Kalashnikov, S.M. Adsorption of gases by microporous adsorbents under pressures up to hundreds of megapascals. *Zeolites* **1991**, *11*, 846–849. [CrossRef]
21. Salehi, E.; Taghikhani, V.; Ghotbi, C. Theoretical and experimental study on the adsorption and desorption of methane by granular activated carbon at 25 °C. *J. Nat. Gas Chem.* **2007**, *16*, 415–422. [CrossRef]
22. Men'shchikov, I.E.; Shkolin, A.V.; Strizhenov, E.M.; Khozina, E.V.; Chugaev, S.S.; Shiryaev, A.A.; Fomkin, A.A.; Zherdev, A.A. Thermodynamic behaviors of adsorbed methane storage systems based on nanoporous carbon adsorbents prepared from coconut shells. *Nanomaterials* **2020**, *10*, 2243. [CrossRef] [PubMed]
23. Shkolin, A.V.; Fomkin, A.A. Thermodynamics of methane adsorption on the microporous carbon adsorbent ACC. *Russ. Chem. Bull.* **2008**, *57*, 1799–1805. [CrossRef]
24. Strizhenov, E.M.; Zherdev, A.A.; Podchufarov, A.A.; Chugaev, S.S.; Kuznetsov, R.A.; Zhidkov, D.A. Capacity and thermodynamic nomograph for an adsorption methane storage system. *Chem. Pet. Eng.* **2016**, *51*, 812–818. [CrossRef]
25. Guggenheim, E.A. *Thermodynamics: An Advanced Treatise for Chemists and Physicists*; North-Holland: Amsterdam, The Netherlands, 1967.
26. Myers, A.; Prausnitz, J.M. Thermodynamics of mixed-gas adsorption. *AIChE J.* **1965**, *11*, 121–127. [CrossRef]
27. Walton, K.S.; Sholl, D.S. Predicting multicomponent adsorption: 50 years of the ideal adsorbed solution theory. *AIChE J.* **2015**, *61*, 2757–2762. [CrossRef]
28. Chen, J.; Loo, L.S.; Wang, K. An ideal adsorbed solution theory (IAST) study of adsorption equilibria of binary mixtures of methane and ethane on a templated carbon. *J. Chem. Eng. Data* **2011**, *56*, 1209–1212. [CrossRef]
29. Rackers, J.A.; Laury, M.L.; Li, C.; Wang, Z.; Lagardère, L.; Piquemal, J.P.; Ren, P.; Jay, W. TINKER 8: A modular software package for molecular design and simulation ponder. *J. Chem. Theor. Comp.* **2018**, *14*, 5273–5289. [CrossRef]
30. Maxwell, D.S.; Rives, J.T. Development and testing of the OPLS All-Atom Force Field on Conformational Energetics and Properties of Organic Liquids. *J. Am. Chem. Soc.* **1996**, *118*, 11225–11236.
31. Tolmachev, A.M.; Anuchin, K.M.; Kryuchenkova, N.G.; Fomkin, A.A. Theoretical calculation of the isotherms of adsorption on active coals using the molecular dynamics method. *Prot. Met. Phys. Chem. Surf.* **2011**, *47*, 150–155. [CrossRef]
32. Andersen, H.C. Molecular dynamics simulations at constant pressure and/or temperature. *J. Chem. Phys.* **1980**, *72*, 2384. [CrossRef]

33. Strizhenov, E.M.; Chugaev, S.S.; Shelyakin, I.D.; Shkolin, A.V.; Men'shchikov, I.E.; Zherdev, A.A. Numerical modeling of heat and mass transfer in an adsorbed natural gas storage tank with monolithic active carbon during charging and discharging processes. *Heat Mass Transf.* **2022**, *1*–14. [CrossRef]
34. Chugaev, S.S.; Strizhenov, E.M.; Men'shchikov, I.E.; Shkolin, A.V. Carbon nanoporous monoblocks for mobile natural gas adsorption storage systems operating under arctic conditions. *Nanobiotechnol. Rep.* **2022**, *17*, 541–549.
35. Strizhenov, E.M.; Chugaev, S.S.; Men'shchikov, I.E.; Shkolin, A.V.; Zherdev, A.A. Heat and mass transfer in an adsorbed natural gas storage system filled with monolithic carbon adsorbent during circulating gas charging. *Nanomaterials* **2021**, *11*, 3274. [CrossRef] [PubMed]
36. Chugaev, S.S.; Strizhenov, E.M.; Men'shchikov, I.E.; Shkolin, A.V. Experimental study of the thermal management process at low-temperature circulating charging of an adsorbed natural gas storage system. *J. Phys. Conf. Ser.* **2021**, *2116*, 012084. [CrossRef]
37. Strizhenov, E.M.; Chugaev, S.S.; Men'shchikov, I.E.; Shkolin, A.V.; Shelyakin, I.D. Experimental study of heat transfer in adsorbed natural gas storage system filled with microporous monolithic active carbon. *J. Phys. Conf. Ser.* **2021**, *2116*, 012085. [CrossRef]
38. Guinier, A. La diffraction des rayons X aux tres petits angles: Application a l'etude de phenomenes ultramicroscopiques. *Ann. Phys.* **1939**, *11*, 161–237. [CrossRef]
39. Dubinin, M.M.; Plavnik, G.M. Microporous structures of carbonaceous adsorbents. *Carbon* **1968**, *6*, 183–192. [CrossRef]
40. Thommes, M.; Kaneko, K.; Neimark, A.V.; Oliver, J.P.; Rodrigues-Reinoso, F.; Rouquerol, J.; Sing, K. Physisorption of gases, with special reference to the evaluation of surface area and pore size distribution (IUPAC Technical Report). *Pure Appl. Chem.* **2015**, *87*, 1051–1069. [CrossRef]
41. Shkolin, A.V.; Fomkin, A.A. Theory of volume filling of micropores applied to the description of methane adsorption on the microporous carbon adsorbent AUK. *Russ. Chem. Bull.* **2009**, *58*, 717–721. [CrossRef]
42. Strizhenov, E.M.; Zherdev, A.A.; Petrochenko, R.V.; Zhidkov, D.A.; Kuznetsov, R.A.; Chugaev, S.S.; Podchufarov, A.A.; Kurnasov, D.V. A study of methane storage characteristics of compacted adsorbent AU-1. *Chem. Pet. Eng.* **2017**, *52*, 838–845. [CrossRef]
43. Men'shchikov, I.E.; Fomkin, A.A.; Tsivadze, A.Y.; Shkolin, A.V.; Strizhenov, E.M.; Khozina, E.V. Adsorption accumulation of natural gas based on microporous carbon adsorbents of different origin. *Adsorption* **2017**, *23*, 327–339. [CrossRef]
44. Shkolin, A.V.; Fomkin, A.A.; Men'shchikov, I.E.; Strizhenov, E.M.; Pulin, A.L.; Khozina, E.V. Monolithic microporous carbon adsorbent for low-Temperature natural gas storage. *Adsorption* **2019**, *25*, 1559–1573. [CrossRef]
45. Solovtsova, O.V.; Chugaev, S.S.; Men'shchikov, I.E.; Pulin, A.L.; Shkolin, A.V.; Fomkin, A.A. High-density carbon adsorbents for natural gas storage. *Colloid J.* **2020**, *82*, 719–726. [CrossRef]
46. Shkolin, A.V.; Men'shchikov, I.E.; Khozina, E.V.; Yakovlev, V.Y.; Simonov, V.N.; Fomkin, A.A. Deformation of microporous carbon adsorbent sorbonorit-4 during methane adsorption. *J. Chem. Eng. Data* **2022**, *67*, 1699–1714. [CrossRef]
47. Men'shchikov, I.E.; Shkolin, A.V.; Fomkin, A.A.; Khozina, E.V. Thermodynamics of methane adsorption on carbon adsorbent prepared from mineral coal. *Adsorption* **2021**, *27*, 1095–1107. [CrossRef]
48. Inagaki, M. *New Carbons. Control of Structure and Functions*; Elsevier: Oxford, UK, 2000.
49. Dubinin, M.M. Microporous systems of carbon adsorbents. In *Carbon Adsorbents and Their Industrial Application*; Nauka: Moscow, Russia, 1983; pp. 100–115.
50. Men'shchikov, I.E.; Fomkin, A.A.; Shkolin, A.V.; Yakovlev, V.Y.; Khozina, E.V. Optimization of structural and energy characteristics of adsorbents for methane storage. *Russ. Chem. Bull.* **2018**, *67*, 1814–1822. [CrossRef]



Article

Extended Line Defect Graphene Modified by the Adsorption of Mn Atoms and Its Properties of Adsorbing CH₄

Chenxiaoyu Zhang , Shaobin Yang *, Xu Zhang, Yingkai Xia and Jiarui Li

College of Material Science and Engineering, Liaoning Technical University, Fuxin 123000, China; ZCXY202201@163.com (C.Z.); zhangxu220120@163.com (X.Z.); xiayingkai200719@126.com (Y.X.); LJ220128@163.com (J.L.)

* Correspondence: ysbld@163.com; Tel.: +86-0418-5110098

Abstract: Extended line defect (ELD) graphene is a two-dimensional (2D) topologically defective graphene with alternate octagonal and quadrilateral carbon rings as basic defective units. This paper reports on the CH₄ adsorption properties of ELD graphene according to the first principles of density functional theory (DFT). The effects on the CH₄ adsorption of ELD graphene when modified by a single Mn atom or two Mn atoms were investigated, respectively. An ELD-42C graphene configuration consisting of 42 C atoms was first constructed. Then, the ELD-42C graphene configuration was used as a substrate, and a Mn-ELD-42C graphene configuration was obtained by modifying it with a single Mn atom. The results showed that the most stable adsorption site for Mn atoms was above the quadrilateral carbon ring. This Mn-ELD-42C graphene configuration could only stably adsorb up to 30 CH₄ molecules on each side, with an average adsorption energy of -0.867 eV/CH₄ and an adsorption capacity of 46.25 wt%. Three 2Mn-ELD-42C graphene configurations were then obtained by modifying the ELD-42C graphene substrate with two Mn atoms. When the two Mn atoms were located on either side of a 2Mn-ELD-42C graphene configuration and above the two octagonal carbon rings adjacent to the same quadrilateral carbon ring, it was able to adsorb up to 40 CH₄ molecules on each side, with an average adsorption energy of -0.862 eV/CH₄ and a CH₄ adsorption capacity of 51.09 wt%.

Keywords: first principles; graphene; extended line defect; CH₄ adsorption; Mn modification

Citation: Zhang, C.; Yang, S.; Zhang, X.; Xia, Y.; Li, J. Extended Line Defect Graphene Modified by the Adsorption of Mn Atoms and Its Properties of Adsorbing CH₄.

Nanomaterials **2022**, *12*, 697.

<https://doi.org/10.3390/nano12040697>

nano12040697

Academic Editor: Mads Brandbyge

Received: 27 January 2022

Accepted: 17 February 2022

Published: 19 February 2022

Publisher's Note: MDPI stays neutral with regard to jurisdictional claims in published maps and institutional affiliations.



Copyright: © 2022 by the authors. Licensee MDPI, Basel, Switzerland. This article is an open access article distributed under the terms and conditions of the Creative Commons Attribution (CC BY) license (<https://creativecommons.org/licenses/by/4.0/>).

1. Introduction

CH₄ is abundant in nature and has a higher energy density than fossil fuels such as petroleum and coal. It is also a relatively clean fuel, with the lowest rate of CO₂ emissions of all carbonaceous fuels [1,2]. It has therefore been widely recognized as a transitional resource until alternatives to oil and coal can be found and developed on a large enough scale [3,4]. As a result, studies on CH₄ adsorption and its storage have important practical significance for energy development and use as well as environmental protection.

Graphene is a new kind of two-dimensional (2D) honeycomb-shaped nanomaterial characterized by good mechanical properties, good hydrogen storage and a high sensitivity to as well as adsorption potential for certain types of gases [5]. Zhao et al. [6] found that pristine graphene has a weak adsorption capacity for CH₄, with an average adsorption energy of -0.227 eV/CH₄. Ghanbari et al. [7] found that the adsorption energy could be improved to -0.166 eV when the graphene was modified with Ag atoms (Ag-G). This implies that physical absorption occurs between Ag atoms and graphene. Xu et al. [8] used Ti atoms to modify graphene and found that the modified graphene was most stable when the Ti atoms were located above the top carbon rings. This had an average adsorption energy of -0.298 eV/CH₄. The United States Department of Energy (DOE) established a CH₄ storage objective for vehicles in 2012, where the goal was to have a CH₄ adsorption capacity of above 50 wt% under standard conditions [9]. Unfortunately, the majority of CH₄ storage materials still fail to meet this requirement.

Pristine graphene is composed of a single layer of carbon atoms in the form of sp^2 hybrid orbitals and has a perfect hexagonal carbon ring structure [10]. During its growth, graphene typically acquires defects such as monovacancy, divacancy, Stone–Wales (SW), and topological lines [11]. These defects have been proven to be conducive to the adsorption of CH_4 . Xiong et al. [12] constructed an extended line defect (ELD) graphene periodically embedded with quadrilateral and octagonal carbon rings by means of surface synthesis. ELD graphene is a type of semiconductor with a unique carbon ring structure and special chemical, electronic and mechanical properties, with a reduced band gap [13]. A large number of studies have shown that the CH_4 adsorption properties of graphene can be further improved by doping atoms to introduce additional structural modifications. Existing studies on transition metal (TM)-modified ELD graphene have concentrated on the magnetic and electronic properties of the configurations after modification. Cheng et al. [14] found that a single TM atom is preferentially adsorbed at defect sites in ELD graphene where there is high chemical activity. When modified by TM atoms, an ELD graphene substrate displays magnetism and spin polarization. Yu et al. [15] investigated the 558-type ELD, which is composed of a periodic repetition of one octagonal and two pentagonal rings, embedded in the hexagonal lattice of a graphene sheet. They found that the magnetism of the TM atom depends on the adsorption sites and the type of the adatoms, which can be obtained by analyzing the underlying hybridization mechanism between 3d orbitals of the TM atom and the electronic states of the ELD. Guan et al. [16] calculated defective graphene nanoribbon and TM adsorption on a line-defective embedded graphene sheet. The results show that TM atom adsorption on graphene can introduce magnetism and spin polarization, which is at the ferromagnetic ground state and shows different electronic properties according to different metals.

Manganese (Mn) is a transition metal, with reserves of about 570 million tons worldwide, that can be made by aluminothermic reduction of soft manganese ore [17,18]. Manganese is easily oxidized to manganese dioxide [19]. Manganese dioxide is an excellent adsorbent material due to its large specific surface area and strong electrochemical properties [20]. Manganese is located in the fourth period of the chemical periodic table in Group VIIB. The valence electronic configuration of manganese atom is $3d^5 4s^2$, with more electrons and empty orbitals at the 3d energy level, which helps to enhance chemical bonding between manganese atoms and other molecules, allowing manganese atoms to adsorb gaseous molecules more efficiently [21,22]. In the laboratory, potassium permanganate or manganese dioxide is used as a catalyst to prepare graphene, resulting in the produced graphene containing a certain number of Mn atoms in its structure [23,24].

This paper presents an analysis of the adsorption properties of ELD graphene for CH_4 , working from first principles [25]. It looks at the CH_4 adsorption properties of ELD graphene modified with a single Mn atom or two Mn atoms and calculates the resulting CH_4 adsorption capacity. This study offers theoretical support for the preparation and industrial application of new CH_4 storage materials.

2. Calculation Methods and Models

This paper is based on a first-principles pseudopotential plane-wave (PSPW) method that comes from density functional theory (DFT) [26,27]. DFT calculations have been applied successfully to analyze the defective carbon-based graphene-like systems containing the same type of defects as in this paper, such as carbon-based fullerene-like sulfocarbide [28], fullerene-like phosphorus carbide [29] and graphene-like model systems based on coronene and corannulene molecules [30]. The goal of the study was to investigate the CH_4 adsorption properties of ELD graphene as well as ELD graphene when modified by a single Mn atom or two Mn atoms at an atomic level by using the Cambridge Sequential Total Energy Package (CASTEP) module in the Materials Studio software [31]. Perdew–Burke–Ernzerhof (PBE) and generalized gradient approximation (GGA) functionals were selected for the calculations [32], and the interaction between electrons and ions was approximately calculated using OTFG ultrasoft. If the adsorption energy calculated by

the GGA functional is weak, the adsorption energy can be corrected by means of a DFT dispersion correction (van der Waals) functional (namely DFT-D) [33]. The convergence criteria to optimize the calculations for atoms within the objects of study were set as follows: a maximum stress of 0.05 eV/Å; a maximum displacement of 0.002 Å; a convergence energy of 2.0×10^{-5} eV/atom; and a self-consistent field (SCF tolerance) convergence threshold of 2.0×10^{-6} eV/atom. To ensure the calculation accuracy and reduce the calculation cost, the truncation energy was set at 450 eV, the K-point sampling was set at $5 \times 5 \times 1$, and the objects of study were integrated in a Brillouin zone with Monkhorst–Pack grids [34,35]. The periodic boundary conditions to be met for the calculation of ELD graphene unit cells and the vacuum layer were set at 30 Å to avoid mutual interference between layers.

An ELD-42C graphene configuration consisting of 42 C atoms was constructed using graphene unit cells, with a main body that was composed of continuous quadrilateral, hexagonal and octagonal carbon rings. Its geometrical configuration after structural optimization is shown in Figure 1. The length of all the C-C bonds that constitute pristine graphene is 1.42 Å. According to an analysis of the ELD-42C graphene configuration after optimization, the lengths of the three C-C bonds that constituted the octagonal carbon rings were 1.48 Å, 1.39 Å and 1.41 Å, respectively. For the two C-C bonds that constituted the quadrilateral carbon rings, the lengths were 1.39 Å and 1.47 Å, respectively. In comparison to pristine graphene, some of the C-C bonds (1.39 Å and 1.41 Å) of the ELD-42C graphene configuration were slightly compressed, and some (1.48 Å and 1.47 Å) were slightly stretched. This is consistent with the experimental results in Liu et al. [36] and Zhao et al. [37] and coincides closely with the simulation results in Ding et al. [38]. This confirms the validity of the ELD-42C graphene configuration design.

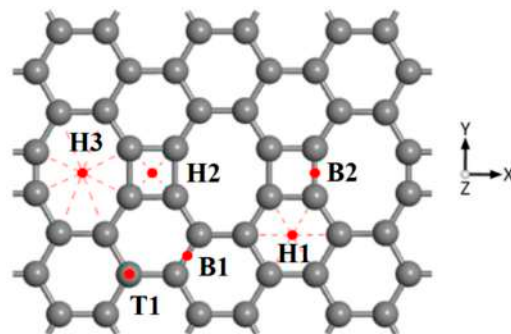


Figure 1. ELD-42C graphene configuration after structural optimization (the gray balls represent carbon atoms). H1, H2 and H3 indicate the hole sites; T1 stands for the top site; and B1 as well as B2 refer to the bridge sites.

For the iMn -ELD-42C graphene configurations obtained after modification by the Mn atoms, the binding energy, $E_{b_{iMn}}$, and average binding energy, $\overline{E_{b_{iMn}}}$, of the Mn atoms can be defined as follows:

$$E_{b_{iMn}} = E_{iMn-ELD-42C} - (E_{ELD-42C} + E_{iMn}) \quad (1)$$

$$\overline{E_{b_{iMn}}} = [E_{iMn-ELD-42C} - E_{ELD-42C} - E_{iMn}] / i \quad (2)$$

where i indicates the number of Mn atoms for modification; $E_{iMn-ELD-42C}$ refers to the total energy of the iMn -ELD-42C graphene configurations; $E_{ELD-42C}$ stands for the total energy of the ELD-42C graphene configurations; and E_{iMn} represents the total energy of the i -free Mn atom(s).

For the CH_4 molecules in the $jCH_4 \leftrightarrow iMn$ -ELD-42C graphene adsorption configurations, the binding energy, E_{ad} , average binding energy, $\overline{E_{ad}}$, and PBW by percentage of weight can be defined as follows:

$$E_{ad} = E_{jCH_4 \leftrightarrow iMn-ELD-42C} - E_{(j-1)CH_4 \leftrightarrow iMn-ELD-42C} - E_{CH_4} \quad (3)$$

$$\overline{E_{ad}} = [E_{jCH_4 \leftrightarrow iMn-ELD-42C} - E_{iMn-ELD-42C} - jE_{CH_4}] / j \quad (4)$$

where j indicates the number of CH_4 molecule(s) adsorbed; $E_{jCH_4 \leftrightarrow iMn-ELD-42C}$ refers to the total energy of the $jCH_4 \leftrightarrow iMn-ELD-42C$ graphene adsorption configurations; $E_{(j-1)CH_4 \leftrightarrow iMn-ELD-42C}$ stands for the total energy of the $(j - 1)CH_4 \leftrightarrow iMn-ELD-42C$ graphene adsorption configurations; jE_{CH_4} represents the total energy of the j -free CH_4 molecule(s); and $M_r(CH_4)$, $M_r(Mn)$ and $M_r(ELD)$ represent the weight of each CH_4 molecule, each Mn atom and the ELD system, respectively.

3. Results and Discussion

3.1. CH_4 Adsorption in the ELD-42C Graphene Configuration

Six typical CH_4 adsorption sites were selected to be studied on account of the symmetry of the geometric structure of the ELD-42C graphene configuration, as shown in Figure 1. H indicates a hole in a carbon ring, with H1, H2 and H3 representing the centroid sites of the hexagonal, quadrilateral and octagonal carbon rings, respectively. T1 stands for the top site of a C atom and B refers to the bridge site of a C-C bond, with B1 indicating the bridge sites in the hexagonal carbon rings and B2 representing the bridge sites in the defective rings (i.e., the quadrilateral and octagonal carbon rings). There were three adsorption forms for CH_4 molecules adsorbed on the ELD-42C graphene configuration according to the orientations of the four H atoms of the CH_4 molecules relative to the plane of the ELD-42C graphene configuration, as shown in Figure 2. Adsorption properties are affected by the adsorption sites for CH_4 molecules on the graphene, not the orientation of H atoms in the CH_4 molecules [39]. Therefore, the CH_4 adsorption form with three H atoms orientated to the plane of the ELD-42C graphene configuration (Figure 2c) was selected to study the adsorption properties at different sites. The CH_4 adsorption energy, E_{ad} ; vertical distance, d , between the C atoms in the CH_4 molecules and the plane of the ELD-42C graphene configuration; and bond angle, $\angle H-C-H$, between the C atoms and the H atoms in the CH_4 molecules were calculated for a CH_4 molecule adsorbed at the six typical adsorption sites of the ELD-42C graphene configuration. The results are shown in Table 1.

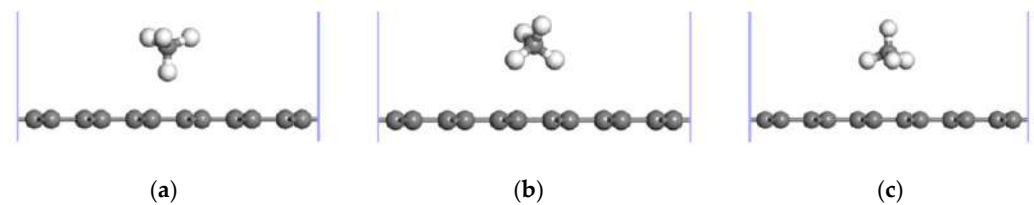


Figure 2. Three adsorption forms of CH_4 molecules in relation to the ELD-42C graphene configuration. (a–c) indicate that 1, 2 or 3 H atom(s) in the CH_4 molecule are oriented to the plane of the ELD-42C graphene configuration, respectively.

Table 1. Adsorption energy, E_{ad} , of the $CH_4 \leftrightarrow$ ELD-42C graphene adsorption configuration; vertical distance, d , between the C atoms in the CH_4 molecules and the plane of the ELD-42C graphene configuration; and bond angle, $\angle H-C-H$, between the C atoms and H atoms in the CH_4 molecules.

The Absorption Point of CH_4	E_{ad} (eV)	d (Å)	$\angle H-C-H$ (°)
H1	−0.824	3.291	109.507
H2	−0.833	3.222	109.878
H3	−0.847	3.081	109.551
T1	−0.835	3.278	109.554
B1	−0.832	3.251	109.811
B2	−0.830	3.251	109.560

Table 1 shows the adsorption energy released, E_{ad} , after one CH_4 molecule was adsorbed at the six adsorption sites in the ELD-42C graphene configuration. The larger its absolute value, the more energy released and the more stable the corresponding $CH_4 \leftrightarrow$

ELD-42C graphene adsorption configuration. It can be seen that the largest absolute value (-0.847 eV) was at H3, indicating that the ELD-42C graphene configuration was at its most stable at H3 when adsorbing CH_4 molecules, compared with the other five adsorption sites. Thus, the CH_4 molecules tended to stay above the octagonal carbon ring, as shown in Figure 3. For free CH_4 molecules, the length of bonds between the C and H atoms is 1.110 Å, and the bond angle is 109.381° . According to [40], the adsorption height of gas molecules is about three times their bond length, so the adsorption height of the CH_4 molecules was preset as 3.28 Å. After structural optimization, the vertical distance, d , between the CH_4 molecules at the six adsorption sites and the plane of the ELD-42C graphene configuration was analyzed. It was found that the difference between the stable adsorption height and the preset adsorption height was between 0.002 Å and 0.199 Å, indicating that the preset adsorption height was reasonable. The bond angle between the C and H atoms was close to that of CH_4 molecules adsorbed by the ELD-42C graphene configuration in their free state [41,42], so the adsorption for CH_4 on the ELD-42C graphene configuration was physical.

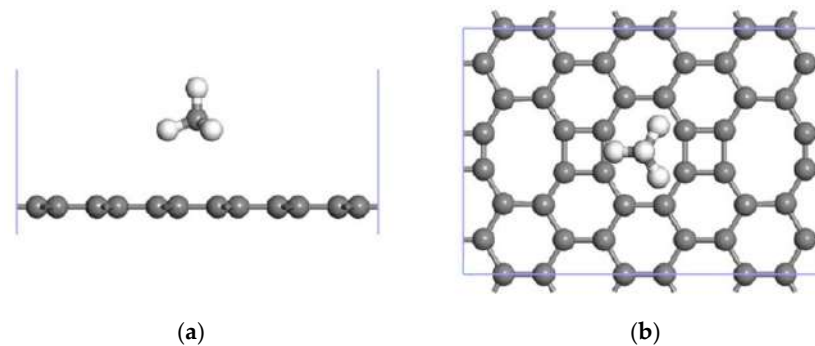


Figure 3. $\text{CH}_4 \leftrightarrow$ ELD-42C graphene adsorption configuration with 1 CH_4 molecule being adsorbed at H3 (gray balls represent carbon atoms, and white balls represent hydrogen atoms). (a) Front view; (b) top view.

CH_4 molecules were preferentially adsorbed by the ELD-42C graphene configuration at H3. They were then adsorbed at T1 after being fully adsorbed at H3. The ELD-42C graphene configuration could stably adsorb 26 CH_4 molecules at most on each side, with an average adsorption energy of -0.842 eV/ CH_4 and an adsorption configuration similar to the one shown in Figure 4. According to the technical standards for natural gas adsorption systems issued by the DOE [43], the adsorption capacity of CH_4 storage materials should not be less than 50 wt%. For $26\text{CH}_4 \leftrightarrow$ ELD-42C graphene adsorption configurations, the CH_4 adsorption capacity was 45.26 wt%, which is lower than the technical standard; therefore, the ELD-42C graphene configuration was still not suitable for practical applications.

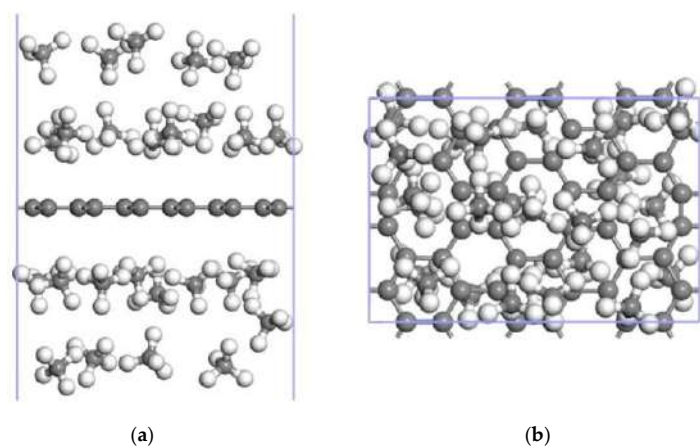


Figure 4. $8\text{CH}_4 \leftrightarrow$ ELD-42C graphene adsorption configuration (gray balls represent carbon atoms, and white balls represent hydrogen carbons). (a) Front view; (b) top view.

3.2. CH₄ Adsorption in the Mn-ELD-42C Graphene Configuration

3.2.1. Modification of the ELD-42C Graphene Configuration by a Single Mn Atom

Jia et al. [2] found that pristine graphene doped with heteroatoms or pristine graphene with structural defects is significantly better able to adsorb gas molecules. Xu et al. [44] believed that the adsorption properties of graphene for gas molecules can be best improved by modifying graphene with alkali metals, alkaline earth metals and TM. Mn is an important TM element that is widely distributed throughout the Earth's crust. Its valence electron configuration is 3d⁵4s², and chemical bonds can be easily formed between Mn and carbon atoms [45–47]. Due to its weak adsorption properties for CH₄ molecules, the ELD-42C graphene configuration was modified with TM Mn atoms to construct iMn-ELD-42C graphene configurations (where *i* indicates the number of Mn atoms, *i* = 1, 2). Their adsorption properties for CH₄ were then studied.

When the ELD-42C graphene configuration was modified by a single Mn atom, there were six optional adsorption sites for the Mn atoms: the hole sites, H1, H2 and H3; the bridge sites, B1 and B2; and the top site, T1 (see Figure 1). A single Mn atom, respectively placed at T1, B1 and B2 during the construction of the Mn-ELD-42C configurations, always moved to the top of the adjacent carbon ring under the action of the chemical bonds as the structure was optimized. This is in line with the optimal adsorption site of TM atoms determined by Zhao et al. [6] and Liu et al. [48]. The adsorption characteristics of the Mn atoms at H1, H2 and H3 were calculated, and the results are given in Table 2.

Table 2. Adsorption characteristics of a single Mn atom at H1, H2 and H3 on Mn-ELD-42C graphene configurations.

The Absorption Point of a Single Mn Atom	$E_{b_{Mn}}$ (eV)	Distance (Å)				$\Delta\rho$ (e)
		BL1	BL2	BL3	BL4	
H1	−2.922	2.037	2.037	2.104	2.105	0.29
H2	−3.453	2.967	2.974	2.974	2.981	0.39
H3	−3.218	2.113	2.128	2.430	2.431	0.33

In the table, $E_{b_{Mn}}$ (eV) indicates the binding energy of a single Mn atom; BL1, BL2, BL3 and BL4, respectively, refer to the length of the bonds between the Mn atoms and C atoms; and $\Delta\rho$ (e) represents the charge transfer between the Mn atoms and the ELD-42C graphene configuration. It can be seen from Table 2 that the binding energy of a single Mn atom was different at H1, H2 and H3. At H2 it was −3.453 eV. This was the largest absolute value out of the three hole sites. The binding energy of a single Mn atom at H1 was −2.922 eV, which was the smallest absolute value. These results indicated that Mn atoms adsorbed above H2 were the most stable, while Mn atoms adsorbed above H1 were the least stable. During modification, four Mn-C chemical bonds were formed between the Mn atoms and the four carbon atoms at H2, with lengths of 2.967 Å, 2.974 Å, 2.974 Å and 2.981 Å, respectively. This suggests that most of the Mn atoms were adsorbed on the central axis of H2. The charge transferred from the Mn atoms to the ELD-42C graphene configuration was 0.33 e at H3 and 0.29 e at H1. Therefore, the interaction between the ELD-42C graphene configuration and Mn atoms adsorbed at H1 and H3 was weaker than it was at H2. The most stable Mn-ELD-42C graphene system configuration (Figure 5) was therefore obtained via structural optimization after it had been modified by a single Mn atom at H2.

The Mulliken layout of the Mn-ELD-42C graphene configuration before and after adsorbing a single CH₄ molecule was analyzed. It was found that the charge transferred from the Mn atoms to the ELD-42C graphene configuration was 0.69 e, indicating a strong electrostatic effect between the two. The partial density of states (PDOS) for the Mn-ELD-42C graphene configuration is shown in Figure 6 (partial). There were resonance peaks between the d orbit of the Mn atoms and the *p* orbit of the C atoms within the range of −1.958 to −1.381 eV, confirming that there was interaction between the two orbits. As a

result, the valence band of the Mn-ELD-42C graphene configuration largely derives from the interaction between the d orbit of the Mn atoms and the p orbit of the C atoms. This is similar to the results obtained by Wu et al. [49] and Zhao et al. [37], who modified graphene substrates by using TM atoms as a doping agent. As extra electrons were provided to the ELD-42C graphene configuration by the Mn atoms, the overall conduction band of the configuration moved to the Fermi level, where the conduction band intersected with the valence band and endowed the Mn-ELD-42C graphene configuration with typical metallic-phase characteristics.

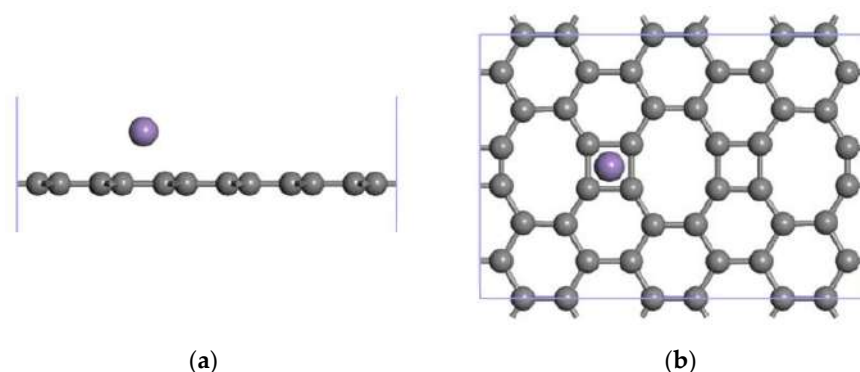


Figure 5. The most stable Mn-ELD-42C graphene configuration was obtained by modifying the hole site H2 with a single Mn atom (gray balls represent carbon atoms, and purple balls represent Mn atoms). (a) Front view; (b) top view.

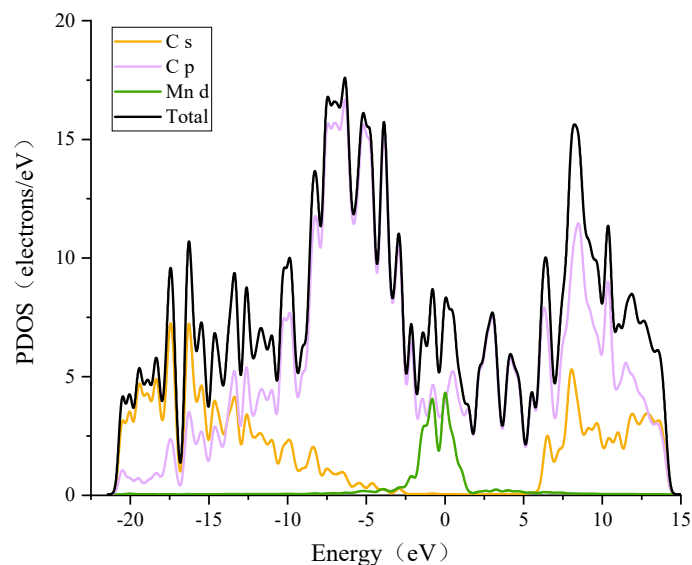


Figure 6. PDOS diagram of the Mn-ELD-42C graphene system (partial).

3.2.2. Adsorption of CH_4 by the Mn-ELD-42C Graphene Configuration

DFT was used to study the CH_4 adsorption capacity of the Mn-ELD-42C graphene configuration by adding CH_4 molecules to one side. A stable $\text{CH}_4 \leftrightarrow \text{Mn-ELD-42C}$ adsorption configuration (Figure 7a) was obtained after the Mn-ELD-42C graphene configuration with the first adsorbed CH_4 molecule had been optimized. The first CH_4 molecule was located above the Mn atom, proving that this was where the adsorption energy was the largest. The adsorption energy of this configuration was -1.717 eV, which is larger than that of the ELD-42C graphene configuration for CH_4 molecules (-0.847 eV), of Li-modified carbon nanotubes for CH_4 (-0.464 eV) [50] and of Pt-modified graphene for CH_4 (-0.488 eV) [51]. Apparently, modifying the ELD-42C graphene configuration with a single Mn atom improved its adsorption properties for CH_4 molecules. A $2\text{CH}_4 \leftrightarrow \text{Mn-ELD-42C}$ adsorption

configuration was obtained after a second CH_4 molecule had been added (Figure 7b). Here, both the first and the second CH_4 molecules were located above the Mn atoms and close to the Mn-ELD-42C graphene configuration. The combined action of the mutual repulsion of the CH_4 molecules and their adsorption by the Mn-ELD-42C graphene configuration enabled a third CH_4 molecule to be adsorbed above the hexagonal carbon ring that was close to the Mn atoms (Figure 7c). A fourth CH_4 molecule was adsorbed at T1 above the C atoms (Figure 7d), and a fifth above the octagonal carbon ring (Figure 7e). Limited by the adsorption space, the repulsive force between the molecules gradually increased as more CH_4 molecules were adsorbed. The adsorption configuration began to arc when an eighth molecule was adsorbed (Figure 7f), and there was a stratification phenomenon when the ninth molecule was adsorbed (Figure 7g). Due to their layered adsorption, the distances between the 9th–16th CH_4 molecules and the Mn atom became larger, and the adsorption energy was reduced. The 16th CH_4 molecule was nowhere near the Mn atom and was the most distant from the Mn-ELD-42C graphene configuration. It also had the lowest adsorption energy (-0.755 eV). When a 17th CH_4 molecule was placed on one side of the configuration, the calculated adsorption energy became positive, indicating that the gas molecule had not been adsorbed. This proved that the Mn-ELD-42C graphene configuration could only stably adsorb up to 16 CH_4 molecules on each side. The geometrical configuration is shown in Figure 7h.

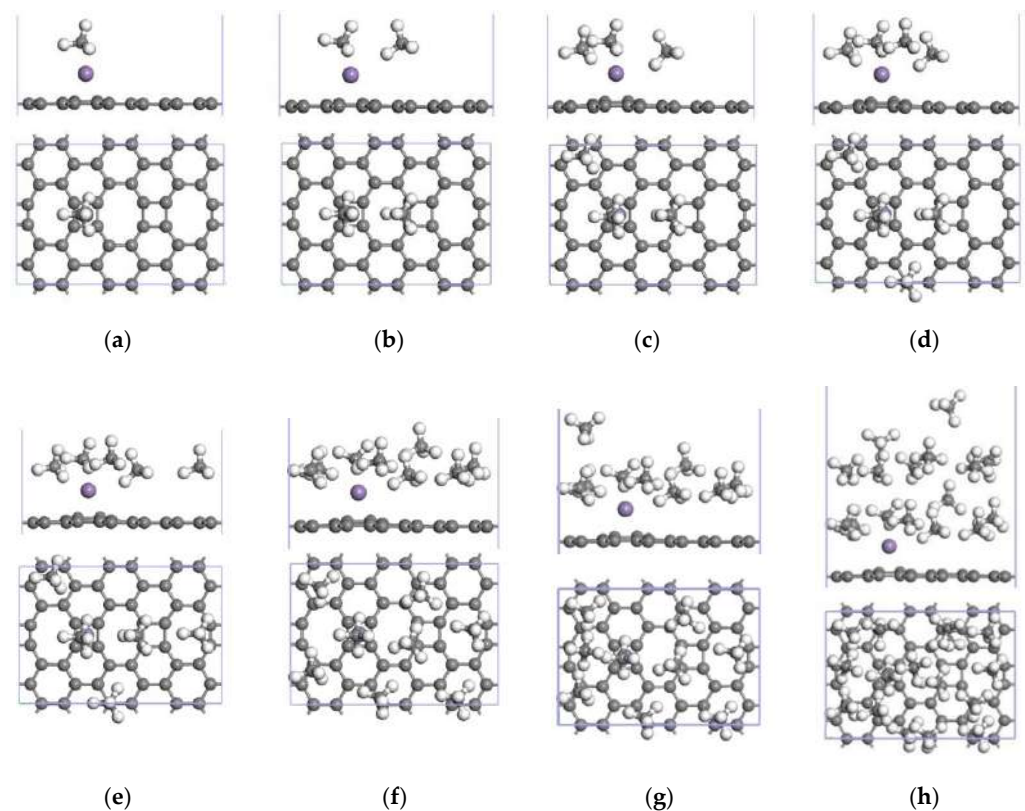


Figure 7. $j\text{CH}_4 \leftrightarrow \text{Mn-ELD-42C}$ adsorption configurations ($j = 1, 2, \dots, 16$). Figures (a–h) respectively demonstrate the Mn-ELD-42C graphene configurations for 1–16 CH_4 molecule(s) adsorbed on one side.

Table 3 shows the average adsorption energy, $\overline{E_{ad}}$, and the adsorption energy, E_{ad} , of the $j\text{CH}_4 \leftrightarrow \text{Mn-ELD-42C} \leftrightarrow j\text{CH}_4$ adsorption configuration for CH_4 adsorption on one side and both sides; the distance, d_{CH_4-s} , between the CH_4 molecules and the plane of the Mn-ELD-42C graphene configuration; the distance, $d_{\text{CH}_4-\text{Mn}}$, between the CH_4 molecules and the Mn atoms; and the adsorption capacity (PBW) of the Mn-ELD-42C graphene configuration for CH_4 in the $j\text{CH}_4 \leftrightarrow \text{Mn-ELD-42C} \leftrightarrow j\text{CH}_4$ adsorption configuration. Analysis of these

data reveals that the absolute value of the average adsorption energy, $\overline{E_{ad}}$, of the CH₄ gradually decreased as j , the number of CH₄ molecules adsorbed, increased. The adsorption energy, E_{ad} , of 16 CH₄ molecules adsorbed on one side was compared. When the gas molecules were not stratified (the first–eighth molecules), the first, third, and seventh CH₄ molecules presented a higher adsorption energy than the other CH₄ molecules because their adsorption sites were close to Mn atoms and their distance from the plane of the graphene configuration was relatively small. When the gas molecules were stratified (the ninth–sixteenth molecules), the interaction between the CH₄ and Mn steadily decreased as the distance between them increased, leading to reduced adsorption properties.

Table 3. Adsorption energy and related parameters for CH₄ molecules in the Mn-ELD-42C graphene configuration.

Number of CH ₄ Molecules	$\overline{E_{ad}}$ (eV/CH ₄)	E_{ad} (eV)	d_{CH_4-S} (Å)	d_{CH_4-Mn} (Å)	PBW (wt%)
1	−1.717	−1.717	3.824	1.967	2.79
2	−1.289	−0.862	3.789	3.614	5.43
3	−1.177	−0.953	3.590	4.483	7.92
4	−1.103	−0.879	4.100	4.956	10.29
5	−1.047	−0.824	3.551	7.299	12.54
6	−1.022	−0.897	3.448	7.293	14.68
7	−1.018	−0.978	3.397	3.928	16.72
8	−0.995	−0.832	4.840	5.319	18.66
9	−0.971	−0.775	7.176	5.724	20.52
10	−0.956	−0.825	7.156	5.777	22.29
11	−0.943	−0.810	7.329	5.612	23.98
12	−0.927	−0.755	7.460	8.228	25.60
13	−0.918	−0.806	7.831	9.377	27.16
14	−0.913	−0.856	8.035	7.837	28.65
15	−0.907	−0.816	9.132	7.743	30.08
16	−0.897	−0.755	11.550	10.780	31.46
30	−0.867				46.25

The above results indicate that the adsorption properties of a Mn-ELD-42C graphene configuration are affected by Mn atom modification and that this can play an important role in CH₄ adsorption. The adsorption energy was also affected by the distance between the CH₄ molecules and the plane of the graphene configuration. The adsorption distance, d_{CH_4-S} , between the 16th CH₄ molecule and the Mn-ELD-42C graphene configuration was 11.550 Å, which was the largest out of the 16 CH₄ molecules. At this point, both the average adsorption energy, $\overline{E_{ad}}$, and the adsorption energy, E_{ad} , of the configuration were at their lowest (−0.897 eV/CH₄ and −0.755 eV, respectively).

Up to 16 CH₄ molecules could be stably adsorbed on one side of the Mn-ELD-42C graphene configuration, with an average adsorption energy of −0.897 eV/CH₄. On this basis, it can be calculated that the Mn-ELD-42C graphene configuration is able to stably adsorb up to 14 CH₄ molecules on the other side, making a total of 30 CH₄ molecules overall (Figure 8), with an average adsorption energy of −0.867 eV/CH₄ and an adsorption capacity of 46.25 wt%. This is much closer to the proposed DOE standard (50 wt%) [9]. The adsorption capacity of the Mn-ELD-42C graphene configuration was 1.02 times that of the basic ELD-42C graphene configuration (45.26 wt%). This makes it clear that the adsorption capacity for CH₄ molecules can be effectively improved by the modification of Mn atoms.

Table 4 gives the Mulliken layout of the Mn-ELD-42C graphene configuration before and after adsorbing one CH₄ molecule, where H₁, H₂, H₃ and H₄ stand for the H atoms and C represents the C atom of the CH₄ molecule. For the CH₄ molecule adsorbed above the Mn atom, H₁, H₂ and H₃ faced the plane of the Mn-ELD-42C graphene configuration, while H₄ faced away from it (Figure 6a). The charge for H₄ was 0.27 e before the CH₄ molecule was adsorbed and 0.36 e after the CH₄ molecule was adsorbed, with 0.09 e of charge having been lost. For free CH₄ molecules, the C atom is negatively charged, and the four peripheral H atoms are positively charged. This results in a strong repulsive force between CH₄ molecules, making it difficult for multiple CH₄ molecules to gather

at the same adsorption site. For the Mn-ELD-42C graphene configuration, the ELD-42C graphene substrate was negatively charged, allowing the positively charged CH_4 molecules on the outer surface to be adsorbed more easily via electrostatic interaction. In the CH_4 molecules adsorbed on the Mn-ELD-42C graphene configuration, both H_1 and H_2 lost their partial positive charge because they received equal numbers of electrons. This reduced the surface area of the positively charged CH_4 molecule, weakening the repulsive force between the CH_4 molecules. In addition, before and after a single CH_4 molecule had been adsorbed by the Mn-ELD-42C graphene configuration, a relatively large charge transfer occurred with the Mn atoms, with 0.29 e of charge being lost. When CH_4 molecules were adsorbed, the electrons of the Mn atoms were transferred to the CH_4 molecules; therefore, a strong Coulomb force was produced between the two, creating favorable conditions for CH_4 adsorption.

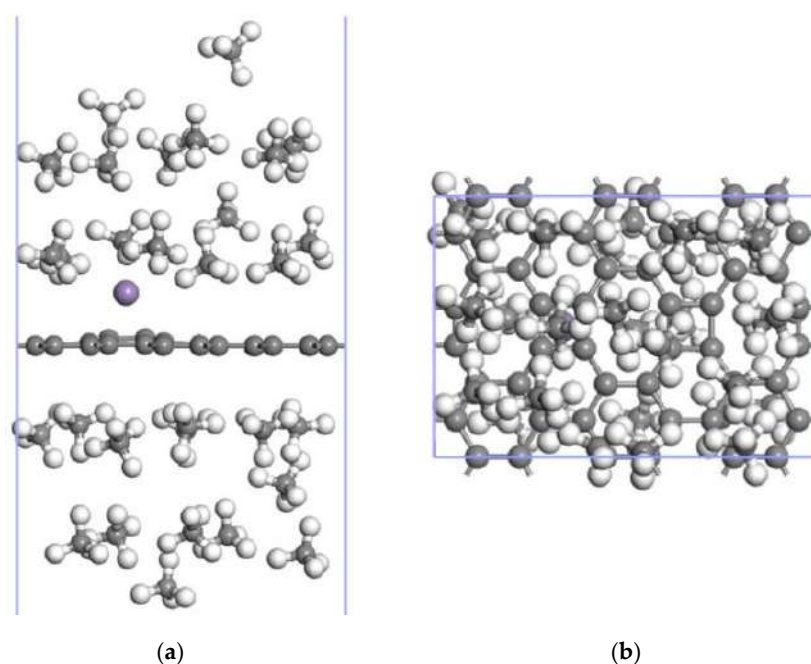


Figure 8. $16\text{CH}_4 \leftrightarrow \text{Mn-ELD-42C} \leftrightarrow 14\text{CH}_4$ adsorption configuration with 16 and 14 CH_4 molecules, respectively, adsorbed on each side. (a) Front view; (b) top view (gray balls represent carbon atoms, white balls stand for hydrogen atoms and purple balls represent Mn atoms).

Table 4. Mulliken layout of the Mn-ELD-42C graphene configuration before and after adsorbing a single CH_4 molecule.

Atom	Before Adsorption (e)				After Adsorption (e)			
	s	p	d	Charge	s	p	d	Charge
H_1	0.73			0.27	0.87			0.13
H_2	0.73			0.27	0.87			0.13
H_3	0.73			0.27	0.72			0.28
H_4	0.73			0.27	0.64			0.36
C	1.51	3.59		−1.10	1.49	3.61		−1.09
C1	1.03	3.00		−0.03	1.05	3.03		−0.08
C2	1.03	3.00		−0.04	1.05	3.03		−0.09
C3	1.05	3.03		−0.09	1.05	3.04		−0.10
C4	1.05	3.04		−0.09	1.05	3.04		−0.10
Mn	2.00	6.00	6.21	0.69	2.01	6.00	6.13	0.98

Figure 9 illustrates the charge density difference for the $\text{CH}_4 \leftrightarrow \text{Mn-ELD-42C}$ adsorption configuration. This directly reveals the charge transfer between the Mn atoms and CH_4 molecules. The blue elements are the electron gain zone, where the CH_4 molecules obtained electrons, and the yellow elements are the electron loss zone, where the Mn atoms lost electrons. As the large charge transfer between the Mn atoms and CH_4 molecules produced a Coulomb force between them, the Mn atoms had a significant effect on CH_4 adsorption. This is consistent with the analysis of the Mulliken layout in Table 4.

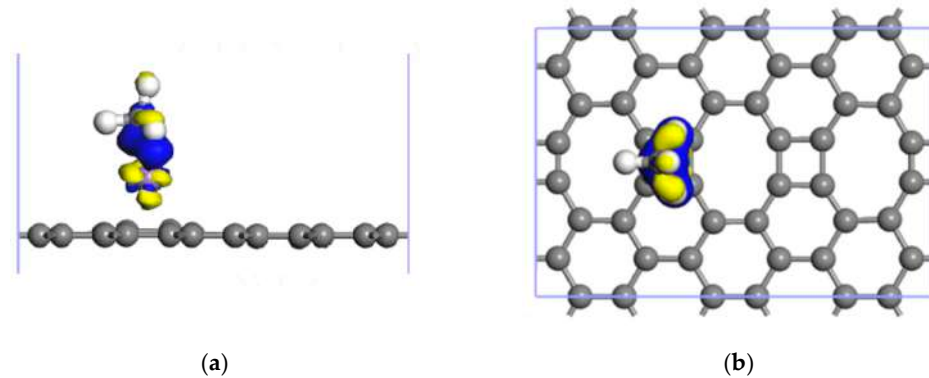


Figure 9. Charge density difference for the $\text{CH}_4 \leftrightarrow \text{Mn-ELD-42C}$ adsorption configuration. (a) Front view; (b) top view.

The interaction between the Mn-ELD-42C graphene configuration and CH_4 molecules was also analyzed in terms of the PDOS of the CH_4 molecules. Figure 10a shows the PDOS of the $\text{CH}_4 \leftrightarrow \text{Mn-ELD-42C}$ adsorption configuration after adsorbing a single CH_4 molecule. The density of states (DOS) peak of the Mn atoms increased from 4.031 eV (before adsorption, as shown in Figure 6) to 4.763 eV (after adsorption), and the energy range enlarged from $(-4.107, 1.547 \text{ eV})$ before adsorption to $(-4.341, 1.637 \text{ eV})$ after adsorption. As a consequence, the CH_4 adsorption enhanced the interaction between the Mn atoms and the Mn-ELD-42C graphene configuration, which is in accord with the analysis of the Mulliken layout in Table 4. After a single CH_4 molecule had been adsorbed, the DOS valence band peak of the $\text{CH}_4 \leftrightarrow \text{Mn-ELD-42C}$ adsorption configuration improved because of the hybridization between the 3d orbit of the Mn atoms and the 1s orbit of the H atoms. The DOS of the C atom in the Mn-ELD-42C graphene configuration also changed slightly.

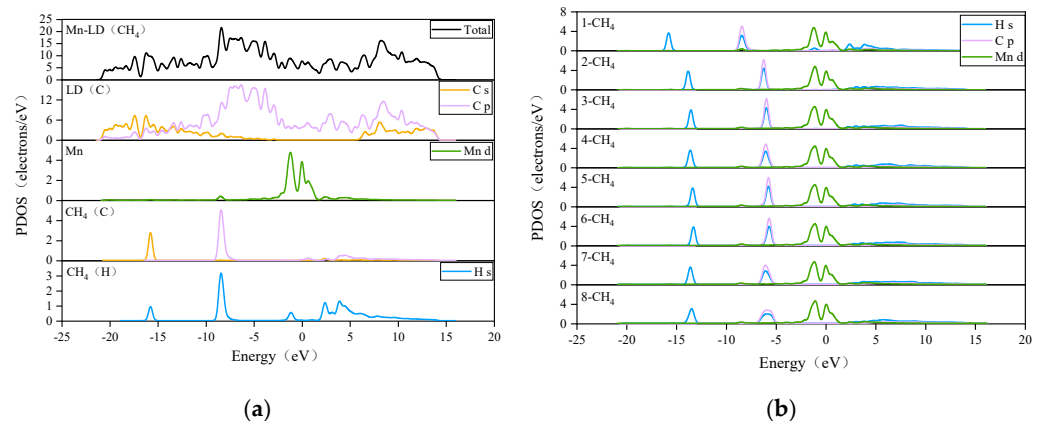


Figure 10. PDOS of the CH_4 molecules in the $j\text{CH}_4 \leftrightarrow \text{Mn-ELD-42C}$ adsorption configuration. (a) For the $\text{CH}_4 \leftrightarrow \text{Mn-ELD-42C}$ adsorption configuration; (b) for the $(1-8)\text{CH}_4 \leftrightarrow \text{Mn-ELD-42C}$ adsorption configurations.

Figure 10b was used to analyze the interaction between the d orbit of the Mn atoms, the s orbit of the H atoms and the p orbit of the C atom on the eight unstratified CH_4 molecules adsorbed on one side of the Mn-ELD-42C graphene configuration. It can be seen

that the s orbit of the H atoms of the first CH₄ molecule overlapped with the 3d orbit of the Mn atoms near -16.0 eV and -8.0 eV. This suggests that there is an interaction between the first CH₄ molecule and the Mn atoms. Compared with the first CH₄ molecule, the 1s orbit of the second CH₄ molecule had shifted to the right, indicating that the interaction between the second CH₄ molecule and the Mn atoms had weakened, making the adsorption energy of the second CH₄ molecule smaller than that of the first CH₄ molecule. The displacement of the PDOS peak for the CH₄ molecules correlated with changes in the adsorption energy, with the PDOS peak moving to the left when the adsorption energy increased and to the right when the adsorption energy reduced. As the number of CH₄ molecules adsorbed increased, the PDOS peak reduced and moved to the right, showing that the interaction between the CH₄ molecules and Mn atoms was gradually weakening. In the interval $[-6.989, -4.893$ eV], the PDOS peak of the eighth CH₄ molecule was significantly lower than that of the other seven CH₄ molecules, indicating that the interaction between the 1s orbit of the H atoms of the eighth CH₄ molecule and the 3d orbit of the Mn atoms was the weakest. This is consistent with the gradual decrease in the average adsorption energy when the CH₄ molecules were adsorbed by the Mn-ELD-42C graphene configuration.

3.3. CH₄ Adsorption in the 2Mn-ELD-42C Graphene Configuration

3.3.1. Modification of the ELD-42C Graphene Configuration by Two Mn Atoms

To further study the effect of Mn modification on the CH₄ storage properties of the ELD-42C graphene configuration, the ELD-42C graphene configuration was modified by two Mn atoms. This enabled three stable structures (Figure 11) to be obtained after optimization, with their structural symmetry being taken into account. In Figure 11a, the two Mn atoms were located on the same side of the ELD-42C graphene configuration. This made it difficult to increase the adsorption capacity for CH₄ molecules because of the limited adsorption space. As each modifying Mn atom forms an active adsorption site, the adsorption capacity for CH₄ can be increased more effectively by placing the two Mn atoms on either side of the ELD-42C graphene configuration. Figure 11b shows the two Mn atoms placed on either side of the same quadrilateral carbon ring of the ELD-42C graphene configuration, with an average binding energy of -2.816 eV. In Figure 11c, the two Mn atoms were placed on either side of two quadrilateral carbon rings separated by an octagonal carbon ring, with an average binding energy of -3.451 eV. This was slightly lower than the graphene configuration shown in Figure 11a (-3.556 eV) but produced a more stable structure. In the structure shown in Figure 11c, the binding energy of the first atom (-3.453 eV) was close to that of the second Mn atom (-3.449 eV), proving that the interaction between the two Mn atoms differed to a lesser degree. On the basis of this analysis, the 2Mn-ELD-42C graphene configuration shown in Figure 11c was selected for the study of its CH₄ adsorption properties.

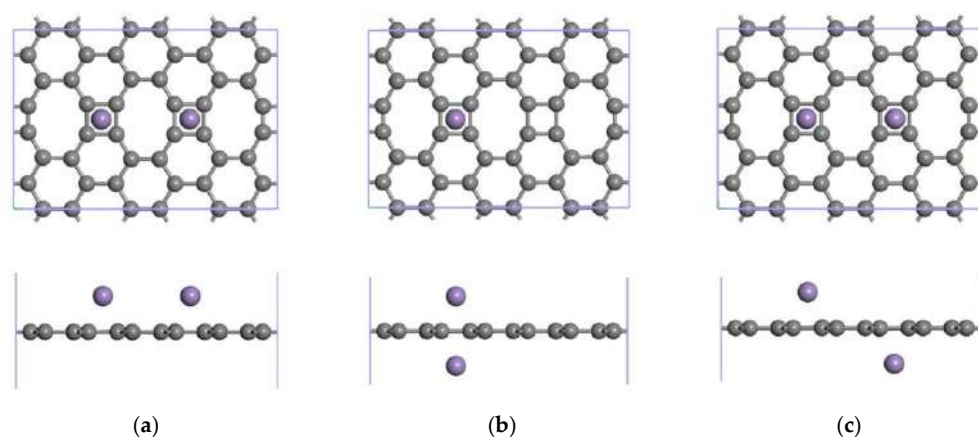


Figure 11. 2Mn-ELD-42C graphene configurations (gray balls represent carbon atoms, and purple balls represent Mn atoms). (a) The two Mn atoms were located on the same side of the ELD-42C

graphene configuration; (b) the two Mn atoms were placed on either side of the same quadrilateral carbon ring of the ELD-42C graphene configuration; (c) the two Mn atoms were placed on either side of two quadrilateral carbon rings separated by an octagonal carbon ring.

3.3.2. Adsorption of CH₄ by the 2Mn-ELD-42C Graphene Configuration

Twenty CH₄ molecules at most could be stably adsorbed on one side of the 2Mn-ELD-42C graphene configuration. The $j\text{CH}_4 \leftrightarrow 2\text{Mn-ELD-42C}$ adsorption configuration ($j = 1, 2, \dots, 20$) after optimization is shown in Figure 12. When the ninth CH₄ molecule was adsorbed by the 2Mn-ELD-42C graphene configuration, stratification occurred due to the repulsion between the positively charged surfaces of the CH₄ molecules and the limited adsorption space near the Mn atoms (Figure 7e). In other words, the preceding eight CH₄ molecules were adsorbed in the first layer (Figure 7a–d), near the Mn atoms. This was similar to the monolayer gas adsorption by the Mn-ELD-42C graphene configuration modified by a single Mn atom. When the second Mn atom was added, the increased CH₄ adsorption sites made the interaction between the Mn atoms and CH₄ molecules exceed the mutual repulsion between the CH₄ molecules, so five CH₄ molecules were able to be adsorbed in the third layer. As noted above, the 2Mn-ELD-42C graphene configuration could stably adsorb twenty CH₄ molecules at most on a single side, with the adsorption substrate of the optimized $20\text{CH}_4 \leftrightarrow 2\text{Mn-ELD-42C}$ adsorption configuration forming an arc (Figure 7h). Clearly, the 2Mn-ELD-42C graphene configuration obtained after the second Mn atom was added improved the CH₄ adsorption capacity of the substrate and increased the number of adsorption sites, effectively remedying the issue with the Mn-ELD-42C graphene configuration when adsorbing CH₄ molecules at a greater distance from the Mn atoms.

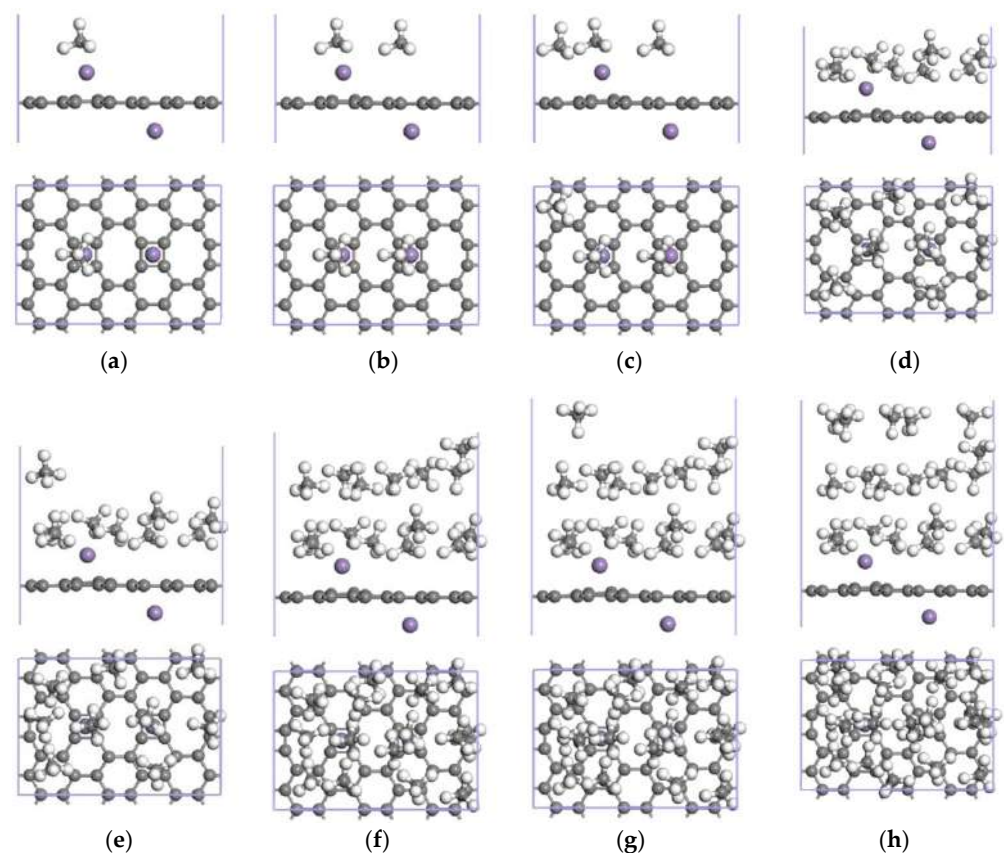


Figure 12. $j\text{CH}_4 \leftrightarrow 2\text{Mn-ELD-42C}$ adsorption configurations ($j = 1, 2, \dots, 20$). (a–h) respectively show the 2Mn-ELD-42C graphene configuration with 1–20 CH₄ molecule(s) adsorbed on one side.

Table 5 gives the average adsorption energy, $\overline{E_{ad}}$, and the adsorption energy, E_{ad} , of the $j\text{CH}_4 \leftrightarrow 2\text{Mn-ELD-42C}$ adsorption configuration for CH_4 adsorption on one side and on both sides; the distance, d_{CH_4-s} , between the CH_4 molecules and the 2Mn-ELD-42C graphene configuration; the distance, $d_{\text{CH}_4-\text{Mn}}$, between the CH_4 molecules and Mn atoms; and the CH_4 adsorption capacity (PBW) of the 2Mn-ELD-42C graphene configuration. It can be seen that the absolute value of the average adsorption energy decreased with an increase in j , the number of adsorbed CH_4 molecules. Comparing the adsorption energy, E_{ad} , of the eight CH_4 molecules adsorbed on one side and in a single layer, the first and fourth CH_4 molecules were closer to the Mn atoms and had smaller adsorption distances from the plane of the graphene configuration, so there was a higher adsorption energy. The adsorption distance between the 20th CH_4 molecule and the 2Mn-ELD-42C graphene configuration was the largest out of the 20 CH_4 molecules (11.600 Å), with the average adsorption energy, $\overline{E_{ad}}$, and adsorption energy, E_{ad} , also being the smallest (−0.868 eV/ CH_4 and −0.726 eV, respectively). Layered adsorption occurred when the CH_4 molecules were adsorbed by the 2Mn-ELD-42C graphene configuration, causing the 20th CH_4 molecule to be the farthest away from Mn atoms; there was repulsion between the positively charged surfaces of the CH_4 molecules, making the adsorption energy the lowest. When a 21st CH_4 molecule was placed on one side of the configuration, the calculated adsorption energy became positive, indicating that the gas molecule had not been adsorbed.

Table 5. Adsorption energy and related parameters for CH_4 molecules in the 2Mn-ELD-42C graphene configuration.

Number of CH_4 Molecules	$\overline{E_{ad}}$ (eV/ CH_4)	E_{ad} (eV)	d_{CH_4-s} (Å)	$d_{\text{CH}_4-\text{Mn}}$ (Å)	PBW (wt%)
1	−1.726	−1.726	3.789	1.943	2.55
2	−1.296	−0.866	3.828	4.045	4.96
3	−1.149	−0.855	3.590	4.406	7.27
4	−1.105	−0.974	3.483	3.996	9.46
5	−1.058	−0.869	4.196	7.647	11.55
6	−1.030	−0.891	3.937	4.558	13.55
7	−1.015	−0.926	3.379	7.596	15.46
8	−0.993	−0.835	4.498	5.836	17.28
9	−0.967	−0.760	7.187	5.871	19.03
10	−0.950	−0.796	7.167	5.827	20.71
11	−0.936	−0.797	7.385	6.282	22.32
12	−0.926	−0.814	7.574	6.176	23.86
13	−0.917	−0.806	7.885	9.321	25.35
14	−0.909	−0.813	7.931	8.754	26.77
15	−0.900	−0.777	9.242	11.033	28.15
16	−0.889	−0.727	11.369	9.523	29.47
17	−0.882	−0.756	11.336	9.868	30.75
18	−0.875	−0.769	11.578	10.493	31.98
19	−0.871	−0.787	11.450	10.427	33.16
20	−0.868	−0.726	11.600	11.992	34.31
40	−0.862				51.09

Up to 40 CH_4 molecules could be stably adsorbed on both sides of the 2Mn-ELD-42C graphene configuration (see Figure 13), with an average adsorption energy of −0.862 eV/ CH_4 and an adsorption capacity of 51.09 wt%. Note that, although the average adsorption energy of the 2Mn-ELD-42C graphene configuration (−0.862 eV/ CH_4) was close to that of the Mn-ELD-42C graphene configuration (−0.867 eV/ CH_4), the CH_4 adsorption capacity of the 2Mn-ELD-42C graphene configuration (51.09 wt%) was 1.11 times that of the Mn-ELD-42C graphene configuration.

Although the CH_4 adsorption capacity of the 2Mn-ELD-42C graphene configuration is lower than some references, as tabulated in Table 6, it goes beyond the specified DOE standard (50 wt%), proving that 2Mn-ELD-42C graphene configurations may offer good opportunities for industrial development and are worth further research and development in the future.

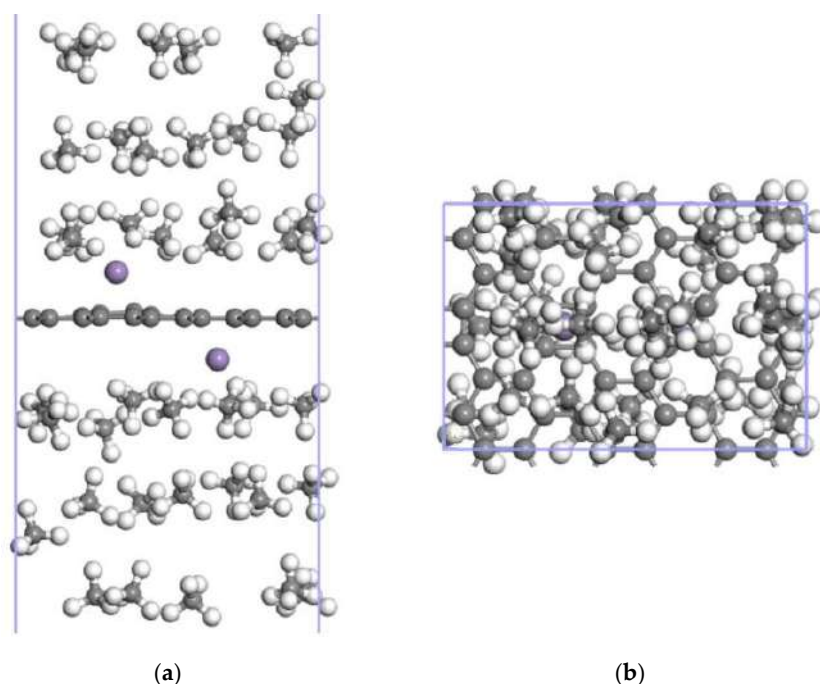


Figure 13. $20\text{CH}_4 \leftrightarrow 2\text{Mn-ELD-42C} \leftrightarrow 20\text{CH}_4$ adsorption configuration with 20 CH_4 molecules being adsorbed on each side. (a) Front view; (b) top view (the gray balls represent carbon atoms, the white balls are hydrogen atoms and the purple balls represent Mn atoms).

Table 6. Comparison of CH_4 adsorption capacity on various carbonaceous structure.

Adsorption Structure	Modified Elements	Temp; Pressure	PBW (wt%)	Interpretation	Ref.
2Mn-ELD-42C	Mn	-	51.09	ELD: Extended line defect	This work
2Ti-GDY	Ti	-	55.24	GDY: graphdiyne	[44]
CNT-PG	-	298 k; 40 bar	44.70	CNT-PG: carbon nanotube-porous graphene	[52]
SWNT	-	303 k; 3.55 MPa	19.80	SWNT: single-walled carbon nanotubes	[53]
2Ti-GY	Ti	-	48.40	GY: graphyne	[8]
2Mn-GR	Mn	-	32.93	GR: graphene	[6]
2Mn-N-GDY	Mn, N	-	58.50	GDY: graphdiyne	[54]
Ti-GDY	Ti	-	63.54	Co-mixing H_2 and CH_4	[55]
GRHA/ACNF	-	298 k; 12 bar	66.40	GRHA: graphene-derived rice husk ashes; ACNF: activated carbon Nanofibers	[56]

4. Conclusions

This paper explored the CH_4 adsorption properties of ELD-42C, Mn-ELD-42C and 2Mn-ELD-42C graphene configurations using DFT to work from first principles. The study results showed that the CH_4 adsorption of a basic ELD-42C graphene configuration is weak. Here, the average adsorption energy was $-0.842 \text{ eV}/\text{CH}_4$, and the CH_4 adsorption capacity was 45.26 wt%. Sixteen CH_4 molecules could be stably adsorbed on the Mn-doped side of the Mn-ELD-42C graphene configuration, and fourteen on the other side, with an average adsorption energy of $-0.867 \text{ eV}/\text{CH}_4$ and an adsorption capacity of 46.25 wt%. Thus, the CH_4 adsorption capacity of Mn-ELD-42C graphene configurations can be effectively enhanced by modification with a single Mn atom. This configuration further improved the CH_4 adsorption and increased the number of adsorption sites, with it being able to stably adsorb up to 40 CH_4 molecules across the two sides, with an average adsorption

energy of -0.862 eV/CH₄ and an adsorption capacity of 51.09 wt%. The adsorption capacity of the 2Mn-ELD-42C graphene configuration was 1.13 times that of the ELD-42C graphene configuration and exceeded the proposed DOE standards (50 wt%). Together, these results indicate that 2Mn-ELD-42C graphene configurations have great potential for the development of industrially viable CH₄ storage materials. The DFT calculation results in this paper only illustrate the CH₄ adsorption properties of ELD graphene configurations when modified by a single Mn atom or two Mn atoms. In subsequent studies, the effects of environmental factors such as temperature and pressure on the CH₄ adsorption properties of ELD-42C, Mn-ELD-42C and 2Mn-ELD-42C graphene configurations will be further investigated using molecular dynamics methods.

Author Contributions: Conceptualization, C.Z. and S.Y.; methodology, C.Z. and X.Z.; software, C.Z. and X.Z.; validation, S.Y.; formal analysis, S.Y.; investigation, C.Z.; resources, C.Z. and S.Y.; data curation, J.L.; writing—original draft preparation, C.Z.; writing—review and editing, S.Y.; visualization, Y.X.; supervision, S.Y.; project administration, X.Z.; funding acquisition, S.Y. All authors have read and agreed to the published version of the manuscript.

Funding: This research was funded by the National Natural Science Foundation of China, grant number 52174253.

Institutional Review Board Statement: Not applicable.

Informed Consent Statement: Not applicable.

Data Availability Statement: The data presented in this study are available on reasonable request from the corresponding author.

Acknowledgments: The authors are grateful for the support of the National Natural Science Foundation of China (grant No. 52174253).

Conflicts of Interest: The authors declare no conflict of interest.

References

1. Pantha, N.; Ulman, K.; Narasimhan, S. Adsorption of methane on single metal atoms supported on graphene: Role of electron back-donation in binding and activation. *J. Chem. Phys.* **2020**, *153*, 244701. [CrossRef] [PubMed]
2. Jia, X.; Zhang, H.; Zhang, Z.; An, L. First-principles investigation of vacancy-defected graphene and Mn-doped graphene towards adsorption of H₂S. *Superlattices Microstruct.* **2019**, *134*, 106235. [CrossRef]
3. Vekeman, J.; Cuesta, I.G.; Faginas-Lago, N.; Wilson, J.; Sánchez-Marín, J.; de Merás, A.S. Potential models for the simulation of methane adsorption on graphene: Development and CCSD(T) benchmarks. *Phys. Chem. Chem. Phys.* **2018**, *20*, 25518–25530. [CrossRef] [PubMed]
4. Hasnan, N.S.N.; Timmiati, S.N.; Lim, K.L.; Yaakob, Z.; Kamaruddin, N.H.N.; Teh, L. Recent developments in methane decomposition over heterogeneous catalysts: An overview. *Mater. Renew. Sustain. Energy* **2020**, *9*, 1–18. [CrossRef]
5. Hassani, A.; Mosavian, M.T.H.; Ahmadpour, A.; Farhadian, N. Improvement of methane uptake inside graphene sheets using nitrogen, boron and lithium-doped structures: A hybrid molecular simulation. *Korean J. Chem. Eng.* **2017**, *34*, 876–884. [CrossRef]
6. Zhao, Y.; Chen, Y.; Song, M.; Liu, X.; Xu, W.; Zhang, M.; Zhang, C. Methane Adsorption Properties of Mn-Modified Graphene: A First-Principles Study. *Adv. Theory Simul.* **2020**, *3*, 2000035. [CrossRef]
7. Ghanbari, R.; Safaiee, R.; Golshan, M. A dispersion-corrected DFT investigation of CH₄ adsorption by silver-decorated monolayer graphene in the presence of ambient oxygen molecules. *Appl. Surf. Sci.* **2018**, *457*, 303–314. [CrossRef]
8. Xu, W.; Chen, Y.; Zhao, Y.; Zhang, M.; Tian, R.; Zhang, C. First-principles study on the methane adsorption properties by Ti-modified graphyne. *Int. J. Quantum Chem.* **2021**, *121*, e26811. [CrossRef]
9. Mahmoud, E. Recent advances in the design of metal–organic frameworks for methane storage and delivery. *J. Porous Mater.* **2020**, *28*, 213–230. [CrossRef]
10. Zhang, X.; Wang, S. Interfacial Strengthening of Graphene/Aluminum Composites through Point Defects: A First-Principles Study. *Nanomaterials* **2021**, *11*, 738. [CrossRef]
11. Feicht, P.; Eigler, S. Defects in Graphene Oxide as Structural Motifs. *ChemNanoMat* **2018**, *4*, 244–252. [CrossRef]
12. Xiong, L.; Gong, B.; Peng, Z.; Yu, Z. Spin-Seebeck effect and thermoelectric properties of one-dimensional graphene-like nanoribbons periodically embedded with four- and eight-membered rings. *Phys. Chem. Chem. Phys.* **2021**, *23*, 23667–23672. [CrossRef] [PubMed]
13. Zhao, Q.; Zhao, Y.; Chen, Y.; Ju, J.; Xu, W.; Zhang, M.; Sang, C.; Zhang, C. First-principles study on methane storage properties of porous graphene modified with Mn. *Appl. Phys. A* **2021**, *127*, 1–12. [CrossRef]

14. Cao, C.; Wu, M.; Jiang, J.; Cheng, H.-P. Transition metal adatom and dimer adsorbed on graphene: Induced magnetization and electronic structures. *Phys. Rev. B* **2010**, *81*, 205424. [CrossRef]
15. Yu, G.; Zhu, M.; Zheng, Y. First-principles study of 3d transition metal atom adsorption onto graphene: The role of the extended line defect. *J. Mater. Chem. C* **2014**, *2*, 9767–9774. [CrossRef]
16. Guan, Z.; Ni, S.; Hu, S. First-Principles Study of 3d Transition-Metal-Atom Adsorption onto Graphene Embedded with the Extended Line Defect. *ACS Omega* **2020**, *5*, 5900–5910. [CrossRef] [PubMed]
17. Ghosh, S.K. Diversity in the Family of Manganese Oxides at the Nanoscale: From Fundamentals to Applications. *ACS Omega* **2020**, *5*, 25493–25504. [CrossRef] [PubMed]
18. Kudyba, A.; Akhtar, S.; Johansen, I.; Safarian, J. Aluminothermic reduction of manganese oxide from selected MnO-containing slags. *Materials* **2021**, *14*, 356. [CrossRef]
19. Luo, X.; Peng, C.; Shao, P.; Tang, A.; Huang, A.; Wu, Q.; Sun, L.; Yang, L.; Shi, H.; Luo, X. Enhancing nitrate removal from wastewater by integrating heterotrophic and autotrophic denitrification coupled manganese oxidation process (IHAD-MnO): Internal carbon utilization performance. *Environ. Res.* **2021**, *194*, 110744. [CrossRef]
20. Ma, J.; Wang, C.; Xi, W.; Zhao, Q.; Wang, S.; Qiu, M.; Wang, J.; Wang, X. Removal of Radionuclides from Aqueous Solution by Manganese Dioxide-Based Nanomaterials and Mechanism Research: A Review. *ACS ES&T Eng.* **2021**, *1*, 685–705. [CrossRef]
21. Mansouri, M. Effects of Vacancy-Defected, Dopant and the Adsorption of Water upon Mn₂O₃ and Mn₃O₄ (001) Surfaces: A First-Principles Study. *Acta Phys. Pol. A* **2018**, *133*, 1178–1185. [CrossRef]
22. Yan, H.; Hu, W.; Cheng, S.; Xia, H.; Chen, Q.; Zhang, L.; Zhang, Q. Microwave-assisted preparation of manganese dioxide modified activated carbon for adsorption of lead ions. *Water Sci. Technol.* **2020**, *82*, 170–184. [CrossRef]
23. Shen, L.; Zhang, L.; Wang, K.; Miao, L.; Lan, Q.; Jiang, K.; Lu, H.; Li, M.; Li, Y.; Shen, B.; et al. Analysis of oxidation degree of graphite oxide and chemical structure of corresponding reduced graphite oxide by selecting different-sized original graphite. *RSC Adv.* **2018**, *8*, 17209–17217. [CrossRef]
24. Jiao, S.; Li, T.; Xiong, C.; Tang, C.; Li, H.; Zhao, T.; Dang, A. A Facile Method to Prepare Silver Doped Graphene Combined with Polyaniline for High Performances of Filter Paper Based Flexible Electrode. *Nanomaterials* **2019**, *9*, 1434. [CrossRef]
25. Ghashghae, M.; Ghambarian, M. Methane adsorption and hydrogen atom abstraction at diatomic radical cation metal oxo clusters: First-principles calculations. *Mol. Simul.* **2018**, *44*, 850–863. [CrossRef]
26. Chen, X.; Liang, Q.H.; Jiang, J.; Wong, C.K.Y.; Leung, S.Y.; Ye, H.; Yang, D.G.; Ren, T.L. Functionalization-induced changes in the structural and physical properties of amorphous polyaniline: A first-principles and molecular dynamics study. *Sci. Rep.* **2016**, *6*, 20621. [CrossRef]
27. Zhao, S.; Larsson, K. First Principle Study of the Attachment of Graphene onto Different Terminated Diamond (111) Surfaces. *Adv. Condens. Matter Phys.* **2019**, *2019*, 9098256. [CrossRef]
28. Goyenola, C.; Stafstrom, S.; Hultman, L.; Gueorguiev, K.G. Structural patterns arising during synthetic growth of fullerene-like sulfocarbide. *J. Phys. Chem. C* **2012**, *116*, 21124–21131. [CrossRef]
29. Gueorguiev, G.K.; Czigány, Z.; Furlan, A.; Stafström, S.; Hultman, L. Intercalation of P atoms in Fullerene-like CP_x. *Chem. Phys. Lett.* **2011**, *501*, 400–403. [CrossRef]
30. Gueorguiev, G.; Goyenola, C.; Schmidt, S.; Hultman, L. CF_x: A first-principles study of structural patterns arising during synthetic growth. *Chem. Phys. Lett.* **2011**, *516*, 62–67. [CrossRef]
31. Zhu, Y.-q.; Su, H.; Jing, Y.; Guo, J.; Tang, J. Methane adsorption on the surface of a model of shale: A density functional theory study. *Appl. Surf. Sci.* **2016**, *387*, 379–384. [CrossRef]
32. Perdew, J.; Burke, K.; Ernzerhof, M. Generalized gradient approximation made simple. *Phys. Rev. Lett.* **1996**, *77*, 3865, Erratum in *Phys. Rev. Lett.* **1997**, *78*, 1396. [CrossRef]
33. Björkman, T.; Gulåns, A.; Krasheninnikov, A.; Nieminen, R.M. van der Waals Bonding in Layered Compounds from Advanced Density-Functional First-Principles Calculations. *Phys. Rev. Lett.* **2012**, *108*, 235502. [CrossRef] [PubMed]
34. Wei, L.; Liu, G.-L.; Fan, D.-Z.; Zhang, G.-Y. Density functional theory study on the electronic structure and optical properties of S adsorbed graphene. *Phys. B Condens. Matter* **2018**, *545*, 99–106. [CrossRef]
35. Akay, T.I.; Toffoli, D.; Ustunel, H. Combined effect of point defects and layer number on the adsorption of benzene and toluene on graphene. *Appl. Surf. Sci.* **2019**, *480*, 1063–1069. [CrossRef]
36. Liu, M.; Liu, M.; She, L.; Zha, Z.; Pan, J.; Li, S.; Li, T.; He, Y.; Cai, Z.; Wang, J.; et al. Graphene-like nanoribbons periodically embedded with four- and eight-membered rings. *Nat. Commun.* **2017**, *8*, 14924. [CrossRef]
37. Zhao, Y.; Chen, Y.; Xu, W.; Zhang, M.; Zhang, C. First-Principles Study on Methane Adsorption Performance of Ti-Modified Porous Graphene. *Phys. Status Solidi B* **2021**, *258*, 2100168. [CrossRef]
38. Ding, Y. Research on the Mechanism of CH₄, CO₂, H₂O and O₂ Adsorption on Coal Molecule. Master's Thesis, North China Electric Power University, Baoding, China, 2018.
39. Li, K.; Li, H.; Yan, N.; Wang, T.; Zhao, Z. Adsorption and dissociation of CH₄ on graphene: A density functional theory study. *Appl. Surf. Sci.* **2018**, *459*, 693–699. [CrossRef]
40. Yuan, W.H. *Study on the Adsorption Properties of Formaldehyde-Methane on Graphene*; Beijing Institute of Technology: Beijing, China, 2016.
41. Zhou, J.; Xuan, H.Y.; Xiao, R.J.; Zhang, X.Y.; Man, M.O.; Fang, Z.J. First-principles study on adsorption property of carbon surface to methane. *J. Guangxi Univ. Nat. Sci. Ed.* **2018**.

42. Liu, J.; Chen, Y.Z.; Xie, Y. The calculation of adsorption properties of H₂S, CO₂ and CH₄ on Fe doped MoS₂ based on first-principles. *J. At. Mol. Phys.* **2020**, *37*, 501–507.
43. Kumar, K.V.; Preuss, K.; Titirici, M.; Rodriguez-Reinoso, F. Nanoporous Materials for the Onboard Storage of Natural Gas. *Chem. Rev.* **2017**, *117*, 1796–1825. [CrossRef]
44. Xu, W.; Chen, Y.-H.; Song, M.; Liu, X.; Zhao, Y.; Zhang, M.; Zhang, C.-R. First-Principles Study on Methane (CH₄) Storage Properties of Graphdiyne. *J. Phys. Chem. C* **2020**, *124*, 8110–8118. [CrossRef]
45. Zhou, X.; Gall, D.; Khare, S.V. Mechanical properties and electronic structure of anti-ReO₃ structured cubic nitrides, M₃N, of d block transition metals M: An ab initio study. *J. Alloy. Compd.* **2014**, *595*, 80–86. [CrossRef]
46. Tawfik, S.A.; Cui, X.Y.; Ringer, S.P.; Stampfl, C. Multiple CO₂ capture in stable metal-doped graphene: A theoretical trend study. *RSC Adv.* **2015**, *5*, 50975–50982. [CrossRef]
47. Hu, X.; Meng, F. Structure and gap opening of graphene with Fe doped bridged trivacancy. *Comput. Mater. Sci.* **2016**, *117*, 65–70. [CrossRef]
48. Liu, X. Theoretical Studies of Interaction between Metal and Graphene and Molecular Clusters. Master's Thesis, Jilin University, Changchun, China, 2011.
49. Wu, M.; Cao, C.; Jiang, J.Z. Electronic structure of substitutionally Mn-doped graphene. *New J. Phys.* **2010**, *12*, 63020. [CrossRef]
50. Chen, J.-J.; Li, W.-W.; Li, X.-L.; Yu, H.-Q. Improving Biogas Separation and Methane Storage with Multilayer Graphene Nanostructure via Layer Spacing Optimization and Lithium Doping: A Molecular Simulation Investigation. *Environ. Sci. Technol.* **2012**, *46*, 10341–10348. [CrossRef]
51. Rad, A.S.; Pazoki, H.; Mohseni, S.; Zareyee, D.; Peyravi, M. Surface study of platinum decorated graphene towards adsorption of NH₃ and CH₄. *Mater. Chem. Phys.* **2016**, *182*, 32–38. [CrossRef]
52. Jiang, H.; Cheng, X.-L. Simulations on methane uptake in tunable pillared porous graphene hybrid architectures. *J. Mol. Graph. Model.* **2018**, *85*, 223–231. [CrossRef] [PubMed]
53. Tanaka, H.; El-Merraoui, M.; Steele, W.; Kaneko, K. Methane adsorption on single-walled carbon nanotube: A density functional theory model. *Chem. Phys. Lett.* **2002**, *352*, 334–341. [CrossRef]
54. Xu, W.; Chen, Y.; Zhao, Y.; Zhang, M.; Tian, R.; Zhang, C. Methane adsorption properties of N-doped graphdiyne: A first-principles study. *Struct. Chem.* **2021**, *32*, 1517–1527. [CrossRef]
55. Zhao, Q.; Chen, Y.; Xu, W.; Ju, J.; Zhao, Y.; Zhang, M.; Sang, C.; Zhang, C. First-principles study of the impact of hydrogen on the adsorption properties of Ti-decorated graphdiyne storage methane. *Chem. Phys. Lett.* **2022**, *790*, 139329. [CrossRef]
56. Othman, F.E.C.; Yusof, N.; Harun, N.Y.; Bilad, M.R.; Jaafar, J.; Aziz, F.; Salleh, W.N.W.; Ismail, A.F. Novel Activated Carbon Nanofibers Compositated with Cost-Effective Graphene-Based Materials for Enhanced Adsorption Performance toward Methane. *Polymers* **2020**, *12*, 2064. [CrossRef] [PubMed]

Review

Comprehensive Review on Zeolite-Based Nanocomposites for Treatment of Effluents from Wastewater

Veena Sodha^{1,*}, Syed Shahabuddin^{1,*}, Rama Gaur¹, Irfan Ahmad², Rajib Bandyopadhyay^{1,*} and Nanthini Sridewi^{3,*}

¹ Department of Chemistry, School of Technology, Pandit Deendayal Energy University, Knowledge Corridor, Raisan, Gandhinagar 382426, Gujarat, India

² Department of Clinical Laboratory Sciences, College of Applied Medical Sciences, King Khalid University, Abha 61421, Saudi Arabia

³ Department of Maritime Science and Technology, Faculty of Defence Science and Technology, National Defence University of Malaysia, Kuala Lumpur 57000, Malaysia

* Correspondence: syedshahab.hyd@gmail.com or syed.shahabuddin@sot.pdpu.ac.in (S.S.); rajib.bandyopadhyay@sot.pdpu.ac.in (R.B.); nanthini@upnm.edu.my (N.S.); Tel.: +91-858-593-2338 (S.S.); +60-124-675-320 (N.S.)

Abstract: All humans and animals need access to clean water in their daily lives. Unfortunately, we are facing water scarcity in several places around the world, and, intentionally or unintentionally, we are contaminating the water in a number of ways. The rise in population, globalization, and industrialization has simultaneously given rise to the generation of wastewater. The pollutants in wastewater, such as organic contaminants, heavy metals, agrochemicals, radioactive pollutants, etc., can cause various ailments as well as environmental damage. In addition to the existing pollutants, a number of new pollutants are now being produced by developing industries. To address this issue, we require some emerging tools and materials to remove effluents from wastewater. Zeolites are the porous aluminosilicates that have been used for the effective pollutant removal for a long time owing to their extraordinary adsorption and ion-exchange properties, which make them available for the removal of a variety of contaminants. However, zeolite alone shows much less photocatalytic efficiency, therefore, different photoactive materials are being doped with zeolites to enhance their photocatalytic efficiency. The fabrication of zeolite-based composites is emerging due to their powerful results as adsorbents, ion-exchangers, and additional benefits as good photocatalysts. This review highlights the types, synthesis and removal mechanisms of zeolite-based materials for wastewater treatment with the basic knowledge about zeolites and wastewater along with the research gaps, which gives a quality background of worldwide research on this topic for future developments.

Keywords: zeolite; wastewater treatment; photocatalysis; nanocomposites

Citation: Sodha, V.; Shahabuddin, S.; Gaur, R.; Ahmad, I.; Bandyopadhyay, R.; Sridewi, N. Comprehensive Review on Zeolite-Based Nanocomposites for Treatment of Effluents from Wastewater. *Nanomaterials* **2022**, *12*, 3199. <https://doi.org/10.3390/nano12183199>

Academic Editor: Meiwen Cao

Received: 23 August 2022

Accepted: 12 September 2022

Published: 14 September 2022

Publisher's Note: MDPI stays neutral with regard to jurisdictional claims in published maps and institutional affiliations.



Copyright: © 2022 by the authors. Licensee MDPI, Basel, Switzerland. This article is an open access article distributed under the terms and conditions of the Creative Commons Attribution (CC BY) license (<https://creativecommons.org/licenses/by/4.0/>).

1. Introduction

Water is an integral part of all living organisms; it is crucial for humans and the environment. Water becomes contaminated after being used for numerous reasons such as bathing, washing, cooking, and manufacturing and is then dumped back into water sources after treatment. Since it is difficult for the wastewater treatment plants to treat the pollutants of emerging industries and the majority of industries levy fees for the same, it is less expensive for enterprises to treat or pre-treat the wastewater before discharging it into sewers. Figure 1 depicts how water is collected from resources, utilized, and then discharged into water bodies [1].

Wastewater can promote diseases such as polio, cholera, vomiting, diarrhoea, nausea, and even cancer in the human body [2,3]. If wastewater is discharged into water bodies, the pollutants in it can inhibit the establishment of marine plants [4]. There are numerous types of water pollutants for which multiple treatment methods have been described,

which includes chemical, biological, and physical methods, such as adsorption [5], photocatalysis [6,7], ultrafiltration [8], and biofiltration [9]. In the area of wastewater treatment, zeolites, which are aluminosilicates with porous structures, are generally utilized as adsorbents [10,11], ion-exchangers [12], and photocatalysts [13,14]. The negatively charged structure of a zeolite attracts a variety of cationic pollutants to it. The use of zeolites in the removal of pollutants is not just restricted to the adsorption of cationic pollutants; by modifying it in various ways, its affinity for anionic pollutants can also be improved [15]. Photoactivity in zeolites has been enhanced by the addition of heteroatom to their framework, as in titanium silicates, exposing it to larger applications [16–18]. Composites are materials made by combining two or more materials known as parent materials. The term zeolite-based composite refers to the coupling of zeolites with other materials to form binary, ternary, and so on composites. The field of study on zeolite-based composites as a pollutant removal medium is broadening owing to their tuneable pore size [16,19], enhanced photoactivity [19], and easy operation [20]. For example, combining zeolites with materials that have a positively charged framework and an affinity towards anionic pollutants, may result in a composite that can be applied for the removal of both cationic and anionic contaminants. Generally, carbon-based materials [21,22], metal oxides [23,24], polymers [25,26], and clay compounds [27] are incorporated with zeolites for a variety of applications including fuel cells [28], catalysis [29], sorption [4], and others. Researchers have demonstrated the removal of contaminants from various model solutions, such as dyes [30,31], heavy metals [32], herbicides [33], etc., using zeolites and zeolite-based materials [34]. These models can also be applied to treat the real wastewater from industries. The synthesis, as well as adsorption and photocatalytic studies, on zeolite-based composites described in this review may help researchers in the treatment of real wastewater samples from industries. In addition, this review not only gives information about the zeolite-based composites, but also gives basic knowledge about wastewater and zeolites. The physicochemical properties of zeolites, synthesis of zeolite-based materials, and their mechanism in adsorption and photocatalysis are explained, which gives basic research background to early researchers and to scientists who aim to devise zeolite-based materials for pollutant remediation. The adsorption and photocatalytic research of zeolite-based composites are more thoroughly examined for the purpose of building a photoactive device for wastewater treatment.

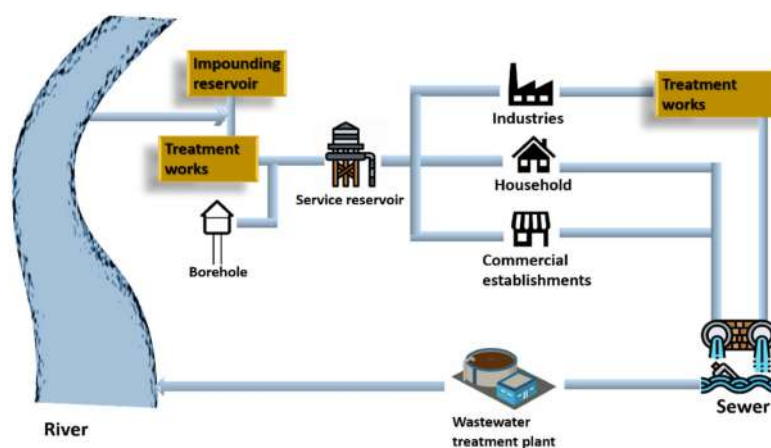


Figure 1. Cycle of water service.

1.1. Wastewater

The combination of the waterborne or liquid wastes removed from institutions, residences, and industrial and commercial establishments is wastewater [35]. Everything that is discharged into the sewers subsequently gets treated in a wastewater treatment plant [1]. It includes pollutants from various domestic activities, such as bathing, cleaning clothes and utensils, and flushing toilets; industrial activities, such as textiles, mining, and manufacturing; commercial activities, such as beauty salons and car washing; agricultural facilities; energy units. Apart from these, a variety of other events, such as surface run-offs,

floods, and storms also produce wastewater. Additionally, if the sewer becomes damaged, groundwater will sweep in, increasing the volume of wastewater. Figure 2 represents major sources of wastewater.

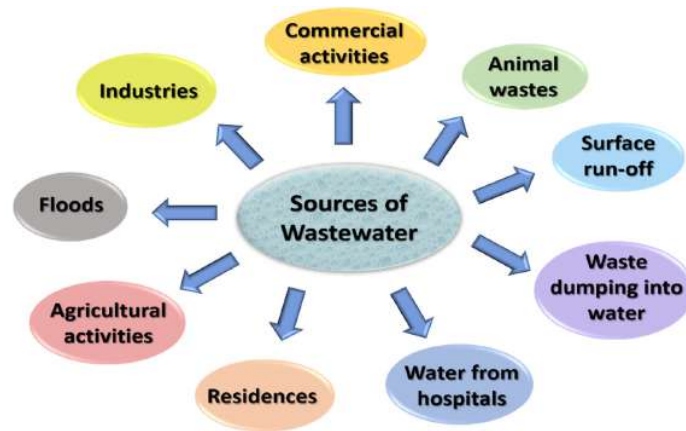


Figure 2. Sources of wastewater.

Wastewater contains a variety of pollutants including organic, inorganic, toxic, non-toxic, thermal, and suspended solids from industries, residences, commercial activities, etc. [36]. Refer to Figure 3.

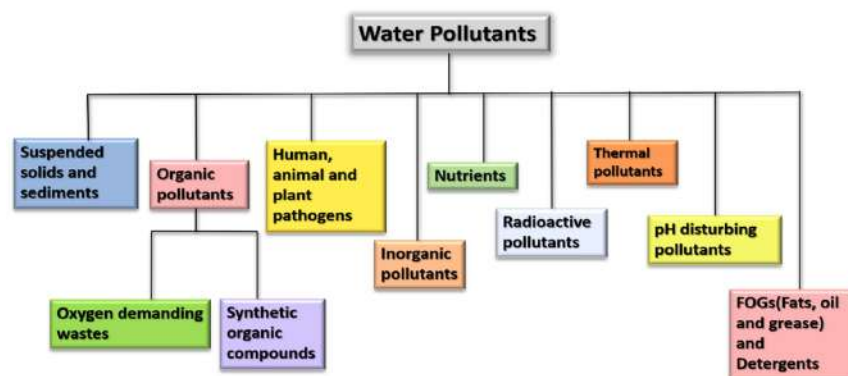


Figure 3. Flowchart representing various pollutants in wastewater.

1.1.1. Total Suspended Solids (TSS)

Suspended solids are particulate matter with a diameter of less than 62 μm . These are too small to settle down and too large to float, hence, they remain suspended in water. Generally, a water stream contains some SS, but an excessive amount might cause issues [37]. These exist in two forms: (i) inert and (ii) oxidizable solids. Sand particles and eroded minerals are examples of inert solids. These are sourced from mining, coal washing, construction sites, etc. Oxidizable solids settle out similar to inert solids but get decomposed on deposition releasing toxic compounds, such as methane, ammonia, and sulphides, causing higher oxygen demand in localized areas of water. These reduce the penetration of light into the water, inhibit the growth of filter feeders, cause temperature change, and other issues [1,37]. Their removal techniques include gravity settling [38], centrifugation [39], and filtration [40], followed by disinfection to remove floating bacteria and pathogens [41].

1.1.2. Organic Pollutants

Organic pollutants can be classified based on two aspects: (i) the nature of the pollutant, i.e., natural or synthetic, and (ii) its persistence, i.e., a persistent or non-persistent organic pollutant. Natural organic pollutants include oxygen demanding wastes, which decrease the oxygen levels of water. Synthetic organic compounds include chemicals from industries, agricultures, etc.

Some organic pollutants are persistent and some are non-persistent. Persistent organic pollutants (POPs) are chemicals that live in the environment for prolonged periods as these are resistant to biochemical and photolytic processes [42]. Moreover, these are lipophilic and hydrophobic pollutants that are receptive to long-range transport and bioaccumulation and are prone to enter the food chain as well [43]. Consider Figure 4 [43].

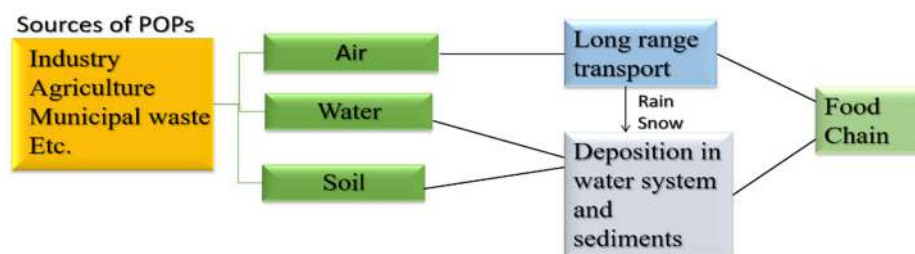


Figure 4. Flowchart representation of flow to POPs in the environment and food chain. Adapted with permission from Ref. [43]. Copyright 2020 Springer Nature.

Locally discharged POPs spread pollution far from its source. Sources of persistent organic pollutants (POPs) include volcanic activity and forest fires that produce dioxins and dibenzofurans. Other sources include agricultural pesticides and industries, such as dichlorodiphenyltrichloroethane (DDT), polychlorinated biphenyls (PCB), perfluoro octane sulfonic acid (PFOS), perfluorooctanoic acid (PFOA), and brominated flame retardants, etc. [44]. In adult studies, POPs have been implicated in a variety of adverse health impacts, such as thyroid and endocrine-related cancers, diabetes, obesity, and reproductive concerns in both males and females [45].

1.1.3. Inorganic Pollutants

Heavy metals, inorganic salts, mineral acids, trace elements, metals, and their complexes with organic compounds are examples of inorganic pollutants. Metals with a density higher than 5 g/cm^3 are classified as heavy metals [46]. Titanium, cobalt, manganese, iron, nickel, copper, zinc, arsenic, silver, gold, and mercury are commonly occurring heavy metals in everyday life. Few heavy metals are essential elements in our life but when present in a large amount they can be toxic. Natural deposits of heavy metals can be discovered in the Earth's crust, hence, one of their sources in wastewater includes surface run-off. Apart from that, metal-based industries, automobiles, roadworks, and metal leaching are the major sources of heavy metals in wastewater. Heavy metal exposure in humans can result in cellular function loss, cell damage, and potentially carcinogenic effects [46].

1.1.4. Radioactive Pollutants

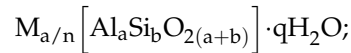
Approximately 11% of the world's electricity is generated by nuclear power plants [47]. The nuclear fission process produces no carbon dioxide, which is a plus, but we still have to deal with nuclear waste. The release of radionuclides in the environment caused disaster during 1986 in the Chernobyl and Fukushima Daiichi plant in 2011 [48]. Radioactive pollutants can cause plant mutations and serious health damage to aquatic life. Their influence on humans may be mild or fatal depending on the magnitude and duration of exposure. When humans have a short time of exposure to a lower level of radioactive pollutants, it can cause mild skin irritations; on the other hand, prolonged exposure at low-intensity causes diarrhea, nausea, vomiting, hair loss, etc. Prolonged exposure to high levels of radiation will lead to some irreversible DNA damages. Apart from that, it can cause several other diseases, such as lung, thyroid, and skin cancers [49]. Several removal methods, including physical, chemical, and biological, are used. (i) Physical methods: evaporation, distillation, dumping; (ii) chemical methods: acid digestion wet oxidation, precipitation; (iii) biological: microbial remediation and plant remediation [3]. For further understanding of various types of pollutants refer to Table 1.

Table 1. Pollutants, their sources, adverse effects, and removal techniques.

Sr. No.	Type of Pollutant	Examples	Sources	Adverse Effects	Removal Techniques	Ref.
1	Suspended solids and sediments.	Sand particles, eroded minerals, etc.	Mining, coal washing, etc.	Reduced light penetration in water, temperature change, etc.	Gravity settling, centrifuge, etc.	[38,39]
2	Oxygen demanding wastes.	Dissolved organic matter.	Domestic wastes, pulp and paper mill, wastes from food processing plants, animal sewage, slaughter houses, agricultural runoff, etc.	Reduce the oxygen levels in water.	Carbon oxidation process, co-aggulation, fluctuation.	[50]
3	Organic dyes.	Methylene blue, methyl orange, crystal violet, rhodamine B, etc.	Textile, pharmaceutical, food, laser printing industries.	Diarrhea, breathing difficulty, nausea, vomiting, gastrointestinal issues, carcinogenic and oncogenic effects.	Adsorption, membrane separation, advanced oxidation processes (AOPs), biological decolorization.	[2,51,52]
4	Pesticides.	Organochlorines such as DDT, chlordane, aldrin, organofluorines such as PFOA, PFOS.	Agricultural activities.	Respiratory and skin conditions, cancer, reproduction issues, endocrine disruption, etc.	Advanced oxidation processes (AOPs), activated sludge treatment, adsorption, membrane technologies, etc.	[53,54]
5	Heavy metals.	Zinc (Zn), mercury (Hg), lead (Pb), arsenic (As), iron (Fe), cadmium (Cd), etc.	Surface run-off, roadworks, metal-based industries, automobiles, etc.	Haze, corrosion, eutrophication, and can lead to acid rain, also inhibits the biodegradation of organochlorines.	Adsorption, ion exchange.	[55,56]
6	Radioactive pollutants.	Caesium, strontium, uranium etc.	Nuclear power plants	DNA damage, thyroid, lung and skin cancers, hair loss etc.	Precipitation, distillation, microbial remediations, etc.	[3]
7	Nutrients.	Nitrogen, phosphorus, etc.	Agricultural fertilizers, run-offs from storm water, household detergents, human wastes, etc.	Eutrophication, reduction in oxygen level of water, reduced sunlight penetration, affect the growth of plants, etc.	To remove phosphorus biological nutrient removal (BNR) and nitrification and denitrification to remove to remove nitrogen.	[57]
8	Human, animal, and plant pathogens (pathogen microorganisms).	Different types of bacteria, viruses, protozoa, and helminths.	Animal and human fecal wastes, household and laundry wastewater.	Waterborne diseases such as polio, hepatitis cholera, anemia, typhoid, gastroenteritis, etc.	Natural elimination by temperature or prolonged life or adsorption to particles and sedimentation disinfection by chlorination and UV radiation.	[58–60]

1.2. Zeolites

Zeolites are crystalline three-dimensional, porous, aluminosilicates with organized structures and building blocks of tetrahedral units TO_4 with an O atom bridged between them, as given in Figure 5, where T denotes Si or Al atom [61]. In the zeolite framework, the gap between the huge cavities holds water and interchangeable cations [15]. The basic chemical formula for zeolites is represented as:



where M stands for [Sr, Ba, Ca, Mg] and/or [Li, K, Na], and cation charge is symbolized by n. The values of b/a range from 1 to 6 while q/a range from 1 to 4 [15].

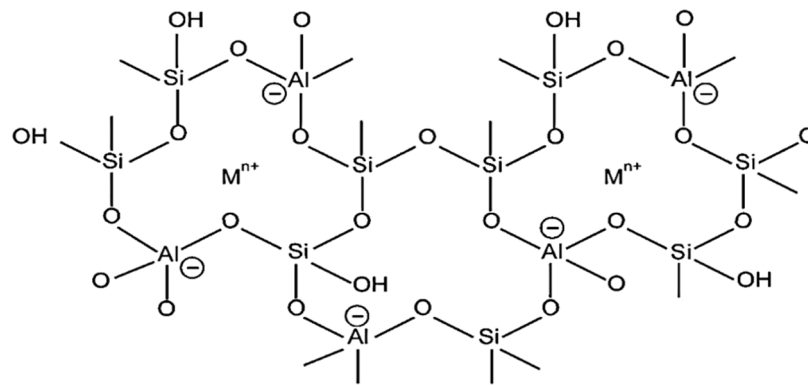


Figure 5. A two-dimensional illustration of the zeolite framework. Reprinted with permission from Ref. [62]. Copyright 2006 Elsevier.

Zeolites occur naturally as well as being synthesized chemically. The source of natural zeolites is volcanogenic sedimentary rocks. Clinoptilolite, phillipsite, mordenite, chabazite, stilbite, analcime, and laumontite are abundant among natural zeolites, while barrerite, offerite, and paulingite are rare.

Some of the natural zeolites with their chemical formula are given in Table 2.

Table 2. Name and chemical formula of some natural zeolites. Reprinted with permission from Ref. [15]. Copyright 2010 Elsevier.

Name of Zeolite	Chemical Formula
Clinoptilolite	$(Na_2, K_2, Ca)_3 Al_6 Si_{30} O_{72} \cdot 21H_2O$
Phillipsite	$K_2 (Na_2, Ca)_2 Al_8 Si_{10} O_{32} \cdot 12H_2O$
Mordenite	$(Na_2, Ca)_4 Al_8 Si_{40} O_{96} \cdot 28H_2O$
Stilbite	$Na_2 Ca_4 Al_{10} Si_{26} O_{72} \cdot 30H_2O$
Chabazite	$(Na_2, Ca, K_2)_2 Al_4 Si_8 O_{24} \cdot 12H_2O$
Analcime	$Na_{16} Al_{16} Si_{32} O_{96} \cdot 16H_2O$
Ferrierite	$(Na_2, K_2, Ca, Mg)_3 Al_6 Si_{30} O_{72} \cdot 20H_2O$
Laumontite	$Ca_2 Al_8 Si_{16} O_{48} \cdot 16H_2O$
Scolecite	$Ca_4 Al_8 Si_{12} O_{40} \cdot 12H_2O$
Heulandite	$Al_8 Si_{28} Ca_4 O_{68} \cdot 24H_2O$

Classification of Zeolites

Zeolites may be categorized as per their occurrence, Si-Al ratio, pore size, crystal structure, and other factors [63]. Figure 6 shows the broad classification of zeolites. Tables 3–5 show how zeolites are classified according to their pore size, silica to alumina ratio, and structure type [63,64]. Some of the many classes of framework types according to the website of international zeolitic association (IZA) are depicted in Table 5.

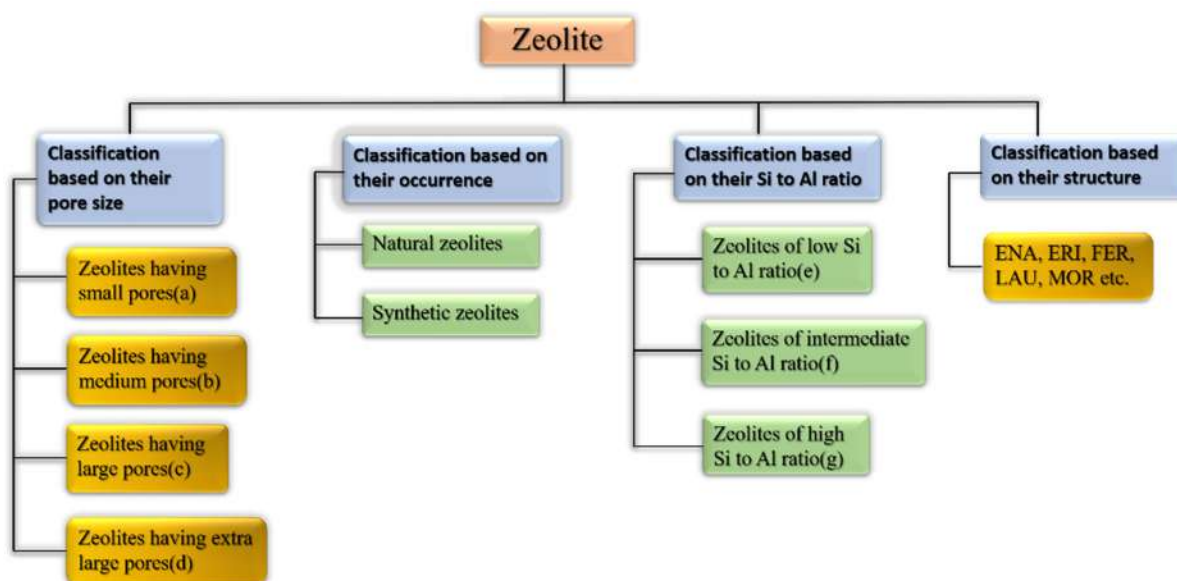


Figure 6. Broad classification of zeolites.

Table 3. Classification of zeolites according to their pore size.

Class of Zeolite	Number of Rings	Free Pore Diameter (nm)
(a) Zeolites with small pores	8	0.3 to 0.45
(b) Zeolites with medium pores	10	0.45 to 0.6
(c) Zeolites with large pores	12	0.6 to 0.8
(d) Zeolites with extra-large pores	14	0.8 to 1.0

Table 4. Classification of zeolites considering Si to Al ratio.

Class of Zeolite	Range of Si:Al Ratio
(e) Zeolites with small Si:Al ratio	1.0 to 1.5
(f) Zeolites with intermediate Si:Al ratio	2 to 5
(g) Zeolites with large Si:Al ratio	10 to several thousands

Table 5. Classification of zeolites as per their structure type [64].

Framework Type Code	Symmetry	Channel Dimensionality	Framework Density (Å ³)	Total Volume (Å ³)	Accessible Volume (%)	Order	Reference Material
ANA	Cubic	3D	19.2 T/1000	2497.2	0.00	Fully ordered	Analcime
BEA	Tetragonal	3D	15.3 T/1000	4178.4	20.52	Partially disordered	Beta polymorph A
CHA	Trigonal	3D	15.1 T/1000	4178.4	20.52	Fully ordered	Chabazite
DFT	Tetragonal	3D	17.7 T/1000	451.7	6.58	Fully ordered	DAF-2
ERI	Hexagonal	3D	16.1 T/1000	2239.5	15.10	Fully ordered	Erionite
FAU	Cubic	3D	13.3 T/1000	14,428.8	27.42	Fully ordered	Faujasite
FER	Orthorhombic	2D	17.6 T/1000	2051.3	10.01	Fully ordered	Ferrierite
HEU	Monoclinic	2D	17.5 T/1000	2054.8	9.42	Fully ordered	Heulandite
LAU	Monoclinic	1D	18.0 T/1000	1333.6	9.57	Fully ordered	Laumontite
MFI	Orthorhombic	3D	18.4 T/1000	5211.3	9.81	Fully ordered	ZSM-5
MOR	Orthorhombic	2D	17.0 T/1000	2827.3	12.27	Fully ordered	Mordenite
MRE	Orthorhombic	1D	19.7 T/1000	2442.5	6.55	Partially disordered	ZSM-48
NAT	Tetragonal	3D	16.2 T/1000	1231.5	9.06	Fully ordered	Natrolite
PHI	Orthorhombic	3D	16.4 T/1000	1953.7	9.89	Fully ordered	Phillipsite

Catalysis, cation exchange, sorption, and molecular sieving are all physiochemical characteristics of zeolites. The tetrahedrons of [SiO₄]⁴⁻ and [AlO₄]⁵⁻ are linked together

in the zeolitic framework to build cages linked via precise and molecular-sized pores. Existence of $[\text{AlO}_4]^{5-}$ gives a negative charge to zeolite structure, which is stabilized by positively charged ions, such as K^+ , Na^+ , and Ca^{2+} . These ions are responsible for ion-exchange processes in zeolites [15]. The porous structure of a zeolite has been proven to have excellent adsorption efficiency for heavy metals, including mercury, fluoride, arsenic, and organic dyes.

1.3. Adsorption

One of the most common wastewater treatment methods is adsorption since it is simple to use and effective [65]. It is a surface phenomenon that occurs when the molecules from fluid bulk come into contact with a solid surface either by physical forces or chemical bonds. Usually, adsorption is a reversible process. Reversible of adsorption is when the adsorbent begins to release the adsorbed molecules; this is referred to as desorption [66]. There are two types of adsorptions: (i) physical adsorption, i.e., adsorption under the influence of physical forces such as weak van der Waals attractions, hydrogen bonding, etc., and (ii) chemical adsorption, i.e., adsorption by chemical bonds [67].

Activated carbon [68], industrial solid wastes [69], biomaterials [70], clay minerals [71], and zeolites [11,14] are among the most commonly used materials in wastewater treatment. In the year 1785, adsorption was first discovered by Lowitz, after that, it was used in sugar refining processes to remove color [72]. Subsequently, in American treatment plants, inactivated charcoal filters were employed for water purification [72]. For the first time, granular activated carbon (GAC) was used for adsorption in 1929 in Hamm, Germany, and Bay City, Michigan, 1930 [73]. When studied, modified and synthetic zeolites showed better adsorption and ion exchange capacities among synthetic, modified, and natural zeolites [72]. Zeolites are mostly used for the adsorption of heavy metals [32], dyes [74], ammonium ions [75], etc. Natural turkey clinoptilolite exhibited low absorptivity for three azo dyes (Everzol black, Everzol red, Everzol yellow) as examined by Armagan et al. [76]. Adsorption capacities of natural zeolite were improved greatly via modification with quaternary amines [76]. Figure 7 elaborates on the adsorption of methylene blue on zeolites which occurs via electrostatic attractions between negatively charged Al ions in the zeolite framework and positively charged nitrogen atom in methylene blue.

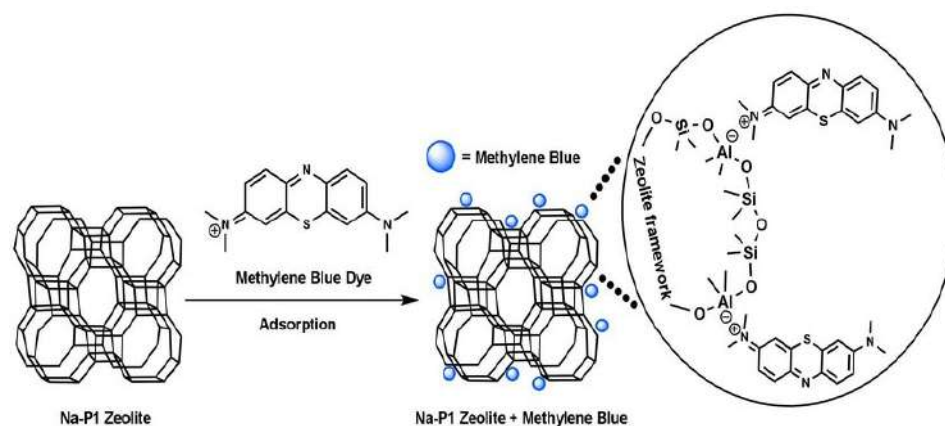


Figure 7. Adsorption of methylene blue on Na-P1 zeolite. Reprinted from Ref. [10].

1.4. Photocatalysis

Photocatalysis is the process in which a photon of light catalyzes a reaction. Materials with photocatalytic characteristics are known as semiconductors [77]. The conduction band and valance band are two different energy bands in a semiconductor. The bandgap is the energy difference between the two above-stated bands. When a photon of light strikes a semiconducting material, electrons (e^-) are excited from the valance band to the conduction band and positively charged holes (h^+) are left behind, as shown in Figure 8. The photo-

generated electron-hole pairs develop the active oxidizing species, which then cause organic pollutants, such as dyes, in wastewater to degrade [43].

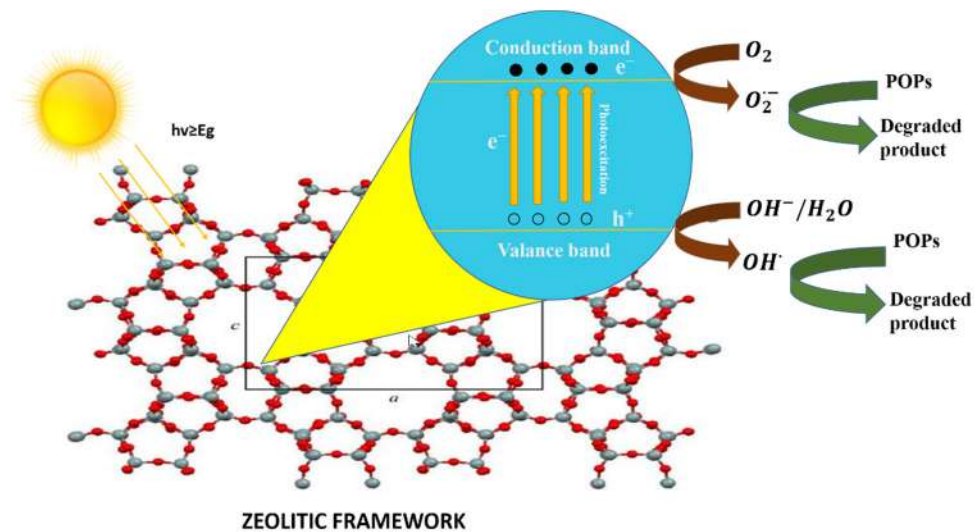
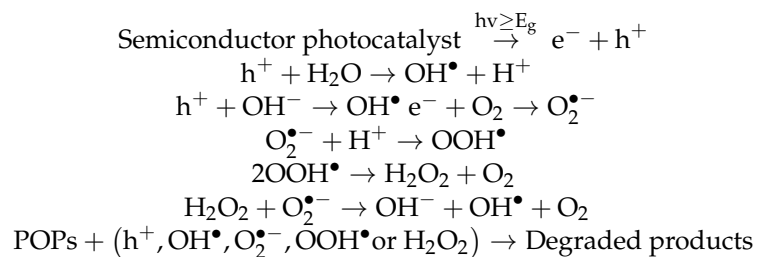


Figure 8. Schematic diagram of photocatalysis in zeolite (image of zeolite framework is reprinted from Ref. [78]).

Photocatalysis can be categorized into two types: (i) homogenous and (ii) heterogeneous photocatalysis. If in a photocatalytic reaction, both photocatalyst and reactant are in a different phase, then it is said to be heterogeneous photocatalysis. On the other hand, if photocatalyst and reactants and all other species, such as photosensitizers, are in the same phase, the system is called homogenous photocatalysis [79]. Due to its great stability, ease of separation, and photocatalyst regeneration, heterogeneous catalysis is superior to homogeneous catalysis [80].

The following steps are part of the heterogeneous photocatalysis mechanism [43].



Photocatalytic activities of zeolite alone are rarely discussed. Research on the photocatalytic activity of zeolites is scarce. Rather, their cavities behave as hosts for semiconducting materials in photocatalysis. In 2003, Krisnandi et al. investigated zeolite ETS-10, a titanosilicate, microporous zeolite with liner Ti-O-Ti-O-chains in the framework as a photocatalyst for oxidation of ethane to CO₂ and water [79]. Before this work, some preliminary analyses have been conducted on the photocatalytic activity of ETS-10 [81]. The basic mechanism in ETS-10 is that the titanium sites present in Ti-O-Ti-O trap the electrons and undergo photoreduction in the existence of ethane. These trapped electrons quickly get shifted to oxygen and generate active oxidation species [79]. In 2020, Aguiñaga et al. reported clinoptilolite–mordenite, natural zeolite as an efficient self-photocatalyst [13]. The obtained results were compared with that of titanium dioxide particles, and it was found that under similar conditions, both zeolite and TiO₂ required the same time for the complete degradation of caffeine.

The NH abbreviation is used for the hydrogenated form of natural zeolite (NZ) and NFe denotes the ion-exchanged version of NZ. The symbol SH stands for synthetic zeolite clinoptilolite–mordenite. Aguiñaga et al. recorded the diffuse reflectance spectra of syn-

thetic and natural zeolites as given in Figure 9. A bandgap analysis was conducted with the Tauc plot. Based on spectroscopic analysis of ZSM-5, it was estimated that bands developed in the range from 200–500 nm are attributed to different states of iron, and in synthetic zeolites, the presence of iron is usual. The aluminosilicate framework has a bandgap of approximately 7 eV. The bandgap of natural mordenite was estimated as 2.63 eV. In the case of synthetic clinoptilolite C, the analyzed band gap was 4.26 and 4.46 eV for direct and indirect transitions, respectively. In the same way, for synthetic mordenite, it was estimated at 3.26 and 3.45 eV. Hence, the wide bandgap of zeolite resembles the semiconductors and its application as a photocatalyst can be of interest in future research [13].

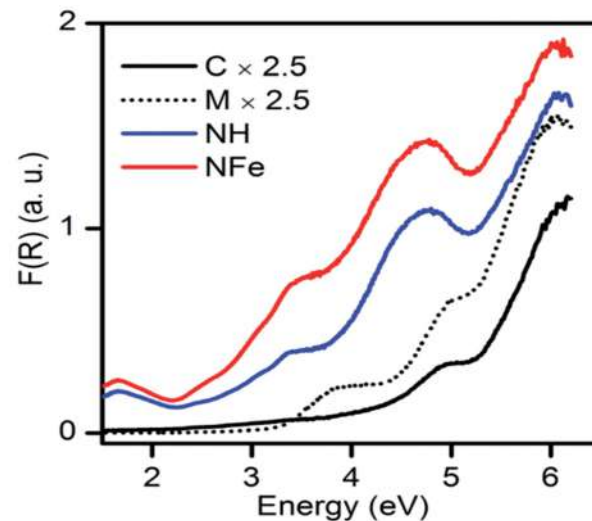


Figure 9. Diffuse reflectance spectra of synthetic and natural zeolites. Reprinted from Ref. [13].

1.5. Ion Exchange

Ion exchange can be defined as a reversible process in which exchangeable ions in an insoluble exchange material replaces similarly charged ions in the solution [82]. Electrostatic attractions are employed between ionic functional groups, which is the driving force of a typical ion exchange reaction. It can easily be employed for the extraction of heavy metals, such as cadmium, chromium, barium, arsenic, silver, lead, as well as nitrates from water [83]. Furthermore, ion exchange is the best process for the removal of radioactive nuclide in small systems [84]. Ion-exchangers can be categorized as cation and anion exchange resins. Cation exchangers are those that interchange their cations, and anion exchangers interchange their anions with the solution [84]. For further clarification refer Figure 10.

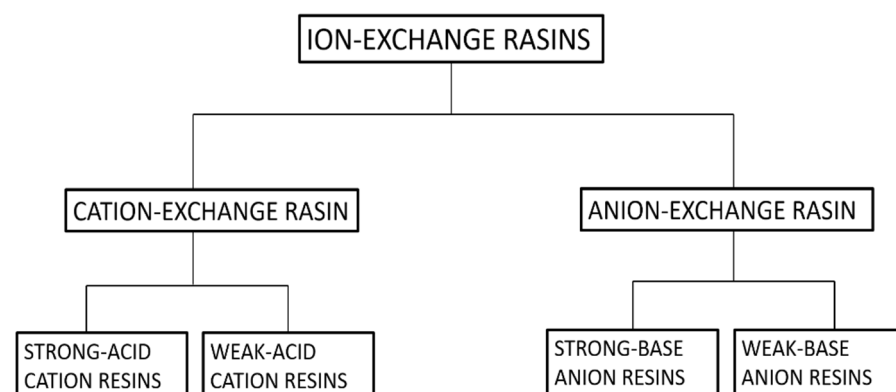


Figure 10. Classification of ion-exchange resins.

Natural inorganic zeolites, clays, and synthetic organic resins are extensively used ion-exchangers [85,86]. One of the major drawbacks that are associated with ion-exchangers

is that their ion-exchange capacity is easily reduced with contamination via organic substances. Luca et al. used ETS-10 zeolite to remove metals originating from zinc ferrite [12]. A titanosilicate, ETS-10, is microporous zeolite with liner Ti-O-Ti-O-chains in its framework. ETS-10 is extensively employed as an ion-exchanger [87]. The major advantage of using ETS-10 as an ion-exchanger is that it is easy to regenerate and is thermally stable up to 550 °C [88]. Hence, if contaminated with organic pollutants, it can easily be regenerated by calcination. Based on ICP-MS elemental analysis, it was estimated that zinc ferrite releases high concentrations of Fe, Zn, Pb, Ca, and Mn. ETS-10 removed all metal ions present very efficiently. ETS-10 showed better cation exchange capacity (CEC) than commercial zeolite A for manganese, zinc, and lead. Nearly 100% removal was observed within 30 min [12]. Figure 11 gives a basic idea about how the ion-exchange mechanism works in zeolites. A natural zeolite, clinoptilolite, which has Ca^{+2} ions trapped in its cavity, is used as an ion-exchanger. Ca^{+2} ions are replaced with Cs^{+2} via ion exchange as depicted in Figure 11.

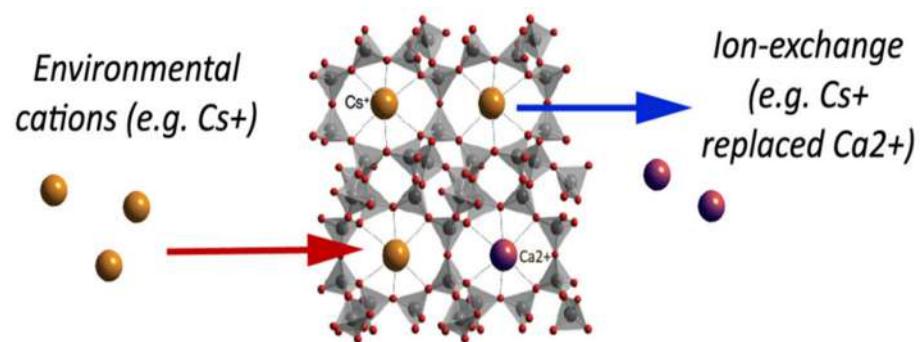


Figure 11. Ion exchange in naturally occurring zeolite, clinoptilolite. Reprinted from Ref. [89].

The adsorption properties of zeolites are influenced by their chemical and structural makeup. The cation exchange capacity (CEC) of zeolites varies with zeolitic framework structure, the density of anionic framework, size, and shape of foreign ions, etc. In raw natural zeolites, the pores are clogged with impurities and there is no uniform pore distribution, crystal structure, or chemical composition throughout the framework [90]. Additionally, raw natural zeolites have a negatively charged surface, hence, they only attract cationic pollutants, such as cationic dyes and heavy metal ions. They have a very low or little affinity toward anionic pollutants, such as anionic dyes and organic pollutants in aqueous media. Their efficiency can be increased by their modification. Table 6 shows some of the modification processes [34,91].

Table 6. Modification of zeolites, their advantages and disadvantages. Reprinted from Ref. [91].

Modification Method	Process	Advantages	Disadvantages	Ref.
Acid/base treatment.	Simple ion exchange using dilute acid solution.	Pore volume and electrostatic surface area is increased.	Decrease in CEC due to dealumination, decrease in thermal stability.	[92]
Surfactant modification.	By introducing cationic organic surfactants such as tetramethylammonium, hexadecyl trimethyl ammonium (HDTMA), n-cetyl pyridinium (CPD), etc.	Increases the hydrophobicity of zeolite, making it appropriate for the adsorption of a wide range of organic pollutants.	Complicated functional groups are formed for cationic exchange sites due to formation of admicelle.	[93–95]
Ultrasonic modification.	By sonicating with a solvent with help of an ultrasonic bath.	Impurities are removed from the channel and the surface area is increased.	Always used in combination with other methods, inefficient.	[96]
Thermal modification.	By heating in the oven or muffle furnace.	Evaporation of water, removal of contaminants from the channel, and expansion of the pore diameter.	Uneven heating.	[97]

We observed that raw, natural zeolites have limited adsorption capacity and carry contaminants. Synthetic zeolites, on the other hand, have a consistent pore distribution across the framework, as well as improved adsorption and ion exchange behavior. Kozera-Sucharda et al. conducted an experiment on the removal of Cd^{+2} and Pb^{+2} by natural and synthetic zeolites [98]. They witnessed faster and efficient removal of Cd^{+2} and Pb^{+2} from multicomponent solutions with synthetic zeolites [98]. Zeolites can be synthesized by using raw natural materials, such as natural silica sources, as well as using synthetic precursors as well. Zeolite produced using natural precursors is inexpensive but lacks precise pore structures and contains contaminants. Zeolite produced from synthetic precursors has a precise structure and fewer imperfections but is expensive.

The challenge of reusability with nanosized synthesized zeolites is another reason that reduces their effectiveness. Zeolites demonstrate improved physiochemical stability, greater adsorption capacity, and simpler reusability when utilized in the form of their composites. Additionally, the characteristics of the materials used to create composites have significant advantages of their own. Most frequently, it has been found that the zeolite-based composites show better optical properties and pore distributions than zeolites themselves, increasing the application of zeolites in adsorption, photocatalysis, and other processes. Zeolites function in photocatalytic reactions in two ways: either as a host for semiconducting materials or by cooperating with those materials' electron transfer processes to significantly reduce the chance of electron-hole recombination.

2. Zeolite-Based Composites

In general, zeolite-based composites for pollutant removal from wastewaters are made by incorporating metal oxide nanoparticles, carbon-based materials, clay compounds, and polymers into zeolites.

2.1. Synthetic Approaches

General methods for the synthesis of zeolite/metal oxide composites are (i) sol-gel, (ii) hydrothermal, (iii) solvothermal, (iv) co-precipitation, (v) ultrasonic, and (vi) microwave. Figure 12 summarizes the techniques used for the preparation of zeolite/metal oxide composites [34].

Zeolite/carbon-based materials are generally synthesized by the conventional synthesis method of zeolites, such as hydrothermal, solvothermal, sol-gel, etc. During the initial stage in the synthesis of zeolites, carbon-based material is added along with the precursors of zeolites, leading to the formation of a zeolite/carbon-based material composite, as given in Figure 13a.

Zeolite/polymer composites are generally fabricated by in situ polymerization. In this process, monomer and zeolite are mixed together followed by polymerization, which leads to the formation of a zeolite/polymer composite. Figure 13b shows the schematic of the synthesis of a zeolite/polymer composite.

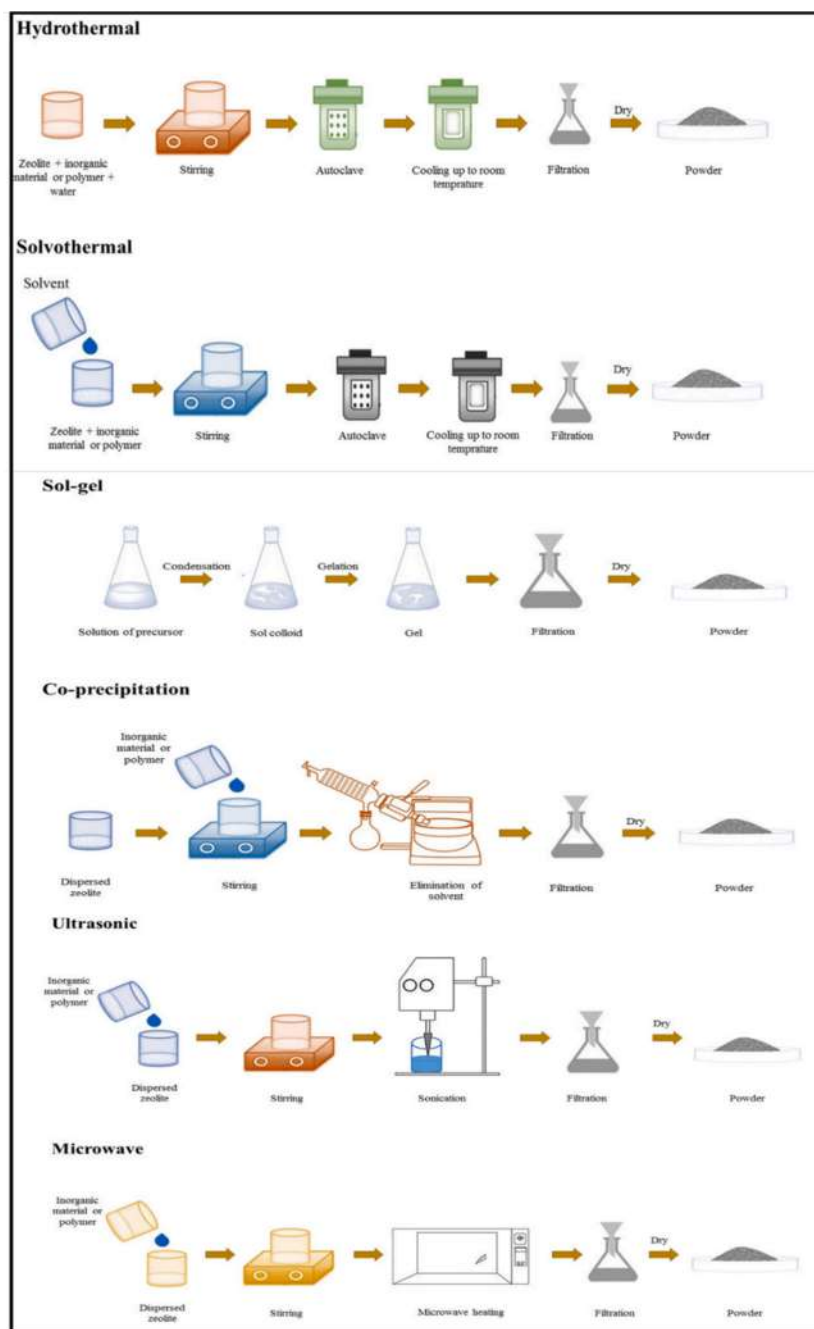


Figure 12. Synthesis processes of zeolite/metal oxide composites. Reprinted with permission from Ref. [34]. Copyright 2021 Elsevier.

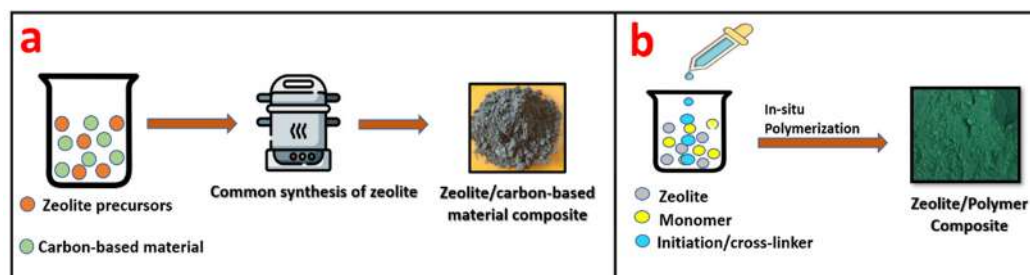


Figure 13. Schematic representation of (a) the synthesis of a zeolite/carbon-based material composite and (b) a zeolite/polymer composite.

2.2. Removal Process

When working with zeolites and zeolite-based composites, adsorption, ion-exchange, and photocatalysis are the general pollutant removal processes in wastewater treatment. In these processes, a known amount of catalyst/adsorbent is added into the model contaminant solution, i.e., dyes, heavy metals, agrochemicals, etc. Then, this suspension is kept under the treatment process and treated samples are centrifuged and analyzed using a UV–Vis spectroscope. Zeolite-based materials are also used in the fixed-bed reactors to remove pollutants from water as depicted in Figure 14.

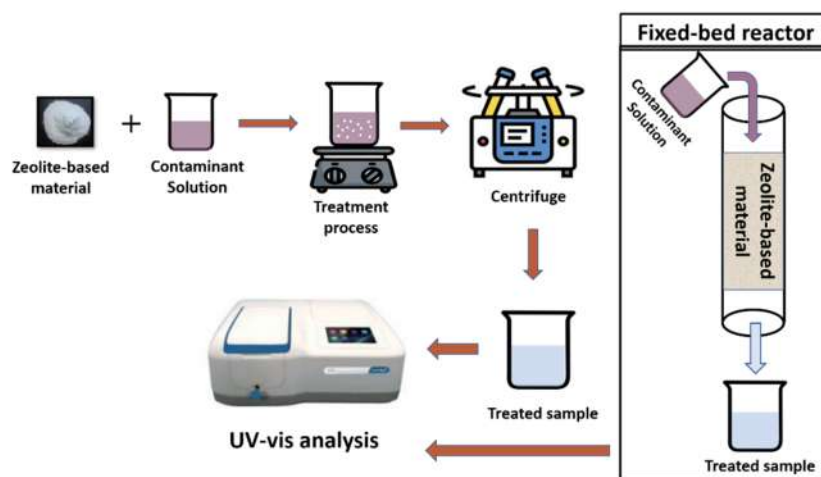


Figure 14. Schematic representation of pollutant removal process using zeolite-based materials.

2.3. Zeolite/Metal Oxide Composites

Metal oxides are employed in a variety of applications, such as adsorption, photocatalysis, energy storage, etc., due to their tunable size and morphology [99]. When employed in their nano form, metal oxides have a large surface area and exhibit excellent adsorption capabilities. Metal oxides are an ideal photocatalyst due to their distinct physicochemical properties, which include shape, size, morphology, composition dependence, and light sensitivity [100]. When doping metal oxides with zeolites, the cavities of zeolites behave as a support for metal oxides, increasing the surface area of metal oxides, thereby improving adsorption and photocatalytic properties.

Alswata et al. synthesized zeolite/ZnO nanocomposites using the co-precipitation method. Prepared samples were examined for the adsorption of lead Pb(II) and arsenic As(V) from its synthetic solution [101]. The FE-SEM images of bare and ZnO-doped zeolite are given in Figure 15. From the FE-SEM, it is evident that zeolite has a cubic shape with a smooth surface, while some granular doping can be observed on the surface of ZnO-doped zeolite. Zeolite's cubic shape remains as it is after doping of ZnO NPs.

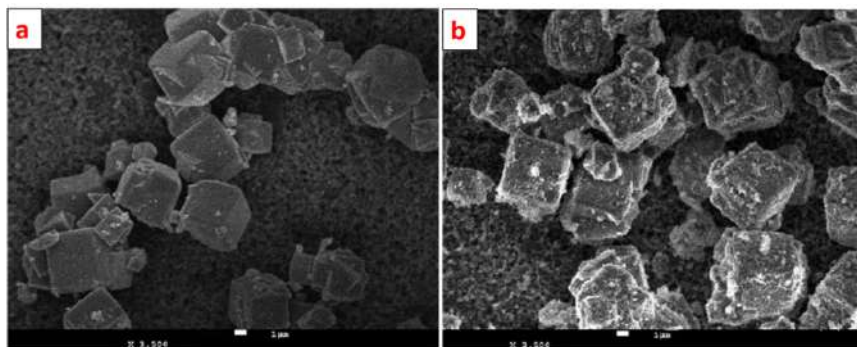


Figure 15. FE-SEM images of (a) zeolite and (b) ZnO nanoparticle-doped zeolite. Reprinted from Ref. [101].

Under similar experimental conditions, the zeolite/ZnO nanocomposite showed better adsorption capacity than zeolite alone for the removal of both arsenic (As) and lead (Pb). When combined with ZnO, zeolite eliminated 92% of the lead and 85.7% of the arsenic, respectively, compared to 43.6% and 32.3% for pure zeolite [101].

Sacco et al. integrated semiconducting ZnO into zeolite cavities by wet impregnation method and prepared ZnO/ZeO pellets [24]. These pellets were evaluated for the removal of caffeine by a simultaneous process of photocatalysis and adsorption. The studies were performed in two stages, i.e., by adsorption and by adsorption assisted photocatalysis. At the initial stage, the adsorption kinetics were found to be faster in the case of zeolite as compared to the composite. This might be due to decreased mesoporous surface area of the composite, though, the total adsorption was approximately 60% for both the ZnO and ZnO/ZeO composite. When the removal of caffeine by adsorption and adsorption/photocatalysis were examined, it was shown that UV irradiation resulted in a significantly higher total removal of caffeine. Almost 100% of caffeine was removed within 120 min of reaction time by using the ZnO/ZeO composite in adsorption/photocatalysis, while only adsorption gave 69% removal in 120 min. Under UV irradiation, ZnO can degrade the adsorbed caffeine and its chemical intermediates, creating active sites for the adsorption of any leftover caffeine molecules in the liquid medium [24].

Mahalakshmi et al. fabricated the zeolite-supported TiO_2 composite by using the H-form of zeolite Y, β , and ZSM-5 and labeled them as HY, H β , and H-ZSM-5, respectively [102]. The prepared materials were investigated for adsorption and photocatalytic degradation of propoxur, an *N*-methylcarbamate pesticide. According to the experimental data, the adsorption of propoxur was better over $\text{TiO}_2/\text{H}\beta$ than HY/ TiO_2 and H-ZSM-5/ TiO_2 . Propoxur degradation efficiency was found to be better in $\text{TiO}_2/\text{H}\beta$ with optimal TiO_2 loading (7 wt%) than in pure TiO_2 . The limited surface area of H-ZSM-5 and the hydrophilic character of HY were responsible for their poor adsorption capacity. The existence of acid sites in H β with high acid strength might be another factor in propoxur adsorption [102].

Liu et al. evaluated the TiO_2 /zeolite composite for the removal of sulfadiazine (SDZ) via adsorption and photocatalysis under UV light [23]. The composite material was synthesized via the sol-gel method. FTIR analysis indicated the formation of the Ti-O-Si bond in the composite. In 60-min dark studies performed, a small amount of adsorption of SDZ was reported. UV light studies showed the 32.76% degradation of SDZ in 120 min without the aid of a catalyst. The prepared TiO_2 /zeolite composite removed 93.31% of SDZ in the presence of UV light within 120 min. The general mechanism of degradation is as given in Figure 16 [23].

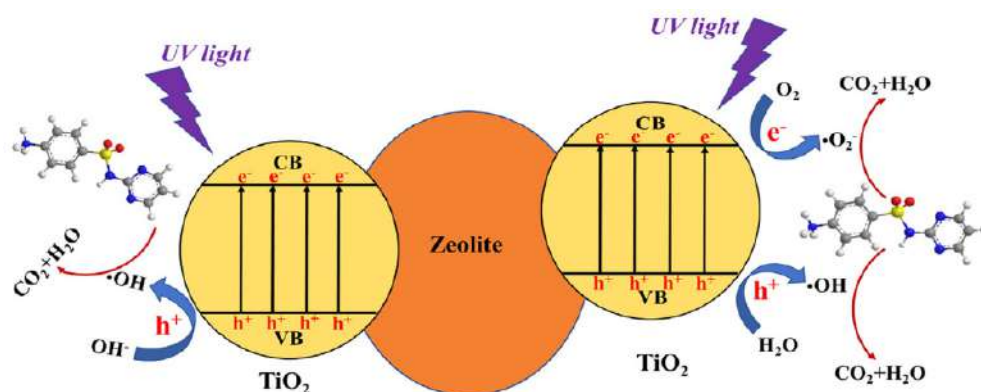


Figure 16. Mechanism of sulphadiazine removal by using zeolite/ TiO_2 composite. Reprinted with permission from Ref. [23]. Copyright 2018 Elsevier.

The participation of reactive oxygen species (ROS), i.e., e^- , h^+ , OH^\bullet , $\text{O}_2^{\bullet-}$, $^1\text{O}_2$ (singlet oxygen), were examined by performing the scavenger studies. It was concluded that ROS contribution in the zeolite/ TiO_2 composite follows the order of $\text{OH}^\bullet > h^+ > \text{O}_2^{\bullet-} > ^1\text{O}_2$.

Additionally, the HPLC–MS/MS study of reaction intermediates was used to hypothesize the four potential degradation pathways [23].

D Mirzaei et al. synthesized the NaX/MgO–TiO₂ zeolite nanocomposite by using the ultrasound-assisted dispersion method [103]. Anionic dye methyl orange was used to investigate adsorption on the prepared composites. To obtain maximum MO adsorption yield from the aqueous solution, different parameters such as initial dye concentration, adsorbent dosage, pH, adsorbent type, and contact time have been assisted and optimized. To estimate the adsorption–desorption isotherm, Freundlich, Temkin, and Langmuir models were used. For subsequent processes, chemical parameters such as 0.3 g L^{−1} adsorbent dosage, 6.5 pH, contact time of 35 min, and temperature of 45 °C were evaluated as the optimized conditions. Under identical experimental conditions, it is determined that the NaX/MgO–TiO₂ nanocomposite led to the highest 95% adsorption efficiency from aqueous solution among NaX, MgO, TiO₂, MgO–TiO₂, and NaX/MgO–TiO₂ adsorbents, and MO adsorption efficiencies over MgO, TiO₂, NaX, MgO–TiO₂, and NaX/MgO–TiO₂ were greater than 30%, 46%, 40%, 68%, and 95%, respectively [103].

A.A. Alswat et al. used a co-precipitation approach to make zeolite/iron oxide (Fe₃O₄) and zeolite/copper oxide (CuO) nanocomposites (NCs) [104]. The adsorption efficiencies were 97.2% and 96.8% for Pb and As, respectively, by zeolite/iron oxide (Fe₃O₄) NCs, and 83.7% and 81.3% for Pb and As, respectively, by zeolite/copper oxide (CuO) NCs at a pH of between 4 and 6 when these composites were kept for 40 min at room temperature and pressure. The Langmuir isotherm model was well followed by the adsorption data [105].

Kong et al. used the co-precipitation method to prepare nanosized Fe–Al bimetallic oxide-doped zeolite spheres and used it to remove Cr(VI) ions from constructed wetlands [106]. The pseudo-second order model was found to be perfectly fitted to the removal of Cr(VI). The composite zeolite spheres outperformed standard fillers in terms of removal, with excellent adsorption across a wide pH range. The Cr(VI) was absorbed and fixed by the composite zeolite spheres, and then it was reduced to Cr(III) using the Fe–Al oxide. Through co-precipitation and ion exchange, the Cr(III) made Cr(OH)₃ and Cr_xFe_{1-x}(OH)₃ precipitates [106].

Zhang et al. used a one-step hydrothermal method to fabricate TiO₂/MoS₂ photocatalysts supported on zeolite utilizing micrometer-MoS₂ as the sensitizer [107]. Under simulated solar-light irradiation, the synthesized photocatalyst TiO₂/MoS₂/zeolite had significantly higher photocatalytic response than the Degussa P25 photocatalyst. The recombination of photogenerated electrons and holes is one of the major factors that limit the efficiency of a photocatalyst. According to Zang et al., during the fabrication procedure, the Z-scheme photocatalyst of TiO₂/MoS₂ was developed where MoS₂ acted as an electron donor in interfacial charge conduction, thereby improving the charge separation. In addition, the generation of superoxide anion radicals (O₂^{•−}), major oxidation species in photocatalytic reactions, can be aided by the micro/nano-MoS₂ generated via the hydrothermal process [107].

D. Wang et al. successfully prepared Cr-doped TiO₂ photocatalysts supported on natural zeolite [104]. Because Ti⁴⁺ and Cr³⁺ have similar ionic radii, Cr ions can be integrated into the TiO₂ lattice by taking the place of Ti⁴⁺ sites. As the calcination temperature rises, the bond strength of Cr–O–Ti increases. Cr dopant is found as Cr⁶⁺ (81.2%) and Cr³⁺ (19.8%) species. In comparison to undoped TiO₂/zeolite, the band gap energy (eV) of 10 mol% Cr/TiO₂/zeolite decreases dramatically from 2.84 eV to 1.70 eV. The percentage degradation of methyl orange by the calcined 10% Cr/TiO₂/zeolite reaches 41.73%, after 5 h of illumination, which is 17.9% higher than the degradation efficiency of undoped TiO₂/zeolite [104].

Italia et al. prepared two composites of zeolite and bentonite separately bonded with titanium and was evaluated for the adsorption of phosphate. Titanium/zeolite and titanium/bentonite composites removed up to 83% and 84% of phosphate at 3 pH [108].

However, it is not always observed that the composites exhibit superior removal efficiencies than the zeolites alone. A. Alcantara-Cobos et al. compared ZnO nanoparticles

and the ZnO-zeolite composite for tetrazine removal [20]. The zeolite-ZnO composite was prepared by the chemical precipitation method. Both adsorption and photocatalysis were working mechanisms behind the removal of tetrazine. The adsorption with ZnO nanoparticles was faster than the ZnO-zeolite composite. The degradation reported followed by adsorption under UV light radiations was 81% and 87% for the zeolite-ZnO composite and ZnO nanoparticles, respectively; although, the latter was difficult to remove from the aqueous solution. Additionally, the ZnO nanoparticles show low toxicity towards *Lactuca sativa* when kept with the dye solution and diluted aqueous solutions [20].

Jaramillo-Fierro et al. synthesized extruded semiconducting $\text{ZnTiO}_3/\text{TiO}_2$ supported on zeolite and its precursor clay [109]. Zeolites were synthesized by using two types of Ecuadorian clays via hydrothermal treatment and the method of alkali fusion, i.e., R-clay and G-clay. Zeolite prepared using R-clay was labeled as R-zeolite and was mostly of the Na-LTA type with a trace quantity of Na-FAU type. Zeolite prepared using G-clay was labeled as G-zeolite and was made up primarily of Na-FAU type zeolite with residues of Na-P1 type zeolite. The semiconducting support $\text{ZnTiO}_3/\text{TiO}_2$ was prepared separately via the sol-gel method. The composites were prepared by mixing zeolites, precursor clays, and $\text{ZnTiO}_3/\text{TiO}_2$ in different ratios. The reported order of adsorption of MB on parent material was G-zeolite > R-zeolite > G-clay > R-clay > $\text{ZnTiO}_3/\text{TiO}_2$. Despite having a higher dye removal capacity than mixed oxide $\text{ZnTiO}_3/\text{TiO}_2$ and precursor clays, the capacity of the extruded composites to remove MB was not increased by zeolites. Additionally, extruded zeolites are less capable of removing the color than powdered zeolites because they have a lower specific surface area [109].

2.4. Zeolite/Carbon-Based Material Composites

Currently, carbon nanomaterials are considered to be the most adaptable materials that can be employed to improve wastewater treatment techniques. Innovative carbon materials have been discovered as a result of extensive research conducted globally and effectively used in wastewater remediation and environmental safety technologies [110,111]. SWNT (single-walled carbon nanotubes), MWNT (multi-walled carbon nanotubes), G (graphene), and GO (graphene oxide) are among the most frequently studied carbon-based nanomaterials. These materials may be employed in their natural forms or as complex hybrid substances [111,112].

Zeolites have been modified by the addition of a heteroatom to their structural framework, giving them new and fascinating qualities, including photoactivity [17,18,113]. Ren et al. produced new generation photocatalysts by combining functional inorganic nanomaterials (such as zeolitic TS-1) with graphene and carbon-nanotube (CNTs) [16]. The performance of these photocatalysts were outstanding owing to (i) the synergistic effect on the basis of interfacial charge and heat transfer reactions and (ii) graphene's ability to modify the shape and size of TS-1. The few layers of graphene were first synthesized via applying direct current discharge to graphene. Zeolite TS-1 was synthesized via the sol-gel process. Zeolite/graphene and zeolite/CNT hybrids were prepared by combining in situ to the common sol-gel synthesis of TS-1. The photocatalytic behavior of these materials was examined through dye degradation in the presence of low-intensity UV radiations. It was observed that the photocatalytic activity of TS-1 zeolite increased 27–28 times with graphene loading and only 4–5 times by CNT loading. The reason is the interfacial charge transfer between the conduction band of zeolite and nanocarbon. Moreover, the high reactivity of edge atoms in graphene might be responsible for high photocatalytic activity [16].

W.A. Khanday et al. synthesized a zeolite/activated carbon composite from oil palm ash using a two-step method, i.e., fusion followed by the hydrothermal process and labeled as Z-AC composite [114]. The adsorption results of MB adsorption on the Z-AC composite were compared with those of activated and non-activated oil palm ash and oil palm ash zeolite. The highest adsorption capacity observed for the Z-AC composite was approximately 90% [114].

H. Li et al. prepared zeolite by granulation, calcination of coal gangue, followed by the hydrothermal process and marked as ZMC [19]. Since the carbon content was removed at the calcination step, prepared ZMC is pure zeolite. By modifying the above-mentioned process, they synthesized a carbon retaining and extra carbon-containing zeolite-activated carbon composite and marked them as ZTC and ZAC, respectively. The prepared samples were examined for the adsorption of Cu^{+2} and rhodamine-B (Rh-B). The adsorption capacities for Cu^{+2} were observed to be 98.2%, 97.1%, 92.8% for ZMC, ZTC, and ZAC, respectively. Similarly, the adsorption capacities for RB were 17.0%, 41.3%, and 94.2% for ZMC, ZTC, and ZAC, respectively. Adsorption capacity for Cu^{+2} decreases upon increasing carbon content. Zeolite has a uniform pore distribution with a pore size of 0.41 nm, which can easily hold small Cu^{+2} ions. On the other hand, activated carbon has variable pore sizes across the network, including micro, meso, and macro pores; high pore sizes are incompatible with holding tiny Cu^{+2} ions and are suitable for adsorption of large organic molecules; hence, adsorption capacity for Rh-B increases upon increasing carbon content [19].

M.A. Farghali et al. synthesized a mesoporous zeolite A/reduced graphene oxide nanocomposite [31]. For this, zeolite was first surface-modified with the help of 3-aminopropyltrimethoxy silane (APTMS), which is used as a binding and mesopore generating agent. Then, using a hydrothermal technique, reduced graphene oxide was added to zeolite-A to create modified mesoporous zeolite-A/reduced graphene oxide NCs (MZ-A/RGO). Following that, the synthesized material was employed to remove lead ions (Pb^{+2}) and methylene blue at the same time. The synthesized composite removed 98% of methylene blue and 93.9% Pb^{+2} [31].

Mahmoodi et al. immobilized the laccase enzyme onto a zeolite and graphene oxide composite via the covalent bond and prepared a biocatalyst for the removal of direct red 23 dye [22]. They used the hydrothermal method for the preparation of zeolite and the Hummers method for the preparation of graphene oxide. The composites were prepared by taking different weight ratios of graphene oxide followed by laccase immobilization. It was observed that the dye degradation increased upon increasing the loading ratio of graphene oxide. Graphene oxides increase the electron transfer between dye and enzyme, thereby enhancing the oxidation ability of the enzyme [22].

Huang T et al. evaluated magnetic graphene oxide-modified zeolite for uptake of methylene blue from an aqueous solution [21]. The magnetic MnFe_2O_3 nanoparticles were synthesized by the co-precipitation method. The Cu-zeolite was made separately as Cu-Z. The Cu-Z-GO-M composite was prepared using the solid-state dispersion method. The composite offered the highest adsorption capacity, i.e., 97.346 mg/g at 318 °C [21].

Using two-step alkali fusion and hydrothermal treatment, Zhao et al. generated a honeycomb-activated carbon-zeolite composite (CZC) using coal fly ash (FA) and utilized it to adsorb Pb^{+2} from an aqueous solution [4]. The pre-treated coal fly ash was heated in a muffle furnace to 750 °C as part of the activation process to produce activated carbon. Activated carbon zeolite CZC owns a specific surface area that is approximately six times greater than FA's, and its average pore size is enlarged from 3.4 to 12.7 μm . At pH 7, CZC demonstrated 185.68 mg/g of $\text{Pb}(\text{II})$ absorption after 40 min of contact time. According to kinetics studies, $\text{Pb}(\text{II})$ ion adsorption onto the surface of CZC is more consistent with pseudo-second order kinetics [4].

2.5. Zeolite/Polymer Composites

Polymers are the organic compounds with a variety of exceptional properties, including high mechanical strength, extraordinary flexibility, large surface area, and chemical stability. Owing to these characteristics, polymers can serve as a host for many inorganic and organic compounds [115]. The application of composite materials, which incorporate both organic and inorganic components, has recently attracted more attention. Combining the materials results in several beneficial properties that the separate materials could not produce. For instance, the elasticity and easy processing of polymers and mechanical properties of inorganic constituents are integrated [116].

Being an amino polysaccharide, chitosan contains several OH and NH₂ groups that might serve as coordination and reaction sites. The fact that chitosan is made from chitin, the second-most abundant natural polymer after cellulose, makes it an extremely abundant and inexpensive material. Chitosan's use as a material in real world applications is, nevertheless, constrained by its weak mechanical characteristics, which can be overcome via crosslinking with high mechanical strength materials, such as zeolites [116]. Khanday WA et al. synthesized composite beads by cross-linking chitosan and zeolite derived from oil palm ash and labeled it as Z-AC/C [117]. The activated oil palm ash was first hydrothermally treated before being beaded with chitosan. The effect of weight percentage of chitosan and Z-AC on the adsorption of MB (methylene blue) and AB-29 (acid blue-29) dyes was studied. Increase in the adsorption of AB29 and decrease in MB adsorption was observed by increasing the percentage of chitosan and vice versa. The Z-AC/C composite with 50:50 weight ratios of chitosan and zeolite well-adsorbed both AB-29 and MB dyes and was used for further studies. For the Z-AC/C composite, the adsorption capacities at 30 °C, 40 °C, and 50 °C were 212.76 mg/g, 238.09 mg/g, and 270.27 mg/g for AB29, 151.51 mg/g, 169.49 mg/g, and 199.20 mg/g for methylene blue, and 212.76 mg/g, 238.09 mg/g, and 270.27 mg/g for acid blue-19, respectively [117].

pH plays a crucial role in adsorption processes as the surface charge, speciation, and degree of ionization of adsorbate are influenced by the pH of the solution. pH influence on the adsorption of AB29 and MB on the Z-AC/C composite was studied in the pH range from 3–13 with 100 ppm initial dye concentration at 30 °C. It was observed that at a pH from 3–5, adsorption of AB29 was great and decreased linearly at pH 13. In the case of MB, the reverse phenomena were reported. At a pH from 3–5, adsorption of MB was less and linearly increased up to a certain pH and stayed constant afterward. At a low pH, electrostatic attractions between the adsorbent's negatively charged surface and the positively charged H⁺ ions of AB29 dye are responsible for faster adsorption. As the pH of the solution increases, the hydrogen ions get diminished, lowering the attraction between the dye molecule and composite resulting in decreased adsorption of AB29. In case of MB, at a low pH, the adsorption is low due to the competition between MB and protons at binding sites. At a higher pH, the surface attains a negative charge, hence, the adsorption increases. Similarly, the initial dye concentration effect on the adsorption was also examined and it was observed that low concentrations reached equilibrium faster than high concentrations in the case of both dyes; the number of unoccupied active sites per dye molecule is low and the motion of dye molecules toward binding sites gets hindered [117].

Pizarro et al. prepared a composite using natural zeolite (NZ) and commercial cationic polymer, Polyammonium cation (SC—581), and labeled it as MZ (Modified zeolite) [118]. The material was investigated for adsorption of sulphate, a pollutant originating from processes of sulphate mining. Modification of zeolite with cationic polymer induces a positive charge on the adsorbent surface, which helps to bind sulphate ions. Also, the positive charge of MZ remains intact above pH 4, while the NZ holds the negative charge. The adsorption capacities of NZ were almost doubled with polymer impregnation. The effect of ion strength was also investigated, indicating that the adsorbent functions well below a KCl concentration of 0.050 mol/liter [118].

Senguttuvan et al. synthesized the zeolite/polypyrrole composite for the removal of reactive blue and reactive red dyes [25]. By performing oxidative polymerization of pyrrole in the presence of zeolite, the composite nano-adsorbent was fabricated. The FE-SEM and TEM images of PPy/Ze composites are shown in Figure 17. The particles are mostly agglomerated with a spherical shape and an average particle size between 40 and 80 nm. Even after adsorption of RB and RR, the PPy/Ze nanocomposites' morphology did not change, which indicates the uniform dye adsorption on the surface of PPy/Ze nanocomposites.

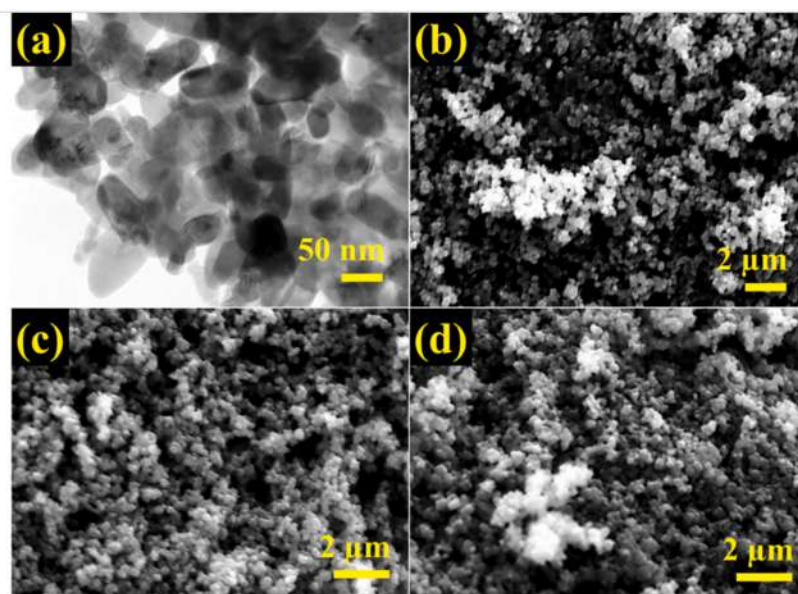


Figure 17. (a) TEM images of PPy/Ze NCs; SEM images of (b) PPy/Ze NCs, (c) PPy/Ze NCs after RB adsorption, (d) PPy/Ze NCs after RR adsorption. Reprinted with permission from Ref. [25]. Copyright 2022 Elsevier.

With a 1.8 mg/mL catalyst dosage, and 75 ppm initial dye concentration, the nanocomposite adsorbed 88.3% of RR and 86.2% of RB within 75 min. Interaction between the dyes and PPy/Ze NCs was mostly mediated by aromatic, hydroxyl, and amide functional groups. The adsorption mechanism involved hydrogen bonding and electrostatic interactions. Senguttuvan et al. also reported the same PPy/Ze NCs for 83.5% removal of Cr(VI) in 50 min [119].

Yigit et al. fabricated beads of natural composite material using clinoptilolite, a natural zeolite, and alginate, a naturally occurring polymer and labeled it A-C (alginate-clinoptilolite) [120]. These A-C beads were employed in the mixture of heavy metals carrying copper (Cu^{+2}), lead (Pb^{+2}), and cadmium (Cd^{+2}) ions. For 10 ppm of initial metal concentration, a constant operation with 2 mL/min flow rate revealed 98% of lead uptake. The repeatability test revealed that the efficiency of the adsorbent was up to the mark until 3 cycles with regeneration via HNO_3 washing [120].

Conducting polymers has attracted a lot of interest because of their appealing features, including electrical conductivity and optical qualities. Due to its fascinating qualities, such as excellent chemical stability, cost-effectiveness, and facile synthesis, Polyaniline (PANI) is a unique and amazing polymer of the conducting polymer family. Additionally, upon visible light excitation, PANI can donate the electrons and act as a good hole transporter [121,122]. Hence, in addition to being adsorbent, PANI can also act as a photocatalyst and degrade organic pollutants.

To make zeolite/conducting polymer-based (nano-)composites, four alternative routes can be used [123]. (i) The organic solvent is enclosed in the zeolite cavities first; subsequently, oxidative polymerization is performed to produce polymeric chains in the zeolitic cavities [124]. (ii) Zeolites containing oxidant ions, such as Fe(III) and Cu(II) are reacted with monomer and acid vapors [125]. (iii) In the presence of zeolite, by performing in situ polymerization of the monomer, polymers can be developed inside or outside the channels of zeolite [126,127]. (iv) Powdered zeolite and conducting polymer are mixed mechanically [128]. Methods (ii) and (iii) of the previously outlined techniques hold the most interest since they produce nanoscale polymeric chains that are embedded in zeolite cavities. Therefore, as the polymeric chains are arranged at the nanoscale, the mechanical, electrical, chemical, and optical characteristics may be enhanced [123].

Abukhadra et al. synthesized the heulandite/polyaniline composite for the efficient removal of light green SF (LGSF), methylene blue (MB), and Congo red dyes from water [129]. Abukhadra et al. prepared the heulandite/polyaniline composite by the mechanical mixing of heulandite, natural zeolite, and synthesized conducting polymer, polyaniline. According to Tauc plot calculations, the optical band gaps of HU/PANI and PANI were 1.69 eV and 2.98, respectively. To examine the photocatalytic activities, studies were carried out both in dark conditions and with artificial visible light. The pseudo-second order and the Elovich model both provided good fits for the kinetic results. The Langmuir isotherm model provided a good description of the adsorption process in the dark, and the estimated q_{\max} was 44.6 mg/g. The experimental data were well-fitted to the Freundlich and Temkin models under visible light illumination compared to the Langmuir model. This shows the function of photodegradation by the HU/PANI composite in improving the multilayer adsorption. The quadratic programming projected that the ideal conditions for the highest elimination percentage in the dark, i.e., 70.9%, 5.5 ppm dye concentration, pH 3, 24 mg dosage of Hu/PANI, and contact duration of 430 min. Whereas, in the presence of visible light, at 15 mg catalyst dosage, 15 ppm dye concentration, contact time of 589 min, pH 3, and 97% dye removal is possible [129].

Milojević-Rakić investigated the polyaniline/FeZSM-5 composite for the removal of glyphosate, a herbicide via oxidative degradation [33]. Different weight ratios of aniline/FeZSM-5 was used. The method employed for synthesis was the oxidation polymerization of FeZSM-5 with ammonium peroxy disulphate as an oxidant, with and without using acid (H_2SO_4). 1/1 and 1/5 weight ratios of aniline/FeZSM-5 were used to make the composites. The composite with the 1/1 and 1/5 ratios of aniline/FeZSM-5 and synthesized without using acid was labeled as PFeZ1/1 and PFeZ1/5, respectively. Similarly, the composite with the 1/5 ratio of aniline/FeZSM-5 and synthesized using acid was labeled as PFeZ1/1S and PFeZ1/5S, respectively. The NH_4OH treated (deprotonated) forms of PFeZ1/1, PFeZ1/5, PFeZ1/1S, and PFeZ1/5S were labeled as PFeZ1/1d, PFeZ1/5d, PFeZ1/1Sd, and PFeZ1/5Sd. Polyaniline was also synthesized and treated similarly and labeled as PANI, PANI/S, PANId, and PANIS/d, the same way as composites. The morphological analysis can be seen in Figure 18.

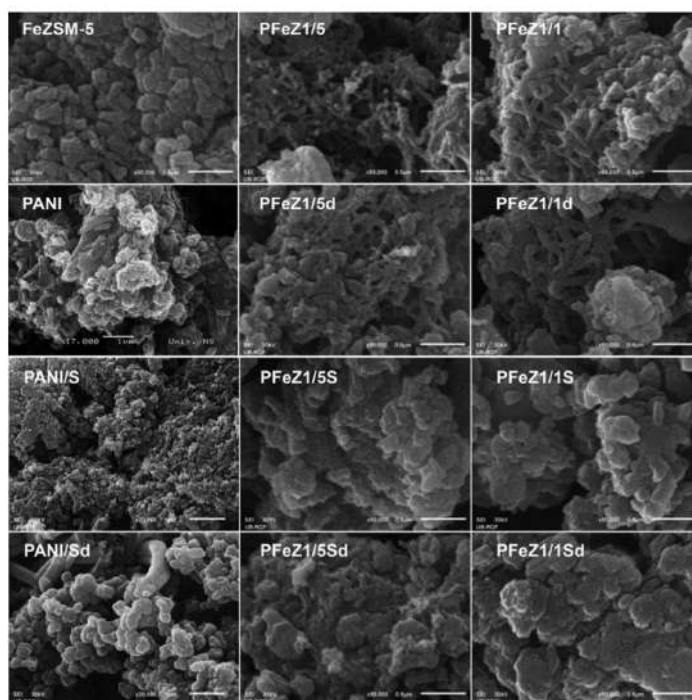


Figure 18. SEM images of PANI, FeZSM-5, and their composites. Reprinted with permission from Ref. [33]. Copyright 2018 Elsevier.

By performing the conductivity analysis, it was observed that the composites synthesized with the use of acid have higher conductivity in comparison to composites synthesized without acid. Additionally, the decrease in conductivity was observed by increasing the loading of zeolite; this elucidates the lower conducting nature of zeolites. Moreover, with the help of thermogravimetric analysis, the weight content of polyaniline and FeZSM-5 in the composites were evaluated. Table 7 gives the weight content of PANI and FeZSM-5 as well as the percentage degradation and removal of glyphosate from the solution [33].

Table 7. Weight contents, percentage removal, degradation, and adsorption in composites. Reprinted with permission from Ref. [33]. Copyright 2018 Elsevier.

Sample	Weight Content		FeZSM/PANI Weight Ratio	% Removal	% Degradation	% Adsorption
	FeZSM-5	PANI				
PANI	-	-	-	12.4	11.6	0.8
ZSM-5	-	-	-	12.8	7.1	5.7
PFeZ1/1	43.1	52.2	0.83	40.8	31.9	8.9
PFeZ1/5	77.9	18.1	4.30	80.4	66.5	13.9
PANI/S	-	-	-	10.2	9.7	0.5
PFeZ1/1S	42.2	51.6	0.82	26.8	22.6	4.2
PFeZ1/5S	76.9	16.8	4.58	18.1	13.6	4.5
PANId	-	-	-	56.6	54.4	2.2
PFeZ1/1d	47.4	48.4	0.98	13.6	8.4	5.2
PFeZ1/5d	78.9	15.0	5.26	20.4	14.6	5.8
PANI/Sd	-	-	-	6.6	2.8	3.8
PFeZ1/1Sd	47.2	48.4	0.98	7.4	1.1	6.3
PFeZ1/5Sd	79.4	15.5	5.12	3.8	0	3.8

The composites prepared without added acids showed better removal and degradation than those synthesized via adding acids. The deprotonation significantly reduced the degradation and removal efficiencies of all catalysts. From the data given in the above Table 7, it can be concluded that composite PFeZ1/5 showed the higher removal efficiency among all other catalysts. The PFeZ1/5 has an increased number of iron sites; hence, an increased amount of degradation is observed [33].

Milojevic-Rakic et al. also prepared the ZSM-5/polyaniline composite by glyphosate adsorption [26]. The ZSM-5/polyaniline composite was prepared by performing the oxidative polymerization of aniline with and without added acid. Similar to the above-reported studies, the deprotonation of samples was also conducted. Among all the adsorbents, the deprotonated form of PANI prepared via acid synthesized polyaniline showed the maximum adsorption of glyphosate, i.e., (98.5 mg/g). The decrease in adsorption capacities was observed by increasing the zeolite loadings. The poor adsorption properties of ZSM-5 and composites containing the high weight ratios of ZSM-5 were most likely caused by its high microporosity, which is unfavorable for adsorption of comparatively huge glyphosate molecules. The linear, regular, and defect-free emeraldine base structure of PANI/Sd chains results in effective interaction with the glyphosate molecules. This was attributed to superior glyphosate adsorption characteristics of PANI/ Sd [26].

3. Comparison of Removal Efficiencies

The brief literature survey on zeolite and its composites for wastewater treatment is compiled in Table 8.

Table 8. Comparison of effluent removal efficiencies of zeolites and zeolite-based composites.

Material	Source /Synthesis Approach	Band Gap (eV)	Contaminant	Mechanism	Dosage (mg/mL)	Concentration (ppm)	Contact Time	Removal	Light Source	Published Year	Ref
Zeolite	Indonesia commercial		NH ₄ ⁺	Adsorption, ion exchange	0.00152	12.9	134.89 min	98%		2020	[76]
Natural zeolite	Chinese commercial		NH ₄ ⁺	Adsorption	0.048	80	180 min	96%		2010	[11]
Natural zeolite	Australia commercial		Methylene blue	Adsorption	0.25	3.55	200 h	6.8 × 10 ⁻⁵ mol/g		2005	[75]
Natural zeolite	Australia commercial		Rhodamine B	Adsorption	0.25	3.55	50 h	2.1 × 10 ⁻⁵ mol/g		2005	[75]
Hydrogenated form of natural zeolite	Caranco Blanco	2.63	Caffeine	Photocatalysis	10	50	4 h	99%	UV	2020	[13]
Synthetic zeolite	Hydrothermal treatment using aluminum iso propoxide	3.29	Methylene blue	Photocatalysis	2	10	180 min	85%	UV	2020	[14]
Titania-Supported zeolite	In situ using TiCl ₄ impregnation	3.31	Methylene blue	Photocatalysis	0.33	30	60 min	40%	UV	2010	[130]
Titania-supported zeolite	In situ using TiCl ₄ impregnation	3.31	Direct blue 71	Photocatalysis	0.33	30	60 min	55%	UV	2010	[130]
Titania-supported zeolite	In situ using TiCl ₄ impregnation	3.31	Direct yellow 8	Photocatalysis	0.33	30	60 min	62.5%	UV	2010	[130]
Heulandite/nickel oxide	In situ polymerization followed by Ni ₂ O ₃ impregnation	1.42	Safranin T	Photocatalysis	0.35	5	1 min	100%	Solar irradiation	2018	[30]
benonite/PANI/Ni ₂ O ₃	In situ polymerization followed by Ni ₂ O ₃ impregnation	1.61	Safranin-O	Photocatalysis	0.5	5	90 min	100%	Sunlight	2018	[131]
Heulandite/polyaniline	Mechanical mixing	1.69	LGSF	Photocatalysis	0.3	15	589 min	97%	VIS	2018	[129]
Heulandite/polyaniline	Mechanical mixing	1.69	MB	Photocatalysis	0.2	20	589 min	68.77%	VIS	2018	[129]
Fe-Al bimetallic oxide loaded zeolite	Co-precipitation		Cr(VI)	Adsorption	40	20	300 min	84.9%		2020	[106]
Zeolite/ZnO	Wet impregnation method		Caffeine	Adsorption/photocatalysis	500	25	120 min	100%	UV	2018	[24]
Zeolite/ZnO	Co-precipitation		Pb(II)	Adsorption	3	100	30 min	92%		2017	[101]
Zeolite/ZnO	Co-precipitation		As(V)	Adsorption	3	10	30 min	85.7%		2017	[101]
Zeolite/TiO ₂	Sol-gel		Sulfadiazine	Photocatalysis	1	1	120 min	93.31%	UV	2018	[23]
Zeolite/Activated carbon	Hydrothermal		Cu ²⁺	Adsorption	2	240	60 min	92.8%		2020	[19]
Zeolite/Activated carbon	Hydrothermal		Rhodamine B	Adsorption	2	240	60 min	94.2%		2020	[19]
Zeolite/Activated carbon	Fusion/Hydrothermal		Methylene blue	Adsorption	1	100	30 h	83%		2016	[114]
Zeolite/Poly pyrrole	In situ polymerization		Reactive Red	Adsorption	1.8	75	75 min	88.3%		2022	[25]
Zeolite/Poly pyrrole	In situ polymerization		Reactive Blue	Adsorption	1.8	75	75 min	86.2%		2022	[25]

4. Conclusions, Challenges, and Future Perspectives

Zeolites are the materials widely used as adsorbents and ion-exchangers for the remediation of pollutants. This study describes the synthesis, removal process, mechanism, and application of zeolite-based materials in wastewater treatment, which gives first-hand information for researchers who want to explore zeolite-based materials.

Researchers have doped various materials, such as metal oxides, polymers, and carbon-based materials, with zeolites to make zeolite-based composites. In most cases, these composites exhibit higher removal efficiency than bare zeolites. Additionally, the composites also enable zeolites to function as an effective photocatalyst for the total breakdown of contaminants, which is noticeably less apparent in bare zeolites. Composites of zeolite with semi-conducting materials, such as semiconducting metal oxides, graphene, CNTs, and conducting polymers, are of great interest because of the photodegradation of the contaminants.

The low efficiency, lack of homogeneous properties, lack of accessibility, and high levels of impurities in natural zeolite led to the synthetic preparation of zeolites. Major challenges are faced in the synthesis of zeolites, such as high-cost, the tedious and time-consuming synthesis and filtration process, generation of alkaline wastewater, etc. Research needs to be conducted for the synthesis of zeolites with homogenous properties, cost minimization, and easy processibility in order to establish the material for its easy application on the industrial level.

The raw natural zeolites, i.e., pristine zeolites without any modifications, have a negative charge across its framework and are only capable of attracting cationic contaminants. Some modifications expand its application for the elimination of anionic pollutants as well. Zeolites can also be modified through doping with foreign materials.

This review motivates researchers to further investigate the photocatalytic behavior of zeolites and zeolite-based materials, since very few studies have been undertaken for the estimation of degradation pathways, contribution of ROS species (scavenger studies), and calculation of band edge positions. In future research, these aspects should also be considered for the better understanding of photodegradation in zeolite-based materials. The photocatalytic devices of zeolite-based materials for wastewater treatment are still not available in the market. Future interest should be on the preparation of zeolite-based wastewater purifiers that work on both the concept of photocatalysis and adsorption, which are easy to synthesize and can be realized in a much cheaper way so they can be easily commercialized and become feasible on an industrial scale.

Author Contributions: Conceptualization, V.S., S.S. and R.G.; methodology, V.S. and S.S.; software, V.S. and S.S.; validation, V.S. and S.S.; formal analysis, V.S.; resources, S.S., N.S. and I.A.; writing—original draft preparation, V.S. and S.S.; writing—review and editing, V.S., S.S., R.G., R.B., I.A. and N.S.; supervision, S.S. and R.B.; funding acquisition, N.S., I.A. and S.S. All authors have read and agreed to the published version of the manuscript.

Funding: The authors would like to thank Pandit Deendayal Energy University, Scientific Research Deanship at King Khalid University, Abha, Saudi Arabia through the Large Research Group Project under grant number (RGP.02/219/43) and the Marine Pollution Special Interest Group, the National Defence University of Malaysia via SF0076-UPNM/2019/SF/ICT/6, for providing research facilities and funding.

Data Availability Statement: Not applicable.

Conflicts of Interest: The authors declare no conflict of interest.

References

1. Gray, N. *Water Science and Technology: An Introduction*; CRC Press: Boca Raton, FL, USA, 2017.
2. Moradihamedani, P. Recent advances in dye removal from wastewater by membrane technology: A review. *Polym. Bull.* **2021**, *79*, 2603–2631. [CrossRef]
3. Natarajan, V.; Karunanidhi, M.; Raja, B. A critical review on radioactive waste management through biological techniques. *Environ. Sci. Pollut. Res.* **2020**, *27*, 29812–29823. [CrossRef] [PubMed]

4. Zhao, M.; Ma, X.; Chen, D.; Liao, Y. Preparation of Honeycomb-Structured Activated Carbon–Zeolite Composites from Modified Fly Ash and the Adsorptive Removal of Pb(II). *ACS Omega* **2022**, *7*, 9684–9689. [CrossRef] [PubMed]
5. Li, Y.; Yu, H.; Liu, L.; Yu, H. Application of co-pyrolysis biochar for the adsorption and immobilization of heavy metals in contaminated environmental substrates. *J. Hazard. Mater.* **2021**, *420*, 126655. [CrossRef]
6. Soni, V.; Singh, P.; Quang, H.H.P.; Khan, A.A.P.; Bajpai, A.; Van Le, Q.; Thakur, V.K.; Thakur, S.; Nguyen, V.H.; Raizada, P. Emerging architecture titanium carbide (Ti₃C₂Tx) MXene based photocatalyst toward degradation of hazardous pollutants: Recent progress and perspectives. *Chemosphere* **2022**, *293*, 133541. [CrossRef]
7. Shahabuddin, S.; Sarih, N.M.; Ismail, F.H.; Shahid, M.M.; Huang, N.M. Synthesis of chitosan grafted-polyaniline/Co₃O₄ nanocube nanocomposites and their photocatalytic activity toward methylene blue dye degradation. *RSC Adv.* **2015**, *5*, 83857–83867. [CrossRef]
8. Zhang, L.; Wang, L.; Zhang, Y.; Wang, D.; Guo, J.; Zhang, M.; Li, Y. The performance of electrode ultrafiltration membrane bioreactor in treating cosmetics wastewater and its anti-fouling properties. *Environ. Res.* **2021**, *206*, 112629. [CrossRef]
9. Lu, W.; Zhang, Y.; Wang, Q.; Wei, Y.; Bu, Y.; Ma, B. Achieving advanced nitrogen removal in a novel partial denitrification/anammox-nitrifying (PDA-N) biofilter process treating low C/N ratio municipal wastewater. *Bioresour. Technol.* **2021**, *340*, 125661. [CrossRef]
10. Prajaputra, V.; Abidin, Z.; Widiatmaka; Suryaningtyas, D.T.; Rizal, H. Characterization of Na-P1 zeolite synthesized from pumice as low-cost materials and its ability for methylene blue adsorption. In *IOP Conference Series: Earth and Environmental Science*; IOP Publishing: Bristol, UK, 2019.
11. Huang, H.; Xiao, X.; Yan, B.; Yang, L. Ammonium removal from aqueous solutions by using natural Chinese (Chende) zeolite as adsorbent. *J. Hazard. Mater.* **2010**, *175*, 247–252. [CrossRef]
12. De Luca, P.; Bernaudo, I.; Elliani, R.; Tagarelli, A.; Nagy, J.B.; Macario, A. Industrial Waste Treatment by ETS-10 Ion Exchanger Material. *Materials* **2018**, *11*, 2316. [CrossRef]
13. Alvarez-Aguinaga, E.A.; Elizalde-González, M.P.; Sabinas-Hernández, S.A. Unpredicted photocatalytic activity of clinoptilolite-mordenite natural zeolite. *RSC Adv.* **2020**, *10*, 39251–39260. [CrossRef] [PubMed]
14. Nassar, M.Y.; Abdelrahman, E.A. Hydrothermal tuning of the morphology and crystallite size of zeolite nanostructures for simultaneous adsorption and photocatalytic degradation of methylene blue dye. *J. Mol. Liq.* **2017**, *242*, 364–374. [CrossRef]
15. Wang, S.; Peng, Y. Natural zeolites as effective adsorbents in water and wastewater treatment. *Chem. Eng. J.* **2010**, *156*, 11–24. [CrossRef]
16. Ren, Z.; Kim, E.; Pattinson, S.W.; Subrahmanyam, K.S.; Rao, C.N.R.; Cheetham, A.K.; Eder, D. Hybridizing photoactive zeolites with graphene: A powerful strategy towards superior photocatalytic properties. *Chem. Sci.* **2011**, *3*, 209–216. [CrossRef]
17. Notari, B. Titanium silicalite: A new selective oxidation catalyst. In *Studies in Surface Science and Catalysis*; Elsevier: Amsterdam, The Netherlands, 1991; pp. 343–352.
18. Hashimoto, S. Zeolite photochemistry: Impact of zeolites on photochemistry and feedback from photochemistry to zeolite science. *J. Photochem. Photobiol. C Photochem. Rev.* **2003**, *4*, 19–49. [CrossRef]
19. Li, H.; Zheng, F.; Wang, J.; Zhou, J.; Huang, X.; Chen, L.; Hu, P.; Gao, J.-M.; Zhen, Q.; Bashir, S.; et al. Facile preparation of zeolite-activated carbon composite from coal gangue with enhanced adsorption performance. *Chem. Eng. J.* **2020**, *390*, 124513. [CrossRef]
20. Alcántara-Cobos, A.; Gutiérrez-Segura, E.; Solache-Ríos, M.; Amaya-Chávez, A.; Solís-Casados, D. Tartrazine removal by ZnO nanoparticles and a zeolite-ZnO nanoparticles composite and the phytotoxicity of ZnO nanoparticles. *Microporous Mesoporous Mater.* **2020**, *302*, 110212. [CrossRef]
21. Huang, T.; Yan, M.; He, K.; Huang, Z.; Zeng, G.; Chen, A.; Peng, M.; Li, H.; Yuan, L.; Chen, G. Efficient removal of methylene blue from aqueous solutions using magnetic graphene oxide modified zeolite. *J. Colloid Interface Sci.* **2019**, *543*, 43–51. [CrossRef]
22. Mahmoodi, N.M.; Saffar-Dastgerdi, M.H. Clean Laccase immobilized nanobiocatalysts (graphene oxide-zeolite nanocomposites): From production to detailed biocatalytic degradation of organic pollutant. *Appl. Catal. B Environ.* **2019**, *268*, 118443. [CrossRef]
23. Liu, X.; Liu, Y.; Lu, S.; Guo, W.; Xi, B. Performance and mechanism into TiO₂/Zeolite composites for sulfadiazine adsorption and photodegradation. *Chem. Eng. J.* **2018**, *350*, 131–147. [CrossRef]
24. Sacco, O.; Vaiano, V.; Matarangolo, M. ZnO supported on zeolite pellets as efficient catalytic system for the removal of caffeine by adsorption and photocatalysis. *Sep. Purif. Technol.* **2018**, *193*, 303–310. [CrossRef]
25. Senguttuvan, S.; Janaki, V.; Senthilkumar, P.; Kamala-Kannan, S. Polypyrrole/zeolite composite—A nanoadsorbent for reactive dyes removal from synthetic solution. *Chemosphere* **2021**, *287*, 132164. [CrossRef] [PubMed]
26. Milojević-Rakić, M.; Janošević, A.; Krstić, J.; Vasiljević, B.N.; Dondur, V.; Ćirić-Marjanović, G. Polyaniline and its composites with zeolite ZSM-5 for efficient removal of glyphosate from aqueous solution. *Microporous Mesoporous Mater.* **2013**, *180*, 141–155. [CrossRef]
27. Kamali, M.; Esmaeili, H.; Tamjidi, S. Synthesis of Zeolite Clay/Fe-Al Hydrotalcite Composite as a Reusable Adsorbent for Adsorption/Desorption of Cationic Dyes. *Arab. J. Sci. Eng.* **2022**, *47*, 6651–6665. [CrossRef]
28. Baglio, V.; Arico, A.S.; Di Blasi, A.; Antonucci, P.L.; Nannetti, F.; Tricoli, V.; Antonucci, V. Zeolite-based composite membranes for high temperature direct methanol fuel cells. *J. Appl. Electrochem.* **2005**, *35*, 207–212. [CrossRef]
29. Pan, X.; Jiao, F.; Miao, D.; Bao, X. Oxide–Zeolite-Based Composite Catalyst Concept That Enables Syngas Chemistry beyond Fischer–Tropsch Synthesis. *Chem. Rev.* **2021**, *121*, 6588–6609. [CrossRef]

30. Abukhadra, M.R.; Shaban, M.; El Samad, M.A.A. Enhanced photocatalytic removal of Safranin-T dye under sunlight within minute time intervals using heulandite/polyaniline@nickel oxide composite as a novel photocatalyst. *Ecotoxicol. Environ. Saf.* **2018**, *162*, 261–271. [CrossRef]
31. Farghali, M.A.; Abo-Aly, M.M.; Salaheldin, T.A. Modified mesoporous zeolite-A/reduced graphene oxide nanocomposite for dual removal of methylene blue and Pb²⁺ ions from wastewater. *Inorg. Chem. Commun.* **2021**, *126*, 108487. [CrossRef]
32. Baker, H.M.; Massadeh, A.M.; Younes, H. Natural Jordanian zeolite: Removal of heavy metal ions from water samples using column and batch methods. *Environ. Monit. Assess.* **2008**, *157*, 319–330. [CrossRef]
33. Milojević-Rakić, M.; Bajuk-Bogdanović, D.; Vasiljević, B.N.; Rakić, A.; Škrivanj, S.; Ignjatović, L.; Dondur, V.; Mentus, S.; Ćirić-Marjanović, G. Polyaniline/FeZSM-5 composites—Synthesis, characterization and their high catalytic activity for the oxidative degradation of herbicide glyphosate. *Microporous Mesoporous Mater.* **2018**, *267*, 68–79. [CrossRef]
34. Rad, L.R.; Anbia, M. Zeolite-based composites for the adsorption of toxic matters from water: A review. *J. Environ. Chem. Eng.* **2021**, *9*, 106088.
35. Tchobanoglus, G.; Burton, F.; Stensel, H.D. Wastewater engineering. *Management* **1991**, *7*, 201.
36. Ilyas, S.; Bhatti, H.N. Microbial Diversity as a Tool for Wastewater Treatment. In *Advanced Materials for Wastewater Treatment*; John Wiley & Sons: Hoboken, NJ, USA, 2017; p. 171.
37. Bilotta, G.; Brazier, R. Understanding the influence of suspended solids on water quality and aquatic biota. *Water Res.* **2008**, *42*, 2849–2861. [CrossRef] [PubMed]
38. Chenglin, Z.; Jing, Y.; Yulei, Z.; Fan, W.; Hao, X.; Shi, C.; Qi, N.; Wei, L. Design and performance of Multiway Gravity Device on removing suspended solids in aquaculture water. *Trans. Chin. Soc. Agric. Eng.* **2015**, *31*, 53–60.
39. Wang, D.; Sun, Y.; Tsang, D.C.; Hou, D.; Khan, E.; Alessi, D.S.; Zhao, Y.; Gong, J.; Wang, L. The roles of suspended solids in persulfate/Fe²⁺ treatment of hydraulic fracturing wastewater: Synergistic interplay of inherent wastewater components. *Chem. Eng. J.* **2020**, *388*, 124243. [CrossRef]
40. Lohani, S.P.; Khanal, S.N.; Bakke, R. A simple anaerobic and filtration combined system for domestic wastewater treatment. *Water-Energy Nexus* **2020**, *3*, 41–45. [CrossRef]
41. Huang, J.; Chen, S.; Ma, X.; Yu, P.; Zuo, P.; Shi, B.; Wang, H.; Alvarez, P.J. Opportunistic pathogens and their health risk in four full-scale drinking water treatment and distribution systems. *Ecol. Eng.* **2021**, *160*, 106134. [CrossRef]
42. Srinivas, N.; Malla, R.R.; Kumar, K.S.; Sailesh, A.R. Environmental carcinogens and their impact on female-specific cancers. In *A Theranostic and Precision Medicine Approach for Female-Specific Cancers*; Elsevier: Amsterdam, The Netherlands, 2021; pp. 249–262.
43. Paumo, H.K.; Das, R.; Bhaumik, M.; Maity, A. Visible-Light-Responsive Nanostructured Materials for Photocatalytic Degradation of Persistent Organic Pollutants in Water. In *Green Methods for Wastewater Treatment*; Springer: Berlin/Heidelberg, Germany, 2020; pp. 1–29.
44. Guo, Y.; Kannan, K. Analytical methods for the measurement of legacy and emerging persistent organic pollutants in complex sample matrices. In *Comprehensive Analytical Chemistry*; Elsevier: Amsterdam, The Netherlands, 2015; pp. 1–56.
45. Silver, M.K.; Meeker, J.D. Endocrine Disruption of Developmental Pathways and Children’s Health. In *Endocrine Disruption and Human Health*; Elsevier: Amsterdam, The Netherlands, 2022; pp. 291–320.
46. Briffa, J.; Sinagra, E.; Blundell, R. Heavy metal pollution in the environment and their toxicological effects on humans. *Heliyon* **2020**, *6*, e04691. [CrossRef]
47. Právělie, R.; Bandoc, G. Nuclear energy: Between global electricity demand, worldwide decarbonisation imperativeness, and planetary environmental implications. *J. Environ. Manag.* **2018**, *209*, 81–92. [CrossRef] [PubMed]
48. Halevi, O.; Chen, T.-Y.; Lee, P.S.; Magdassi, S.; Hriljac, J.A. Nuclear wastewater decontamination by 3D-Printed hierarchical zeolite monoliths. *RSC Adv.* **2020**, *10*, 5766–5776. [CrossRef]
49. Kautsky, U.; Lindborg, T.; Valentin, J. Humans and Ecosystems Over the Coming Millennia: Overview of a Biosphere Assessment of Radioactive Waste Disposal in Sweden. *Ambio* **2013**, *42*, 383–392. [CrossRef] [PubMed]
50. Ødegaard, H. Advanced compact wastewater treatment based on coagulation and moving bed biofilm processes. *Water Sci. Technol.* **2000**, *42*, 33–48. [CrossRef]
51. Gouamid, M.; Ouahrani, M.; Bensaci, M. Adsorption Equilibrium, Kinetics and Thermodynamics of Methylene Blue from Aqueous Solutions using Date Palm Leaves. *Energy Procedia* **2013**, *36*, 898–907. [CrossRef]
52. Ginimuge, P.R.; Jyothi, S. Methylene blue: Revisited. *J. Anaesthesiol. Clin. Pharmacol.* **2010**, *26*, 517. [CrossRef]
53. Zacharia, J.T. Ecological Effects of Pesticides. In *Pesticides in the Modern World-Risks and Benefits*; InTech Publisher: London, UK, 2011; pp. 129–142.
54. Jatoi, A.S.; Hashmi, Z.; Adriyani, R.; Yuniarto, A.; Mazari, S.A.; Akhter, F.; Mubarak, N.M. Recent trends and future challenges of pesticide removal techniques—A comprehensive review. *J. Environ. Chem. Eng.* **2021**, *9*, 105571. [CrossRef]
55. Pratush, A.; Kumar, A.; Hu, Z. Adverse effect of heavy metals (As, Pb, Hg, and Cr) on health and their bioremediation strategies: A review. *Int. Microbiol.* **2018**, *21*, 97–106. [CrossRef]
56. Darban, Z.; Shahabuddin, S.; Gaur, R.; Ahmad, I.; Sridewi, N. Hydrogel-Based Adsorbent Material for the Effective Removal of Heavy Metals from Wastewater: A Comprehensive Review. *Gels* **2022**, *8*, 263. [CrossRef]
57. Gerardi, M.H. *Troubleshooting the Sequencing Batch Reactor*; John Wiley & Sons: Hoboken, NJ, USA, 2011.
58. Cai, L.; Zhang, T. Detecting Human Bacterial Pathogens in Wastewater Treatment Plants by a High-Throughput Shotgun Sequencing Technique. *Environ. Sci. Technol.* **2013**, *47*, 5433–5441. [CrossRef]

59. Chahal, C.; Van Den Akker, B.; Young, F.; Franco, C.; Blackbeard, J.; Monis, P. Pathogen and particle associations in wastewater: Significance and implications for treatment and disinfection processes. *Adv. Appl. Microbiol.* **2016**, *97*, 63–119.
60. Karim, M.R.; Manshadi, F.D.; Karpiscak, M.M.; Gerba, C.P. The persistence and removal of enteric pathogens in constructed wetlands. *Water Res.* **2004**, *38*, 1831–1837. [CrossRef]
61. Auerbach, S.M.; Carrado, K.A.; Dutta, P.K. (Eds.) *Handbook of Zeolite Science and Technology, 1st ed*; CRC Press: Boca Raton, FL, USA, 2003.
62. Baile, P.; Fernández, E.; Vidal, L.; Canals, A. Zeolites and zeolite-based materials in extraction and microextraction techniques. *Analyst* **2018**, *144*, 366–387. [CrossRef] [PubMed]
63. Ramesh, K.; Reddy, D.D. Zeolites and Their Potential Uses in Agriculture. *Adv. Agron.* **2011**, *113*, 219–241.
64. Available online: https://asia.iza-structure.org/IZA-SC/ftc_table.php (accessed on 1 August 2022).
65. Ma, Y.; Qi, P.; Ju, J.; Wang, Q.; Hao, L.; Wang, R.; Sui, K.; Tan, Y. Gelatin/alginate composite nanofiber membranes for effective and even adsorption of cationic dyes. *Compos. Part B Eng.* **2019**, *162*, 671–677. [CrossRef]
66. Artioli, Y. Adsorption. In *Encyclopedia of Ecology Fath, SEJD*; Academic Press: Oxford, UK, 2008.
67. Hu, H.; Xu, K. Physicochemical technologies for HRP and risk control. In *High-Risk Pollutants in Wastewater*; Elsevier: Amsterdam, The Netherlands, 2020; pp. 169–207.
68. Wang, X.; Zhu, N.; Yin, B. Preparation of sludge-based activated carbon and its application in dye wastewater treatment. *J. Hazard. Mater.* **2008**, *153*, 22–27. [CrossRef] [PubMed]
69. Soliman, N.; Moustafa, A. Industrial solid waste for heavy metals adsorption features and challenges; a review. *J. Mater. Res. Technol.* **2020**, *9*, 10235–10253. [CrossRef]
70. Rangabhashiyam, S.; Suganya, E.; Selvaraju, N.; Varghese, L.A. Significance of exploiting non-living biomaterials for the biosorption of wastewater pollutants. *World J. Microbiol. Biotechnol.* **2014**, *30*, 1669–1689. [CrossRef]
71. Bhattacharyya, K.G.; Sen, G.S. Adsorption of chromium (VI) from water by clays. *Ind. Eng. Chem. Res.* **2006**, *45*, 7232–7240.
72. Yuna, Z. Review of the Natural, Modified, and Synthetic Zeolites for Heavy Metals Removal from Wastewater. *Environ. Eng. Sci.* **2016**, *33*, 443–454. [CrossRef]
73. Hawari, A.H.; Mulligan, C.N. Biosorption of lead (II), cadmium (II), copper (II) and nickel (II) by anaerobic granular biomass. *Bio-Resour. Technol.* **2006**, *97*, 692–700. [CrossRef]
74. Wang, S.; Zhu, Z. Characterisation and environmental application of an Australian natural zeolite for basic dye removal from aqueous solution. *J. Hazard. Mater.* **2006**, *136*, 946–952. [CrossRef]
75. Khamidun, M.; Fulazzaky, M.A.; Al-Gheethi, A.; Ali, U.; Muda, K.; Hadibarata, T.; Razi, M.M. Adsorption of ammonium from wastewater treatment plant effluents onto the zeolite; A plug-flow column, optimisation, dynamic and isotherms studies. *Int. J. Environ. Anal. Chem.* **2020**, *1*–22. [CrossRef]
76. Armağan, B.; Turan, M.; Elik, M.S. Equilibrium studies on the adsorption of reactive azo dyes into zeolite. *Desalination* **2004**, *170*, 33–39. [CrossRef]
77. Ameta, R.; Solanki, M.S.; Benjamin, S.; Ameta, S.C. Photocatalysis. In *Advanced Oxidation Processes for Waste Water Treatment*; Elsevier: Amsterdam, The Netherlands, 2018; pp. 135–175.
78. Pirc, G.; Stare, J. Titanium Site Preference Problem in the TS-1 Zeolite Catalyst: A Periodic Hartree-Fock Study. *Acta Chim. Slov.* **2008**, *55*, 951–959.
79. Krisnandi, Y.K.; Southon, P.D.; Adesina, A.A.; Howe, R.F. ETS-10 as a photocatalyst. *Int. J. Photoenergy* **2003**, *5*, 131–140. [CrossRef]
80. Tahir, M.B.; Rafique, M.; Rafique, M.S. Nanomaterials for photocatalysis. In *Nanotechnology and Photocatalysis for Environmental Applications*; Elsevier: Amsterdam, The Netherlands, 2020; pp. 65–76.
81. Fox, M.A.; Doan, K.E.; Dulay, M.T. The effect of the “inert” support on relative photocatalytic activity in the oxidative decomposition of alcohols on irradiated titanium dioxide composites. *Res. Chem. Intermed.* **1994**, *20*, 711–721. [CrossRef]
82. Arthur, J.D.; Langhus, B.G.; Patel, C. *Technical Summary of Oil & Gas Produced Water Treatment Technologies*; All Consulting LLC: Tulsa, OK, USA, 2005.
83. Shahryar, J. 6-Treatment of Oily Wastewater. In *Petroleum Waste Treatment and Pollution Control*; Shahryar, J., Ed.; Butterworth-Heinemann: Oxford, UK, 2017; pp. 185–267.
84. Artegiani, A. Ion Exchange and Demineralization. In *Tech Brief A National Drinking Water Clearing House Fact Sheet*; National Drinking Water Clearinghouse: Morgantown, WV, USA, 1997.
85. Guida, S.; Potter, C.; Jefferson, B.; Soares, A. Preparation and evaluation of zeolites for ammonium removal from municipal wastewater through ion exchange process. *Sci. Rep.* **2020**, *10*, 12426. [CrossRef]
86. Moran, S. Chapter 7—Clean water unit operation design: Physical processes. In *An Applied Guide to Water and Effluent Treatment Plant Design*; Moran, S., Ed.; Butterworth-Heinemann: Oxford, UK, 2018; pp. 69–100.
87. De Raffe, G.; Aloise, A.; De Luca, P.; Vuono, D.; Tagarelli, A.; Nagy, J.B. Kinetic and thermodynamic effects during the adsorption of heavy metals on ETS-4 and ETS-10 microporous materials. *J. Porous Mater.* **2016**, *23*, 389–400. [CrossRef]
88. Anderson, M.; Terasaki, O.; Ohsuna, T.; Philippou, A.; MacKay, S.P.; Ferreira, A.; Rocha, J.; Lidin, S. Structure of the microporous titanosilicate ETS-10. *Nature* **1994**, *367*, 347–351. [CrossRef]
89. Pavelić, S.K.; Medica, J.S.; Gumbarević, D.; Filošević, A.; Przulj, N.; Pavelić, K. Critical Review on Zeolite Clinoptilolite Safety and Medical Applications in vivo. *Front. Pharmacol.* **2018**, *9*, 1350. [CrossRef]

90. De Magalhães, L.F.; da Silva, G.R.; Peres, A.E.C. Zeolite application in wastewater treatment. *Adsorpt. Sci. Technol.* **2022**, *2022*, 4544104. [CrossRef]
91. Shi, J.; Yang, Z.; Dai, H.; Lu, X.; Peng, L.; Tan, X.; Shi, L.; Fahim, R. Preparation and application of modified zeolites as adsorbents in wastewater treatment. *Water Sci. Technol.* **2018**, *2017*, 621–635. [CrossRef] [PubMed]
92. Cakicioglu-Ozkan, F.; Ulku, S. The effect of HCl treatment on water vapor adsorption characteristics of clinoptilolite rich natural zeolite. *Microporous Mesoporous Mater.* **2005**, *77*, 47–53. [CrossRef]
93. Bouffard, S.C.; Duff, S.J. Uptake of dehydroabietic acid using organically-tailored zeolites. *Water Res.* **2000**, *34*, 2469–2476. [CrossRef]
94. Cortés-Martínez, R.; Solache-Ríos, M.; Martínez-Miranda, V.; Alfaro-Cuevas, V.R. Sorption Behavior of 4-Chlorophenol from Aqueous Solutions by a Surfactant-modified Mexican Zeolitic Rock in Batch and Fixed Bed Systems. *Water Air Soil Pollut.* **2007**, *183*, 85–94. [CrossRef]
95. Ghiaci, M.; Abbaspur, A.; Kia, R.; Seyedeyn-Azad, F. Equilibrium isotherm studies for the sorption of benzene, toluene, and phenol onto organo-zeolites and as-synthesized MCM-41. *Sep. Purif. Technol.* **2004**, *40*, 217–229. [CrossRef]
96. Zielirski, M.; Zielirska, M.; Dębowski, M. Ammonium removal on zeolite modified by ultrasound. *Desalination Water Treat.* **2015**, *57*, 8748–8753. [CrossRef]
97. Bagheri, S.; Hir, Z.A.M.; Yousefi, A.T.; Hamid, S.B.A. Progress on mesoporous titanium dioxide: Synthesis, modification and applications. *Microporous Mesoporous Mater.* **2015**, *218*, 206–222. [CrossRef]
98. Kozera-Sucharda, B.; Gworek, B.; Kondzielski, I.; Chojnicki, J. The Comparison of the Efficacy of Natural and Synthetic Aluminosilicates, Including Zeolites, in Concurrent Elimination of Lead and Copper from Multi-Component Aqueous Solutions. *Processes* **2021**, *9*, 812. [CrossRef]
99. Wang, L.; Shi, C.; Pan, L.; Zhang, X.; Zou, J.-J. Rational design, synthesis, adsorption principles and applications of metal oxide adsorbents: A review. *Nanoscale* **2020**, *12*, 4790–4815. [CrossRef]
100. Khan, M.M.; Adil, S.F.; Al-Mayouf, A. Metal oxides as photocatalysts. *J. Saudi Chem. Soc.* **2015**, *19*, 462–464. [CrossRef]
101. Alswata, A.A.; Bin Ahmad, M.; Al-Hada, N.M.; Kamari, H.M.; Bin Hussein, M.Z.; Ibrahim, N.A. Preparation of Zeolite/Zinc Oxide Nanocomposites for toxic metals removal from water. *Results Phys.* **2017**, *7*, 723–731. [CrossRef]
102. Mahalakshmi, M.; Priya, S.V.; Arabindoo, B.; Palanichamy, M.; Murugesan, V. Photocatalytic degradation of aqueous propoxur solution using TiO₂ and H β zeolite-supported TiO₂. *J. Hazard. Mater.* **2009**, *161*, 336–343. [CrossRef] [PubMed]
103. Mirzaei, D.; Zabardasti, A.; Mansourpanah, Y.; Sadeghi, M.; Farhadi, S. Efficacy of Novel NaX/MgO–TiO₂ Zeolite Nanocomposite for the Adsorption of Methyl Orange (MO) Dye: Isotherm, Kinetic and Thermodynamic Studies. *J. Inorg. Organomet. Polym. Mater.* **2020**, *30*, 2067–2080. [CrossRef]
104. Wang, C.; Shi, H.; Li, Y. Synthesis and characterization of natural zeolite supported Cr-doped TiO₂ photocatalysts. *Appl. Surf. Sci.* **2012**, *258*, 4328–4333. [CrossRef]
105. Alswat, A.A.; Bin Ahmad, M.; Saleh, T.A. Zeolite modified with copper oxide and iron oxide for lead and arsenic adsorption from aqueous solutions. *J. Water Supply Res. Technol.* **2016**, *65*, 465–479. [CrossRef]
106. Kong, F.; Zhang, Y.; Wang, H.; Tang, J.; Li, Y.; Wang, S. Removal of Cr(VI) from wastewater by artificial zeolite spheres loaded with nano Fe–Al bimetallic oxide in constructed wetland. *Chemosphere* **2020**, *257*, 127224. [CrossRef]
107. Zhang, W.; Xiao, X.; Zheng, L.; Wan, C. Fabrication of TiO₂/MoS₂@ zeolite photocatalyst and its photocatalytic activity for degradation of methyl orange under visible light. *Appl. Surf. Sci.* **2015**, *358*, 468–478. [CrossRef]
108. Italiya, G.; Ahmed, H.; Subramanian, S. Titanium oxide bonded Zeolite and Bentonite composites for adsorptive removal of phosphate. *Environ. Nanotechnol. Monit. Manag.* **2022**, *17*, 100649. [CrossRef]
109. Jaramillo-Fierro, X.; González, S.; Montesdeoca-Mendoza, F.; Medina, F. Structuring of ZnTiO₃/TiO₂ adsorbents for the removal of methylene blue, using zeolite precursor clays as natural additives. *Nanomaterials* **2021**, *11*, 898. [CrossRef]
110. Madima, N.; Mishra, S.B.; Inamuddin, I.; Mishra, A.K. Carbon-based nanomaterials for remediation of organic and inorganic pollutants from wastewater. A review. *Environ. Chem. Lett.* **2020**, *18*, 1169–1191. [CrossRef]
111. Piaskowski, K.; Zarzycki, P.K. Carbon-Based Nanomaterials as Promising Material for Wastewater Treatment Processes. *Int. J. Environ. Res. Public Health* **2020**, *17*, 5862. [CrossRef] [PubMed]
112. Zarzycki, P.K. *Pure and Functionalized Carbon Based Nanomaterials: Analytical, Biomedical, Civil and Environmental Engineering Applications*; CRC Press: Boca Raton, FL, USA, 2020.
113. Krissanasaerane, M.; Wongkasemjit, S.; Cheetham, A.K.; Eder, D. Complex carbon nanotube-inorganic hybrid materials as next-generation photocatalysts. *Chem. Phys. Lett.* **2010**, *496*, 133–138. [CrossRef]
114. Khanday, W.; Marrakchi, F.; Asif, M.; Hameed, B. Mesoporous zeolite-activated carbon composite from oil palm ash as an effective adsorbent for methylene blue. *J. Taiwan Inst. Chem. Eng.* **2017**, *70*, 32–41. [CrossRef]
115. Berber, M.R. Current Advances of Polymer Composites for Water Treatment and Desalination. *J. Chem.* **2020**, *2020*, 7608423. [CrossRef]
116. Alver, E.; Metin, A.Ü.; Çiftçi, H. Synthesis and characterization of chitosan/polyvinylpyrrolidone/zeolite composite by solution blending method. *J. Inorg. Organomet. Polym. Mater.* **2014**, *24*, 1048–1054. [CrossRef]
117. Khanday, W.; Asif, M.; Hameed, B. Cross-linked beads of activated oil palm ash zeolite/chitosan composite as a bio-adsorbent for the removal of methylene blue and acid blue 29 dyes. *Int. J. Biol. Macromol.* **2017**, *95*, 895–902. [CrossRef] [PubMed]

118. Pizarro, C.; Escudey, M.; Bravo, C.; Gacitua, M.; Pavez, L. Sulfate Kinetics and Adsorption Studies on a Zeolite/Polyammonium Cation Composite for Environmental Remediation. *Minerals* **2021**, *11*, 180. [CrossRef]
119. Senguttuvan, S.; Janaki, V.; Senthilkumar, P.; Kamala-Kannan, S. Biocompatible polypyrrole/zeolite composite for chromate removal and detoxification. *Mater. Lett.* **2021**, *308*, 131290. [CrossRef]
120. Yiğit, M.Y.; Baran, E.S.; Moral, Ç.K. A polymer—Zeolite composite for mixed metal removal from aqueous solution. *Water Sci. Technol.* **2021**, *83*, 1152–1166. [CrossRef]
121. Shahabuddin, S.; Sarih, N.M.; Mohamad, S.; Ching, J.J. SrTiO₃ Nanocube-Doped Polyaniline Nanocomposites with Enhanced Photocatalytic Degradation of Methylene Blue under Visible Light. *Polymers* **2016**, *8*, 27. [CrossRef]
122. Parekh, K.; Shahabuddin, S.; Gaur, R.; Dave, N. Prospects of conducting polymer as an adsorbent for used lubricant oil reclamation. *Mater. Today Proc.* **2022**, *62*, 7053–7056. [CrossRef]
123. Jaymand, M. Conductive polymers/zeolite (nano-)composites: Under-exploited materials. *RSC Adv.* **2014**, *4*, 33935–33954. [CrossRef]
124. Flores-Loyola, E.; Cruz-Silva, R.; Romero, J.; Angulo-Sánchez, J.; Castillon, F.; Fariás, M. Enzymatic polymerization of aniline in the presence of different inorganic substrates. *Mater. Chem. Phys.* **2007**, *105*, 136–141. [CrossRef]
125. Nascimento, G.M.D.; Temperini, M.L.A. Structure of polyaniline formed in different inorganic porous materials: A spectroscopic study. *Eur. Polym. J.* **2008**, *44*, 3501–3511. [CrossRef]
126. Sakellis, I.; Papathanassiou, A.; Grammatikakis, J. Effect of composition on the dielectric relaxation of zeolite-conducting polyaniline blends. *J. Appl. Phys.* **2009**, *105*, 64109. [CrossRef]
127. Malkaj, P.; Dalas, E.; Vitoratos, E.; Sakkopoulos, S. pH electrodes constructed from polyaniline/zeolite and polypyrrole/zeolite conductive blends. *J. Appl. Polym. Sci.* **2006**, *101*, 1853–1856. [CrossRef]
128. Vitoratos, E.; Sakkopoulos, S.; Dalas, E.; Malkaj, P.; Anestis, C.D.C. conductivity and thermal aging of conducting zeolite/polyaniline and zeolite/polypyrrole blends. *Curr. Appl. Phys.* **2007**, *7*, 578–581. [CrossRef]
129. Abukhadra, M.R.; Rabia, M.; Shaban, M.; Verpoort, F. Heulandite/polyaniline hybrid composite for efficient removal of acidic dye from water; kinetic, equilibrium studies and statistical optimization. *Adv. Powder Technol.* **2018**, *29*, 2501–2511. [CrossRef]
130. Petkowicz, D.I.; Pergher, S.B.; da Silva, C.D.S.; da Rocha, Z.N.; dos Santos, J.H. Catalytic photodegradation of dyes by in situ zeolite-supported titania. *Chem. Eng. J.* **2010**, *158*, 505–512. [CrossRef]
131. Abukhadra, M.R.; Shaban, M.; Sayed, F.; Saad, I. Efficient photocatalytic removal of safarnin-O dye pollutants from water under sunlight using synthetic ben-tonite/polyaniline@ Ni₂O₃ photocatalyst of enhanced properties. *Environ. Sci. Pollut. Res.* **2018**, *25*, 33264–33276. [CrossRef]